NASA CR-135115



# SOME EXPERIMENTS IN SWIRLING FLOWS: DETAILED VELOCITY MEASUREMENTS OF A VORTEX BREAKDOWN USING A LASER DOPPLER ANEMOMETER

by James Henry Faler

Cornell University
Ithaca, New York

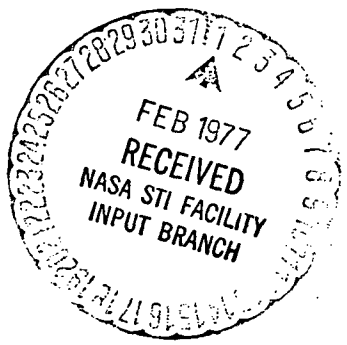


Prepared for

NATIONAL AERONAUTICS AND SPACE ADMINISTRATION
Lewis Research Center
Cleveland, Ohio 44135

September 1976

Grant NSG-3019

| 1. Report No. | 2. Government Accession No. | 3. Recipient's Catalog No. |
|---|---|---|
| NASA CR-135115 | | |

| 4. Title and Subtitle | 5. Report Date |
|---|---|
| SOME EXPERIMENTS IN SWIRLING FLOWS: DETAILED VELOCITY MEASUREMENTS OF A VORTEX BREAKDOWN USING A LASER DOPPLER ANEMOMETER | 6. Performing Organization Code |

| 7. Author(s) | 8. Performing Organization Report No. |
|---|---|
| James Henry Faler | None |
| | 10. Work Unit No. |

| 9. Performing Organization Name and Address | 11. Contract or Grant No. |
|---|---|
| Cornell University<br>Ithaca, New York 14850 | NSG-3019 |
| | 13. Type of Report and Period Covered |
| 12. Sponsoring Agency Name and Address | Contractor Report |
| National Aeronautics and Space Administration<br>Washington, D.C. 20546 | 14. Sponsoring Agency Code |

15. Supplementary Notes

Final Report. Project Manager, Cecil J. Marek, Airbreathing Engines Division, NASA Lewis Research Center, Cleveland, Ohio. Report was submitted as a thesis in partial fulfillment of the requirements for the degree Doctor of Philosophy at Cornell University in September 1976.

16. Abstract

The results of an experimental study of spiraling flows in a slightly diverging, circular duct are reported. Seven types of flow disturbances were observed. In addition to the spiral and axisymmetric vortex breakdowns and the double helix mode, four other forms were identified and are reported for the first time. The type and axial location of the disturbance depended on the Reynolds and circulation numbers of the flow. Detailed velocity measurements were made by using a laser Doppler anemometer. Measurements made far upstream of any disturbance showed that the introduction of swirl resulted in the formation of a high axial velocity jet centered around the vortex center. A mapping of the velocity field of a so-called axisymmetric breakdown, formed at a Reynolds number of 2560, revealed that the recirculation zone is a two-celled structure, with four stagnation points on the vortex axis marking the axial extremes of the concentric cells. The dominant feature of the flow inside the bubble was the strong, periodic velocity fluctuations. Existing theoretical models do not predict the two-celled structure and the temporal velocity fluctuations that were observed.

| 17. Key Words (Suggested by Author(s)) | 18. Distribution Statement |
|---|---|
| Flow visualization<br>Vortex breakdown<br>Laser anemometer<br>Swirling flows | Unclassified - unlimited |

| 19. Security Classif. (of this report) | 20. Security Classif. (of this page) | 21. No. of Pages | 22. Price* |
|---|---|---|---|
| Unclassified | Unclassified | 216 | |

* For sale by the National Technical Information Service, Springfield, Virginia 22161

CONTENTS

LIST OF ILLUSTRATIONS

SUMMARY

Spiralling flows in which the axial and swirl velocity components are comparable often undergo a change in structure at some axial location along the vortex axis. The flow upstream of the change is typically steady and axisymmetric, and has small radial speeds and axial gradients. At the disturbance location, significant axial gradients and radial velocities develop and the flow becomes asymmetric and unsteady. A change which is abrupt and causes stagnation is called vortex breakdown. In this experimental study, spiralling flows were produced in a circular duct which had a divergence angle of 1.43°. Detailed velocity measurements were made and, using dye injection, extensive flow visualization studies were performed. In addition to the three previously reported disturbances (the spiral, axisymmetric, and double helix modes), four other types were identified and are reported for the first time. Each form is discussed in detail and photographs are presented. The type of disturbance formed and its axial location depended on the Reynolds number and swirl-vane angle. The velocity measurements were made using a laser Doppler anemometer. This non-invasive optoelectronic technique circumvented the difficulty encountered by previous researchers attempting to measure this sensitive flow with probes. Laser Doppler anemometry is discussed briefly and the particular instrumentation used is described in detail. Axial and swirl velocity profiles were measured far upstream of the disturbance for Reynolds numbers of 3220, 4540, and 6000, with various values of swirl. In each case, the introduction of significant swirl

STAR category 34

resulted in an axial velocity profile which was sharply peaked near the vortex center, with the centerline axial velocity increased to about twice its zero swirl value. A detailed map of the velocity field associated with a so-called axisymmetric breakdown, formed at a Reynolds number of 2560, was obtained. The centerline axial velocity decreased rapidly upstream of the breakdown, decaying from its peak value to zero in one bubble length. Although the velocities upstream of the disturbance were steady, the dominant feature of the flow inside the bubble was the strong, regular temporal fluctuations of velocity. The time averaged velocity data showed the bubble to be a two celled structure, with four stagnation points on the vortex axis marking the axial extremes of the concentric cells. The streamline pattern of the mean flow inside the recirculation zone is presented. The temporal fluctuations were strongest and most regular in the rear portion of the breakdown and resulted in a continual exchange of fluid across the mean bubble envelope. Spectral analysis of the fluctuations showed a fundamental frequency of about 2 Hz, which showed good correlation with the angular frequency at which the asymmetric rear portion of the bubble rotated about the tube axis. This indicates that the temporal fluctuations correspond to an azimuthal periodicity associated with a disturbance propagating about the vortex axis. Neither the periodic velocity fluctuations nor the mean flow patterns observed are predicted by existing theoretical models. Two approaches are suggested for future simulations.

CHAPTER ONE

## 1.0. Introduction

Spiralling flows in which the axial and swirl, or azimuthal, velocity components are of comparable magnitude often undergo an abrupt change in structure near the axis of the vortex. This abrupt change in vortical structure is commonly referred to as vortex breakdown or vortex bursting. The base flows upstream of the breakdown generally are characterized by a small (or zero) radial velocity component, axial symmetry (or near symmetry) about the vortex axis, small axial gradients, and roughly equal swirl and axial components of velocity. The occurrence of breakdown results in severe retardation or stagnation of the axial flow near the vortex axis, large axial gradients, and significant radial velocity.

Vortex breakdowns have, in the past, been classified as either asymmetric or axisymmetric. The asymmetric, or spiral, form shown in Figure [3.8] has been observed both in rotating flows in tubes and in radially unbounded swirling flows over delta wings at high incidence angles. The so-called axisymmetric form (thus named because the envelope of the recirculating cell of fluid is quite axisymmetric) has been observed mainly in tube flow experiments and, evidently, occurs only occasionally in leading edge vortex flows.

The occurrence of vortex breakdown can be significant in many circumstances. The abrupt formation of a breakdown over a delta wing results in a sudden change in the lift characteristics of the wing. The performance of pumps and compressors could be deleteriously affected by the

presence of a vortex breakdown in the inlet sections. Contrarily, it has been suggested that vortex breakdown may be useful in dissipating the trailing vortices generated by large aircraft which can otherwise persist for long periods of time and have caused upsets of trailing aircraft. Vortex breakdown may be useful as a flame holder in gas turbine combustor cans to increase combustion efficiency, reduce the combustor size, and help control the amount of pollutants formed.

## 1.1. Theoretical Explanations

Because of its practical importance and its remarkable nature, vortex breakdown has been the subject of many studies, both experimental and theoretical, since the first recorded observation of the phenomenon (Peckham and Atkinson, 1957). Hall (1972) presented a summary of the experimentally observed features of vortex breakdown and critically reviewed the various theoretical studies that had been proposed to predict the occurrence and mechanism of formation of this phenomenon. The interested reader is referred to this review for a more detailed explanation of the theoretical studies published prior to 1972.

In summary, the explanations proposed can be generally divided into three categories.

a) Ludwieg (1962,1964) and Jones (1964) proposed that the phenomenon is the result of the hydrodynamic instability of the vortex core with respect to spiral disturbances.

b) Hall (1966,1967) and Gartshore (1962) contended that vortex breakdown is analogous, in some sense, to the separation of a two-dimensinal boundary layer. That is, the assumption is made that the flow

sufficiently far upstream of breakdown is quasi-cylindrical (small radial speeds and axial gradients). The appropriate forms of the Navier-Stokes equations are then integrated using given upstream conditions and the integration is continued until the initial assumption of small axial gradients appears to be violated. The contention is made that even though the quasi-cylindrical approximation is no longer valid, the actual flow would also develop large axial gradients at approximately the same axial location and thus vortex breakdown would occur there. This is analogous to using the boundary layer equations to predict the point of separation even though the boundary layer approximation may no longer be valid in that region.

An inherent shortcoming of this method is that only the location of the breakdown can be predicted and nothing can be learned about the flow pattern near or downstream of breakdown. Bossel (1969) used a similar approach, but by making additional assumptions was able to compute the flow field inside the axisymmetric bubble (only axisymmetric breakdowns are admitted with this model because the equations are axisymmetric). Mager (1972) used the quasi-cylindrical momentum integral equations and claimed agreement between his results and the experimental observations of Sarpkaya (1971 A,B).

c) The third proposal offered to explain the vortex breakdown flow involves the idea of a critical state, which is the dividing point between a supercritical flow, which cannot support axisymmetric disturbance waves, and a subcritical flow, which can. This is analogous to a hydraulic jump in open channel flow or the sonic condition in compressible flow. Squire (1960) first introduced the concept by seeking the flow

conditions that could result in the existence of standing waves in the flow field. The concept of a critical state was further delineated and amplified by Benjamin (1962,1967), who dealt with steady, axisymmetric, inviscid flow in a tube of constant area. Benjamin showed that for a given upstream supercritical flow a number of conjugate flows were possible that were subcritical. This theory proposes that the vortex breakdown is the transition from the supercritical flow to a subcritical conjugate flow. No details of the flow in the transition region itself can be predicted by this method.

Leibovich (1970), Leibovich and Randall (1973), and Randall and Leibovich (1973) expanded on the work of Benjamin and dealt with finite amplitude waves in tubes of slowly varying cross sections. The transition region was considered in detail in these papers, and in Randall and Leibovich the wall pressure distribution and bubble shape and size were predicted. The predictions agree reasonably well with experimental results.

Other theoretical studies dealing with vortex breakdown have been primarily numerical. Kopecky (1971) and Torrance and Kopecky (1971) did numerical computations for rotating flows in tubes at relatively low Reynolds numbers. Grabowski (1974) obtained numerical solutions for an unconfined, viscous vortex embedded in an irrotational flow with uniform upstream axial velocity.

## 1.2. Experimental Studies

The theoretical studies summarized above attempted, in large part, to explain the experimental observations reported by a considerable number of researchers. The preponderance of early experimental work was concerned with vortex breakdowns occurring over delta wings at high angles

of attack [22-24]. Lambourne and Bryer (1962) did extensive flow visualization studies of the bursting of leading edge vortices above delta wings of various sweep back angles for a range of angles of attack. They were able, through photographic techniques, to describe the spiral mode of breakdown in detail, such as the sense and frequency of rotation of the spiral filament and the approximate fluid particle path along the surface of an imaginary body of revolution swept by the rotating spiral filament. The effect on breakdown position caused by changes in sweepback angle, incidence angle, and Reynolds number was reported. Various other factors affecting breakdown position were also investigated, such as sudden alterations to free stream velocity and the introduction of bodies near the breakdown. In addition, the effects that the breakdown had on surface flow patterns and surface pressure distributions were studied. It should be noted that the so-called axisymmetric form of breakdown was observed only occasionally by Lambourne and Bryer and it persisted for short durations.

Although Lambourne and Bryer did not perform detailed velocity measurements of the vortex breakdown flow, they suggested that such measurements should be possible, even in the immediate vicinity of the breakdown. They based this judgment on their observations of the response of the breakdown to the insertion of slender bodies into the flow near the breakdown. However, Hummel (1965) reported that the insertion of a probe upstream of the breakdown resulted in an upstream movement of the breakdown that made meaningful measurements impossible. Hummel, working with an experimental set-up similar to that used by Lambourne and Bryer (and others), was able to minimize this disturbance effect caused by the probe

by placing an obstacle downstream of the inclined delta wing. With the obstacle in place downstream, he was able to perform measurements which were used to plot contours of constant speed and constant pressure in four planes. These planes were at various axial locations, perpendicular to the line of symmetry of the wing, upstream and downstream of the breakdown as well as near the breakdown region itself. The results showed that the flow upstream of the breakdown was quite symmetric about the vortex axis. Near the breakdown, the vortex became quite asymmetric and there was pronounced retardation near the vortex axis. Hummel claimed good agreement between these results and those predicted by Ludwieg's instability theory. Hall (1972) pointed out inconsistencies between the two, however.

The complicated nature of the leading edge vortex flow prompted researchers to attempt to produce breakdowns in a simpler geometry, the vortex tube. Lambourne and Bryer (1961, Appendix A1) produced breakdowns in a constant diameter duct using an apparatus similar to that used by Titchener and Taylor-Russell (1956). The swirl was imparted by a set of swirl vanes placed in the entrance region of the tube. This method of swirl generation was also used by Harvey (1962), Kirkpatrick (1964), and Sarpkaya (1971A, 1971B, 1974) and is used in the present study.

Harvey, using a tube of constant diameter, produced a so-called axisymmetric breakdown and was able to measure the swirl angle distribution upstream of the breakdown using smoke injection techniques. He found that the maximum swirl angle was approximately 50°-51° and that the swirl angle distribution approximated the exponential form,

$$\phi = \tan^{-1}[Ar^{-1}(1-e^{-Br^2})],$$

where A and B are constants. Harvey also reported the results of an experiment in which an insert was placed into the constant diameter duct. This insert had a center section of constant, reduced diameter which was smoothly joined to the existing tube by an upstream, converging section and downstream, diverging section. Harvey found that, under the appropriate flow conditions, an axisymmetric type of breakdown could be precipitated upstream of the insert (by using a probe) and that a second vortex breakdown existed in the reduced diameter throat of the insert.

Sarpkaya (1971A) performed extensive flow visualization studies of the vortex breakdown phenomenon in a slightly diverging tube. He presented striking photographs of the spiral and axisymmetric modes of breakdown and, in addition, reported the observation of a third form of disturbance which he called the double helix form (see Chapter 3). Sarpkaya found that the type and location of breakdown, for a fixed vane angle, varied strongly with Reynolds number. For each of the vane angles used, a spiral mode was formed relatively far downstream of the start of the diverging section at the lowest flow rates. As the flow rate was increased the breakdown moved upstream and at some higher value of Reynolds number the spiral changed into, in most cases, the axisymmetric mode. Once this transformation had occurred, subsequent increases in Reynolds numbers served only to move the axisymmetric mode further upstream. Sarpkaya reported that occasionally, at high vane angles and low Reynolds numbers, the double helix mode was observed as an intermediate form between the spiral and axisymmetric modes.

The strong relationship between Reynolds number and breakdown location found by Sarpkaya was at variance with the weak relationship reported by Lambourne and Bryer (1961) for leading edge vortex flows.

Another difference between the two studies concerned the sense of the spiral filament. While both found that the geometric form rotated about the vortex axis in the same direction as the upstream flow, Lambourne and Bryer reported that the spiral filament was of the opposite hand to the outer helical streamline and Sarpkaya reported that both were of the same hand.

Sarpkaya also studied the effects that sudden alterations in the flow rate and vane angle had on breakdown location and form. The measurements presented by Sarpkaya were axial profiles of wall pressure near the breakdown (also reported by Kirkpatrick), centerline axial velocity just upstream of the breakdown, and the radial distribution of swirl angle upstream of breakdown. Sarpkaya found the maximum swirl angle to be 50° for axisymmetric breakdowns and 38° to 45° for spiral breakdowns. For all cases, the swirl angle distribution was similar to the exponential form found by Harvey. In later reports Sarpkaya presented more detailed descriptions of the double helix mode (1971B) and studied the effects of various tube divergence angles (1974).

The experimental studies summarized above provided considerable information about the vortex breakdown flow, especially with regard to those features which one is able to observe using flow visualization techniques. The various forms of breakdown, the parameters affecting its location and form, and its response to sudden alterations of the flow were studied extensively and this research supplied the information and insight which stimulated the various theoretical attempts to explain this phenomenon. Due to the limitations of visualization techniques, however, previous experimental researchers were unable to provide detailed

velocity measurements of the vortex breakdown flow field. Detailed velocity measurements are necessary both to provide a foundation for theoretical models of the flow and as a standard against which the results of theoretical simulations can be compared.

## 1.3. Outline of Study

The two major difficulties associated with obtaining detailed velocity measurements of the vortex breakdown flow are the extreme sensitivity of the flow and the quasi-steady nature of the breakdown. In this study, these difficulties were circumvented by using the non-invasive technique of laser Doppler anemometry and by using a flow apparatus which was carefully constructed to minimize disturbances to the flow.

The experimental flow apparatus is described in Chapter 2. The fundamental principles of the laser Doppler anemometry technique are presented, a detailed description of the optical and electronic equipment is given, and the optical alignment procedure is outlined. The swirl vane array, which was used to impart a precisely controlled swirl to the flow, is discussed in Appendix A1. The refraction effects caused by using a circular cross section test section are presented in Appendix A2.

Chapter 3 deals with the results of extensive flow visualization studies. In addition to the three disturbance forms reported previously [Sarpkaya, 1971 A,B] four other distinguishable forms were observed. These forms are described in detail and photographs of each are presented. The transformations from one disturbance type to another are discussed and supporting evidence is given to explain why some disturbance forms are seen **only** at low Reynolds numbers. Some apparant discrepancies between these results and those of Sarpkaya (1971 A,B) are noted. The

response of the breakdown to sudden alterations in swirl or flow rate and the accompanying changes in the centerline axial velocity far upstream of breakdown are also presented in Chapter 3.

Detailed velocity measurements of the vortex breakdown flow are presented in Chapter 4; tabulated velocity data are given in Appendix A3. A discussion of experimental accuracy and equipment limitations is also presented in Chapter 4. The first group of results deals with the base flow profiles of axial and swirl velocity. These profiles were measured far upstream of the flow disturbance for three fixed Reynolds numbers, with swirl as a parameter. The measurements show the strong effect that the presence of a significant swirl velocity has on the axial velocity profiles, with the most dominant change being the development of a high axial velocity near the tube axis.

Finally, the results of extensive measurements of the velocities associated with a single vortex breakdown are presented. The breakdown was a so-called axisymmetric mode, and a detailed mapping of the velocity field, both outside of and within the breakdown envelope, is shown. The profiles of axial and swirl velocity at various axial locations approaching the breakdown are given which show the development of large axial gradients near the breakdown nose. The measurements inside of the bubble envelope and in the wake region indicate that the flow is dominated by strong, regular fluctuations of velocity. The time average profiles are presented and the mean streamlines inside the breakdown are given. These results show that a two cell structure exists within the bubble and, for time averaged velocities, four stagnation points are present along the tube axis inside of, and on, the bubble envelope. The fluctuation

amplitudes within the bubble are shown to be quite strong, especially in the downstream portion of the bubble. Spectral analysis of the axial velocity at several locations shows that these fluctuations have a dominant frequency that does not vary with location.

The fluctuations indicate that the flow is not, in fact, axisymmetric even though the bubble envelope shows a high degree of axial symmetry over most of its length. Thus, the results indicate that models based on assumptions of axial symmetry and steadiness cannot be expected to predict the flow patterns actually measured in the important recirculation zone of the vortex breakdown flow. The mean, time-averaged flow patterns differ significantly from those predicted by all existing simulations.

# CHAPTER TWO

## 2.0. Experimental Apparatus

The primary objective of this study was to provide detailed velocity measurements of the vortex breakdown flow field. Previous investigators [11, 27] had reported two major difficulties which had prevented them from making these measurements in the vicinity of the breakdown. First, the vortex breakdown was only quasi-steady in position and was continually shifting slightly in a slow, random manner along the axis of the vortex. The second problem, related to the first, was that the introduction of a probe into the vortex core upstream of breakdown disturbed the flow in such a way that accurate velocity measurements were not possible.

It was hoped that the first difficulty, although probably inherent in the phenomenon, could be minimized by exercising great care in the design and construction of the flow system. The second problem was circumvented by the use of the non-invasive method of flow measurement known as laser Doppler anemometry. In addition to eliminating the insertion of mechanical probes into the flow, this technique also offered good spatial resolution, unambiguous resolution of a velocity into its components, and excellent temporal response to transients and required no tedious calibration.

## 2.1 The Flow Device

The device used in this study is similar in form to that used successfully by Sarpkaya [11, 12, 29]. As illustrated by the schematic [2.1], the apparatus consisted of upper and lower constant head tanks, a test tank, a rotameter, and the necessary piping, valves, and filters.

The constant head tanks were fixed in position and were baffled to help eliminate pressure fluctuations. The upper tank, with a capacity of .132 $m^3$, was continuously supplied with fresh, filtered, constant temperature tap water by a control valve. This valve, which was fed by the building's hot and cold water lines, automatically compensated for temperature and pressure fluctuations in the supply pipes. The temperature of the water at the valve exit was set initially to match room temperature. This value was then maintained automatically by the valve, within a tolerance of $\pm$ .5°C. The flow rate was set so that the upper tank was continuously overflowing.

Six inlet pipes, 2.5 cm I.D., supplied water from the upper constant head tank to the test tank. Each inlet was equipped with an inline filter and on-off valve. After flowing through the test tank, the water was routed through a 2.5 cm I.D. exit pipe, a precision rotameter, and a large needle valve to the lower constant head tank, of capacity .057 $m^3$. The absolute accuracy of the rotameter corresponded to an error in Reynolds number, based on flow rate and test section diameter, of $\pm$ 220. The reproduceability was $\pm$ .25% of the indicated flow rate (Reynolds number). The flow rate was varied by

Figure 2.1. Schematic of Flow Apparatus

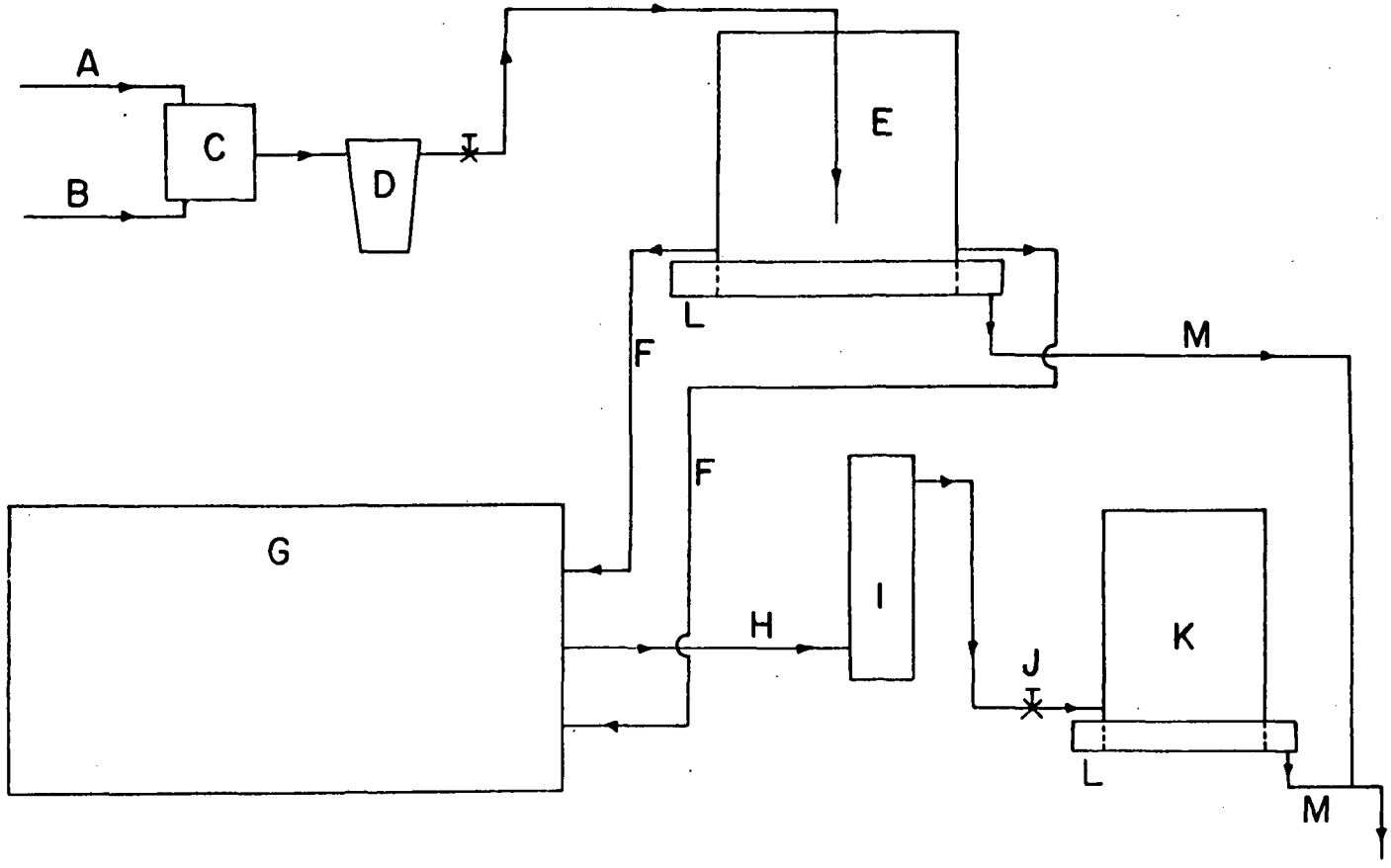


A. Cold Water Line
B. Hot Water Line
C. Automatic Mixing Valve
D. Filter
E. Upper Constant Head Tank
F. Inlet Pipes (2 of 6 shown)
G. Test Tank
H. Exit Pipe
I. Rotameter
J. Needle Valve for Flow Rate Control
K. Lower Constant Head Tank
L. Overflow Trays
M. Overflow Pipes to Building Drain

adjusting the needle valve placed between the rotameter and lower constant head tank. Water overflowing from both head tanks was collected in trays and piped down the building drain.

The test tank, Figures [2.2, 2.3], was constructed of 2.54 cm thick Plexiglas and had inside dimensions of 1.37 m long, .4 m wide and .4 m high. Water entered the tank through the six inlet pipes. These pipes were connected to nipples embedded in one end wall of the tank. The nipples were evenly spaced on the circumference of a 25 cm circle which was concentric with the centerline of the device.

A baffle, made of fully reticulated polyurethane foam and Plexiglas discs, was placed inside the tank near this end wall. This baffle served to disperse the inlet jets and helped insure uniform flow across the height and width of the tank.

A brass plate, 2.20 cm thick, was bolted to the other end-wall of the tank. This plate supported the 32 guide vanes, the planetary gear system which controlled the vane orientation, and a Plexiglas center-body, which helped direct the flow into the test section entrance, Figure [2.10]. The vanes, which imparted the desired swirl to the fluid, were symmetric foils with a chord of 4.37 cm and a span of 2.89 cm. See Appendix A1 for details of vane construction and alignment. Each foil was rigidly attached to a shaft which was supported by bearings mounted in the brass plate. These 32 shafts were equally spaced on the circumference of a 22.86 cm diameter circle which was concentric with the centerline of the brass plate. An O-ring provided the necessary rotary seal for each shaft.

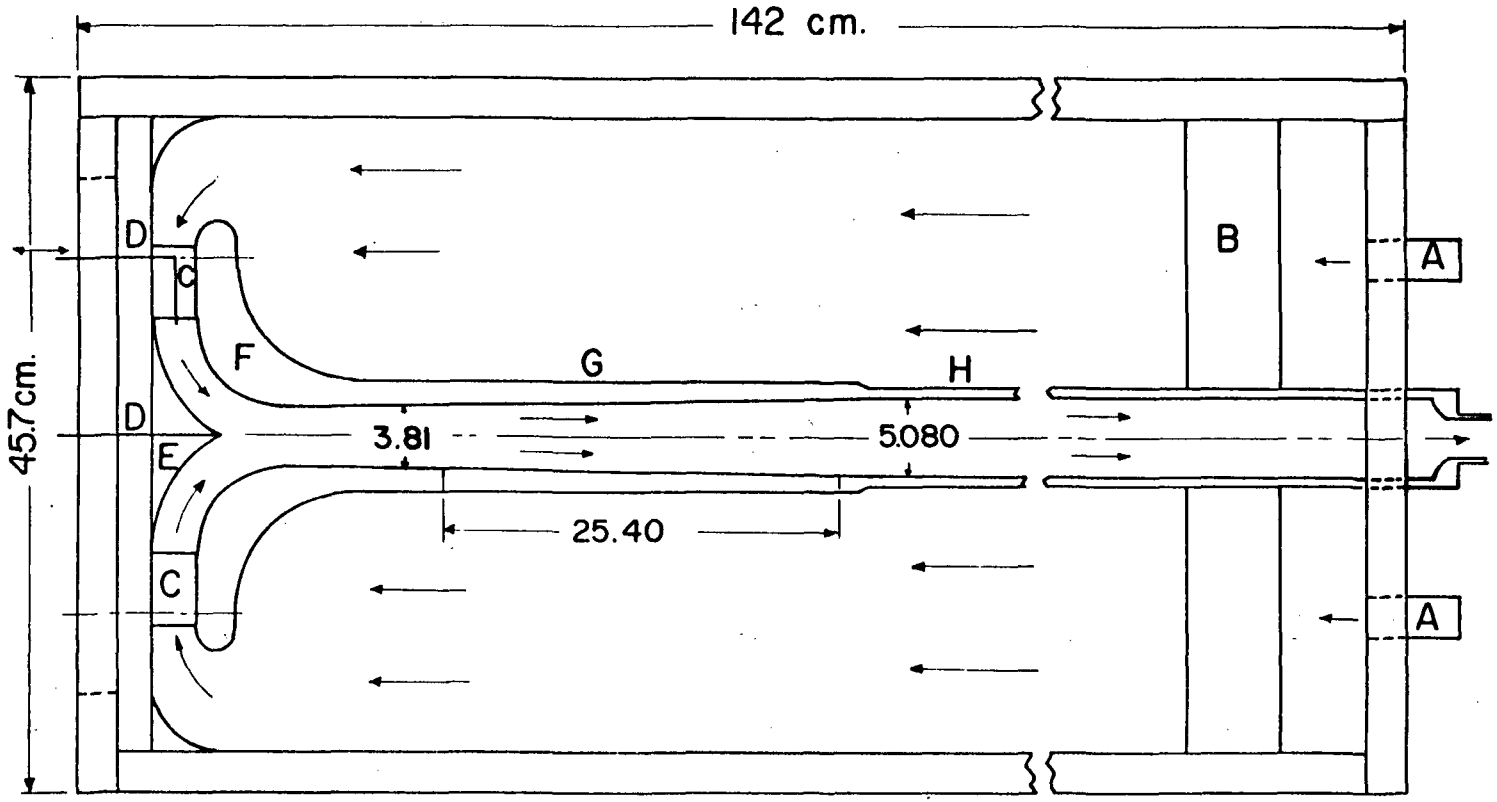


Figure 2.2. Test Tank Layout and Dimensions

A. Inlet Pipes (2 of 6 shown)
B. Foam Baffle
C. Swirl Vanes (2 of 32 shown)
D. Dye Injector Tubes
E. Centerbody
F. Entrance Channel Bell-Mouth
G. Test Section
H. Exit Pipe

A planetary gear system, as seen in Figure [2.4], rotated each of these shafts in unison so that, at any one setting, each vane made the same angle with a radial line drawn from the center of the brass plate to the pivot line of the vane. This angle could be varied continuously from 0° to 60°. A 9000 to 1 gear reduction between the actuating wheel and the vane shafts, as well as individual torsion springs used to eliminate lash between the planet and the sun gears, guaranteed accurate and reproduceable vane settings. A small, variable speed motor was used to drive the gear system when continuous, rather than incremental, vane angle adjustment was desired. An instrument counter indicated the vane angle setting.

The fluid was directed through the vane array by an annular channel formed on one side by the brass plate and attached center body, and on the other by a bell-shaped piece, also made of Plexiglas. Radiused strips were placed along the tank wall - brass plate junction. These helped to direct the flow radially inward. The entrance channel was designed so that the pressure gradient was always favorable to minimize the possibility of flow separation. All joints were kept smooth to reduce flow disturbances.

The test section, machined from Plexiglas and highly polished, was joined at the upstream end to the bell-shaped piece and at the downstream end to a constant diameter Plexiglas exit pipe. This assembly was supported at its upstream end by a wire and screw arrangement, with the screws threaded into the tank sidewalls. This permitted the vertical and

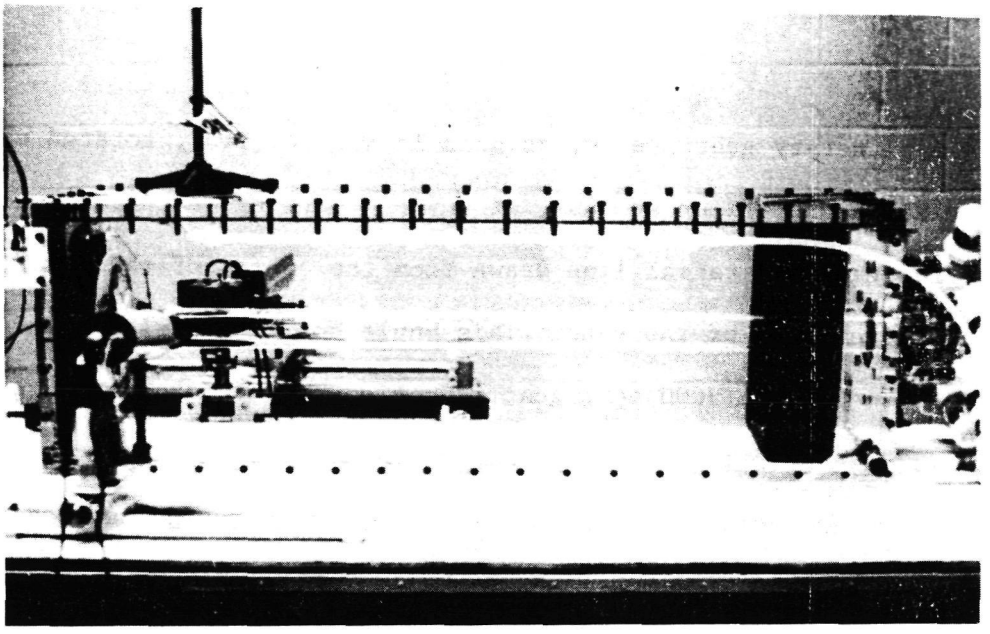

Figure 2.3. A Photograph of the Test Tank and Optical Equipment. The Laser, Input Optical Unit, and Traversing Mechanism May be Seen in the Background. The Receiving Optics and Their Traversing Slide are in the Foreground. The Stand on Top of the Tank Held a Viewing Mirror.

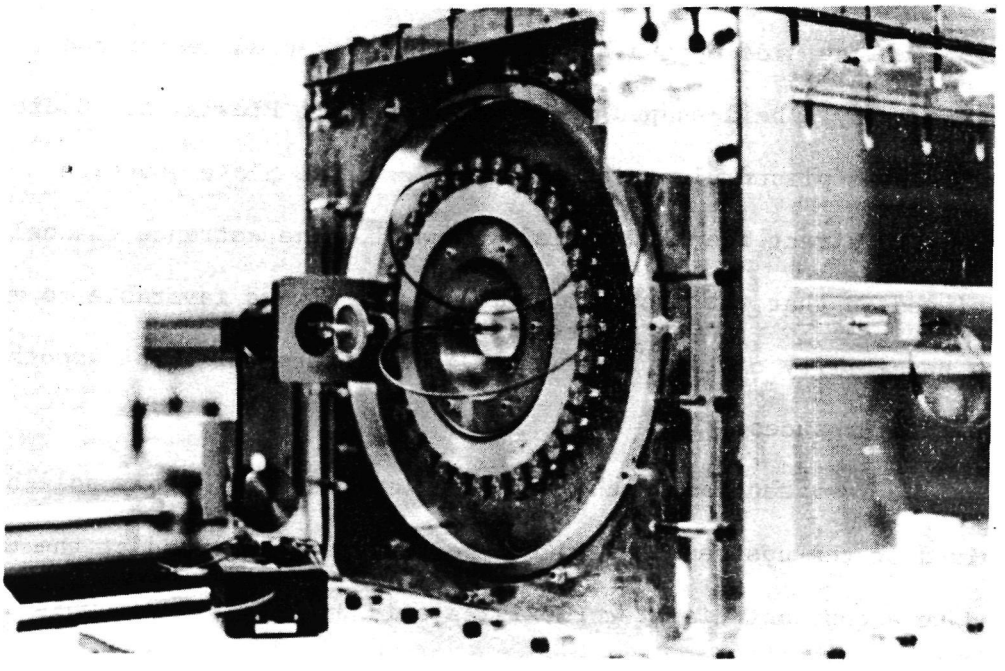

Figure 2.4. A Photograph of the Planetary Gear System Which Controlled Swirl Vane Orientation.

horizontal adjustment necessary to ensure that the centerline of the bellmouth was coincident with the centerline of the brass plate.

In order to keep the tube axis perpendicular to the brass backing plate, any adjustment at the upstream end was compensated for at the downstream end by another assembly which permitted vertical and horizontal adjustment. This assembly was mounted on the outside face of the downstream end wall of the tank and included the following; a roll-sock sleeve of neoprene rubber provided a seal which permitted motion in three directions, an annular ring with locating screws to provide vertical and horizontal adjustment of exit tube position, a wire and screw arrangement to provide axial adjustment of the bellmouth-test section-exit tube assembly (to control bellmouth-face to vane-end clearance), and a reducer-connector which provided a smooth reduction in tube I.D. and had an integral nipple for connection to the tube leading to the rotameter.

The axial variation of the inside diameter of the tube assembly was; a converging entrance section formed by the bellmouth and centerbody, a 10.5 cm long throat with an inside diameter of 3.81 cm, a test section in which the I.D. changed linearly from 3.81 to 5.08 cm in a length of 25.4 cm (a divergence angle of 1.43°), an exit portion of inside diameter 5.08 cm which extended past the tank end wall, and the reducer which smoothly reduced the inside diameter to 2.54 cm. A scale, attached to the outside of and running the length of the test section, served to indicate axial distance.

Dye could be introduced into the flow at two locations. One dye injector was a piece of hypodermic tubing which extended along the centerline of the Plexiglas centerbody and protruded slightly into the fluid.

This provided a marker filament along the tube axis. The second injector was installed into one specially modified guide vane. The tip of the hypodermic tubing extended slightly beyond the trailing edge of the vane, and a slot allowed the injector to be moved in the spanwise direction. This permitted dye to be introduced at various radial locations in the tube. Since it rotated with the vane, this injector was always aligned correctly, with its axis parallel to the flow. Each injector was fed by its own reservoir, and the flow of dye was controlled by needle and shut-off valves. The marker fluid could be introduced continuously or in short pulses. Both washable inks and biological stains were used at various times. These were diluted with water to ensure that no great density difference existed between the dye and the water flow.

Two manifolds, each feeding three branches leading into the tank, extended along one of the tank sidewalls. One of these, close to the bottom edge of the tank, was connected to the inlet side of a small centrifugal pump. The other manifold, which was close to the top of the tank, was connected to the pump outlet. This system was one of a number of improvements made to solve problems that became apparent during the initial running of the experiment. Specifically, it was found that any significant difference in temperature between the room air and the water caused secondary, natural convection flows near the tube entrance. This effect resulted in an asymmetric feeding of fluid into the vane array and thus produced a non-uniform swirl velocity.

This difficulty led to the installation of the mixing valve to control the temperature of the water fed to the upper constant-head tank. A variation in room temperature could thus be compensated for by manually

changing the feed water temperature. A second problem then appeared.

A sudden adjustment in water temperature led to stable stratification inside the test tank. This stratification took the form of a stagnant layer of fluid trapped in either the top or bottom regions of the test tank. This also resulted in an asymmetric feeding of fluid into the entrance channel of the tube. This layer would often persist for hours if remedial action was not taken. The centrifugal circulation pump/manifold system was used to mix the water in the tank to destroy the stratification in a few minutes. The system was then shut off and the residual secondary flow the pump caused was allowed to decay before proceeding with the experiment. Eventually, an air conditioner was installed and this, in conjunction with the mixing valve, resolved the problems completely.

The test tank rested on the top of a table which was mounted on air bags. The pneumatic support system permitted adjustment of the height and inclination of the flow apparatus centerline. This adjustment was necessary to provide accurate alignment of the test section centerline with respect to the laser anemometer traversing mechanism.

## 2.2. The Laser Doppler Anemometer: Background of Technique

The opto-electronic technique, usually known as Laser Doppler Anemometry (LDA) or Laser Doppler Velocimetry (LDV) is a fairly new method of fluid velocity measurement. A brief discussion of the principals of operation will be presented. The technique was first reported by Yeh and Cummins [30] in 1964, and since that time a significant amount of research and development work has been done to improve the method. Considerable improvements have been made in the optical configurations used and in the

electronics systems necessary to utilize the technique in transient and/or turbulent flows. Several systems are now commercially available. An extensive bibliography of LDA literature can be found in reference [31].

Various optical configurations have been used successfully in laser anemometry, and the technique may be viewed in several different ways. All of these viewpoints yield the same end result however since all ultimately depend on the Doppler effect. This well known phenomenon, as illustrated in Figure [2.5], states that light scattered from a particle moving with velocity $\bar{v}$ will be shifted in frequency, relative to the incident, by an amount $f = \frac{1}{\lambda} \bar{v} \cdot (\hat{e}_s - \hat{e}_i)$. The following derivation, which does not explicitly include this equation, is perhaps easier to understand and yields the same result produced by applying the Doppler equation to the beam geometry described below.

If two monochromatic beams of light, Figure [2.6], of comparable intensity and wavelength $\lambda$, intersect at an angle $\theta$, they will form an interference fringe pattern. These fringes will be parallel to the bisector of the angle formed by the two beams and equally spaced a distance d apart, where $d = \lambda/(2\sin(\theta/2))$. If a particle, with diameter comparable to $\lambda$, intersects this fringe pattern, the intensity of the light scattered by the particle will vary as the particle traverses alternately light and dark fringes. If the particle has a velocity component, v, perpendicular to the fringes the frequency, $f_D$, of this variation in scattered intensity is the velocity divided by the fringe spacing, or $f_D = (2v \sin(\theta/2))/\lambda$. Therefore, if $\theta$ and $\lambda$ are known from the optical configuration used, a measurement of $f_D$ provides the velocity component, v.

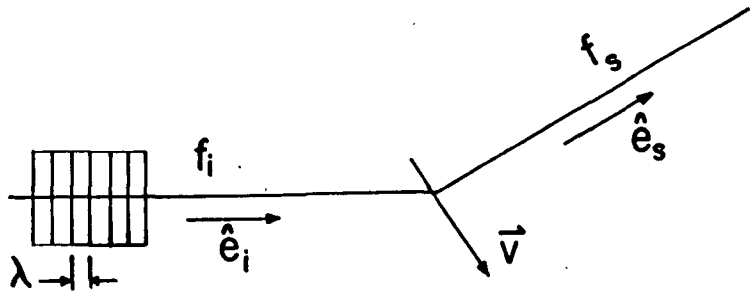


Figure 2.5. The Doppler Effect. When a Particle with Velocity $\vec{V}$ Scatters Light, of Initial Frequency $f_i$, Wavelength $\lambda$, and Direction $\hat{e}_i$, the Light Scattered in Direction $\hat{e}_s$ is of Frequency $f_s$, where $f_s - f_i = 1/\lambda \, \vec{V} \cdot (\hat{e}_s - \hat{e}_i)$.

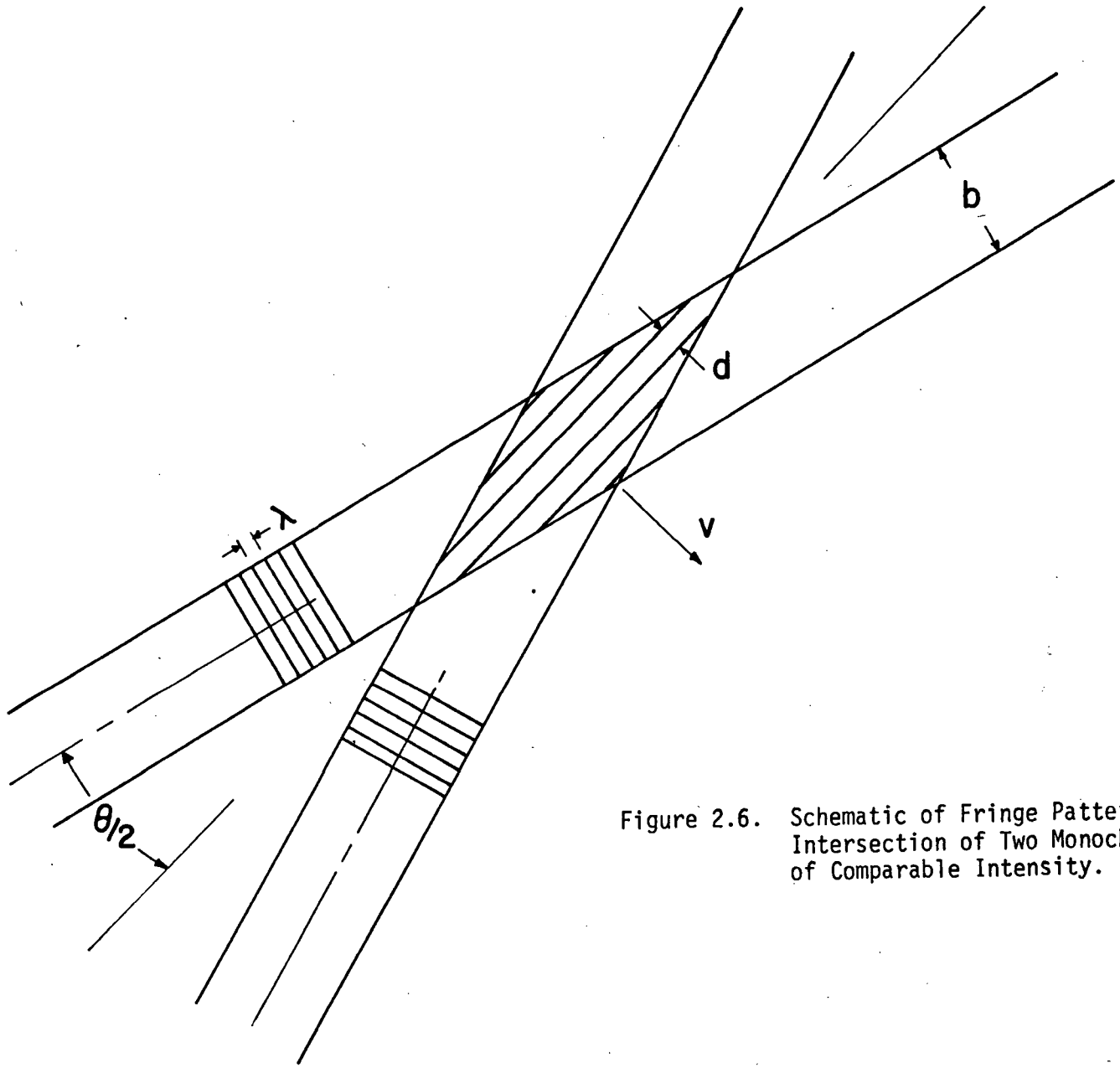


Figure 2.6. Schematic of Fringe Pattern Formed by the Intersection of Two Monochromatic Beams of Comparable Intensity.

It should be noted that the velocity measured is actually the particle velocity. But since these particles have diameters comparable to the light wavelength, the particle velocity is assumed to be equal to the local fluid velocity. LDA measurements of air flows usually require the introduction of scattering particles, but water usually contains sufficient amounts of impurities and additional seeding is unnecessary. No seeding was done in this study.

The frequency, $f_D$, is generally measured by collecting some of the scattered light with a lens system which focuses it onto the photocathode of a photomultiplier tube. $f_D$ is independent of the collector lens location. Thus, the scattered light may be collected in any convenient location. However, the intensity of back-scattered light (light scattered back towards the incident beams) is small compared to forward scattered light. For this reason, the photomultiplier is usually placed so that it detects forward scattered light. Back-scattering may be used in conjunction with sufficiently high output lasers, usually $CO_2$ or argon.

The spatial resolution of the instrument is determined by the size of the scattering volume, which is defined as that volume common to both intersecting beams. This is an important consideration, since it determines the dimensions over which the velocity is averaged in the measurement. Referring again to Figure [2.6], for two beams of diameter b intersecting at an angle $\theta$ the dimensions of the scattering volume are: the height, perpendicular to the plane defined by the two beams, is equal to b; the width, **perp**endicular to the bisector, is equal to $b/\cos(\theta/2)$; and the length, along the bisector, is equal to $b/\sin(\theta/2)$. Thus spatial resolution is improved by decreasing the beam diameter and/or increasing the intersection angle.

The problem of processing the photomultiplier signal is a difficult one, and much of the research in laser Doppler anemometry has been concerned with the subject. Typically, the signal is difficult to process for a number of reasons. In general,

a) The signal usually has a low signal/noise ratio.

b) The frequency of the signal, which is proportional to the velocity, is varying in time, often over a braod range.

c) The signal is usually characterized by frequency phase shifts caused by having two (or more) particles in the scattering volume at any one time.

d) Conversely, there may be relatively long periods in which no signal exists due to having an absence of particles in the scattering volume.

The two methods that have proven most successful are the direct counter (time domain) and Doppler frequency tracker (frequency domain). In the direct counter technique, the time that a particle takes to traverse N fringes is actually measured, and from this the particle velocity is determined. The Doppler frequency tracker, as the name implies, employs a feedback circuit to allow the instrument to follow a semi-continuous, time-varying frequency. The output is usually an analog voltage proportional to the instantaneous signal frequency, and thus proportional to the instantaneous fluid velocity. Since a fairly continuous signal is necessary for the tracker technique, it is most suitable for flows which contain a fairly large number of particles, such as water flows.

The direct counter technique, on the other hand, needs relatively few scattering particles. More specifically, these processors are designed

to reject data taken during periods in which more than one particle is in the scattering volume, since this would result in an inaccurate time measurement. The direct counter is used, then, for air flows which are only lightly seeded (or even unseeded), or for water flows in which the water is highly filtered.

Consider again the basic equation relating signal frequency to particle velocity, $f = (2v \sin(\theta/2))/\lambda$. Two difficulties associated with the basic method can be seen. First, low velocities give rise to low frequency signals. Low frequencies are difficult to demodulate and most tracker systems operate poorly in the low frequency ranges. In many cases, low velocities occur in regions of high velocity gradients, which give rise to large amplitude, rapid fluctuations in frequency. As a result, the practical lower limit for most tracker systems, using the basic optical system described above, is several cm/sec.

The second difficulty is that the basic equation indicates that there is an ambiguity in the sign of velocity. The signal contains no information to indicate the direction in which the particle is traversing the fringe pattern.

Both of these difficulties can be resolved by shifting the frequency of one or both input beams before they intersect. If the two intersecting beams differ in frequency by an amount $f_o$, it can easily be shown that the basic equation relating the frequency of the scattered light, $f_D$, to the particle velocity component, v, becomes

$$f_D = f_o + \frac{2v \sin(\theta/2)}{\lambda} \qquad 2.1$$

This effect can be thought of as providing fringes which are moving through

the intersection volume. Thus, a particle with velocity component, v, moving in the opposite direction that the fringes are moving will result in a frequency higher than $f_o$; similarly, a particle moving in the same direction as the fringe system will result in a frequency less than $f_o$. This modification to the basic method yields a considerable improvement in system performance. It allows the technique to be used to measure velocity unambiguously in applications in which the flow direction is unknown or is changing in time.

## 2.3. The Laser Doppler Anemometer System Used

The anemometer used in this study was the DISA type 55L system. Only minor modifications were made to the system to improve the spatial resolution and to allow either of two velocity components to be measured with a minimum of re-alignment.

A schematic of the optical system used is shown in Figure [2.7]. As supplied, the system consisted of a laser, an optical unit (enclosed in dotted lines in the figure), and the photomultiplier tube assembly.

Laser - The laser used was a Spectra-Physics model 120. This was a Helium-Neon laser which had an output power of 5 mW. A 3X beam expander, made from two telescope eyepiece lenses, was mounted on the front of the laser head. This beam expander was added to improve the spatial resolution of the system (see Appendix A2 for explanation).

Optical Unit - The optical unit combined its various components into a single, compact package. The entire optical assembly could be rotated about the centerline of the unit. Mirrors $M_1$ and $M_2$ were added to the system to reduce alignment difficulties associated with the optical support/traversing system used (see Sections 2.5, 2.7 for details).

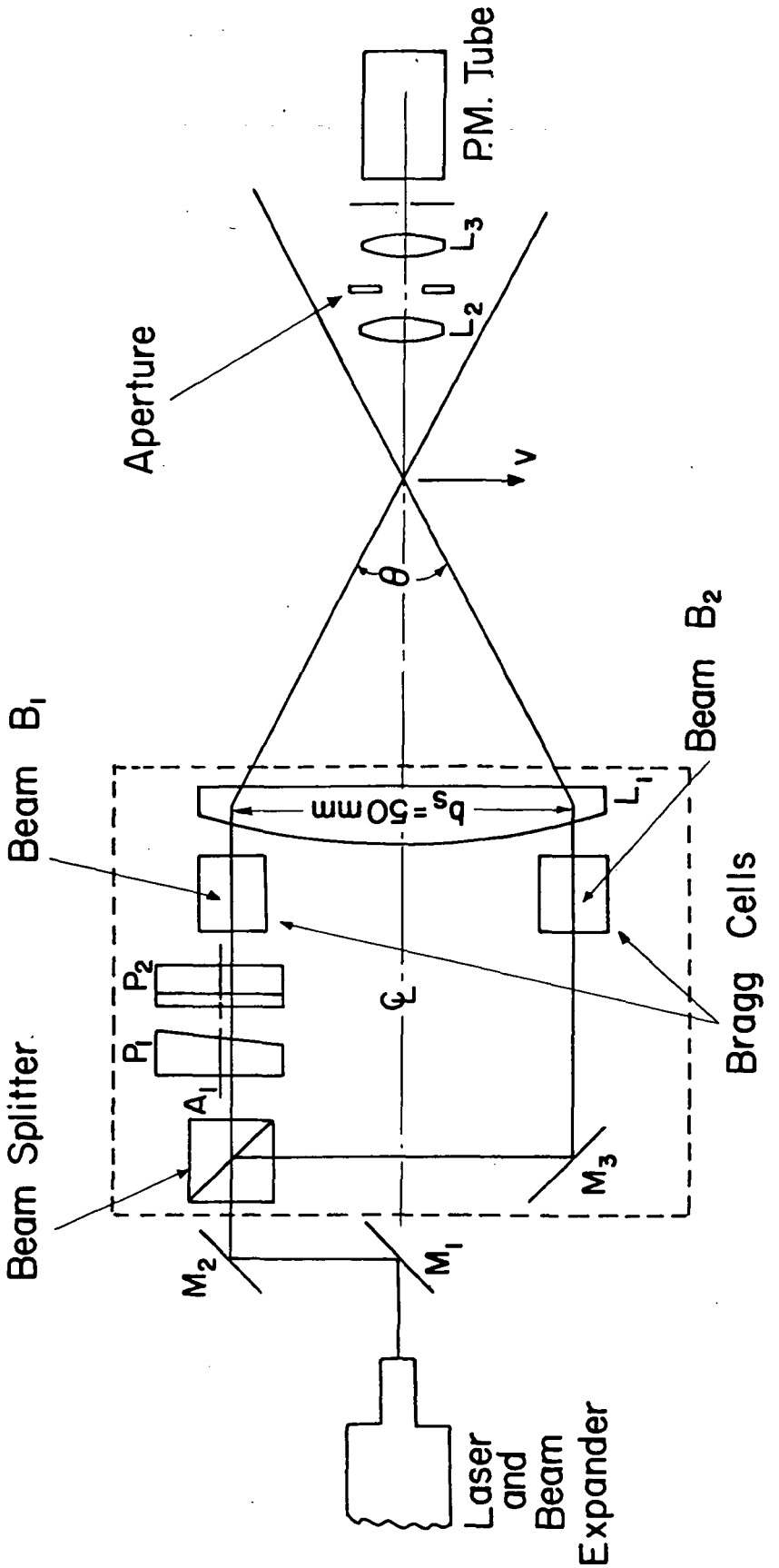


Figure 2.7. Schematic of the Optical System.

These two mirrors were mounted on a small platform rigidly attached to the originally supplied optical assembly. $M_1$ was rigidly attached to this platform and $M_2$ was mounted in a gimballed holder which also was attached to the platform. $M_2$ could rotate about two perpendicular axes and the distance from $M_1$ to $M_2$ was variable.

The input laser beam, which was aligned to be coincident with the centerline of the unit, was reflected by $M_1$ and $M_2$ and impinged on a biprism beamsplitter which split the beam into two beams, $B_1$ and $B_2$, approximately equal in intensity. $B_2$ was reflected by mirror $M_3$; the distance between the beamsplitter and $M_3$ was adjustable. The direction of $B_1$ could be altered slightly by rotating the prisms $P_1$ and/or $P_2$ about axis $A_1$. $P_1$ and $P_2$ were 3° wedge prisms which were oriented so that their wedge angles were nominally 90° apart, with rotation measured with respect to axis $A_1$.

By carefully adjusting

a) The $M_1$-$M_2$ distance and $M_2$ orientation

b) The beam splitter - $M_3$ distance

c) The wedge prisms $P_1$ and $P_2$

it was possible to align the beams $B_1$ and $B_2$ to be parallel to, in the plane of, and equidistant from the centerline of the optical assembly. The distance between the beams, $b_s$, was equal to 50 mm. This insured that each beam would then be accurately centered on the aperture of one of the Bragg cells.

The Bragg cells used were opto-acoustic modulators which shifted the frequency of the laser light. Each cell consisted of a block of glass with piezo-electric transducers bonded along one side and an acoustic absorber mounted on the opposite side. The piezo-electric transducers

were driven by an oscillator and sent acoustic wavefronts across the glass block. When properly aligned with respect to the incident laser beam, the laser light would interact with the acoustic wavefronts with the result that the output beam frequency would differ from the input frequency by an amount equal to the acoustic frequency (oscillator frequency).

As supplied, the oscillators which drove the cells were set so that the output beam frequency of each cell differed from the other by a known, incrementally adjustable amount. This difference in frequency is the value of $f_o$ in equation [2.1].

The two beams then struck lens $L_1$, of focal length F, This lens simultaneously focused each beam and caused them to intersect at their focal points. As previously stated, beams $B_1$ and $B_2$ were aligned to be parallel to, in the plane, and equidistant from the optical axis. These alignment conditions insured that,

a) the two output beams would intersect, with the intersection point on the optical axis.

b) the two intersecting beams and the optical axis would be coplanar.

c) the bisector of the angle formed by the two intersecting beams would be coincident with the optical axis.

The focal length of this lens, F, determined both the distance between the lens and the intersection point and, since the beam separation, $b_s$, was fixed, the intersection angle, $\theta$. The focal length was also an important parameter in determining the spatial resolution of the instrument

(see Appendix A2). Three lenses, with focal lengths equal to 13 cm, 30 cm and 60 cm, were supplied with the optical unit. In order to maximize the spatial resolution in applying this unit to the flow device previously described, it was necessary to obtain a fourth lens, with a focal length of 20 cm.

In summary, the goal of the alignment of the laser head/optical unit (i.e. the input optics) was to have the bisector of the angle formed by the intersecting beams, the optical unit centerline, and the input laser beam colinear.

Photomultiplier Assembly - As a particle traverses the intersection volume, it scatters light in all directions. The intensity of the scattered light varies as a function of viewing angle. However, the frequency, which is linearly related to the particle velocity, is independent of the viewing angle. Therefore, it is possible to collect scattered light over a finite solid angle, and in any convenient location in which the scattered light intensity is sufficiently high.

In the system used, the photomultiplier assembly was placed on the opposite side of the flow device from the input optics. Some of the scattered light was collected by lens $L_2$, passed through a variable aperture to lens $L_3$, which focused the light onto a small pinhole placed in front of the photocathode of the shielded photomultiplier tube. A viewing system, mounted integrally with the photomultiplier assembly, allowed the intersection point image to be observed on the pinhole disc for focusing and alignment. The image of the two intersecting beams, which took the form of an X, could easily be seen on this disc. The final focusing and alignment were carried out by moving the photomultiplier assembly, with

respect to the intersection volume, so that the cross-over point was sharply focused and centered on the pinhole.

## 2.4. Electronics and Instrumentaion

The photomultiplier tube converted the information carried by the scattered light into an FM electrical signal. Thus, the photomultiplier output was an FM signal with frequency equal to the scattered light frequency, $f_D$. The electronics system used was necessary to process this FM signal and convert it into a more suitable form for data acquisition.

1. High Voltage Supply - This unit supplied a continuously adjustable DC voltage to the photomultiplier tube. This voltage and the resulting anode current level were displayed on meters mounted on the instrument. The anode current depended on the amount of light hitting the photocathode and the DC voltage level. Thus, the DC voltage was adjusted to provide a suitable anode current for the amount of scattered light present.

2. Doppler Signal Processor - This instrument, composed of a preamplifier and frequency tracker, frequency demodulated the photomultiplier output. The output was an analog voltage proportional to the instantaneous input frequency. The frequency range, 2.25 KHz to 15 MHz, was covered in seven ranges: 2.25 to 15 KHz, 7.5 to 50 KHz, 22.5 to 150 KHz, 75 to 500 KHz, .225 to 1.5 MHz, .75 to 5 MHz, and 2.25 to 15 MHz. The Bragg cell oscillators were set so that the frequency shift, $f_o$, was incrementally adjustable to be 7.5 KHz, 25 KHz, 75 KHz, 250 KHz, .75 MHz, 2.5 MHz, and 7.5 MHz. Thus, the Bragg cell frequency shift, which corresponded to zero fluid velocity, could be set, if desired, to be at the center of any chosen frequency range. The accuracy of the instrument, as supplied, was ±1% of full scale deflection of the range in use. However, this accuracy was improved to be ±.25% of

indicated frequency by carefully calibrating the signal processor using a frequency generator and a frequency counter.

The signal processor was capable of tracking a frequency input which was varying in time. Periodic input frequency fluctuations of up to ±70% of mean could be tracked successfully. Since tracking ability was enhanced by higher mean frequencies, but accuracy suffered, the choice of the Bragg cell frequency shift used was a compromise between these two effects.

A "dropout" circuit and indicating meter, integral with the unit, were used to determine the relative duration of periods in which no signal existed. The meter had a scale of 0% (signal always present) to 100% (no signal present). In general, the instrument required manual tuning until the feedback circuit was completed, as indicated by a low dropout, and thereafter the unit would automatically follow any changes in input frequency. Long periods of dropout, or large, rapid fluctuations in frequency would result in loss of tracking, and manual retuning was necessary.

The input frequency was indicated directly on a panel meter. For more accurate readings, an analog voltage was available. This voltage, e, was proportional to meter deflection. Specifically, for input frequency, $f_D$, and full scale reading for range in use, $f_{MAX}$,

$$e = 10 \times f_D/f_{MAX}$$

Thus, e varied from 0 to 10 volts, and for a fluid velocity which varied in time about a mean value, the output voltage had an AC component, proportional to the fluctuations, and a DC component proportional to the mean velocity. The following instruments were used in this study to further process or record this analog voltage.

3. Signal Conditioner - This unit had a variable high and low pass filter section. This could be used to spectrum analyze the AC component of the analog voltage. A zero suppression circuit was included, and this could be used to suppress the DC component.

4. RMS Voltmeter - This voltmeter measured the true root mean square value of the AC component, either with or without prior filtering with the signal conditioner. Various integration times could be selected, from .3 to 100 sec, depending on the frequency range of the signal. The r.m.s. value was indicated on a meter, and an analog voltage output, proportional to meter deflection, was also available.

5. Digital Voltmeter - This voltmeter was used to measure the DC component of the analog voltage. A choice of seven time constants, from .1 to 100 sec, allowed the measurement of the mean voltage within the selected time interval. The readout could be held at any desired instant by means of a remote switch.

6. Strip Chart Recorder - A multi-channel strip chart recorder was used to simultaneously record the analog voltage, either with or without filtering and suppression, and the r.m.s. value of the AC component. A third channel was also used to record a signal which indicated the vortex breakdown position (see Chapter 4).

## 2.5. Optical System to Flow Device Alignment

The primary goal of this study was to measure the axial and swirl velocities at various locations in the test section of the flow device. The following conditions had to be met in order to do this successfully.

1. The two laser beams had to intersect in the flow.

2. The wavelength, $\lambda$, of the laser light and the angle between the intersection beams, $\theta$, had to be known. It should be emphasized that in equation [2.1], which relates frequency shift to velocity, $\theta$ and $\lambda$ are local values, measured in the flow medium at the point of intersection. These parameters also affect the size of the intersection volume and, therefore, the spatial resolution of the measurement.
3. The location of the intersection point, measured with respect to the cylindrical coordinate system defined by the test section centerline, had to be known.
4. The velocity component measured by the laser Doppler anemometer is determined by the input laser beams. Specifically, the component measured is in the plane defined by the intersecting beams and normal to the bisector of the angle formed by the beams. Therefore, the input beams had to be aligned so that their orientation with respect to the tube coordinate system was known. This insured that the velocity measured corresponded to either the axial or swirl velocity.
5. A traversing mechanism had to be built which could move the optics in a precise way so that measurements could be taken at various locations. The movement of the optics had to be accomplished in such a way that the various alignment criteria were maintained.

The alignment of the laser head/optical unit had to be done outside of the flow device. The laser head was first adjusted so that the beam was in a horizontal plane, parallel to one axis of the traversing system. Then the alignment of the optical unit, as described in section 2.3, was

done and this resulted in two laser beams which intersected at their focal points. A short focal length lens (4 mm) was placed near the intersection point and the magnified image of the intersecting beams was displayed on a screen. In this way, final adjustments to the beams could be made to insure intersection and, with the Bragg cell oscillators turned off, the interference fringe pattern could be seen.

Great care was taken to insure that the centerline of the optical unit and the bisector of the angle formed by the intersecting beams were coincient with the input laser beam, which served to define a reference line. Since this criterion was met, the optical unit could be translated in the direction of this reference line with the only result being a simple translation of the intersection point along the same reference line. Similarly, the optical unit could be rotated about its centerline and this resulted in a rotation of the plane defined by the two intersecting beams about the same reference line.

Using a precision level to indicate the horizontal, the optical unit was rotated until the beams were in the horizontal plane. Scribe lines on the optical unit mounting ring were made to indicate this position. This position was used to measure axial velocities. Similarly, a thin plumb line was used to indicate the vertical, the optical unit was rotated until the beams were in the vertical plane, and a scribe line was made to indicate this position of the optical unit. The vertical position was used to measure the swirl velocities.

With the beams in the horizontal plane, the angle formed by the two beams in air, $\theta_a$, was measured. This was done by mounting a needle point in a precision traversing device which allowed motion in two orthogonal

directions in the horizontal plane. Using simple geometry, the angle could be calculated by measuring the length of the two normal legs of two right triangles, each one having a laser beam as its hypotenuse. Several trials were made, and the average was used. The precision which resulted was ±.3%.

Since the velocity measurements were to be done in water flowing through a test section which was circular in cross section, the refraction effects had to be considered in detail. In order to minimize the difficulties associated with the circular test section, the optical system was oriented, with respect to the flow device, so that the horizontal plane which contained the reference line was normal to the tank side walls and passed through the centerline of the test section. This alignment was maintained at all times in the experiment.

Figure [2.8] is a schematic of the input optics system and flow device, with the input beams in the horizontal plane. This setup was used to measure axial velocity. The optical system was mounted on a traversing mechanism which allowed motion in two orthogonal directions in the horizontal plane, X and Y. The X axis was parallel to the centerline and sidewalls of the flow device. The air bags which supported the flow device allowed the height and inclination of the device centerline to be adjusted so that it was contained in the horizontal plane formed by the input beams. This could be checked by injecting a thin dye streak onto the tube centerline and visually checking to insure that the beams intersected the dye streak, independent of the X position of the optical system.

The X axis was aligned to be parallel to the tank sidewalls, tube O.D., and the centerline of the device. This was done by moving the X axis laterally until it was equidistant from the tank wall. The final adjustment

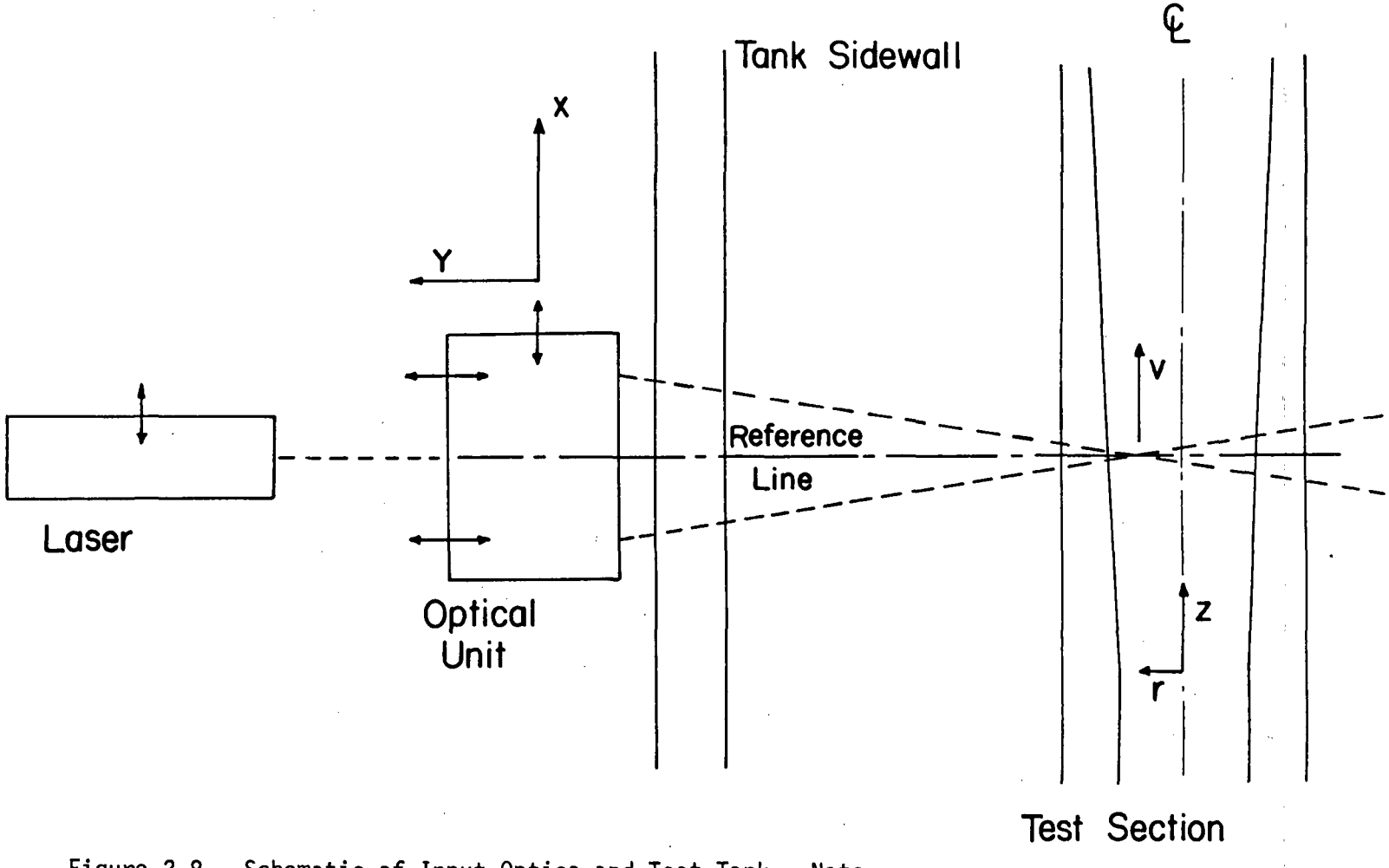


Figure 2.8. Schematic of Input Optics and Test Tank. Note Orientation of Traversing Axes (X,Y) and Reference Line with Respect to Test Section Coordinates (z,r).

of the flow device consisted of rotating the whole flow device about its centerline, using the pneumatic support system until the sidewalls were vertical. This was checked using a precision level.

Since the reference line, defined by the input laser beam, was parallel to the Y axis this alignment procedure insured that the reference line remained in the horizontal plane which contained the centerline of the test section and was normal to this centerline for all X, Y positions of the optical system. The X, Y position of the optical system could be continuously adjusted and monitored. Initially, the optical unit was traversed in the Y direction until the beams intersected on the thin dye streak located at the center of the test section. This Y position, with the beams intersecting at r = 0 of the cylindrical coordinate system defined by the tube centerline, was taken as a reference position, $Y_o$.

The axial reference location, $X_o$, was determined in the following way. A mirror and magnifying lens were mounted on the top of the flow device. This system was carefully aligned to eliminate parallax between the scale, running axially along the outside diameter of the test section and the centerline of the test section. This permitted the viewing of the beam intersection point on the dye streak from a convenient location, and provided an accurate indication of the axial location of the intersection point. The optical system was moved in the X direction until the intersection point was located .5 cm downstream of the start of the diverging portion of the test section. This X reference was denoted as $X_o$. Since z = 0 was taken as the start of the diverging portion, $X = X_o$ corresponded to z = .5 cm.

The accuracy of the initial alignment of optical system to flow device

was difficult to ascertain, since there was no way, other than visual, to check it. Since the intersection volume dimension along the bisector was about five times greater than its dimensions perpendicular to the bisector, the $Y_o$ reference was more difficult to determine with great accuracy. It was estimated that for $Y = Y_o$, $r = 0. \pm .55$ mm. This assumed that the dye streak provided an accurate indication of $r = 0$. Since any significant deviation of the dye streak from $r = 0$ resulted in a helical filament, because of the swirl velocity present, this assumption could be checked visually for validity. The accuracy of the axial reference was estimated to be for $X = X_o$, $z = 0 \pm .15$ mm.

## 2.6. Beam Intersection Details; Spatial Resolution

In order to develop a relationship between the position of the optical system in the X, Y coordinate system and the location of the intersection point in the z, r coordinate system, the refraction effects of the various interfaces had to be considered. This analysis also provided information on the intersection angle in the water, $\theta$, the light wavelength in water, $\lambda$, and the orientation of the bisector of the angle with respect to the test section centerline.

A summary of the results developed in Appendix A2 are presented here. For each optical unit orientation, beams in horizontal plane (axial velocity) or beams in the vertical plane, a new optical system coordinate system x, y was used, where $x = X - X_o$, $y = Y - Y_o$. As shown in Appendix A2, the effects of the divergence of the test section could be ignored in the region where measurements were made, $|x| < 4$ cm. (For large x, the optical unit would have to be moved in the Y direction and a new $Y_o$ established.)

For axial velocity, u, the equations necessary were

$$z = .5 + x$$

$$r = n_w\, y$$

$$f_D = f_o + \frac{u\theta_a}{\lambda_a}$$

where

$n_w$ = index of refraction of water

$\lambda_a$ = light wavelength in air

For swirl velocity, v,

$$\theta = \frac{\theta_a}{n_w} + \left(\frac{r_o - r_i}{r_o r_i}\right)\left(\frac{n_p - n_w}{n_p}\right)\theta_a\, y$$

where

$n_p$ = index of refraction of Plexiglas

$r_o$ = outside radius of test section

$r_i$ = inside radius of test section

In addition, the intersection volume is shown to be, approximately, a cylinder with the diameter equal to

$$\frac{4}{\pi}\lambda_a \frac{F}{B}$$

where

F = focal length of optical unit lens

B = diameter of input laser beam

and a length, along the bisector of the angle formed by the beams, equal to

$$\frac{4}{\pi}\lambda_a \frac{n_w}{b_s}\frac{F^2}{B}$$

The length was of concern in the experiment because it was oriented radially, and thus regions of high radial gradients would be difficult to measure. To reduce this length it was necessary to increase B and decrease F as much as possible. B was increased by fitting a 3X beam expander to the laser head.

As shown in Appendix A2, the minimum F that was possible, due to the minimum working distance between test section and optics, was approximately 185 mm. Due to availability, a lens with a nominal focal length of 200 mm was used.

With this equipment, the dimensions of the cylindrical intersection volume were approximately; diameter = .08 mm and length = .43 mm.

## 2.7. Traversing Systems

As developed in the previous sections,

1. The goal of the optical unit to laser head alignment was to have the input laser beam coincident with the centerline of the optical unit.
2. The goal of the input optics to flow device alignment was to insure that the reference line, defined by the input laser beam, was in the horizontal plane which contained the centerline of the flow device and was normal to that centerline.

The traversing system and adjustment mechanisms, Figure [2.9], which supported the laser head and optical unit were designed to permit the above goals to be met and maintained, while also allowing the optical unit to be moved in the X, Y coordinate system.

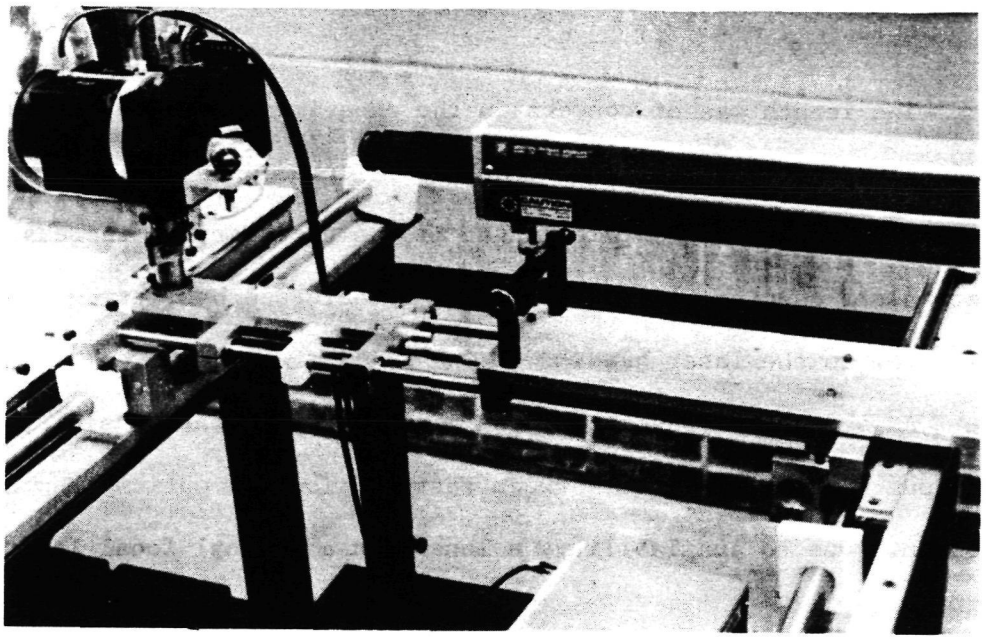

Figure 2.9. A Photograph of the Laser Head and Optical Unit Mounted on the Traversing Mechanism.

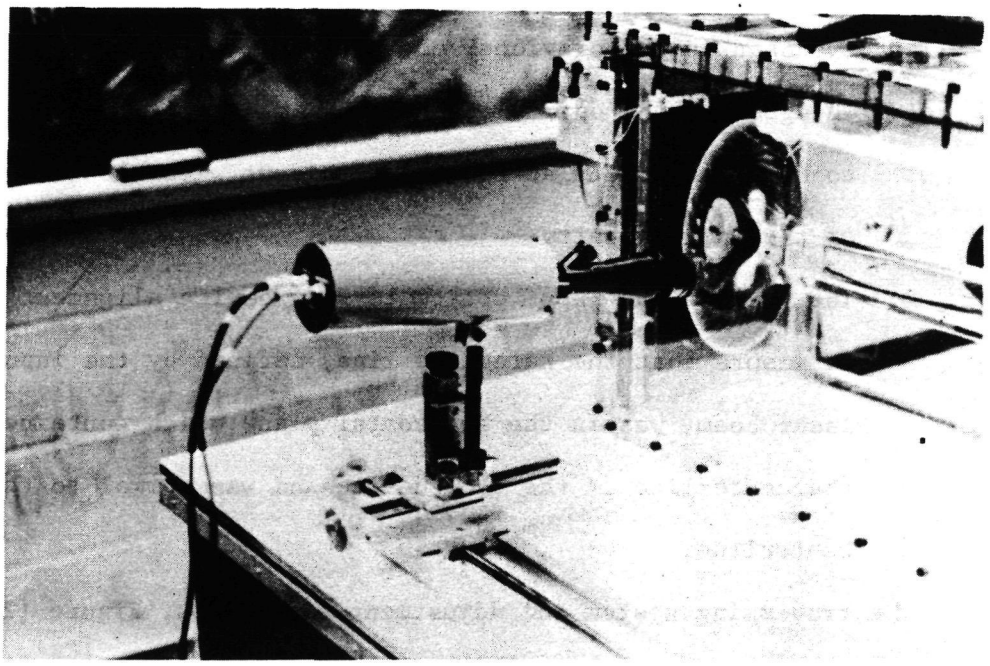

Figure 2.10. A Photograph of the Photomultiplier Assembly Mounted on its Three-Dimensional Traversing Device. The Entrance Channel Region of the Flow Device and the Swirl Vane Array May be Seen in the Background.

The X axis of the system consisted of two precision-ground steel rods. These rods were 2.540 cm in diameter and approximately 100 cm long. Their axes were horizontal, parallel to each other, and parallel to the flow device centerline. Each was held rigidly in position by mounts bolted to a steel table. The center to center distance between these X-rods was approximately 70 cm. Two linear ball bearings were fitted to each rod. These permitted motion in the X direction, and supported a second pair of precision-ground, steel rods, which formed the Y axis.

The Y-axis rods were 1.270 cm in diameter and approximately 72 cm in length. Their axes were horizontal, parallel to each other at a distance 10.5 cm apart, and perpendicular to the X axis. Two linear ball bearings were mounted on each of these rods, and these four bearings supported a small aluminum plate. A vertical-travel optical mount was bolted to this plate and supported the optical unit. The method of support allowed the optical unit centerline to be aligned parallel to the Y axis at a variable height. The optical unit also could be rotated about its centerline. The plate/optical unit position along the Y axis was controlled and monitored by a micrometer head.

A second aluminum plate, which supported the laser head mounts, was rigidly bolted to the Y axis rods. The laser head was supported, at each end, by mounts which allowed the laser beam to be aligned parallel to the Y axis and coincident with the optical unit centerline. Thus, the optical unit could be moved along the Y axis and rotated in its holder without affecting the laser head/optical unit alignment.

The optical unit and laser head moved together along the X rods. The X position of this assembly was also controlled and monitored by a

micrometer head. After initial adjustment to determine $X_o$ and $Y_o$, the optical unit position, (x,y), could be determined to an accuracy of .025 mm.

The height of the laser beam/optical unit centerline could be accurately adjusted while keeping them coincident. This was necessary for small, final adjustments to insure that the reference line would intersect the flow device centerline.

The photomultiplier assembly, Figure [2.10], was mounted on a smaller traversing system placed directly on the table top which supported the flow device. This traversing system consisted of three orthogonally disposed, dove-tailed slides. The position along each axis was controlled by a lead screw. This system was aligned so that the photomultiplier assembly could be moved parallel to the X and Y axes, at a variable height. After initial alignment with respect to the intersection point, the photomultiplier assembly would remain aligned if it was moved in unison with the input optics.

# CHAPTER THREE

## 3.0 Flow Visualization Studies

The first series of experiments undertaken after construction of the apparatus were flow visualization studies utilizing the dye injection system. The aim of these studies was to observe the flow patterns in the test section for various settings of the flow rate and vane angle. Similar studies had been done by previous investigators [11,12,27,28,29].

The work of Sarpkaya [11], which utilized a similar flow apparatus, was especially noteworthy. Sarpkaya's study, in part, presented descriptions and photographs of three forms, or modes, of flow disturbance. This report also included information on the type and axial location of the disturbance as a function of flow rate and vane angle. In a later report [29], Sarpkaya extended this work to include the effects of varying the divergence angle of the test section.

## 3.1 Procedure

Before observations were made, it was necessary to adjust the bell-mouth-test section-exit tube assembly to insure that it was concentric with the vane array and centerbody. The supply water temperature was first set to be equal to the room temperature. The circulating pump was then run, if necessary, for about ten minutes to destroy the stable

stratification in the test tank which resulted from any significant alteration to the temperature of the supply water. Pockets of air, which collected under the tank cover over a period of time, were removed via bleed screws placed in the top of the tank. Small air bubbles located along the test section I.D. were forced out by increasing the flow rate through the tube.

After removing the air and insuring that the temperature of the water inside the box was uniform throughout and equal to room temperature, the circulation pump was shut off and the flow rate control valve was adjusted to give a tube Reynolds number of approximately 4000. Before proceeding, ten minutes was allowed for the secondary flow patterns caused by the circulation pump to decay.

The vane angle was then set at 20° and the centerline dye injection was adjusted so that a thin, steady filament resulted. Mis-alignment of the bell-mouth test section assembly resulted in an asymmetry which caused the filament to follow a helical path into the entry section. The location of this assembly was adjusted until the filament was straight. When this alignment was carefully done, the filament remained straight for all the flow rates and vane angles used.

Once aligned, the bell-mouth-test section assembly was fixed in position. It was found that any subsequent deviation of the filament from a straight path was due to an asymmetric flow in the entrance channel caused by the previously discussed temperature effects. Observations were made only when the filament showed no significant deviation from a straight path in the entry section.

## 3.2 Discussion of Flow Parameters

As indicated, the parameters that were systematically varied and monitored were the volume flow rate and vane angle. However, the non-dimensional parameters of Reynolds number, Re, and circulation number, $\Omega$, were used to describe the flow.

The Reynolds number used was based on the average axial velocity, $\overline{u}$, the diameter of the test section (measured at the throat, before the divergence), D, and the kinematic viscosity, $\nu$. Thus,

$$Re = \frac{\overline{u}D}{\nu}$$

By definition, for a volume flow rate = Q,

$$\overline{u} \equiv Q/(\frac{\pi D^2}{4})$$

Therefore,

$$Re = \frac{4Q}{\pi D \nu}$$

The kinematic viscosity was evaluated, at the water temperature used, by consulting property tables for water.

The non-dimensional circulation number, $\Omega$, was used to characterize the swirl. The defining equation used was

$$\Omega \equiv \frac{\Gamma}{\overline{u}D} \quad ,$$

where $\Gamma$ is the circulation. As shown in Figure [3.1], $\Omega$ is a function of the vane angle and the geometry of the vane array and entrance section of the apparatus. A physically more meaningful interpretation of $\Omega$ may be derived by assuming that $\Gamma$ is constant. In that case

$$\Gamma = \pi v_w D$$

where $v_w$ is the swirl velocity at the tube wall. By definition

$$\Omega \equiv \frac{\Gamma}{\bar{u}D} = \pi \frac{v_w}{\bar{u}}$$

and $\Omega$, then, is seen to be a measure of the ratio of a swirl to an axial velocity.

### 3.3. Flow Patterns Observed - Steady Flow Conditions

In the first set of experiments run, the Reynolds number was fixed and $\Omega$ was incrementally varied. For each vane angle setting, the flow patterns were observed and the type and axial position of the flow disturbance were noted. The observation time was, on average, approximately ten minutes for each Re, $\Omega$. Similarly, a second set of experiments were done in which $\Omega$ was held fixed and the Reynolds number was varied in suitable increments. The results were the same in both cases.

It was found that, for a wide range of Re and $\Omega$, two (or more) types of flow disturbance could exist. One type would occur and would wander slightly, in a random fashion, about some mean axial location. Often, however, after a considerable time, the flow pattern would then change,

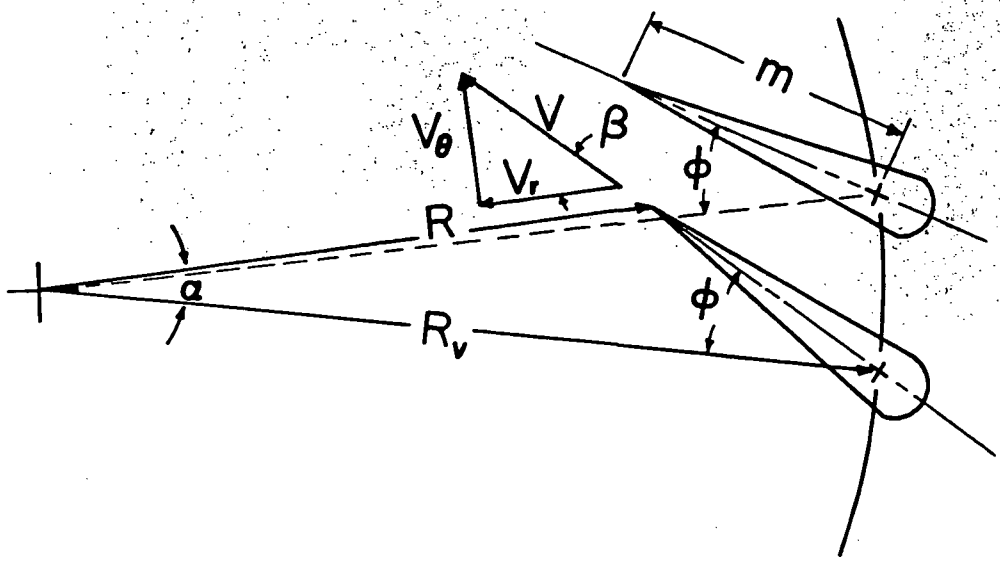


$$\Omega \equiv \frac{\Gamma}{\bar{u}\, D}$$

$$\Gamma = 2\pi\, R\, V_\theta$$

$$\bar{u} = \frac{Q}{(\frac{\pi\, D^2}{4})}, \quad \text{and } Q = 2\pi\, R\, S\, V_r$$

$R_v$ = 11.43 cm

m = 3.81 cm

s = 2.89 cm

D = 3.81 cm

where S = span of vane

Substituting for $\Gamma$ and $\bar{u}$ gives $\Omega = \frac{\pi\, D}{4\, S} \frac{V_\theta}{V_r} = \frac{\pi\, D}{4\, S} \tan \beta$

where $$\beta = \phi + \alpha = \phi + (\tan)^{-1} \frac{m \sin \phi}{R_v - m \cos \phi}$$

Figure 3.1. Schematic of the Vane Array and Derivation of the Swirl Parameter Ω.

spontaneously, to a different pattern. The new pattern often moved to a new mean axial location. Sometimes this new disturbance type would persist for several minutes (or longer) and sometimes it would almost immediately be destroyed and revert back to the original one, at the original axial location. It should be emphasized that these changes took place with no prompting and with Re and $\Omega$ held fixed.

All of the various types of disturbances observed, and photographs of each, are presented here.

### 3.3.1. Type 0

This is the so-called axisymmetric mode of vortex breakdown. This form has been reported previously by many others and has been the subject of extensive photographic/flow visualization studies. It is characterized by a stagnation point on the swirl axis, the dyed filament then expanding abruptly and symmetrically to form the envelope of a bubble of recirculating fluid. The envelope has a high degree of symmetry over most of its length, but the rear is not closed and is asymmetric.

It appeared that the bubble was simultaneously filled and emptied at the rear portion, and this process seemed to occur in either of two ways. The first structure, Figure [3.2], more commonly observed, resulted in the bubble being filled and emptied at diametrically opposite locations near the rear of the bubble, i.e. at any point in time the bubble was being filled at one azimuthal location and was being emptied at another azimuthal location, 180° away from the first. The downstream end of the breakdown was tilted, and the filling took place at that point furthest upstream and the emptying occurred near the furthest downstream point.

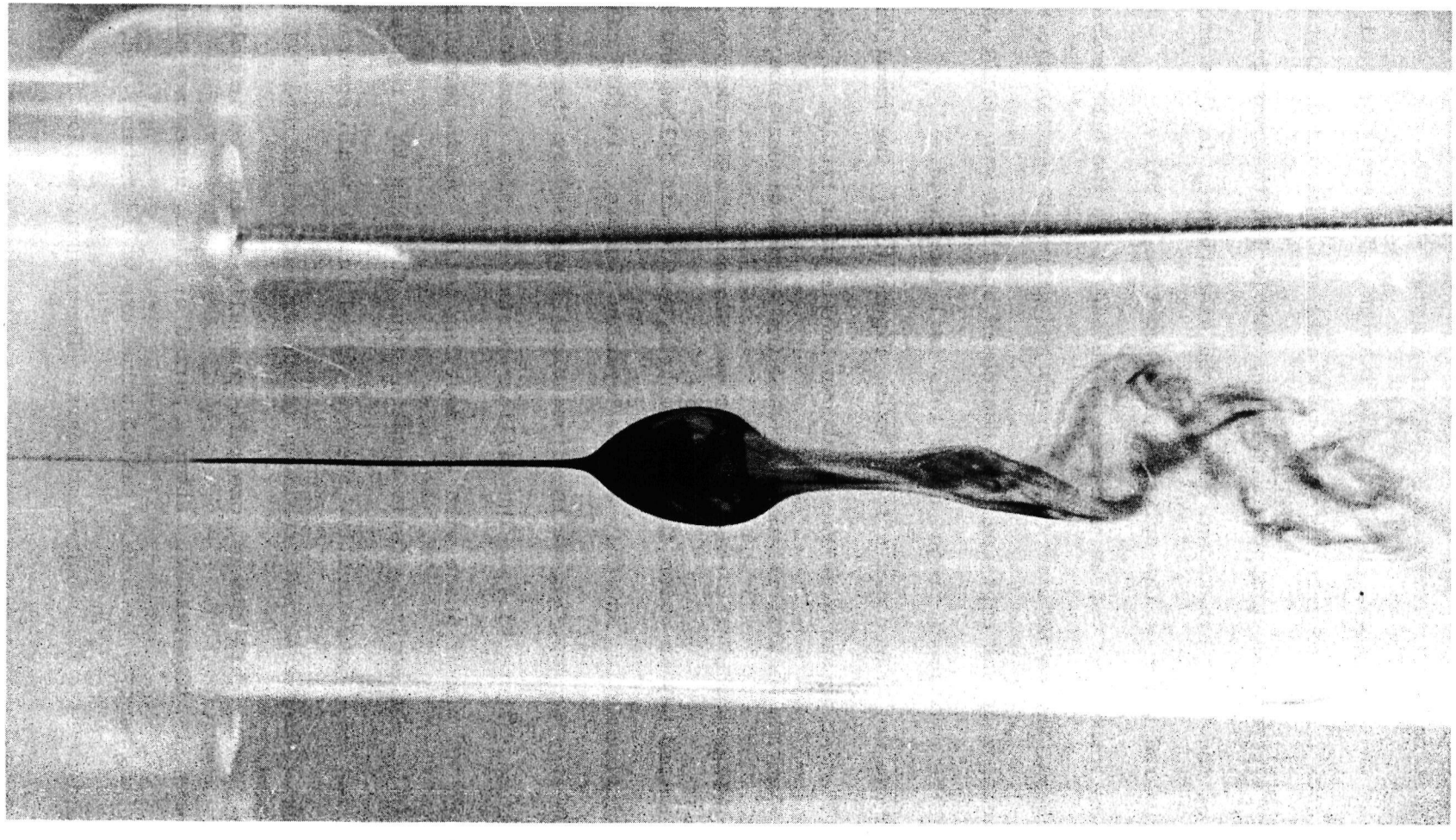

Figure 3.2. The Type O, So-Called Axisymmetric, Vortex Breakdown. The Bubble Shown is of the Single-Tailed Type and was Produced by Flow Conditions Re = 2560 and $\Omega$ = 1.777, the Flow Conditions Used for the Detailed Velocity Measurements Presented in Chapter 4.

This whole structure rotated about the swirl axis, with the same sense of rotation as the base flow, in a periodic fashion. The emptying tail of the breakdown tended to return to the tube axis and a second disturbance was nearly always evident approximately one bubble length downstream of the rear of the first breakdown. The second disturbance, in this study, always appeared to be of the spiral type, (see type 2, below).

It was found that for an increase in Re and/or $\Omega$, the bubble would move upstream, shrink in size (both length and diameter decreased), the radial location of the emptying tail decreased until it was nearly on the axis, and the rotational frequency of this tail increased.

When dye was introduced off the axis, Figure [3.3], the resultant helical filament passed over the breakdown bubble with little, if any, change. When the helical filament reached the second disturbance, or slightly downstream of it, this filament was distorted and broken up.

The second way in which the axisymmetric bubble was filled and emptied was seen infrequently, and only at low Reynolds numbers. In this case, the bubble had two emptying tails, diametrically opposed at the rear of the breakdown, Figure [3.4]. The filling points were also diametrically opposed and 90° out of phase with the emptying tails. As in the single tailed bubble, the emptying tails rotated about the axis in a regular, periodic fashion. Occasionally, the two-tailed bubble would spontaneously change into a single tailed breakdown in approximately the same axial location. During this change, one tail gradually diminished in color until it totally disappeared. After a period of time, sometimes minutes and sometimes hours, the double tailed structure would return, and, in turn, would persist for minutes or hours. The transformation from two

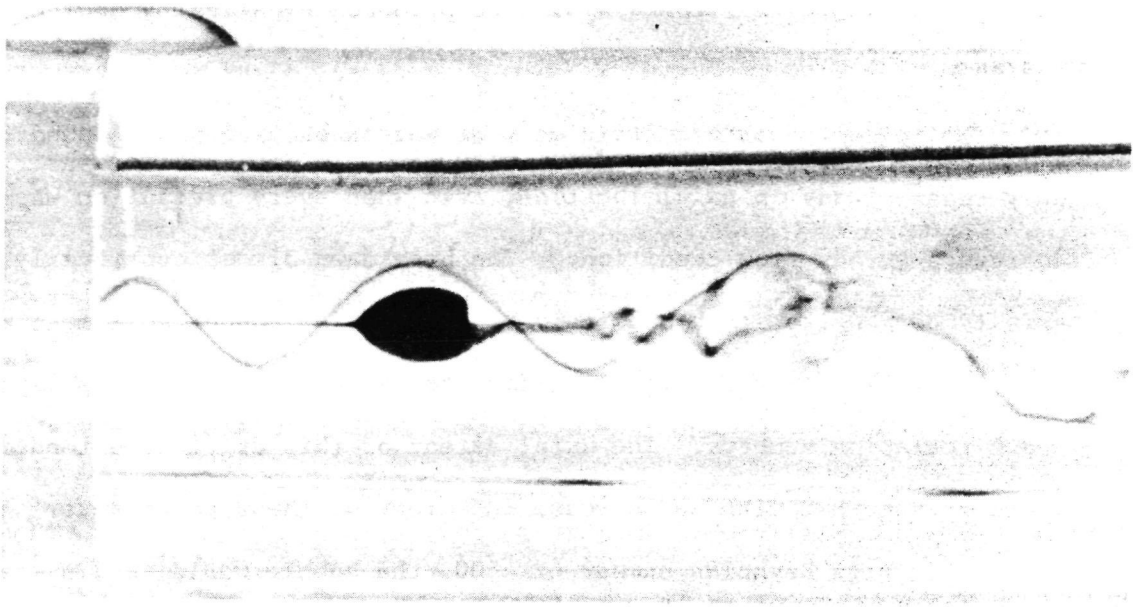

Figure 3.3. The Outer, Helical Dye Filament Passes Over the Type O Bubble Without Disturbance and is Broken Up Only After Reaching the Second, Spiral Type of Breakdown.

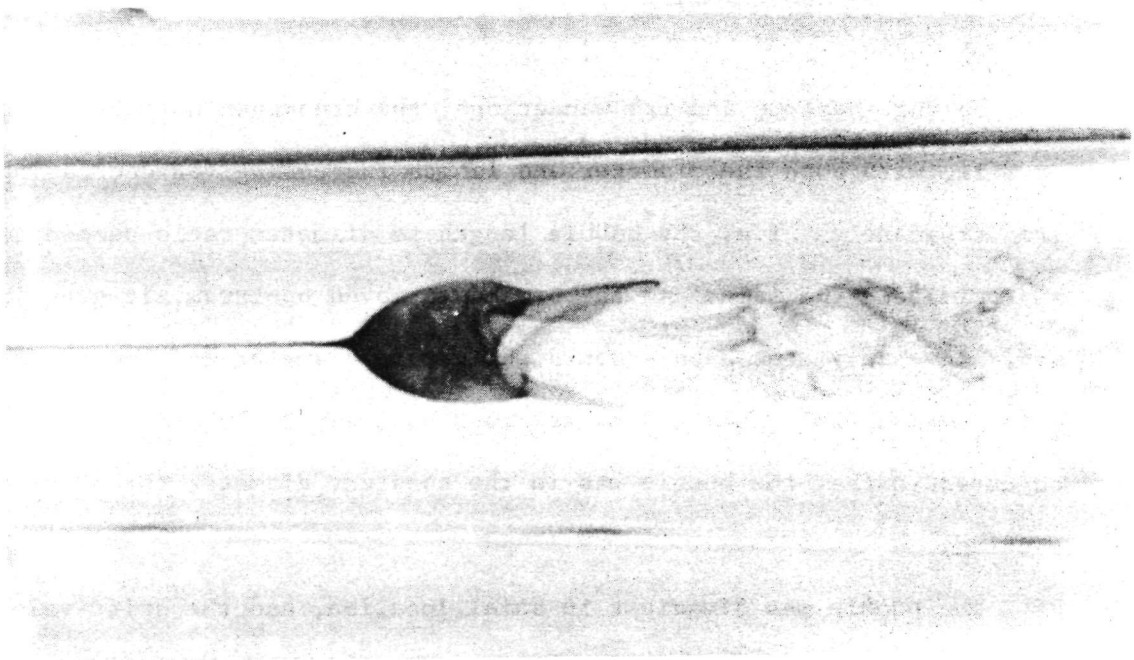

Figure 3.4. A Two Tailed Type O Bubble.

tails to a single tail could always be produced by slightly increasing Re and/or $\Omega$.

The so-called axisymmetric mode of vortex breakdown was found to be only quasi-steady in axial location, even when every precaution was taken to insure steady flow conditions. The breakdown almost continually drifted axially to and fro, in a seemingly random fashion, about some mean axial location. The velocity of this drift increased with increasing Reynolds and circulation numbers. The axial extent of this drift also tended to increase somewhat with an increase in either of these parameters. At a relatively high Reynolds number of 4500, the bubble would remain stationary near its mean axial location for, at best, a second or two, and would then dart to and fro axially a distance of, typically, one half of a tube radius. After one or two cycles of this motion, the bubble would often settle near its mean position momentarily before beginning its axial motions again.

During these to and fro wanderings, the breakdown noticeably changed in size, with both the diameter and length increasing (or decreasing) proportionately; i.e. the bubble length to diameter ratio seemed to stay approximately the same. As the breakdown moved upstream, it grew in size and, conversely, the bubble would shrink, in diameter and length, as it moved downstream. This effect was most noticeable when Re and $\Omega$ were adjusted so that the bubble was in the constant diameter throat of the test section.

The bubble was steadiest in axial location, and the drift velocity was lowest, at relatively low Reynolds numbers and with the swirl adjusted just high enough so that this mode of breakdown was the only type that

occurred (at still lower circulation numbers, type 2 and type 0 occurred alternately in time). For these conditions, the breakdown would drift back and forth very slowly and seldom travelled more than a quarter of a tube radius from its mean position. Often, the bubble would remain fixed in one location for 5 or more seconds. In addition, for these flow conditions the bubble was relatively large, the emptying and filling took place quite far off-axis and the emptying tail rotated about the tube axis at a relatively low frequency (approximately 2Hz). Compare, for example, the radial location of the emptying tail in Figure [3.5] for Re = 2560, with that in Figure [3.6], for Re = 4200. The bubble appears more nearly closed at the rear for the higher Reynolds number. At lower Reynolds numbers, then, it was possible to see quite clearly some of the previously mentioned features of this type of vortex breakdown and to make velocity measurements of the associated flow field using the LDA.

Another feature of this type of breakdown that was frequently observed was the temporary appearance of a filament of dye on the axis inside the bubble, Figure [3.6]. This occurred, for a suitable, fixed $\Omega$, at higher Reynolds numbers. The filament took the form of a screw-worm which had the same sense of axial and swirl velocity as the base flow. The origin of the screw-worm seemed to be just downstream of the nose of the bubble and slightly off axis, and the filament moved rapidly downstream, reaching a point approximately 2/3 of a bubble length downstream of the nose before being broken up. The reservoir of dye which fed this filament appeared to be a darkened region near the nose of the breakdown, and slightly off axis. This reservoir, it appeared, usually was emptied by a streak of dye which extended from the reservoir along the envelope

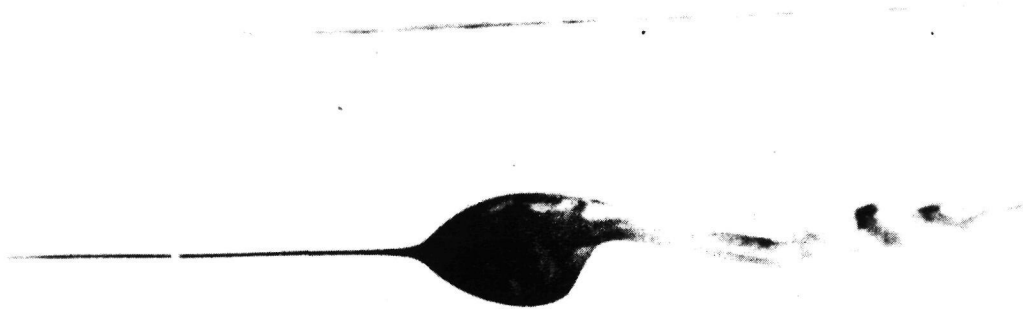

Figure 3.5. The Type O Breakdown with Re = 2560.

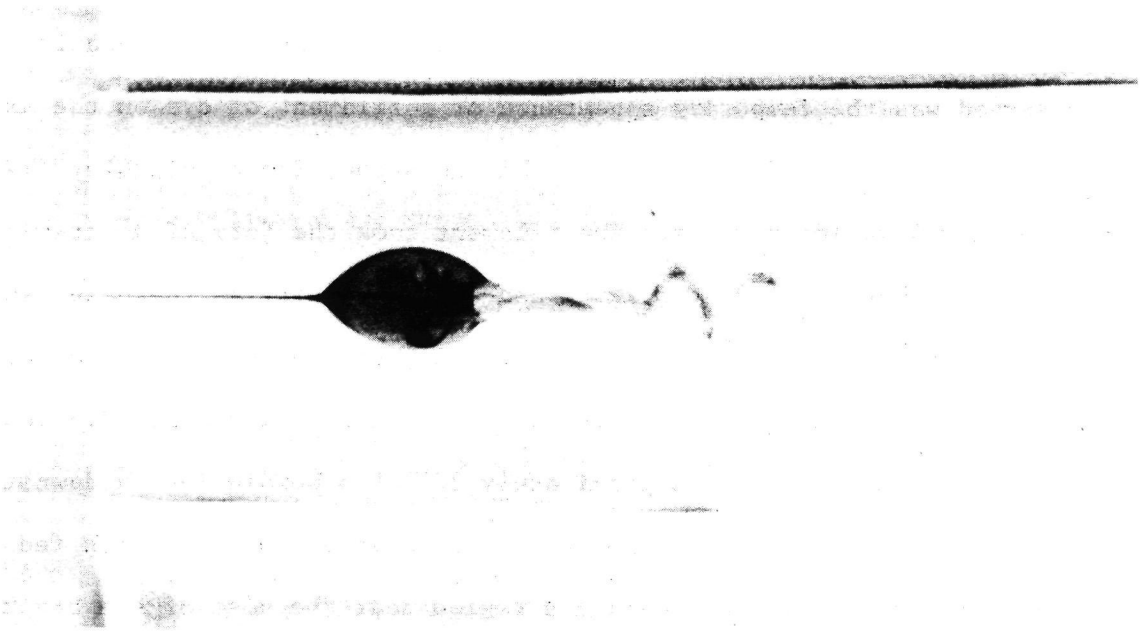

Figure 3.6. The Type O Breakdown with Re = 4200. The Screw-worm Dye Filament May be Seen and Marks the Axis of the Bubble.

of the bubble. The streak rotated very slowly (at a much slower rate than the gyrating tail, but in the same sense) around the outer surface of the breakdown. The screw worm filament would then appear and persist until the reservoir was exhausted. This occurred randomly in time, but quite often.

It was not possible to determine how this reservoir was replenished. However, the screw worm sometimes appeared after the flow of dye had been interrupted, and this seemed to indicate that the screw worm was not the result of the initial, upstream filament penetrating the bubble envelope (as suggested by Sarpkaya [11]). When the flow of dye was stopped, the bubble and emptying tail would remain visible for as long as 20 seconds, gradually lightening in color as more and more dye exited via the tail.

### 3.3.2. Type 1

At relatively low circulation numbers and high Reynolds numbers, the smooth, nearly closed type 0 bubble occurred alternately, in time, with the type 1 structure shown in Figure [3.7]. The type 1 mode of breakdown did not have the smooth envelope, distinct emptying tail, and clearly evident downstream vortex core displayed by type 0. The nose region of both seemed similar, with a front stagnation point and abrupt expansion of the dyed filament. The nose of the type 1 breakdown, however, appeared to be slightly asymmetric and the envelope was ragged in appearance. The exiting dye showed little tendency to return to the tube axis, but instead seemed to break up into large scale turbulence.

When the flow of dye was stopped, the type 1 breakdown remained visible for only a few seconds (as opposed to the 15-20 seconds for type 0).

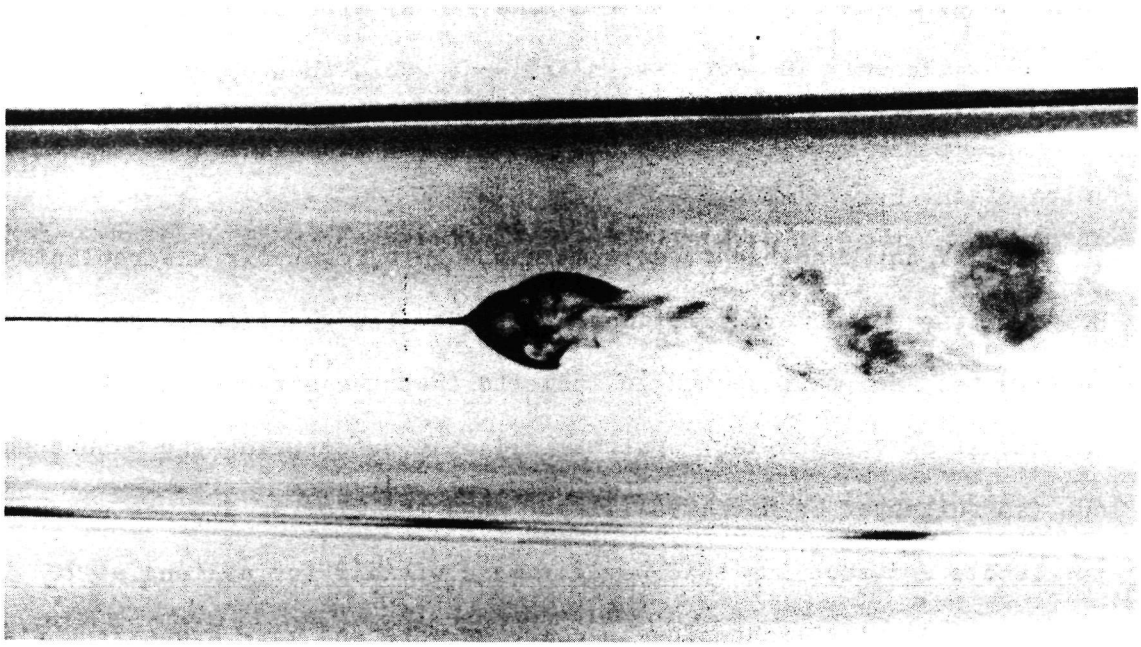

Figure 3.7. The Type 1 Breakdown.

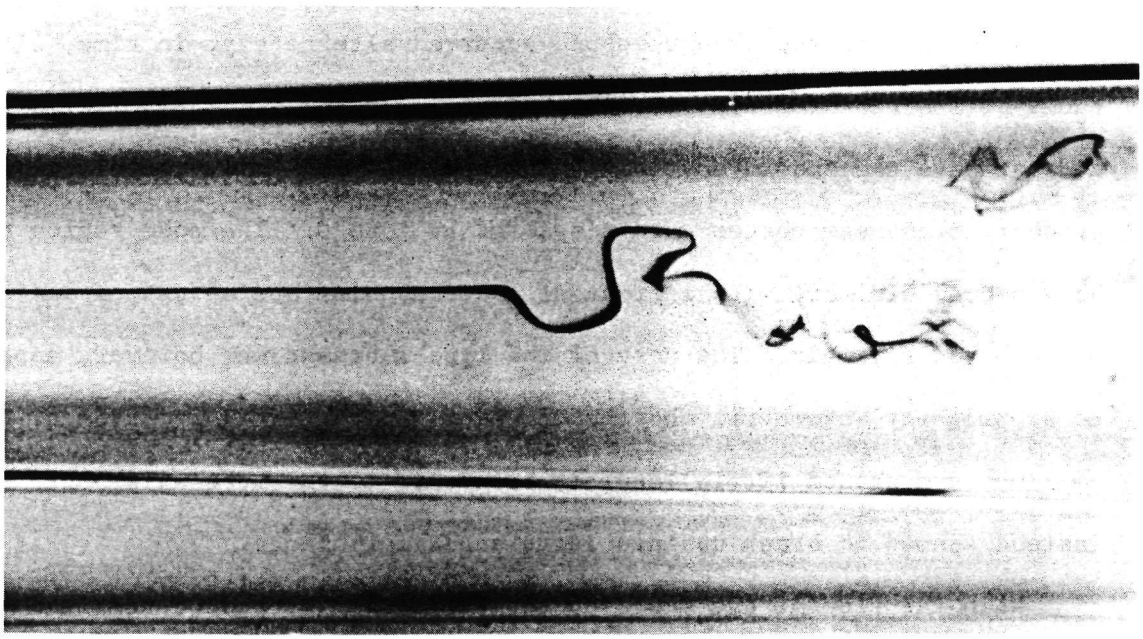

Figure 3.8. The Type 2, Spiral Mode of Vortex Breakdown.

For constant flow conditions (Re and $\Omega$ fixed), the type 1 breakdown often changed spontaneously to type 0. The mean axial location of the type 0 bubble was nearly always upstream of the mean axial location of the corresponding type 1 breakdown, usually by about 2/3 of the tube radius. Each form would persist for a considerable time (often 20 minutes or so) before changing into the other mode. The transformation seemed to occur in the following way.

The type 1 breakdown would drift to and fro about its mean location in a seemingly random fashion. Gradually, however, the breakdown appeared to travel further and further upstream with each successive cycle of this motion. Eventually, it would change, abruptly, into the type 0 bubble. The transformation from type 0 to type 1 occurred in a similar fashion. The smooth, type 0 bubble drifted further downstream until changing suddenly into the type 1 breakdown. The whole process suggested that there were two quasi-equilibrium "valleys' separated by a "peak" which was only occasionally surmounted.

The transformations described above occurred without prompting. However, it was often possible to precipitate the change from type 0 to type 1 by introducing a slight disturbance into the flow upstream, either by slightly oscillating one vane or by rapidly pulsing the dye shut-off valve. No method was found which could consistently retrieve the type 0 form, once the transformation to type 1 had occurred.

### 3.3.3. Type 2

This form of vortex breakdown, Figure [3.8], is generally referred to as the spiral mode. It is the form which, apparently, is most commonly observed in the flow over delta wings at high angles of attack, e.g. see

Lambourne and Bryer [24]. In this mode, the dyed filament, which was initially on the swirl axis, decelerated rapidly and formed an abrupt kink. The filament did not spread out appreciably, but instead took the form of a spiral which persisted for one or two turns before breaking up into large scale turbulence. In agreement with the study done in tubes by Sarpkaya [11], and contrary to the results obtained by Lambourne and Bryer in unconfined flows, the resultant spiral had the same sense (geometrically) as the base flow rotation. In addition, the whole spiral configuration rotated in a periodic fashion about the tube axis, also in the same direction as the base flow.

With Re and $\Omega$ held fixed at values for which the spiral mode was the usual breakdown form observed, it was found that the spiral breakdown drifted to and fro, just as for type 0 and type 1. The range of this axial drift was slightly greater than that observed for type 0 and type 1. Usually, the spiral wandered back and forth, in a seemingly random manner. It appeared that the upstream drift of the breakdown was often preceded by a slight increase in the frequency of rotation of the spiral around the swirl axis and a decrease in the pitch of the geometric form itself (i.e. the spiral turns moved closer together, with an increased tendency to fold back towards the initial kink.). Conservely, the downstream drift seemed to be preceded by a decrease in rotation frequency and an increase in pitch.

Occasionally, the frequency of rotation would increase significantly, the first turn of the spiral would fold back towards the initial kink on the tube axis, and the spiral changed into a type 0/1 breakdown. The resultant bubble, usually with the rear portion not fully developed, then moved quite rapidly upstream.

For lower values of Re and/or $\Omega$, the newly formed bubble would persist only a few seconds and would travel only some fraction of a tube radius upstream. The bubble would then change abruptly to the spiral mode which immediately moved downstream to its original location.

For an increase in either Reynolds number (with $\Omega$ constant) or circulation number (with Re constant), the following changes occurred;

a) The mean axial location of the spiral moved upstream.

b) The maximum radius that the spiralling filament reached, before breaking up, decreased slightly.

c) Perhaps related to b. it was found that when dye was introduced off axis (at approximately 1/2 $r_t$) the resultant helical filament was noticeably distorted at an axial location which was as much as one tube radius upstream of the position of the spiral breakdown, for lower Re and/or $\Omega$. As Re, say, was increased and the spiral moved upstream, the helical filament disturbance was at about the same location as the spiral position. For still higher Reynolds numbers, the helical filament passed over the initial kink in the central filament without noticeable change and was distorted and broken up downstream of the spiral breakdown. Similar results were found for an increase in $\Omega$.

d) The frequency of rotation of the spiral form around the tube axis increased. For example, with Re = 3120, this frequency increased from 1.3 Hz at $\Omega$ = 1.34 to about 1.75 Hz at $\Omega$ = 1.54. Similarly, with $\Omega$ = 1.34, the

frequency increased from 1.1 Hz at Re = 2730 to 1.3 Hz at Re = 3120.

e) As Re or $\Omega$ was increased, the previously described transformation to the type 0/1 breakdown occurred more often and the resultant type 0/1 breakdown persisted longer. Eventually, at sufficiently high Reynolds number and/or circulation number, the type 0/1 breakdown and the type 2-spiral had approximately the same frequency of occurrence. For still higher settings of these two parameters, the type 0/1 mode predominated and the spiral form was seen less and less frequently, and lasted only momentarily before changing into the type 0/1 mode.

When the flow conditions were fixed at, say, $Re_1$, $\Omega_1$ in the range in which both the type 2 and type 0/1 breakdowns had about the same frequency of occurrence, each form could persist for as long as 3-5 minutes before changing into the other. As in the case of the type 0 to type 1 transformation, previously described, there seemed to be two quasi-equilibrium "valleys" separated by a "peak". The mean axial location of the type 0/1 breakdown was always appreciably upstream of the mean location of the spiral type.

There seemed to be no evidence that the type of breakdown formed depended on how this flow setting was achieved. For example, for $\Omega = \Omega_1$, an increase in Re up to $Re_1$ gave the same results, on the average, as a decrease in Re down to $Re_1$. In other words, the "vortex breakdown hysteresis" reported by Sarpkaya [11,12] was, for long observation times, not evident in this study.

At relatively high circulation numbers and low Reynolds numbers, the type 2 breakdown nearly always changed, directly, into type 0 for a suitable increase in either $\Omega$ or Re. (In fact, the type 1 was never seen for these conditions.) For lower circulation numbers, the transformation either was from type 2 to type 1, with no type 0, or from type 2 to type 0, with type 1 as an intermediate step. The randomness with which these changes took place and the multiplicity of forms observed made impossible any attempt to further delineate the dependence of breakdown type formed on flow settings used.

Because of the way in which they evolve, it is more convenient to describe the remaining forms of flow disturbances observed in reversed order, beginning with the form observed at lowest $\Omega$ and/or Re. While types 0, 1, and 2 have generally been referred to as vortex breakdown modes, and have been observed previously by many investigators over a wide range of Reynolds numbers, the types 3-6 occur only at relatively low Reynolds numbers. In some cases, these low Reynolds number forms appear to be similar to the previously described modes (type 4 similar to type 0, type 3 similar to type 2). However, it is not clear that they originate from the same mechanism.

For quite low, fixed Reynolds numbers, the full range of disturbance forms described below was consistently observed and evolved in a systematic way, one from the other, as the swirl was increased in suitably small increments. Similar results were obtained by fixing $\Omega$ at a relatively high value, and slowly increasing Re. Only the fixed Re, increasing $\Omega$ case will be considered at present, and the slight differences in the two cases will be described later.

With the Reynolds number fixed at, say, 2500 and with no swirl, the central dye filament travelled the length of the apparatus with no visible change. As the swirl was increased, slight oscillations in the filament were noted near the downstream end of the uniform diameter exit tube. For further increases in swirl, the axial location of these oscillations moved upstream and, at $\Omega$ approximately equal to 0.6, the oscillations began near the downstream end of the diverging test section. The dyed filament remained on the tube axis until this point and then began to oscillate, with steadily increasing amplitude, until it broke up into random disorder.

As the swirl was further increased, it was noted that the filament seemed to decelerate slightly and deviate from the centerline at a point upstream of that location where the above mentioned oscillations began. At times, the filament also showed a noticeable tendency to shear into a tape as it moved off the tube axis.

### 3.3.4. Type 6

Further slight increases in swirl led to the formation of the type 6 form shown in Figures [3.9,3.10]. In this form, the central filament moved gently, but distinctly, off axis at a nearly constant aximuthal location. Only after it had moved off axis a significant distance (typically, equal to about 1/2 $r_t$) did the filament seem to acquire the spiralling sense of the base flow. It continued to expand in radius until it nearly reached the tube wall, and then noticeable oscillations became evident which broke the filament up.

At times, the filament retained its shape as a filament during these deviations, Figure [3.9]. Usually, however, the filament simultaneously deflected off the axis and sheared into a tape, Figure [3.10]. It should

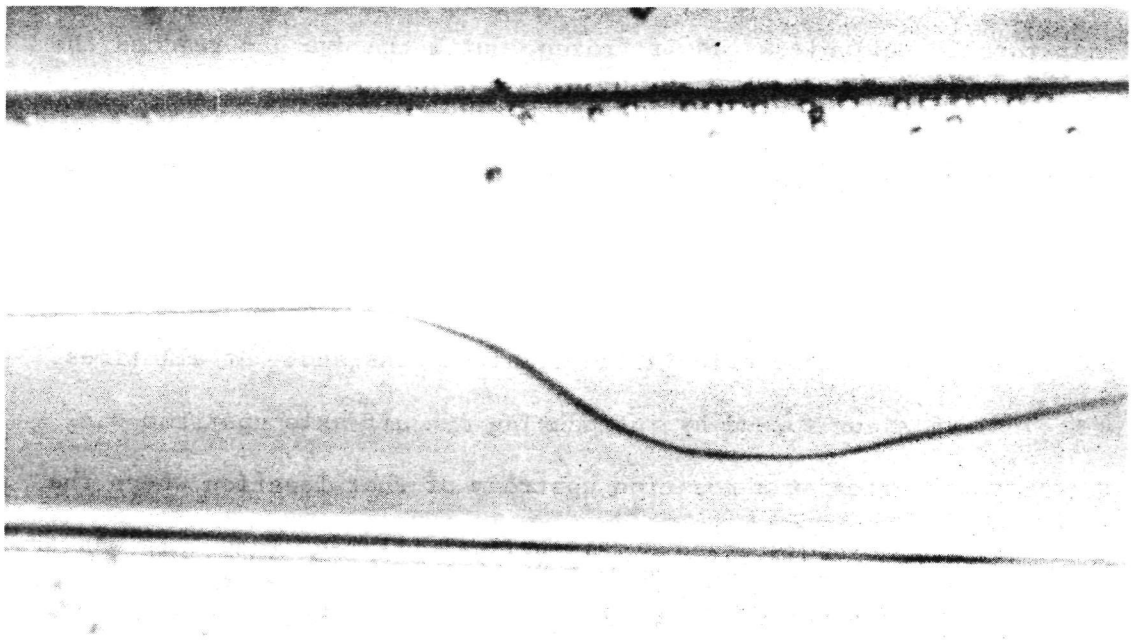

Figure 3.9. A Type 6 Disturbance in which the Central Dye Filament Did Not Shear, but Only Deflected Off-axis.

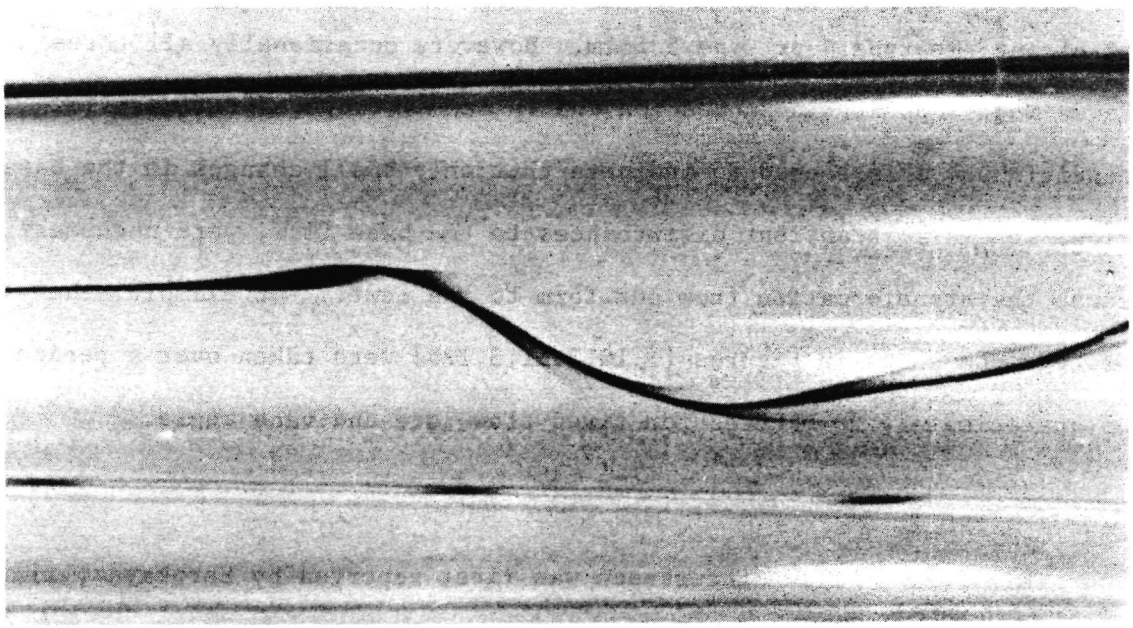

Figure 3.10. A Type 6 Disturbance in which Central Filament Simultaneously Moved Off-axis and Sheared into a Tape.

be emphasized that, in both cases, the distorted, sinuous pattern appeared almost totally motionless, as if frozen, until the dye had reached the downstream location where oscillations began.

As the swirl setting was increased, this shearing tendency seemed to increase, the form moved upstream in location, and the shear plane rotated slightly with respect to the laboratory frame. At any one setting however, the shear plane orientation remained constant. At all times, the helical filament formed by introducing dye off axis upstream was noticeably distorted at a position upstream of that location where the central filament was disturbed. This helical filament (and this was true for types 3-6) also moved noticeably outwards until it had nearly reached the tube wall. The forms taken by this filament were indescribably complex.

For constant Re and $\Omega$, the axial location of the type 6 disturbance was very steady. A further small increase in $\Omega$ resulted in the formation of either the type 4 or type 5 form. However, occasionally all three forms would appear, in succession and in random order, for fixed flow conditions. This seemed to indicate that only small changes in the base flow, or small, transient disturbances to the base flow, were necessary to cause the transformation from one form to the next. For example, the photographs shown in Figures [3.10,3.11,3.12b] were taken over a period of approximately 20 minutes for fixed flow rate and vane angle.

### 3.3.5. Type 5

This form of flow disturbance was first reported by Sarpkaya [11], and he referred to it as the double helix mode. The double helix evolved, in most cases, directly from the type 6 form. Figure [3.11] shows this

evolution quite clearly. These photographs were taken at fixed flow conditions over a period of about 5 minutes.

The type 6 form is shown in Figure [3.11a] and the simultaneous shear and deflection off axis of the central filament can be seen. As time progressed, the filament began to shear into a tape, but remained on the axis, slightly upstream of the type 6 location. As this tape widened, another "branch", similar to the one that had been present, became more and more visible, and the type 5 double helix resulted.

Once formed, the whole pattern was quite steady in form and location. The central filament sheared, on axis, into an ever widening, triangular shaped sheet. Each half wound around the other, both with the same sense of rotation as the base flow, and moved outwards until nearly reaching the tube wall.

The similarity between the double helix form and the type 6 disturbance is obvious, and they perhaps should not be differentiated. However, because of its unique appearance, and to confirm the observations of Sarpkaya, type 5 has been included here as a separate form. In fact, after a considerable time, the newly emerged branch often became predominant, the original branch disappeared, and a type 6 form resulted. This new type 6 was similar to the original one, rotated 180° relative to the laboratory frame.

### 3.3.6. Type 4

This remarkable form of disturbance usually evolved directly from type 6. This transformation either occurred spontaneously, at fixed flow conditions, or could be induced by slightly increasing the swirl. In both cases, the sheared, deflected filament of the type 6 disturbance abruptly

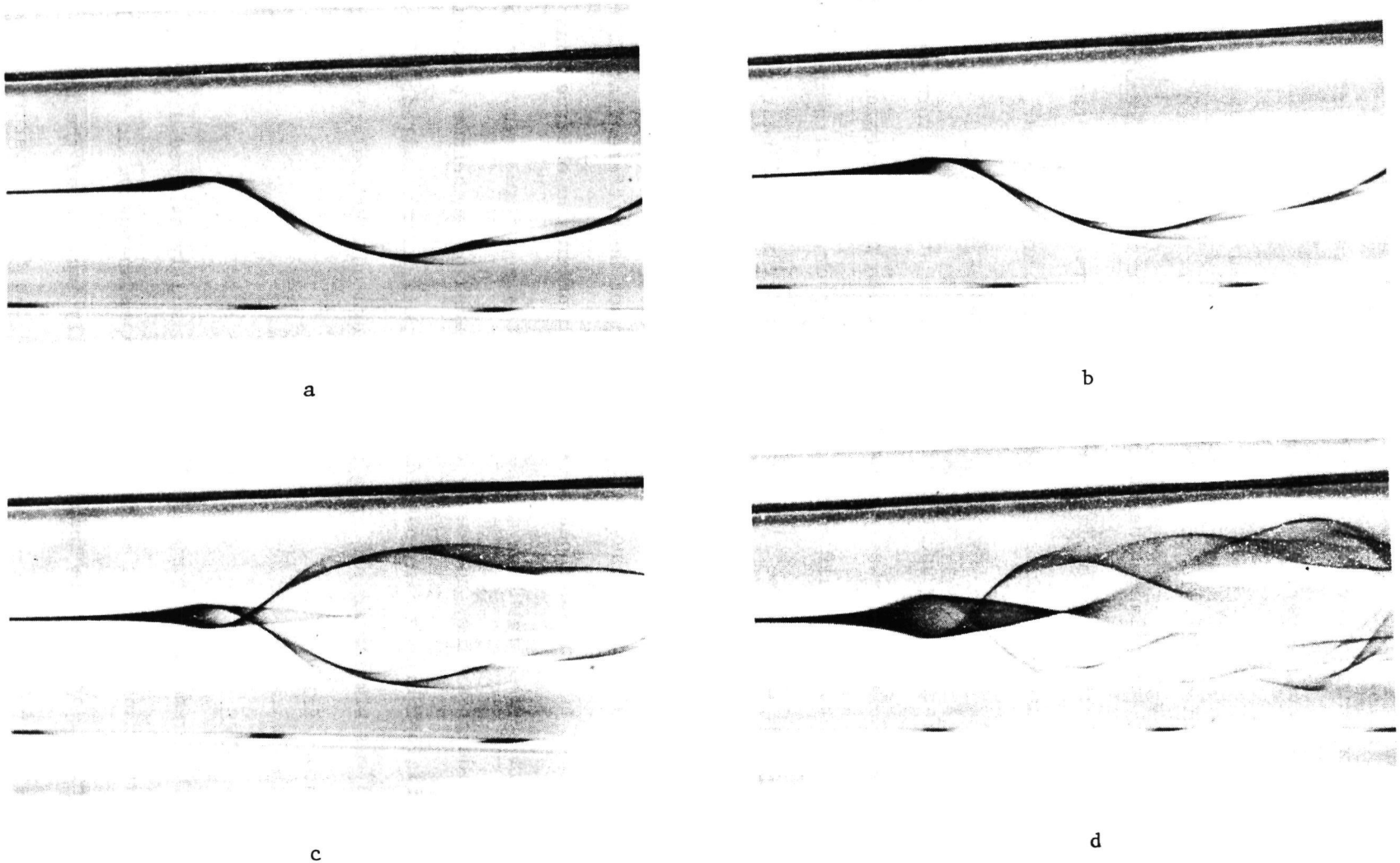

a

b

c

d

Figure 3.11. The Evolution of a Type 5 Double Helix from a Type 6 Disturbance.

began to roll up, back towards the initial point of deflection, into a tight spiral. As this occurred, the filament downstream totally disappeared, indicating that all of the dye reaching the disturbance was being recirculated, Figure [3.12b]. After a short time (about 5 seconds), dye began to exit from this recirculation zone and travel downstream, and the type 4 disturbance was fully formed.

Figure [3.13] shows various views of this disturbance form. The most remarkable feature is best seen by comparing Figures [3.13a] and [3.13b]. Figure [3.13a] was the form as seen by looking in along the horizontal, and Figure [3.13b] is the same disturbance as viewed in the vertical direction. As seen, the recirculation zone was nearly 3 times as wide (in the horizontal plane) as it was high (in the vertical plane).

For any one flow setting, the orientation of the wide surfaces was nearly constant, i.e. if the swirl, say, was changed and then brought back to its original setting, the resultant flattened bubble orientation was nearly identical to the original one. However, if the swirl and Reynolds number were changed in an appropriate way so that the flattened bubble was formed in a new axial location, the orientation did change. For example, Figure [3.14] was taken at a higher Reynolds number and lower swirl than Figure [3.13a]. Each was taken with the camera axis horizontal. It can be seen that the wide plane has rotated about 90°, and in Figure [3.14], is nearly vertical.

With the Reynolds number fixed at an appropriate value and the swirl setting adjusted just high enough for the type 4 form to appear, the recirculation zone seemed to be filled and emptied in the following way. (To simplify the discussion, the recirculation zone that has its larger

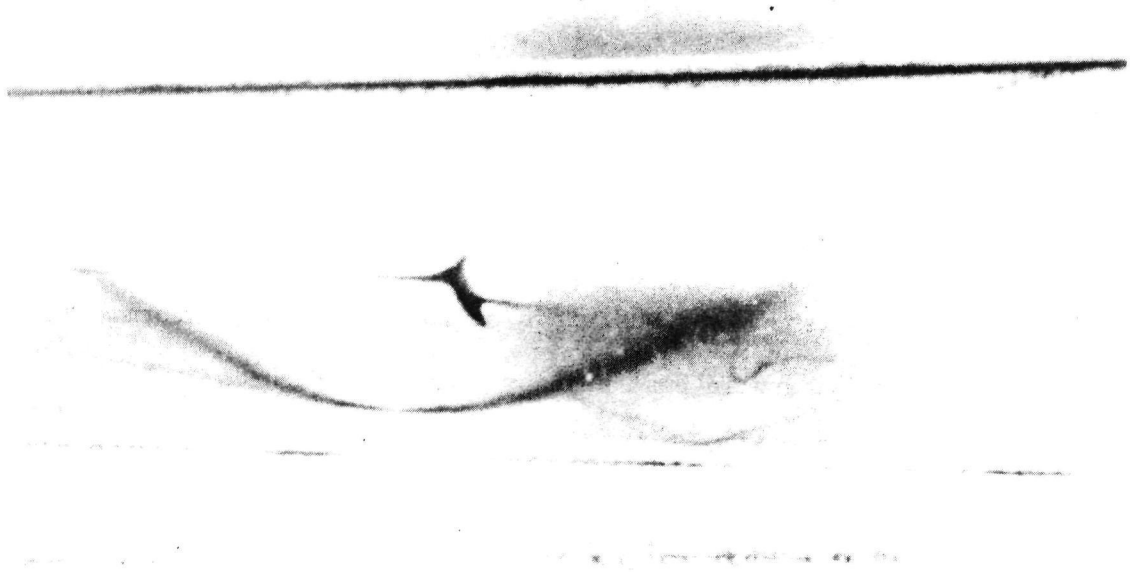

Figure 3.12 a. A Partially Formed Type 4 Disturbance, Note that Outer, Helical Dye Ribbon was Distorted Well Upstream of the Central Filament Disturbance.

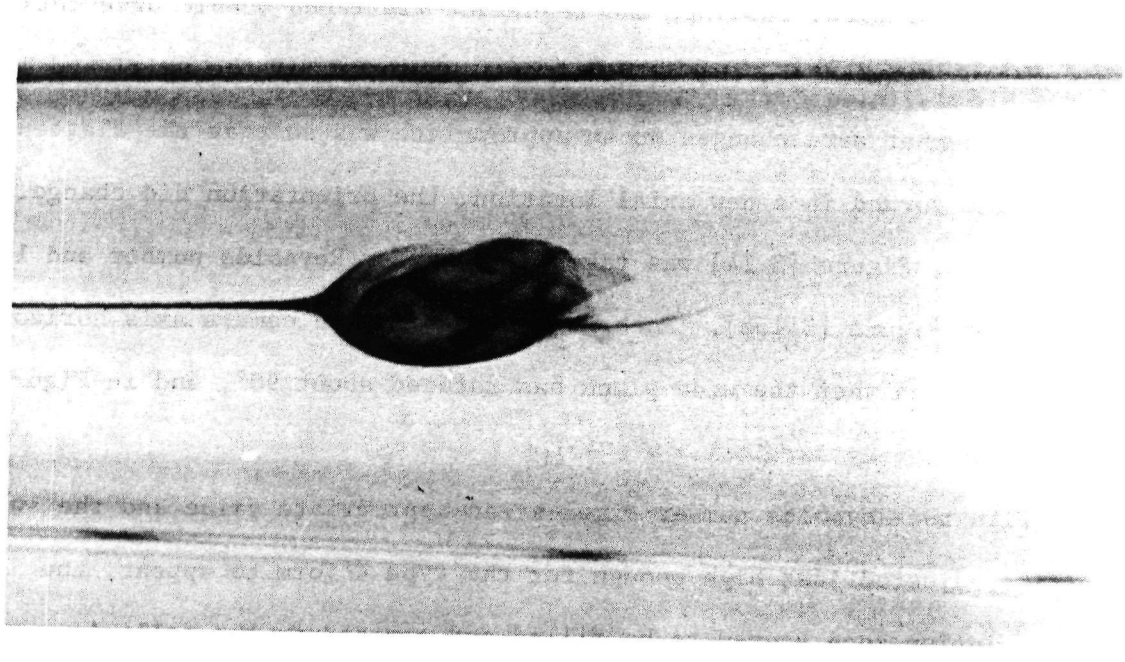

Figure 3.12 b. The Birth of a Type 4 Flattened Bubble.

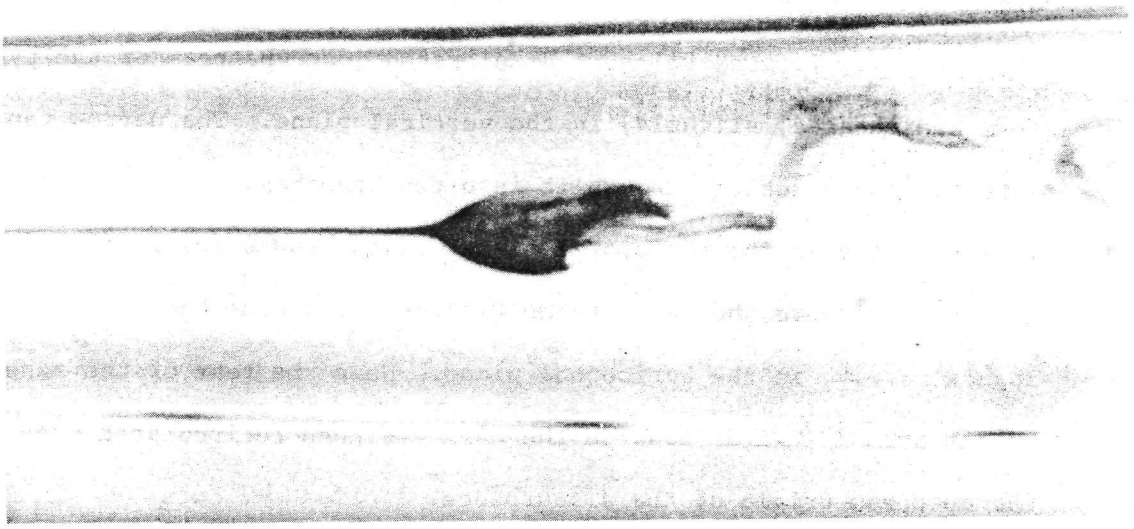

Figure 3.13 a. The Same Type 4 Flattened Bubble as Viewed From the Horizontal Direction.

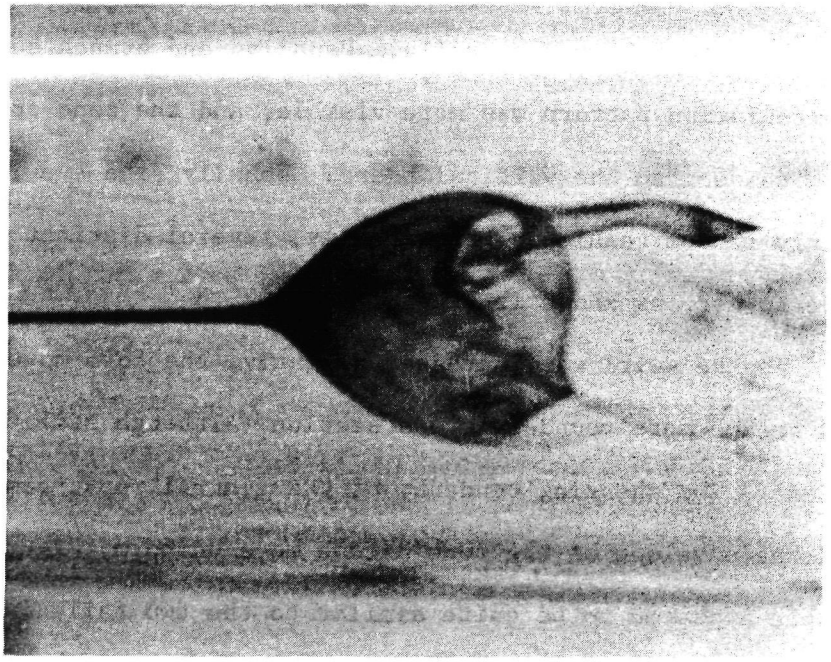

Figure 3.13 b. The Same Type 4 Flattened Bubble as Viewed From the Vertical Direction.

dimension aligned parallel to the horizontal plane will be described). The centrally located filament decelerated just upstream of the type 4 form and sheared, slightly, in the vertical plane. The narrow tape simultaneously rotated and split into two branches, each of these being approximately in the horizontal plane. Each branch moved off axis and downstream toward the rear of the recirculation zone but remained, approximately, in the horizontal plane. Near the rear of the zone, each branch turned inwards towards the axis and then recirculated back towards the upstream origin of the disturbance.

The centers of the two recirculating branches were almost motionless, and both were located, approximately, in the horizontal plane. The motion around each center was like that induced by a line vortex (oriented vertically). All the velocities were quite low, and the motion of the dye could be followed visually. Usually, one branch seemed dominant, its recirculation pattern was more visible, and the zone appeared asymmetric with respect to the vertical plane. Usually, the dye left the zone in a fairly random fashion. Occasionally, several distinct emptying paths were formed, as shown in Figure [3.15].

As the swirl was increased slightly, the form moved slightly upstream and became more round in cross section (although still noticeably flattened). The shearing tendency of the central, upstream filament decreased and the envelope of the zone became more uniform, Figure [3.14]. The bubble appeared to be quite similar to the two tailed, type 0 bubble described previously except that, in addition to being oblate, the exit tails and filling points were approximately fixed in location and did not rotate about the tube axis.

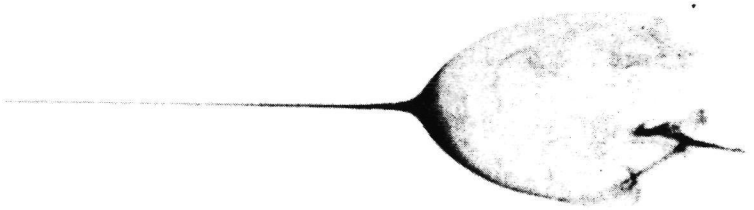

Figure 3.14. A Type 4 Disturbance with an Envelope that is Quite Uniform in Color. The Viewing Plane is Horizontal, Perpendicular to the Wide Plane of the Bubble.

Figure 3.15. A Type 4 Disturbance with Several Distinct Emptying Tails.

Figure 3.16. This Disturbance Shows the Transition from the Type 4 to Type 3. As the Dye Spreads Rearward over the Top Surface, a Previously Recirculated Amount of Dye Exits Near the Bottom Surface.

A further slight increase in swirl resulted in the form moving, again, slightly upstream. The central filament had less tendency to shear, but instead seemed to oscillate slightly in a plane. For a recirculation zone that was wide in the horizontal plane, the central filament oscillations were in the vertical plane. The filament first deflected upwards, say, and injected a quantity of dye to the upper surface of the bubble. As the filament deflected downwards (to supply the bottom surface) the quantity of dye that had been supplied to the top simultaneously spread laterally and moved towards the downstream end of the zone. When it had reached the rear of the zone, the dye sheet curled abruptly and moved back towards the nose of the bubble. As the bubble was being filled at the top, it was simultaneously being emptied at the bottom. During the next half cycle, the bubble filled at the bottom and emptied near the top surface. Thus, the periodic, planar oscillations of the central filament resulted in a periodic emptying and filling of the bubble near both the top and bottom surfaces.

The frequency of the oscillations of the upstream filament (and subsequent top and bottom feeding) was low enough so that the whole process could be closely followed. For example, with Re = 2330 and $\Omega$ = 1.37, this frequency was approximately 1.2 Hz. The frequency increased as the swirl was increased, and at Re = 2330 and $\Omega$ = 1.47 the frequency was approximately 1.4 Hz.

As previously noted, the form of flattened bubble observed at slightly lower swirls was similar to the two tailed, type 0 mode. Likewise, this form was similar to the single tailed, type 0 breakdown. In both cases, however, the type 4 bubbles were flattened and the emptying and filling

points were nearly fixed in location. In addition, there was no apparent tendency for the tail to return to the tube axis to mark a new, downstream vortex core.

As the swirl was increased and the type 4 bubble moved upstream, the planar oscillations of the central filament increased in frequency and amplitude. The dye seemed to have less tendency to spread laterally over the bubble envelope, and therefore the bubble form became less visible. In Figure [3.16], the bubble envelope may still be seen, but it is noticeably faint. Further increases in swirl led to the gradual formation of the type 3 form of disturbance.

### 3.3.7. Type 3

This type of flow disturbance had characteristics of both the type 4 flattened bubble and the type 2 spiral. The transitions from type 4 to type 3 and from type 3 to type 2 were, in fact, so gradual that it is not possible to define the transitions precisely.

In the type 3 disturbance, Figure [3.17], the centrally located filament decelerated rapidly and moved abruptly off axis to form a sharp kink, similar to the type 2 spiral. However, in type 3 the dye filament appeared to simultaneously shear slightly and some of the dye spread laterally to mark the envelope of the remnants of the type 4 bubble. In addition, the kinked filament oscillated from side to side in a preferential plane and did not rotate, as a geometric form, around the tube axis (as in type 2). As for the flattened bubble, the orientation of the plane of oscillation with respect to the laboratory frame was relatively constant for any one setting of Re, $\Omega$. If Re and $\Omega$ were changed in a suitable way this orientation did change.

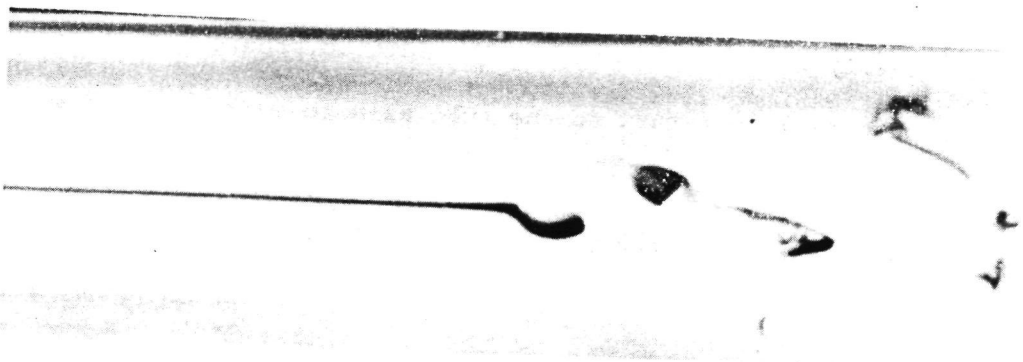

Figure 3.17. A Type 3 Disturbance. Fragments of Dye Previously Broken Off of the Preferentially Oscillating Filament Can be Seen Downstream of the Initial Disturbance.

Figure 3.18. A Type 4 Disturbance Located at Approximately the Same Point at Which Oscillation of the Central Filament Began.

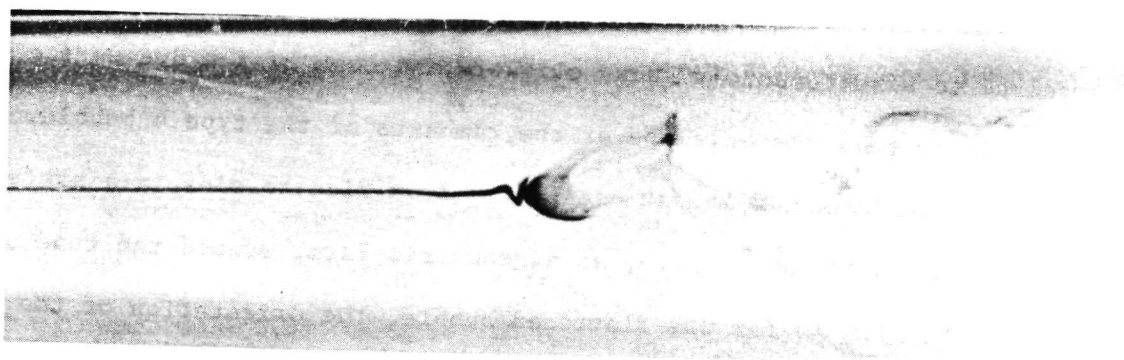

Figure 3.19. Slight Oscillations of the Central Filament Can be Seen Upstream of this Type 4 Disturbance.

As $\Omega$ was increased, the preferential plane became less distinct and the kink began to take a more circular path around the tube axis. Simultaneously, the tendency of the dye to shear and spread out decreased, the filament retained its form as a filament, and the recirculation zone was no longer apparent. Thus, the type 2 spiral evolved.

### 3.4. The Disappearance of Types 3-6 at High Reynolds Numbers

As previously indicated, for a fixed, relatively low value of Reynolds number the full range of the disturbance forms could be observed by altering the swirl setting. As the swirl was decreased, say, from a relatively high value the existing form moved downstream until it transformed into the next form, which, upon decreasing the swirl further, moved further downstream, etc. The transformations between 0 and 2, 2 and 3, etc. were sometimes gradual, but occurred quite consistently. Occasionally, type 5 was never formed, probably due to the relatively short observation times. Type 1 was never seen at low Reynolds numbers. Eventually, the transformation to type 6 occurred and its axial location move downstream as the swirl was further decreased.

When the type 6 form had moved sufficiently far downstream, to about one exit tube diameter upstream of the end of the diverging test section, it became more difficult to clearly identify. As noted in the description of type 6, the filament moved gradually off axis, sometimes shearing into a tape, moved outwards to a larger radius, and then, at some downstream location, oscillations began which broke the filament up into a random pattern. However, as the swirl was decreased and the point at which the initial deviation was noted moved downstream, the location which marked the onset of oscillations remained nearly constant (or perhaps moved only slightly downstream).

Eventually, these two points nearly coincided and the filament simultaneously deviated off axis and developed ever growing oscillations. Subsequent reductions in swirl resulted in the gradual disappearance of the type 6 form, and the filament remained on axis until oscillations developed and broke the filament up. Upon further reducing the swirl, the point at which oscillations began moved downstream until, at zero swirl, the filament remained on axis until exiting from the apparatus.

These results are indicated, in a schematic way, by the low Reynolds number, AA curve in Figure [3.20]. If the mean location and type of the furthest upstream disturbance was plotted as a function of circulation number, a single curve, AA would result. However, there seemed to be evidence which indicated that, in fact, there were two curves for each Reynolds number.

The first curve, AA', plots the location vs. swirl for the types 0-6, and the type observed for a particular swirl is noted on the curve. The intersection of AA' and A"A represents the approximate swirl and location at which oscillations in the central filament and the noticeable filament deviations characteristic of type 6 occurred simultaneously. Curve A"A, then, plots the axial location of the onset of oscillations in the filament vs. swirl. As shown, for sufficiently low values of $\Omega$ there was no tendency for the filament to develop oscillation anywhere in the tube.

The evidence which seemed to substantiate this two-intersecting-curve interpretation was tenuous, especially if based on observations made only at low Reynolds numbers. At swirls just higher than the "intersection point", the onset of oscillations downstream of type 6, at progressively closer locations (as described previously), seemed to indicate the existence

of a second curve. Similarly, at swirls just lower than the intersection point it was occasionally possible to see, downstream of the oscillations, the remnants of a type 6 disturbance. Since the identification of type 6 required the existence of an on-axis filament and since the oscillation of the filament usually moved it off-axis, more positive identification was impossible. However, the behavior of the off-axis, helical filament did seem to show indications that a type 6 form was present downstream of the onset of oscillations. The characteristic expansion of this helical filament, (cf. Figure 3.12a) which always occurred upstream of type 6, could still be clearly seen. At swirls significantly lower than this, it was not possible to see even the remnants of the type 6 form (assuming a type 6 still existed at some downstream location), and the helical, off-axis filament did not expand significantly, but simply began to break up into large scale turbulence.

This two curve interpretation seemed to be consistent with the observations made at progressively higher, fixed values of Reynolds number. When the Reynolds number was fixed at a higher value, the transformation between two given types of flow disturbance occurred at a swirl setting that was lower than that required for the same transformation at a lower Reynolds number. Moreover, the transformation took place at an axial location that was downstream of the position where it had occurred at the lower Reynolds number. Thus, for a suitable increase in Re, at fixed $\Omega$, a given type of flow disturbance could be retrieved by reducing the swirl, and the given type was, in general, located downstream of its initial position. This effect can best be seen by considering the higher Reynolds number, BB' curve in Figure [3.20]. Only if, at the higher Reynolds

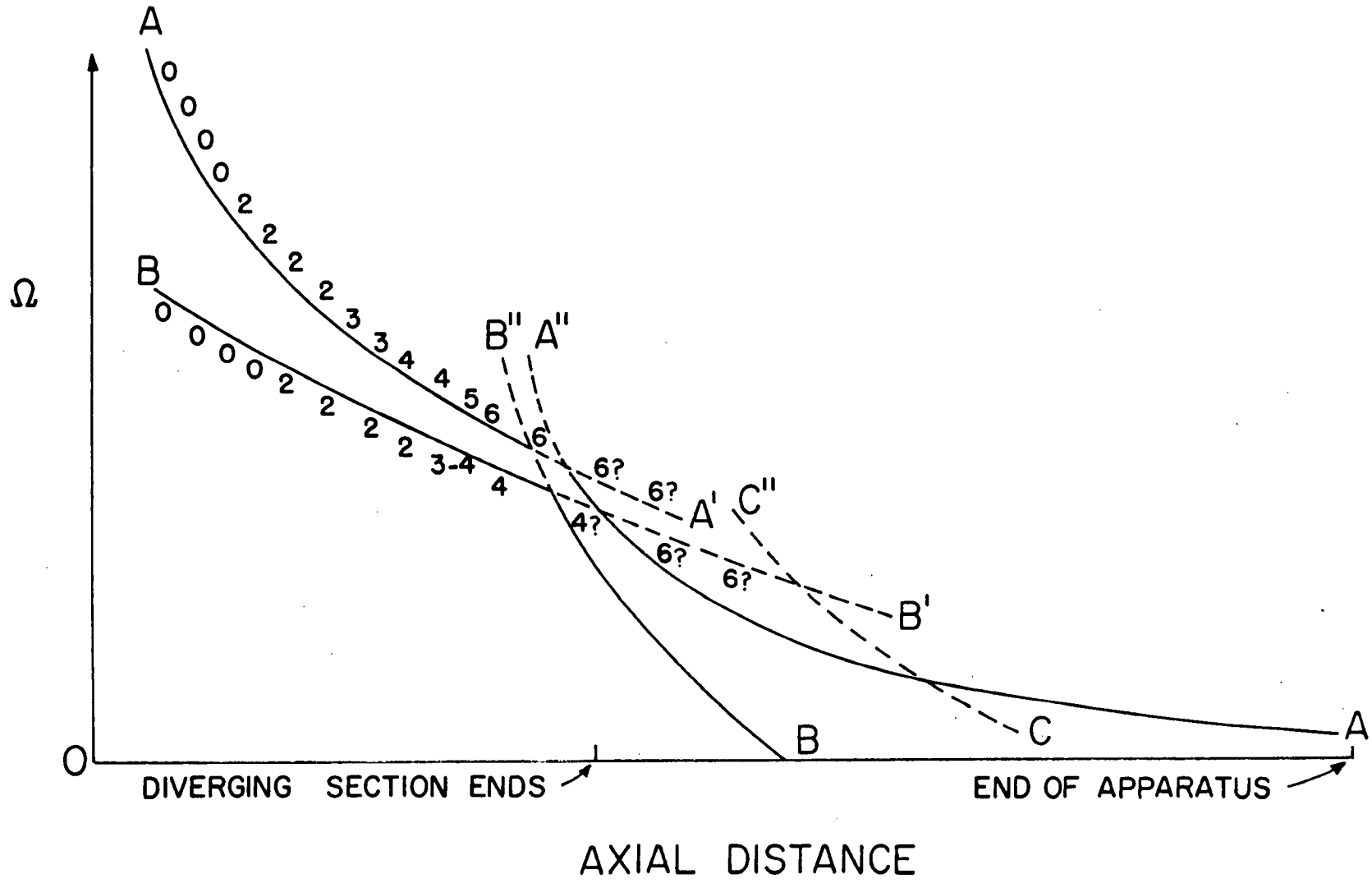


Figure 3.20. Schematic Illustrating the "Two Intersecting Curve" Explanation of Why all Disturbance Forms are seen Only at Low Reynolds Numbers.

number, the "intersection point" had moved to sufficiently lower swirls and downstream, as noted by the hypothetical C"C curve, could all of the disturbance types be observed.

But, in fact, it was found that the onset of oscillations in the central filament appeared at an approximately constant swirl setting and at about the same axial location, independent of Reynolds number, as indicated by B"B. The sum of these two effects was the gradual disappearance of some of the disturbance forms at higher Reynolds numbers. A disturbance type could, in general, be observed only if it existed at swirls higher than the intersection point (and, therefore, occurred upstream of the intersection point). Since this intersection point remained relatively fixed for all the Reynolds numbers used, each of the types 6-3, gradually disappeared as the swirl setting necessary for their formation slipped below the critical swirl which led to oscillations in the filament. This critical value of $\Omega$ appeared to be about .90.

The type 6 (and related type 5) was the first to disappear. For a fixed Reynolds number greater than about 4000, represented by curve BB, the type 6 was never clearly seen (although the expansion and deviation of the off-axis helical filament could still be seen). As the swirl was increased to values above the "intersection point", the type 4 recirculation zone evolved. At this higher Reynolds number, the type 4 and type 3 became indistinguishable from each other, but the flattened nose section of the recirculation zone was still visible, as shown in Figure [3.18]. The nose section was quite unstable in form and position and occasionally disappeared and only random oscillations were observed. (The sharp, clearly defined "intersection point", as shown for clarity in the

schematic Figure [3.20], was, in fact, not a well defined point, but was smeared out in swirl and location).

Further increases in swirl produced the eventual evolution of, first, type 2 and then types 1 and/or 0. Note that decreases in swirl below the intersection point caused the point at which oscillations began to move downstream toward the end of the apparatus. However, as indicated by curve B"B, for this Reynolds number there were oscillations developing in the filament even at zero swirl.

For still larger Reynolds numbers, the type 3/4 disturbance type also gradually disappeared. For Re greater than about 5500, the type 2 spiral was the first form that could be distinguished and it evolved gradually, with increasing swirl, just upstream of that point, relatively fixed in axial location, where oscillations always seemed to exist. As the swirl was further increased the spiral moved upstream and eventually the transformation to type 1 and/or 0 occurred. Further substantiation of the two-intersecting-curve interpretation of these observation seemed evident at these higher Reynolds numbers.

Because the type 3/4 disturbance was less dependent than type 6 on the existence of a relatively undistorted central filament, it was more easily observed even if located downstream of the point at which oscillations began. When it was located more than a tube radius or so downstream of the oscillation point, the type 3/4 disturbance appeared as a zone in which the fragmented dye remnants seemed to decelerate noticeably. As the swirl was increased slightly, the deceleration zone moved upstream and approached the oscillation point. The filament, with its oscillations growing as it moved downstream, seemed to nearly stagnate and "pile up"

as it reached this zone. For Re about equal to 4000, a further increase in swirl led to the upstream movement of this zone and resulted, as noted previously, in the unsteady but identifiable type 3/4, shown in Figure [3.19]. For Re about equal to 5500, the deceleration zone was evident downstream of the oscillations, but increases in swirl led to the gradual evolution of the type 2 spiral, and type 3/4 was never identified.

Although the evidence to substantiate the two curve interpretation is inconclusive, this interpretation does seem to explain the observations made for all of the Reynolds numbers used. The masking effect caused by the upstream occurrence of a disturbance made the identification of any downstream form difficult at best. This prevented further substantiation of the existence of a downstream disturbance. It should be noted that the axial location at which all these curves seemed to intersect was approximately constant. This point appeared to be about one exit tube diameter (5 cm) upstream of the downstream end of the diverging test section. Disturbance types could only be positively identified if they occurred upstream of this point.

The significance of a) the relative proximity of this point to the end of the diverging portion and, b) the approximately constant value of swirl necessary for the appearance of identifiable disturbance types is not apparent. In fact, the significance of the possible existence of two intersecting curves for each Reynolds number is not clear at this time. These observations, the detailed descriptions of each disturbance type, and the presentation of the two-intersecting-curve interpretation are reported in hopes that they will provide some clues which will, perhaps, give a more complete understanding of the mechanism leading to the formation of such

remarkable flow forms.

3.5. Type and Axial Location of Disturbance vs. Flow Conditions.

The flow visualization studies were done both by holding the flow rate (Reynolds number) constant and incrementally varying the swirl ($\Omega$) and by holding $\Omega$ constant and systematically altering the flow rate. For a given set of parameters, (Re,$\Omega$), the type(s) of flow disturbance observed and the mean axial location of the disturbance were identical in each case. These results are summarized for five values of $\Omega$ and a range of Reynolds numbers in Figure [3.21].

The axial location, z, has been normalized with the tube radius at the upstream, non-divergent section, $r_t$ = 1.905 cm, and $z/r_t$ = 0 represents the start of the diverging section. The types of disturbances observed are denoted by the numbers 0-6, as previously described, and the position of these numbers indicates the mean axial location of the disturbance. As previously mentioned, for fixed Re, $\Omega$ a given type of flow disturbance wandered to and fro axially and sometimes spontaneously changed to another type at a different axial location. In the figure, the horizontal bars represent the approximate extent of the axial drift of the type noted. For each $\Omega$, the solid curve is drawn through that type which seemed predominant in terms of frequency of occurrence. The numbers connected by the dashed curve represent a type (and location) which either formed only momentarily and did not persist or persisted, on average, for less time than the predominant mode.

For all swirls shown, the lowest values of Reynolds number resulted in the formation of the type 6 mode. For all Re an increase in $\Omega$ always resulted in the disturbance moving upstream, with a suitably large increase

C-2

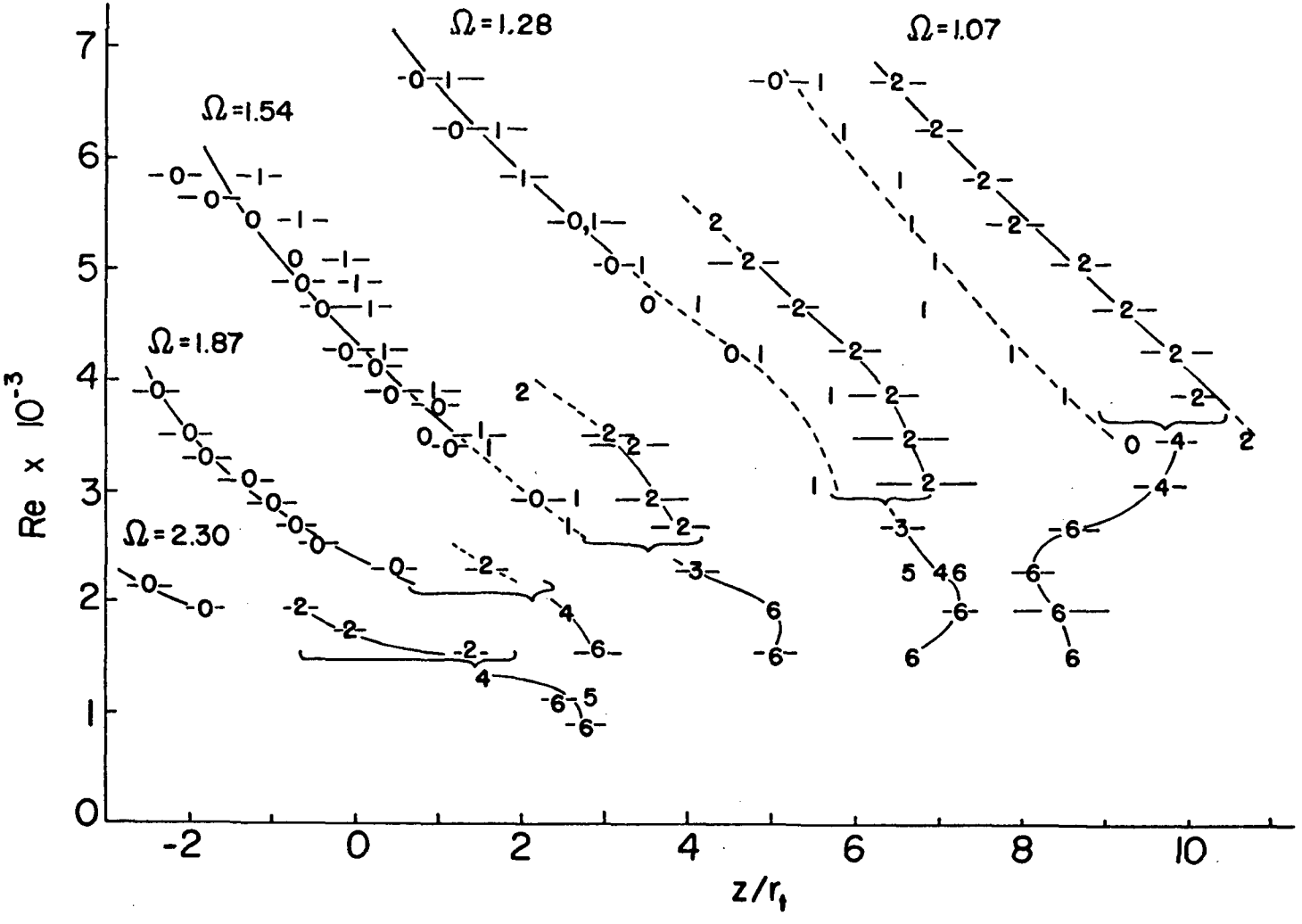


Figure 3.21. The Type of Disturbance (0-6) and its Mean Axial Location vs. Reynolds Number for Five Values of Ω.

leading to a transformation to another type. An upstream movement of the disturbance also resulted, in general, when the flow rate was increased. However, note that for values of swirl less than $\Omega \simeq 1.54$ an increase in Re from a low value sometimes led to a downstream movement of the disturbance. This behavior was observed consistently, but only for a limited range of flow rates.

When the Reynolds number had been increased sufficiently and the transition to the type 2 breakdown had occurred, subsequent increases in flow rate always caused an upstream movement in mean axial location. For example, with $\Omega = 1.28$ and beginning at the lowest value of Re used the type 6 disturbance was located at $z/r_t \simeq 6.7$. As Re was incrementally increased, the disturbance first moved downstream. The next increase resulted in an upstream movement of the type 6 and, during the observation time, the disturbance changed spontaneously into types 5 and 4. Further increases in Re caused the disturbance to move upstream until the transformation to type 2 occurred.

Even at the lowest flow rates for which the type 2 spiral mode was predominant the type 0,1 formed occasionally. The type 0, 1 seldom persisted longer than a few seconds and was always upstream of the mean position of the type 2. As Re was increased, the 0, 1 mode formed more frequently and tended to persist longer. The axial location of the type 0, 1, relative to the mean location of the type 2, remained approximately constant, i.e., the solid and dashed curves indicating $\Omega = 1.28$ remain roughly equidistant.

At a Reynolds number of about 5000, the frequency of occurrence of each type (0, 1 and 2) was approximately the same. Each type would persist

for several minutes or more before changing into the other type. At Reynolds numbers higher than 5000, the type 0, 1 became predominant, the type 2 formed less and less frequently and finally, for Re > 5800, the type 2 was never formed.

Similar behavior was observed for other swirls, as can be seen in Figure [3.21]. Note that for $\Omega = 1.07$ the type 2 breakdown was still the predominant mode at the highest Reynolds number used.

A figure indicating the type and axial position of the breakdown formed at various Reynolds numbers and swirls was presented by Sarpkaya [11,12]. Some differences exist between Sarpkaya's results and the results of this study. Figure [3.22] is essentially a repeat of Figure [3.21], but with the type numbers deleted and solid curves indicating the present results. The plots presented by Sarpkaya [11], are included (dashed curves) for these values of swirl; $\Omega_s = 1.2$, 1.5, and 1.75. The numbers in parenthesis along the abscissa indicate the axial locations observed by Sarpkaya. Note that a relative shift of five units in axial location is necessary to give some agreement between the curves representing similar values of swirl.

The letter "e", denotes the Reynolds number at which, in Sarpkaya's study, the transition from type 2 to type 0 occurred. In comparison to this study, it appears that for similar values of $\Omega$:

a) Equal values of Re resulted in the formation of a breakdown that was considerably further downstream in Sarpkaya's study.

b) The Reynolds number necessary to cause the transition from type 2 to type 0 was substantially higher in the experiments done by Sarpkaya.

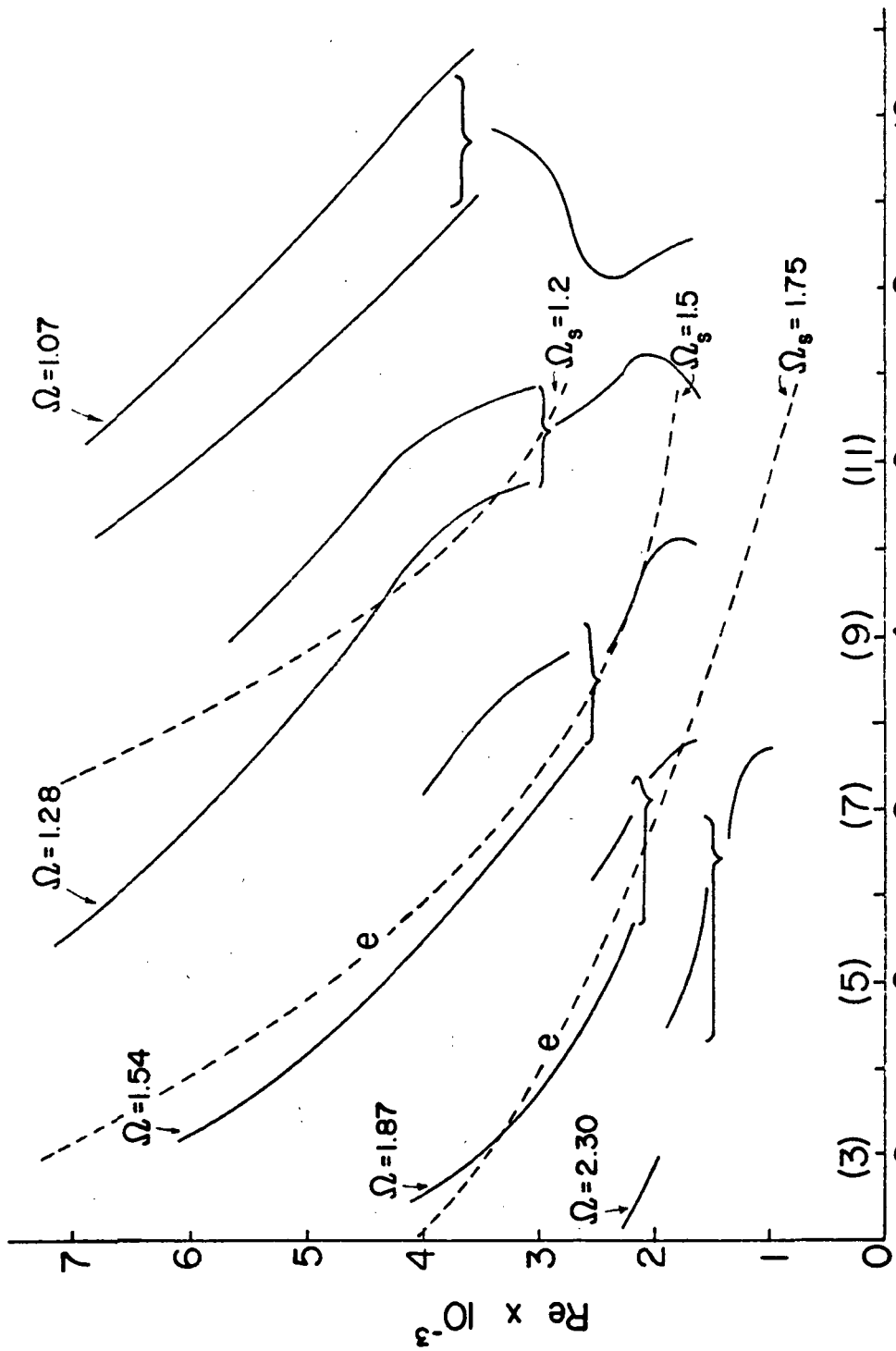


Figure 3.22. A Comparison Between the Results of the Present Study and the Study Reported by Sarpkaya (dashed curves).

These discrepancies result, perhaps, from the differences that exist in the length and shape of the entrance sections used in the two flow devices. The exact shape and/or dimension of the bellmouth, centerbody, and constant diameter throat section used by Sarpkaya are not included in his report. However, based on figures and data given by Sarpkaya, it is believed that the constant diameter throat, immediately upstream of the diverging test section, is somewhat longer in the apparatus used in this study. The vane arrays, bellmouths, and centerbodies used in the two devices also appear to be different in size and/or shape. As shown in Chapter 4, the introduction of a swirl component of velocity has a strong effect on the axial velocity profile in the tube. It is very likely that relatively small changes in the entrance section geometry can lead to substantial alterations in the downstream flow profiles, with resultant changes in breakdown type and location.

Another apparant inconsistency between Sarpkaya's study and the present results is not apparant in Figure [3.22]. As discussed previously, for fixed Reynolds numbers less than about 4000 a succession of disturbance types was observed as the swirl was slowly increased from some low value. The order in which they appeared, starting with type 6, then type 5, type 4, etc. was quite repeatable. Specifically, the type 5, double helix disturbance always formed either from type 6 (spontaneously or with a slight increase in swirl) or, occasionally, spontaneously from type 4.

An increase in swirl from a value resulting in a type 5 double helix led to the formation of the type 4 "flattened bubble" disturbance. In general, as the swirl was increased further the other modes (types 3, 2, 0/1) were formed. The type 2 spiral was always the form that immediately

preceded the type 0/1 axisymmetric mode (for small, incremental increases in swirl).

These results are quite different than those noted by Sarpkaya [11]. In that study, Sarpkaya (who was the first to report the observation of the double helix mode and included striking photographs of the dye pattern) stated that the double helix mode appeared as an intermediate form between the type 2 spiral and type 0/1 axisymmetric bubble. Furthermore, Sarpkaya observed the double helix only at Reynolds numbers less than about 2000 and did not report the other types (6, 4, 3). In a subsequent article, [12] Sarpkaya confirmed these findings and presented descriptions and photographs of the transition from the double helix to the axisymmetric mode due to a slight increase in swirl. Further increases in swirl were reported to result, in all cases, in a fully formed axisymmetric ( or near-axisymmetric) breakdown and a spiral mode was not observed.

At this time, no explanation can be offered to resolve these apparent differences. They may be due to differences in the flow devices or experimental techniques used. In addition, there may be differences in the nomenclature used by Sarpkaya and in this study. For example, some of the photographs presented by Sarpkaya [12] to illustrate the "near axisymmetric" bubbles formed directly from the double helix disturbance bear great resemblance to the disturbance that is herein referred to as the type 4 flattened bubble. Nonetheless, it is unlikely that the differences between the two studies are only semantic.

All of the preceding discussions of the types and locations of the flow disturbances are based on observations done by incrementally varying Re (with $\Omega$ fixed) or $\Omega$ (with Re fixed). Similar results were obtained

when the flow rate was held constant and the vane angle was slowly and continuously altered. This was accomplished by driving the vane array control mechanism with a small motor. In this way, the steady progression of the disturbance upstream and the transformation from one type to another could be closely and conveniently observed. No noticeable differences existed between these results and the results obtained by incrementally changing $\Omega$.

### 3.6. The Transient Response of the Breakdown

The response of the type 0/1 and type 2 breakdowns to a step change in Re or $\Omega$ was also studied. The behavior observed was essentially the same as that discussed in detail by Sarpkaya [11]. In his report, Sarpkaya described the changes that occurred in breakdown type and location due to a sudden change in flow rate or swirl angle. Included also were sequential photographs of the travelling flow disturbance. The following examples illustrate the transient response of the breakdown.

#### 3.6.1. Response to a Change in Reynolds Number

The swirl angle was set at $\Omega = 1.54$ and the Reynolds number was 4500. A type 0 breakdown was located at about $z/r_t = -.3$ and the off-axis dye injector was set to give a helix that had a diameter of approximately one-half the tube diameter. The flow rate control valve was then rapidly opened to give an increase in Reynolds number to Re = 4900.

The axisymmetric breakdown began to drift, almost immediately, downstream. Simultaneously, the helical dye pattern appeared to "stretch out" somewhat (the pitch increased) and the bubble moved downstream about 3 cm. Then, perhaps after a short delay, the bubble and helix seemed to move downstream together (with no change in helix pitch) an additional distance of about 1 cm. After a brief delay, the helix pitch appeared to decrease

rapidly, (i.e. the distance between adjacent turns decreased), the bubble moved rapidly upstream and became much longer and smaller in diameter than it was at steady conditions. After a slight upstream overshoot, the breakdown settled in its new axial location, about 1.5 cm upstream of its original position.

A decrease in Re yielded the opposite response, with the bubble moving initially upstream before travelling to its new location downstream of the initial axial location. Similar behavior was observed for other values of Re and $\Omega$, with various Reynolds number step sizes. Those increases in Re which led to a transformation from the type 2 spiral to a type 0/1 bubble resulted in changes that were especially dramatic. The new bubble appeared to be formed from an abrupt, axisymmetric "swelling" of the dye filament. This often occurred just ahead of the upstream-travelling spiral, with the spiral breakdown subsequently being washed downstream and disappearing. In some cases, the new bubble persisted only momentarily before changing into a spiral form located upstream of the axial location of the initial spiral.

### 3.6.2. Response to a Change in $\Omega$

The Reynolds number was fixed at 4500, with $\Omega = 1.62$. A type 0 bubble was located at $z/r_t \approx -.8$. The vane angle was then increased rapidly to $\Omega = 1.83$. After a noticeable time delay (about 4-5 seconds) the helix pitch increased and the bubble moved downstream about 1.5 cm. After another, shorter delay the helix pitch decreased and the bubble moved rapidly upstream about 5.5 cm. The breakdown then drifted downstream about 1 cm, finally reaching its new mean location about 3 cm upstream of the initial axial position. A decrease in swirl gave similar results, but in reversed order, with the breakdown moving initially upstream before moving

downstream to its new location.

If the initial flow conditions were set to give a type 2 spiral, a suitably large increase in swirl resulted in the formation (sometimes only momentarily) of a type 0/1 bubble. This occurred in the way described previously for a sudden increase in flow rate. That is, as the spiral form moved rapidly upstream (after having reached its furthest downstream location) a type 0/1 bubble suddenly formed upstream of the travelling spiral. The bubble formation was very abrupt and appeared to result from a sudden expansion of the central dye filament. The initial upstream travelling spiral was "lost" in the wake of the bubble and washed downstream. Then, depending on which form was predominant at the new flow conditions, the bubble either persisted or changed into a new spiral.

### 3.6.3. The Transient Behavior of the Centerline Axial Velocity

The rather surprising response of the breakdown to a sudden change in flow conditions (i.e. the disturbance initially moving in a direction opposite to the direction it must finally move to reach its new steady state location) prompted an experiment in which the axial velocity upstream was monitored as the swirl or flow rate was rapidly altered. Figures [3.23] and [3.24] are traces of the strip chart recordings taken during two of these trials. The time and velocity axes are superimposed on the traces, the dashed lines indicating constant time arcs. In both cases, the velocity was measured at the tube centerline upstream of the start of the diverging test section. Since the measuring point was located quite far upstream of the breakdown, there was a discrepancy between the time a certain change in velocity was measured and the time that this change was "felt" by the breakdown.

Figure [3.23] shows the changes in velocity that occurred due to a step increase in Reynolds number from 3720 to 4380. As one would expect, the axial velocity increased almost immediately and the spiral moved slowly downstream. After about seven seconds however, the velocity decreased sharply and reached a value lower than the initial one. The velocity then increased rapidly to its new steady state value. The time at which the velocity increased rapidly seemed to show some correlation with the rapid upstream movement of the breakdown. The momentary dip in axial velocity did not occur when $\Omega$ was set to zero.

Figure [3.24] is a velocity vs. time trace recorded during and subsequent to a rapid increase in $\Omega$ from $\Omega = 1.068$ to $\Omega = 1.282$. Note the rather long delay between the time at which the swirl was changed and the time at which a significant increase in velocity occurred. As in the previous case, there is a sharp decrease in velocity just prior to the rapid increase to the new steady state value. Again, there appeared to be a correlation between this rapid increase and the initiation of the rapid upstream movement of the breakdown.

The two traces presented are typical of those recorded for various combinations of initial and final conditions. There were some changes, from trial to trial, in the amplitude and shape of the velocity dip and the relative times at which certain changes in breakdown location were noted. In general, however, the results were quite repeatable. The velocity profiles presented in Chapter 4 indicate that an appreciable swirl velocity causes significant changes in the axial profile. The changes are greatest in magnitude on the tube axis. Evidently, the strong interaction between swirl and axial velocity results in a transient behavior typified by the velocity vs. time traces presented above.

Figure 3.23. Centerline Axial Velocity vs. Time. Velocity was Measured at ($r = 0$, $z/r_t = -.1.43$), with $\Omega = 1.282$.

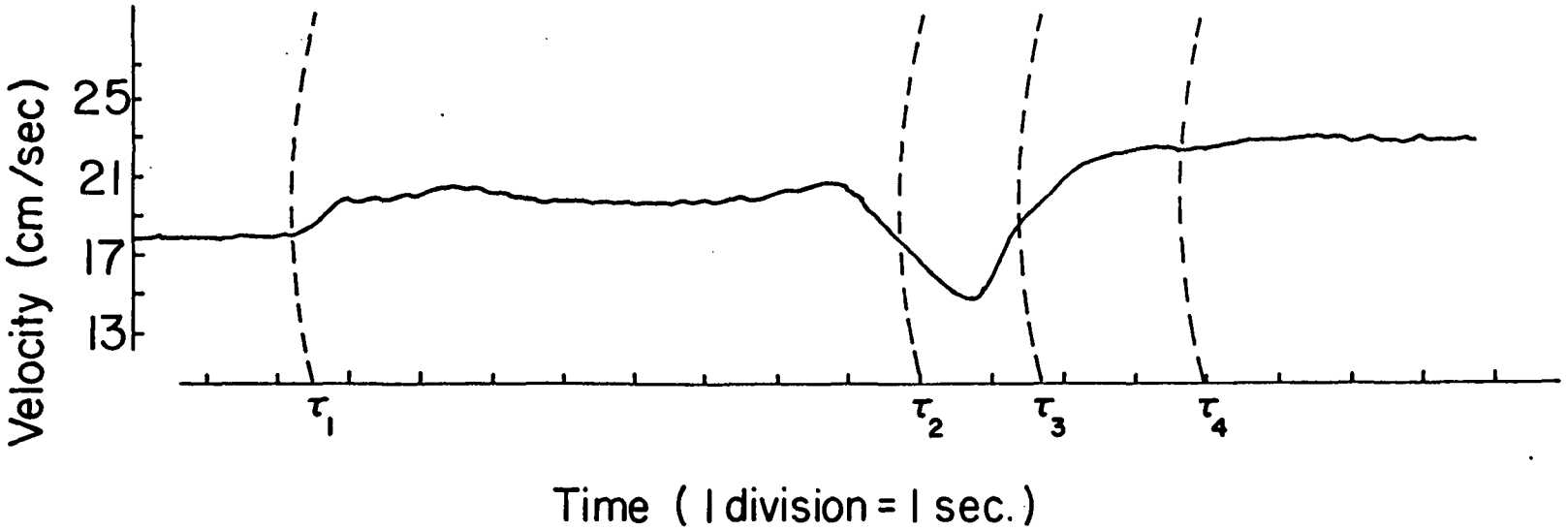


1. $t < t_1$; Re = 3720: Breakdown was a Type 2 Spiral located at $z/r_t \approx 4.9$.
2. $t = t_1$; Re was increased abruptly to Re = 4380 and spiral began drifting downstream almost immediately.
3. $t = t_2$; spiral reached furthest downstream location, $z/r_t = 7.5$, and remained there until $t_3$.
4. $t = t_3$; spiral began moving rapidly upstream.
5. $t = t_4$; A Type 0/1 Bubble formed abruptly at $z/r_t \approx 2.8$. Bubble resulted from sudden, axisymmetric swelling of dye filament ahead of upstream-travelling spiral mode. Spiral was then washed downstream and broken up.

Figure 3.24. Centerline Axial Velocity vs. Time. Velocity was Measured at ($r = 0$, $z/r_t = -.67$), with Re = 4540.

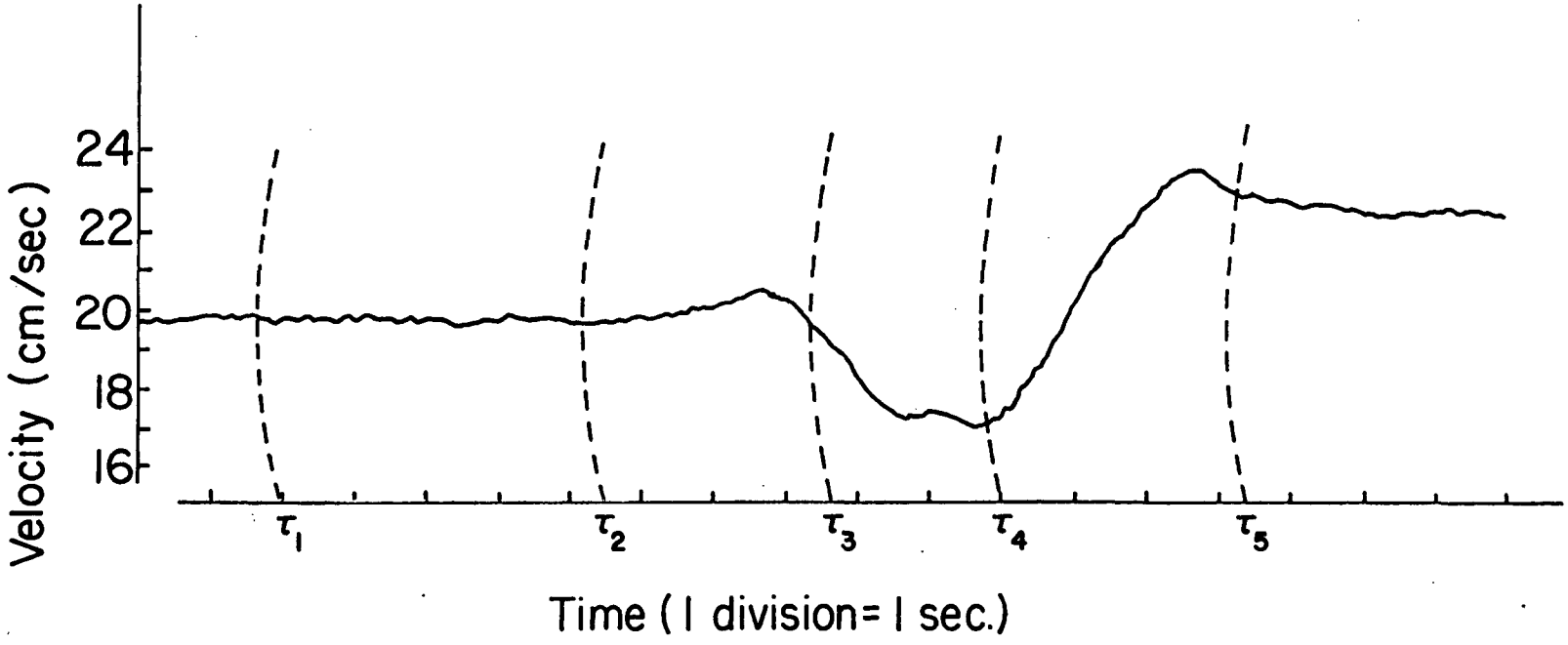


1. $t < t_1$; $\Omega = 1.068$, breakdown was a Type 2 Spiral located at $z/r_t \approx 7.5$.
2. $t = t_1$; $\Omega$ was increased rapidly to $\Omega = 1.282$.
3. $t = t_2$; first meaningful change in spiral location noted as breakdown began to drift slowly downstream.
4. $t = t_3$; spiral reached its furthest downstream location, $z/r_t \approx 8.6$.
5. $t = t_4$; spiral began moving rapidly upstream.
6. $t = t_5$; a Type 0/1 Bubble formed abruptly at $z/r_t \approx 3.1$. Bubble resulted from sudden, axisymmetric swelling of dye filament just in front of upstream-travelling spiral, which was then broken up in the Type 0/1 Bubble wake.

CHAPTER FOUR

## 4.0. Velocity Measurements

The objective of the studies described in this chapter was to provide detailed velocity measurements of the swirling flows which were produced in the test section described previously. In the first series of experiments, the radial variation of axial and swirl velocity was measured at an axial location 1.2 cm upstream of the start of the diverging section of the tube ($z/r_t = -.67$). The second experiment, which was much more difficult to perform, resulted in a mapping of the flow field associated with a fixed Re and $\Omega$. The Reynolds and circulation numbers used for this mapping resulted in the formation of a relatively stable type 0 breakdown.

## 4.1. Accuracy

The equipment used to measure the flow velocities is discussed in Chapter 2. A further discussion of the sources and magnitude of the errors in the measurements is presented here. Firstly, there was an uncertainty in the position of the measuring probe (the intersection of the two laser beams) in the tube. The greatest source of uncertainty in determining this position was the initial alignment prodecure. As indicated in Chapter 2, the initial alignment was done visually, using the central dye filament to indicate r = 0 and a scale attached to the outside diameter of the test section to indicate axial location. The equations relating the position coordinates (r,z) of the probe volume in the tube to the position of the optical unit (X,Y) are, for axial velocity:

$$r = n_w(Y-Y_o) \tag{4.1}$$

$$z = .5 + (X-X_o) \tag{4.2}$$

where $n_w$ = index of refraction of water

$X_o, Y_o$ = the reference values of X,Y noted after initial alignment.

The quantities $(Y-Y_o)$ and $(X-X_o)$ could be determined with good accuracy (error less than .05 mm) since micrometers were used to measure these values. The major source of error, however, was in determining $X_o$ and $Y_o$. By repeating the initial alignment several times it was possible to estimate the probable error in r, z for $X = X_o$, $Y = Y_o$. If these estimated errors are included in equations (4.1), (4.2), they become

$$r = n_w(Y-Y_o) \pm .60 \text{ mm} \tag{4.3}$$

$$z = .4 + (X-X_o) \pm .20 \text{ mm} \tag{4.4}$$

where the absolute error in r,z, of .55 mm and .15 mm respectively, has been added to the relative error in $(Y-Y_o)$, $(X-X_o)$. Thus, the uncertainty in position between two measuring points (i.e., in moving the optical unit) was quite small compared to the error in knowing the exact location of each measuring point relative to the fixed r,z, coordinate system.

For velocity profiles in which velocity is plotted as a function of radius, r, or non-dimensional radius, $r/r_i$, the above discussion implies that the profiles could be shifted along the r (or $r/r_i$) axis by .55 mm (or .029 for non-dimensional plots), but that the relative spacing between individual points was quite accurate.

A similar set of equations (but slightly more complicated for r) can be written for swirl velocity. However, the initial alignment procedure to locate r = 0 could be checked, after the Bragg cell optical frequency shift unit had been installed, by demanding a swirl velocity of zero on the tube centerline.

An analysis to determine the error in the velocity measurements must be done in several parts. This is because some experiments were done prior to the installation of the optical frequency shift unit and without day to day tracker calibration, while the later experiments were done using the frequency shift unit and accurate tracker calibration.

The equation relating velocity to the measured (or known) parameters was presented in Chapter 2.

$$V = \lambda \frac{(f_D - f_o)}{\theta}$$

where $V$ = velocity (cm/s)

$\lambda$ = wavelength of laser light in water (cm)

$\theta$ = angle between the two intersecting beams (radians)

$f_D$ = frequency of photomultiplier output signal (Hz)

$f_o$ = difference in optical frequency between two intersecting beams, due to Bragg cell frequency shift unit (Hz).

Except for $\lambda$, there is an uncertainty, or tolerance, associated with each of the measured parameters. Using primes to indicate the nominal (measured) value, double primes to indicate the tolerance, and no superscript to denote actual value, then

$$\theta = \theta' \pm \theta''$$

$$f_D = f_D' \pm f_D''$$

$$f_o = f_o' \pm f_o''$$

$$V = V' \pm V''$$

Substituting these values into the above equation, rearranging, and neglecting products of double primed quantities gives:

$$V = V' \pm V'' = \lambda \left(\frac{f_D'-f_o'}{\theta'}\right) \pm \left(\frac{f_D'-f_o'}{\theta'}\right) \frac{\theta''}{\theta'} \pm \frac{f_D''}{\theta'} \pm \frac{f_o''}{\theta'}$$

Noting that $\frac{\lambda(f_D'-f_o')}{\theta} = V'$, then

$$V - V' = \pm V'' = \pm \frac{\theta''}{\theta'} V' \pm \frac{\lambda f_o''}{\theta'} \pm \frac{\lambda f_D''}{\theta'} \qquad (4.5)$$

In assigning numerical values to each term of equation (4.5), consideration must be given to the procedure and equipment used in conducting the experiments. In general, all of the velocity measurements taken can be categorized into one of three groups. The groups will be A, B, and C and in the tabulated data presented in Appendix A3 the letter will identify which error analysis is appropriate for each velocity measurement.

Group A - For this group, the velocity measurements were made before the frequency shift unit was installed ($f_o = f_o'' = 0$), the frequency tracker was not calibrated, and the analog voltage output from the tracker was monitored by a digital voltmeter to indicate time averaged voltage, which was used to calculate mean velocity. The strip chart recorder, when used, also monitored the tracker output voltage to obtain the amplitude of the velocity fluctuation.

The specifications of the frequency tracker indicated an accuracy of ± 1% of full scale deflection, with an analog voltage output of 10 volts corresponding to full scale deflection. A calibration done after the Group A measurements were taken indicated an error in excess of this (average error of 6%). Therefore, all of the Group A readings were corrected using this calibration curve. This correction assumed that the

error, although quite large, had not changed considerably during the time, prior to calibration, that these measurements were taken. This assumption could not be checked in an absolute way, but a comparison of readings of the same velocity using two frequency channels could be used to verify whether a given accuracy claim was possible. Such comparisons indicated that an accuracy claim of 1% of full scale deflection for the corrected data was, in all cases, possible. In other words, for a fixed velocity the difference between two readings taken on different channels was always less than the possible error obtained by assuming the 1% full scale deflection accuracy level. Although this is not an absolute check (it is a necessary but not sufficient check on an accuracy claim), the assumption of an error of 1% full scale deflection seems quite reasonable.

The digital voltmeter error was .02 volts, which included the ± 1 digit error usually present in digital readout instruments. Since the equation relating analog voltage to frequency was $e = 10 \times f_D/f_{max}$, where e = analog voltage and $f_{max}$ = full-scale-deflection frequency, then the digital voltmeter error can be written as .002 f.s.d. (full scale deflection). Adding the voltmeter error to the tracker error (± 1% f.s.d.) and including the value $\theta''/\theta' = .003$ (see Chapter 2) gives the following results from equation (4.5), with $f_o'' = 0$, $\lambda/\theta' = .240 \times 10^{-3}$cm.

| Channel Used | Velocity Range | $f_D''$ | V" |
|---|---|---|---|
| 15 KHz | 0.7 - 2.9 CM/s | 180 Hz | (± .003V' ± .04) CM/s |
| 50 KHz | 2.4 - 9.6 CM/s | 600 Hz | (± .003V' ± .14) CM/s |
| 150 KHz | 7.2 - 28.8 CM/s | 1800 Hz | (± .003V' ± .40) CM/s |
| 500 KHz | 24.0 - 96.0 CM/s | 6000 Hz | (± .003V' ± 1.40) CM/s |

Group B - Results in this group were obtained after the frequency shift unit was installed. The accuracy of the frequency shift, $f_o''$, was specified by the manufacturer to be .5% $f_o'$, and this error limit was primarily due to the effects of temperature drift of the instrument oscillators [32]. For these measurements, the frequency tracker was calibrated daily using a frequency generator and a frequency counter. The 1% full-scale-deflection tracker accuracy, used in Group A and specified by the supplier, was due in large part to the non-linearity of the voltage controlled oscillator. By calibrating the tracker daily, this error could be reduced to .25% of the frequency reading [32]. This remaining error (.25%) was due to thermal drift of the voltage controlled oscillator.

All of the measurements in Group B were made using the 150 KHz range, with $f_o$ = 75 KHz or 25 KHz. The digital voltmeter was used to indicate time averaged frequency (actually, analog voltage) and the accuracy associated with this method was, as in Group A, ± .02 volts. In summary, the errors for Group B were

$$\frac{\theta''}{\theta} = .003$$

$$f_o'' = .5\%\ f_o' = \begin{cases} 125 \text{ Hz} & f_o' = 25 \text{ KHz} \\ 375 \text{ Hz} & f_o' = 75 \text{ KHz} \end{cases}$$

$$f_D'' = .0025\ f_D' + (.002)(150 \text{ KHz})$$

Noting that $\lambda/\theta'(f_D'-f_o') = V'$ and using $\lambda/\theta = .246 \times 10^{-3}$cm, equation (4.5) gives the following results for maximum errors for Group B measurements;

$$V'' = \pm .003V' \pm .0025V' \pm \begin{cases} .12 \text{ cm/s} & f_o' = 25 \text{ KHz} \\ .21 \text{ cm/s} & f_o' = 75 \text{ KHz} \end{cases}$$

Group C - These measurements were made using the same calibration procedure used in Group B and with the same equipment, except that a signal conditioner/D.C. voltage suppressor, in series with a strip chart recorder, were used to measure the analog voltage output of the frequency tracker. The signal conditioner was used to filter out analog voltage fluctuations with frequencies greater than 10 Hz. The D.C. voltage suppressor and strip chart recorder were carefully checked periodically during the tests to alleviate drift in gain and null point. The level of accuracy using this set-up was primarily determined by the accuracy with which one could estimate mean velocities (voltages) from the recorder strips. This accuracy varied from ~.02 to .05 volts, depending upon the fluctuation amplitude. The frequency range used was 150 KHz f.s.d. and $f_o'$ was 75 KHz. The possible errors in Group C measurements were, then

$$V'' = \pm .003V' \pm .0025V' \pm .14 \text{ cm/s} \pm \begin{matrix} .07 \text{ cm/s a} \\ .19 \text{ cm/s b} \end{matrix}$$

a = small amplitude fluctuations

b = large amplitude fluctuations

It should be pointed out that in all of the above groups the numerical values of the errors represent the maximum errors, or worst possible case. The only systematic error was the $\theta''/\theta'$ term and the others were random in nature. Since the systematic error contribution was small (.003V') it is improbable that the error in any single measurement would be as large as the maximum possible. Furthermore, the tabulated data are, in most cases, the result of averaging several trials. The error associated with an average value, obtained by separate trials having random errors $\varepsilon$, is approximately $\varepsilon/\sqrt{\eta}$ where $\eta$ is the number of trials. Therefore, the

probable error in the tabulated data is, in most cases, a fraction of the maximum possible error resulting from the preceding analysis.

## 4.2 Equipment Limitations

The equipment used to measure the flow velocity had several limitations.

1. In regions where the radial velocity gradients were high, the tracker was unable to process the rapidly changing frequency. The frequency of the signal fluctuates, in these regions, because the long dimension of the probe volume was aligned radially and thus particles traversing opposite end portions of the probe volume had significantly different velocities. The signal frequency varied rapidly as particles passed alternately through these end portions. Under these conditions, the velocity readings obtained showed considerable scatter and reproducibility was poor. This was true for readings taken close to the tube wall and, for swirl velocity, near the tube centerline. The addition of the frequency shift unit alleviated this difficulty, to a great extent, for the case of swirl velocity near the centerline.

2. In addition to the limitation described above, measurements very close to the tube wall were not possible because a certain fraction of the light from the laser beams was reflected from the inside surface of the tube. As the probe volume was moved closer and closer to the tube wall it became more difficult to prevent this reflected light (by means of the pinhole aperture) from reaching the photomultiplier tube. Since the light reflected from the tube wall was not Doppler shifted it served only to increase the noise level of the photomultiplier output. When a radial position was reached such that the quantity of this reflected light was

much larger than that of frequency shifted light it became impossible to process the signal to extract velocity information.

3. The optical set-up used did not permit traversing across the entire diameter of the tube. It was possible to make radial traverses along the horizontal line extending from just inside the tube wall closest to the optical unit to a point slightly beyond the tube centerline. Thus, the axisymmetry of the velocity profile could be checked only near the tube centerline.

## 4.3 Base Flow Profiles

The first series of velocity measurements were done at a fixed axial station, $z/r_t = -.67$, located just upstream of the start of the diverging section of the tube. The radial profiles of axial and swirl velocity at this axial location (herein called base flows) were measured at three Reynolds numbers. For each Reynolds number the axial velocity profile was measured for four values of $\Omega$. Then the optical unit was rotated $90^o$, the initial alignment procedure to determine $X_o$, $Y_o$ was repeated, and the swirl velocity profiles were measured at the same values of $\Omega$ (except for $\Omega = 0$). These base flow profiles, unknown before this study, are shown in Figures [4.1 - 4.7]. (All the velocity data presented graphically are tabulated in Appendix A3). For all of these measurements, the flow disturbance (when one existed) was located well downstream of the measuring point and the velocity readings were unaffected by the axial wanderings of the disturbance.

Perhaps the most striking feature of these figures is the very marked changes that occur in the axial velocity profiles as the swirl angle was increased from zero. For all the Reynolds numbers used, a vane angle of

zero ($\Omega = 0$) resulted in an axial velocity that was nearly constant with radius until the boundary layer along the tube wall was reached, and at that point the velocity began to decrease sharply. An increase in $\Omega$ led to the formation of a region of high velocity near the tube centerline. The magnitude of the change in centerline axial velocity was quite high. For example, the axial velocity at $r = 0$ was nearly doubled by increasing the swirl from $\Omega = 0$ to $\Omega = 1.28$. The percentage change in centerline velocity, for the same change in $\Omega$, was increased as the Reynolds number was increased. For an increase in $\Omega$ from .73 to 1.07, the change in axial centerline velocity was 19%, 23%, and 30%, respectively, for Reynolds numbers of 3220, 4540, and 6000.

The existence of high axial velocities near the center of the vortex core formed by the leading edge of delta wings has been reported previously, c.f. Lambourne and Bryer [24]. In those unconfined, swirling flows, the velocity along the vortex axis has been reported to be as much as three times greater than the velocity upstream of the delta wing. The results of this study show that the same effects occur in confined swirling flows.

For each of the Reynolds numbers used, there were two radial locations at which the axial velocity remained nearly constant, independent of $\Omega$. The first point, $r = r_c$, say, can be seen in the figures as that point at which the curves representing various values of $\Omega$ intersect. The second point $r = r_b$, say, was near the tube wall and all of the curves appeared to merge at that point. For $r < r_c$, an increase in swirl caused an increase in axial velocity. This increase was compensated for (the volume flow rate was constant) by a decrease in velocity for $r_c < r < r_b$. Note also that at a fixed, non-zero swirl the velocity increased slightly as r was increased

to a value just less than that r which marked the edge of the boundary layer. This effect was most noticeable at the highest value of Re used.

For each set of curves, i.e. for a fixed Re and velocity component and various values of $\Omega$, a fixed value of $Y_o$ was used, as determined by the initial alignment procedure. Thus, all of the profiles of a given set can be assumed to be quite accurately located, relative to each other, in radial location. However, since the alignment procedure was repeated between sets, it is not possible to say, with absolute certainty, that a given radial location of one set corresponds exactly with the same, noted radial location of a different set. Nevertheless, the profiles do seem to indicate that $r_c$, the radial location at which the curves of a given set intersect, tended to move closer to the centerline as the Reynolds number was increased. Furthermore, for a fixed Reynolds number $r_c$ appears to correlate quite well with the radial location at which the swirl velocity profiles change from noticeably concave down ($\partial^2 v/\partial r^2 < 0$) to slightly concave down ($\partial^2 v/\partial r^2 \to 0$, Re = 3220), or linear ($\partial^2 v/\partial r^2 = 0$, Re = 4540) or concave up ($\partial^2 v/\partial r^2 > 0$, Re = 6000). In other words, $r_c$ apparently marks the inside boundary of a region in which the swirl velocity exhibits a 1/r type of behavior.

Finally, some of the profiles seem to show a slight velocity defect at the tube centerline indicating that the remnants of the centerbody wake still existed at this axial location. This was most noticeable at the lower values of swirl.

The swirl velocity profiles for these base flows all indicate that a solid body type of velocity distribution existed near the tube centerline. In this solid-body core the velocity increased rapidly with increasing r

until reaching a maximum value at $r = r_p$, say. For $r > r_p$ the velocity decreased with increasing r, but as indicated previously the profiles in this outer region exhibit a positive second derivative (concave up, 1/r type behavior) only for Re = 6000. For both Re = 3220 and Re = 4540 the velocity decreased faster than a 1/r distribution, with the second derivative being always negative for Re = 3220 and being approximately zero for Re = 4540.

Note that, in contrast to the axial profiles, the three curves for Re = constant and various values of $\Omega$ do not tend to merge into one curve near the tube wall. It was possible to make measurements closer to the tube wall for swirl velocity than axial velocity due to the smaller radial gradients of swirl. The swirl velocity boundary layer was considerably thinner than the axial velocity boundary layer.

Also in contrast to the axial velocity, the percent change in maximum swirl velocity, for a given change in $\Omega$, was essentially independent of Reynolds number. For example, the percentage changes in maximum swirl for a change in $\Omega$ from .73 to 1.07 was 44%, 44%, 47%, respectively, for Reynolds numbers of 3220, 4540, and 6000. The figures for a change in $\Omega$ from 1.07 to 1.28 were 23%, 22% and 20%. The radial position of the maximum swirl velocity, $r_p$, remained essentially constant when the Reynolds number was held constant and $\Omega$ was varied. However, $r_p$ decreased slightly with increasing Reynolds numbers indicating that a smaller solid body core, as well as higher swirl velocities, existed at the higher Reynolds numbers. The resultant high radial gradients made reliable velocity measurements difficult in the deep interior of this core. Before the installation of the frequency shift unit, measurements closer to the centerline than

$r/r_i \approx .07$ showed poor reproducibility and it was impossible to obtain data very close to r = 0.

Measurements on and near the centerline were possible after the frequency shift unit was installed, Figures [4.3, 4.5]. The data indicate that a sub-core region existed near r = 0 in which the swirl was essentially zero. By traversing in small increments on either side of r = 0, it was possible to check the initial alignment (to determine $Y_o$) and to measure the diameter of the sub-core. The diameter was approximately 1.9 mm for Re = 3220 and 4540. The region just outside of this sub-core was characterized by very high radial gradients and at high Re and $\Omega$ it was not possible to obtain accurate data at these radial locations (note missing data points at $r/r_i \approx .09$, Re = 4540, $\Omega$ = 1.07, 1.28).

The swirl measurements at Re = 3220 were made both before, Figure [4.2], and after, [Figure 4.3], the installation of the frequency shift unit. There is some discrepancy in both $r_p$ and the value of the peak swirl velocity. The difference in $r_p$ is probably due to the variations in initial alignment (Figures [4.3, 4.5] should be considered to be quite accurate regarding actual versus indicated radial location). The difference in peak velocity may, in part, be due to instrument errors. However, it is more likely that the velocities were actually different. This conjecture is based on the fact that on several occasions a noticeable change in peak swirl velocity occurred over a span of 10 - 20 minutes.

For example, the measuring point was traversed until the point of maximum swirl velocity was determined and then the location was held fixed. The velocity was then measured for 30 - 60 minutes and changes were noted. In some cases the velocity remained essentially constant. In others, the

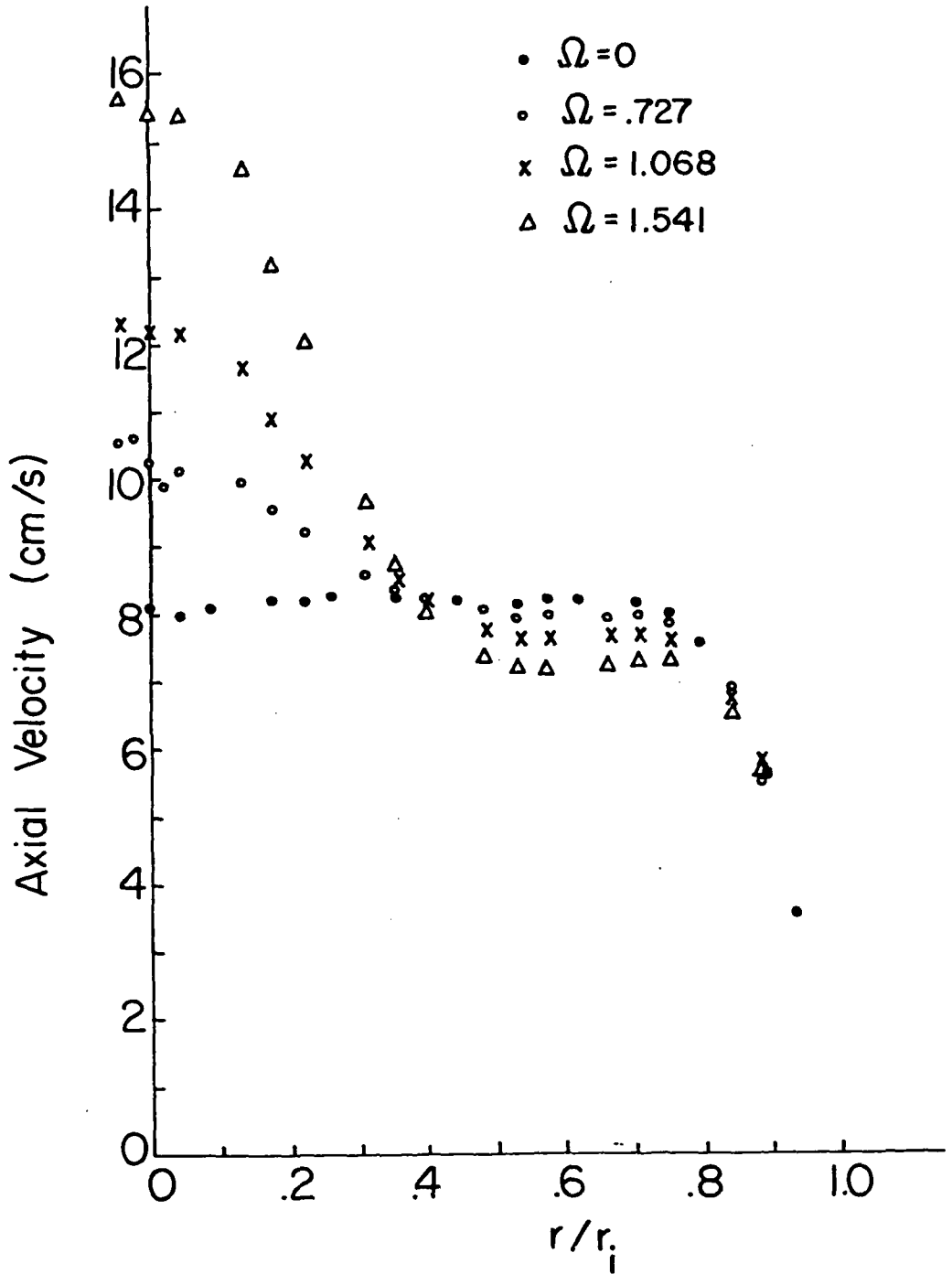


Figure 4.1. Axial velocity vs. non-dimensional radius for Re = 3220 and various values of the swirl parameter, Ω. The axial location was $z/r_i = -.67$.

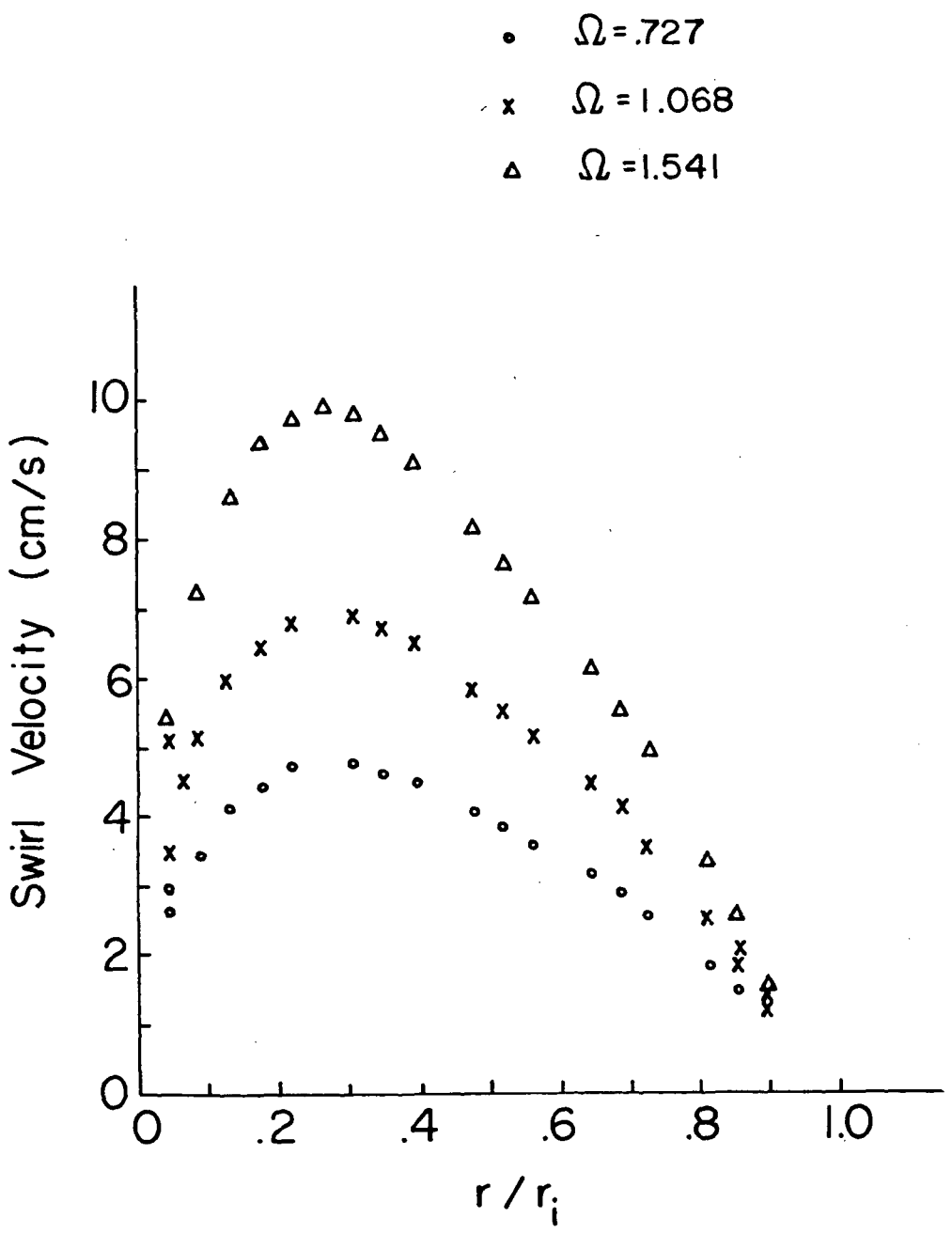


Figure 4.2. Swirl velocity vs. non-dimensional radius for Re = 3220 and various values of the swirl parameter, Ω. The axial location was $z/r_i$ = -.67. The data were obtained before installation of the frequency shift unit.

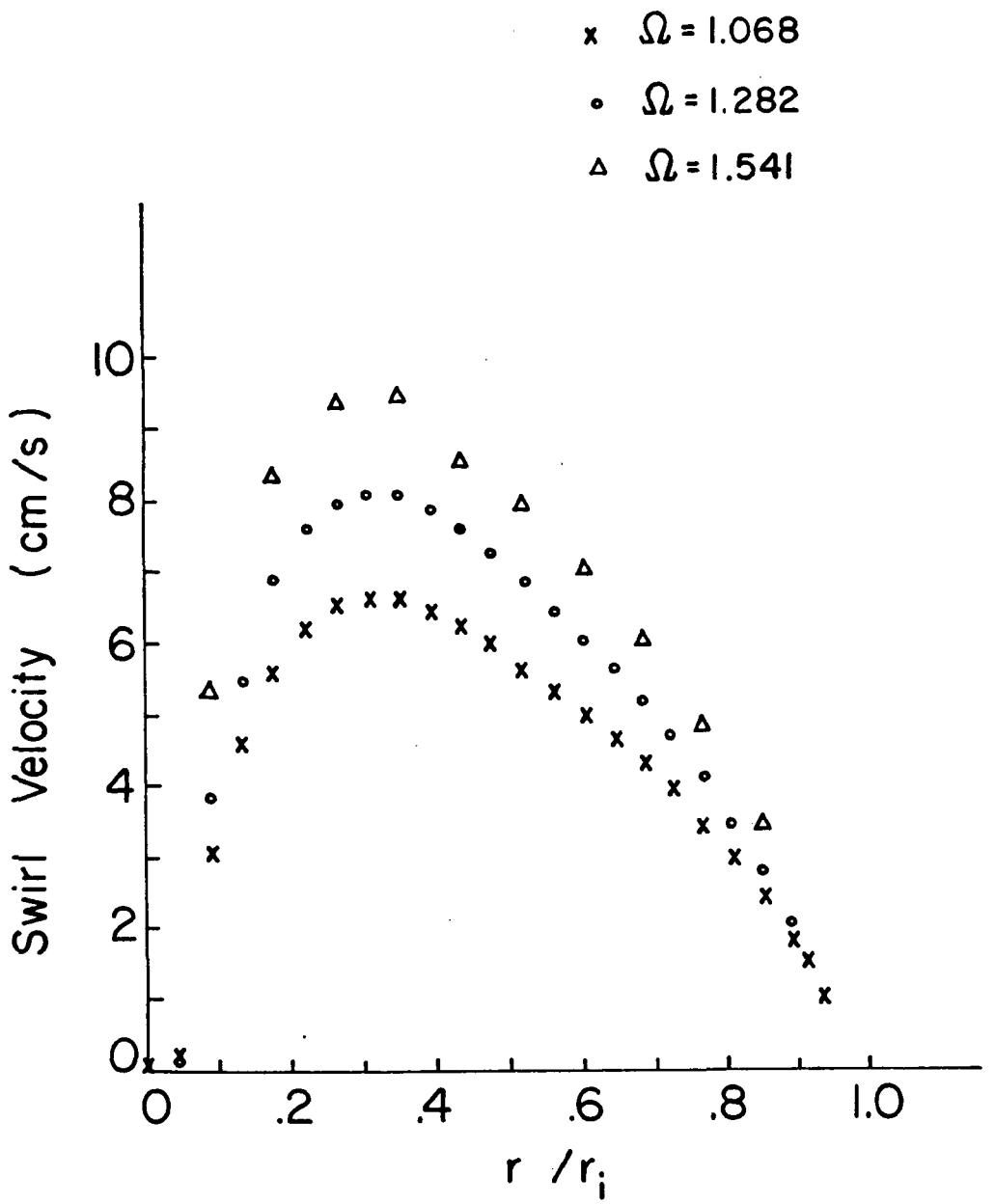


Figure 4.3. Swirl velocity vs. non-dimensional radius for Re = 3220 and various values of the swirl parameter, Ω. The axial location was $z/r_i$ = -.67. The data were obtained while using the frequency shift unit.

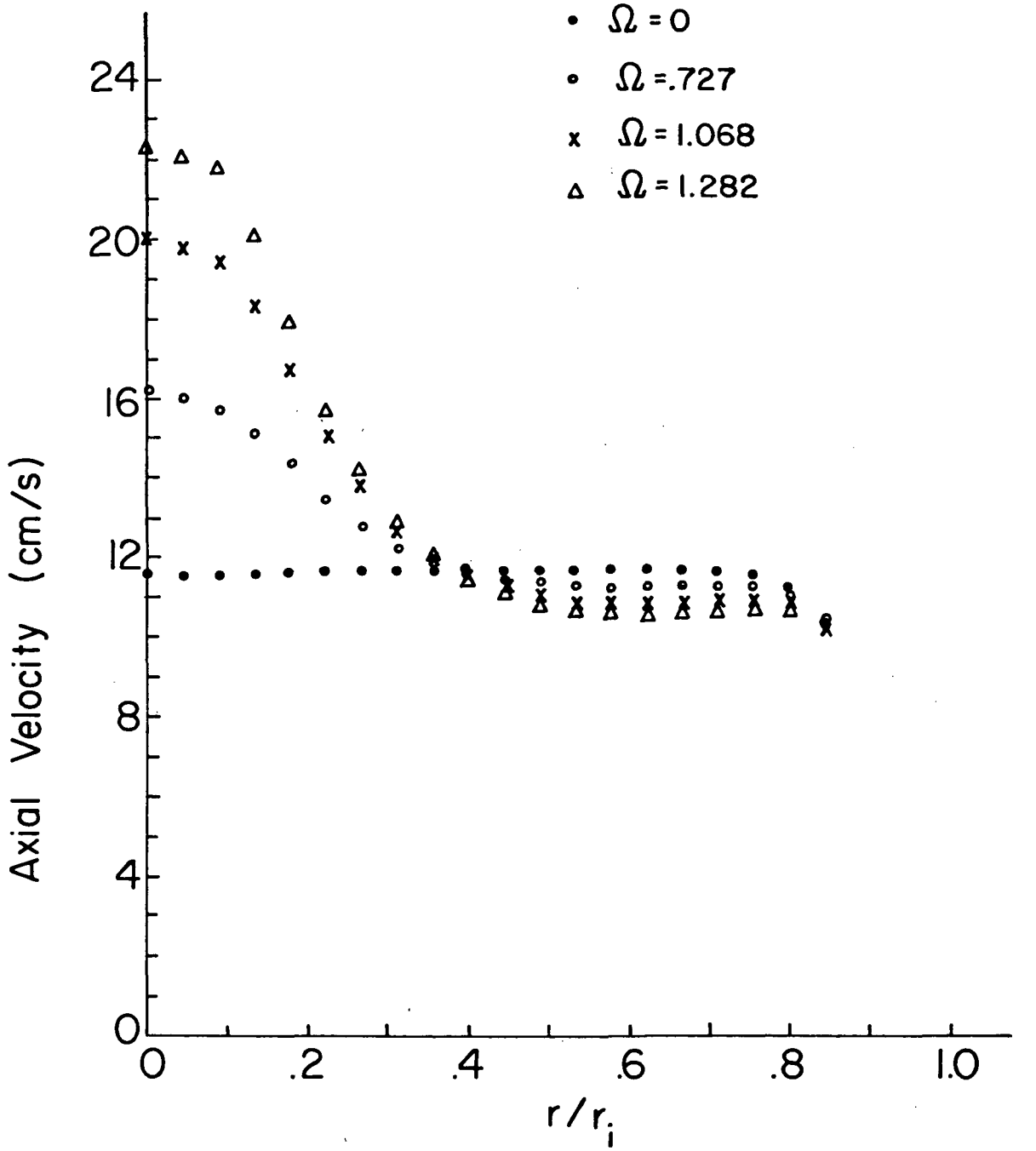


Figure 4.4. Axial velocity vs. non-dimensional radius for Re = 4540 and various values of the swirl parameter, Ω. The axial location was $z/r_i = -.67$.

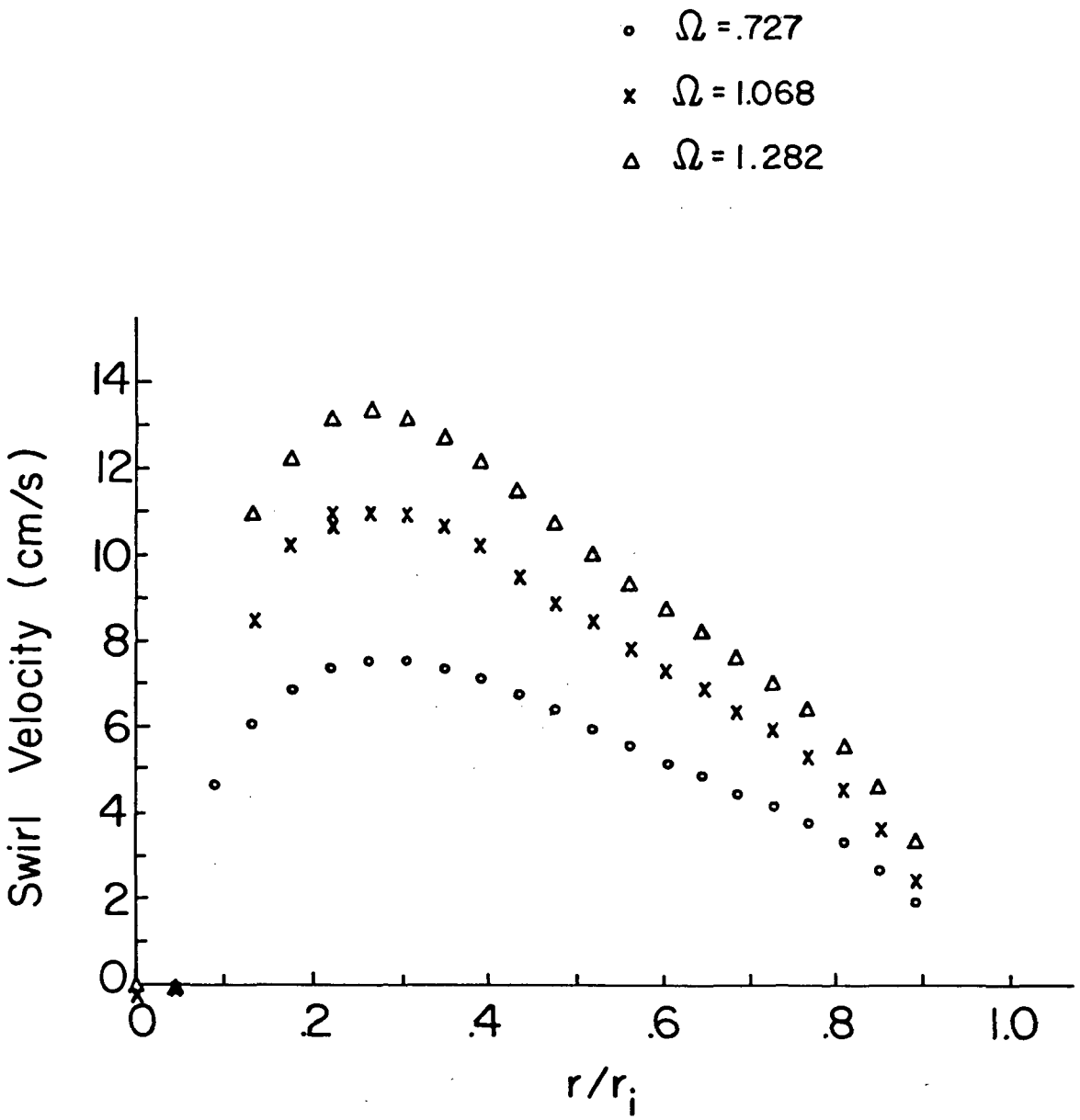


Figure 4.5. Swirl velocity vs. non-dimensional radius for Re = 4540 and various values of the swirl parameter, Ω. The axial location was $z/r_i = -.67$.

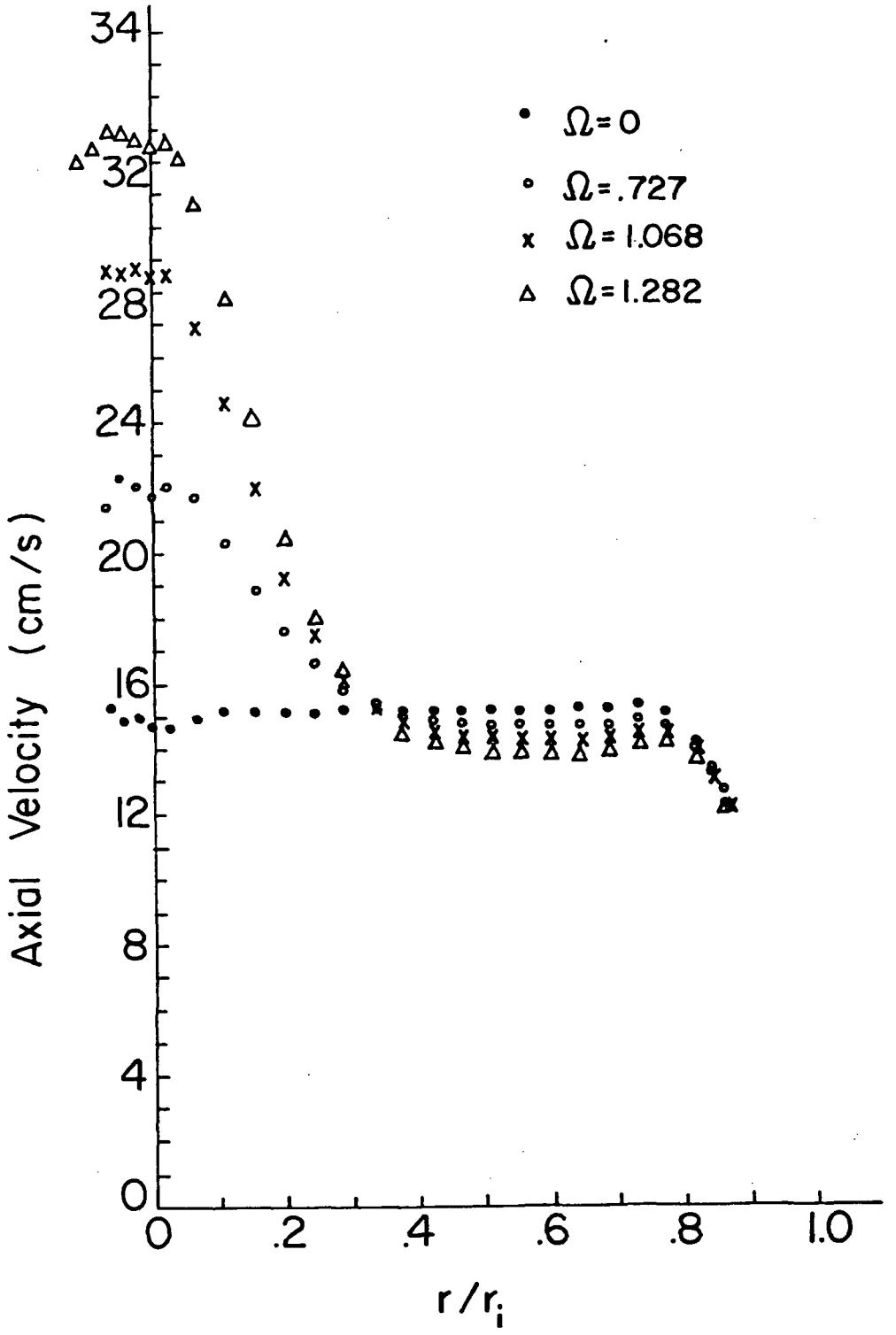


Figure 4.6. Axial velocity vs. non-dimensional radius for Re = 6000 and various values of the swirl parameter. Ω. The axial location was $z/r_i = -.67$.

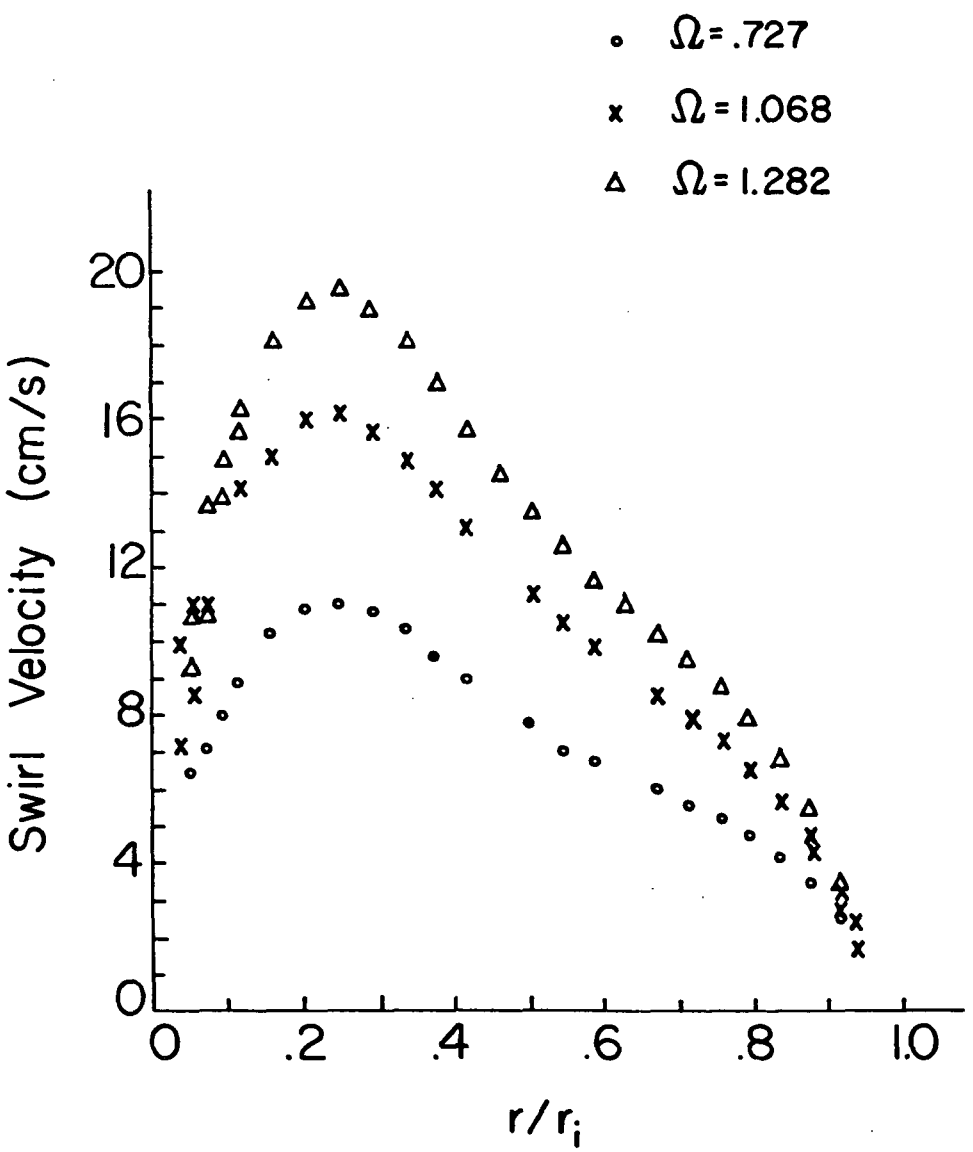


Figure 4.7. Swirl velocity vs. non-dimensional radius for Re = 6000 and various values of the swirl parameter, Ω. The axial location was $z/r_i = -.67$.

velocity varied, over a period of 10 - 20 minutes, by as much as 6% ($\pm$ 3% from some mean value). During this time the flow rate and vane angle were held constant, with no changes evident in rotameter setting. It was not possible to determine with certainty whether $r_p$ was moving about slowly (i.e., the profile was changing shape) or whether the entire profile was shifting up and down, because it was not possible to make simultaneous measurements at two different radial locations. It did appear, however, that a general reduction or increase in swirl velocity was occurring over a region which was of considerable radial extent. The magnitude of these velocity changes was greatest in the neighborhood of $r = r_p$ (see Figure [4.48] and related discussion).

This same effect was noted for axial velocity measurements near the centerline, but the magnitude of the velocity changes was significantly less. This is not surprising in light of the strong effect that the swirl velocity has on the centerline axial velocity. No firm explanation of the cause of these relatively slow changes in base flow can be offered.

## 4.4. The Detailed Mapping of a Type 0 Vortex Breakdown Flow Field

The next experiments conducted were those which resulted in a detailed velocity mapping of the flow field associated with a type 0 vortex breakdown. For this work the flow conditions were held fixed, with Re = 2560 and $\Omega$ = 1.777. These values were chosen because they resulted in a type 0 breakdown which was relatively stable in form and position. The position stability of the breakdown was an important criterion in selecting these flow conditions. It was suspected, and later confirmed, that the velocity measured at a fixed value of $r/r_i$ would vary only slightly as a function of

absolute axial position, if the axial position of the measuring point relative to the bubble were constant. Conversely, velocity measurements made at a point which was fixed in position near the breakdown showed large variations due to the to and fro axial drift of the breakdown. Thus, in order to obtain a meaningful and detailed velocity map of the flow it was essential to have a breakdown which was quite stable in position.

### 4.4.1 Procedure

The procedure used in these experiments was dictated by the circumstances described in the preceding paragraph. A magnifying lens and mirror were mounted on top of the flow apparatus and adjusted to eliminate parallax over the axial range in which the bubble was located. When properly placed, an observer could view the nose region of the bubble as it drifted axially. The transparent scale running axially along the top outside surface of the test section allowed the axial position of the nose of the breakdown to be determined quite accurately, with a precision of better than .5 mm.

The first step in the procedure was to select an appropriate axial location for the measuring point. For each radial position of the probe volume the velocity was continuously measured by the frequency tracker and the position of the breakdown nose was continuously monitored visually by observation through the viewing system. For measurements of average velocity outside of the bubble envelope, the analog voltage output of the frequency tracker was measured by the digital voltmeter. The voltmeter averaging time was usually kept at either .1 or .3 seconds to provide a time response that was rapid enough to measure a varying average velocity. As the breakdown wandered to and fro, it occasionally rested in one axial

position for a brief period of time (typically a few seconds). When this occurred, the voltmeter output was held fixed by means of a remote switch. The voltage reading, proportional to velocity, and the position of the probe volume and bubble nose were then recorded. Several or more velocity readings were taken for each value of measuring point position and relative breakdown position. The readings obtained in this manner were quite repeatable, even for those locations in which the velocity varied considerably with bubble position (e.g., just upstream of the bubble nose and near the tube centerline). In nearly all cases the standard deviation of the velocity readings (with measuring point and relative breakdown position fixed) was less than about 4% of the mean of the readings. By repeating this procedure at various axial and radial locations it was possible to build, bit by bit, a quite detailed velocity map of the flow outside of the bubble envelope.

For measurements of velocity in regions where the velocity fluctuations, as well as mean velocity, were of interest a slightly different procedure was used (e.g., inside the bubble and in the wake region). The analog voltage output was first low pass filtered (a 10 Hz cut-off was used) to remove spurious fluctuations and then the signal was further conditioned by suppressing it with a known D.C. voltage. This conditioning allowed the signal then to be recorded on one channel of a strip chart recorder which was set at a fairly high sensitivity. In this way an accurate and continuous record of velocity was made.

Another channel was used at times to record the time average of the true R.M.S. of the conditioned signal to indicate the mean amplitude of the velocity fluctuations. A third channel was used to record a

verification signal denoting bubble nose position. When the bubble remained briefly in one axial position a switch was depressed which caused the pen of this third channel to deflect. The verification signal was maintained as long as the bubble remained at this axial location and was discontinued when the bubble moved an axial distance of greater than .5mm. The bubble position was then noted on the strip chart paper. This process was repeated for various locations of the measuring point and for a range of relative bubble positions. In this manner it was possible to produce a composite picture of the velocity field inside the breakdown envelope. In some regions, such as in the wake of the bubble, both the digital voltmeter and the strip chart recorder were used simultaneously.

In the discussions that follow, the axial location denoted indicated the position of the measuring point relative to the apparent nose of the bubble, (-) indicating upstream and (+), downstream. For reference, it should be noted that for these flow conditions the mean location of the bubble nose was $\approx z = -3$ mm and the bubble length was 15.5 mm. In those cases where the radius has been nondimensionalized, $r_i$ is the tube radius at the axial location where the measurements were made.

### 4.4.2. Time Averaged Axial Velocity Profiles

The three profiles of axial velocity shown in Figure [4.8] were measured at three axial locations well upstream of the type 0 bubble. At all three locations the profiles were characterized by the same features evident in the base flow profiles previously presented. There was a region of high velocity near the tube centerline, followed by a region in which the axial velocity was nearly constant with r, and there was a slight increase in velocity just inside the boundary layer. At the -30.6 mm and

-22.6 mm locations the velocity readings were unaffected by the slight changes in bubble position, while at the -14.6 mm location some slight changes in velocity were noticeable near r = 0 as the bubble wandered axially. As can be seen, the axial velocity profiles changed only slightly with axial distance in the upstream region in which velocity was independent of bubble position.

As seen in Figures [4.9, 4.10], in the region extending from -14.6 mm to the breakdown nose the velocity near the centerline decreased rapidly as the bubble was approached. The centerline velocity decayed from a maximum to zero in an axial distance of ~15 mm, or one bubble length, Figure [4.11]. The collapse of the high velocity jet near r = 0 led to a slight increase in velocity in the flat region of the profile ($r/r_i$ = .5 to .7) and a more noticeable increase closer to the tube wall, indicating a thinning of the boundary layer. All of the profiles shown in Figures [4.8 - 4.10] were measured using the same initial alignment to determine r = 0. The profile shapes near r = 0 seem to indicate that the centerline was actually located at $r/r_i \approx .028$, the location denoted by the dashed line.

The -1 mm profile has been repeated in Figure [4.12] as a reference for comparison to the two profiles measured downstream of the bubble nose. The velocities inside the bubble envelope are discussed in a following section. At present, note that the outward displacement of the fluid caused by the presence of the bubble resulted in a substantial increase in velocity for $r/r_i$ greater than about .35. This convergence of the stream tubes had to occur because of the confinement by the tube walls. The bubble diameter was a maximum at about +10 mm and thus the area of the

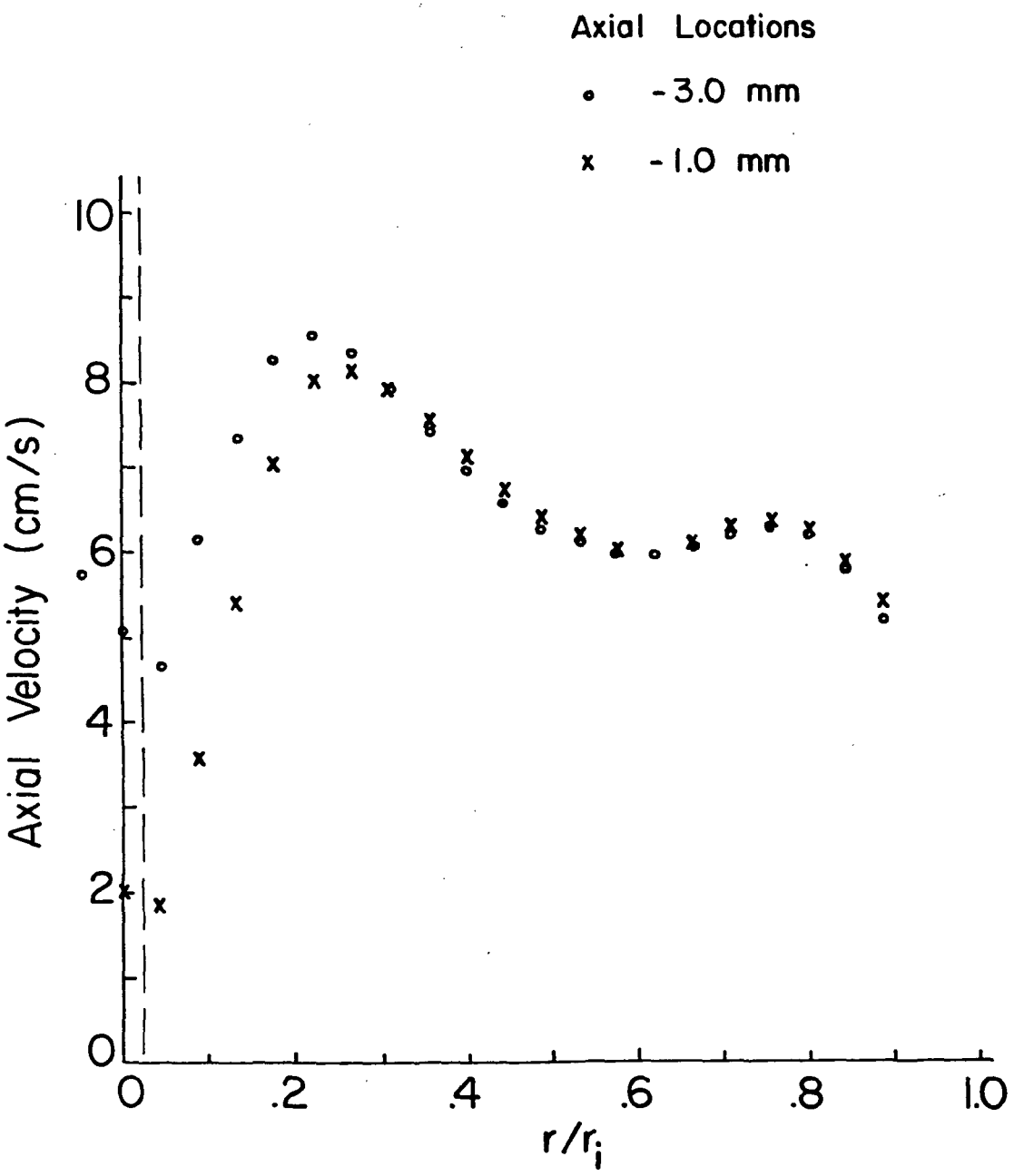


Figure 4.8. Axial velocity vs. non-dimensional radius; Re = 2560, $\Omega$ = 1.777. Axial distance denotes distance upstream of bubble nose.

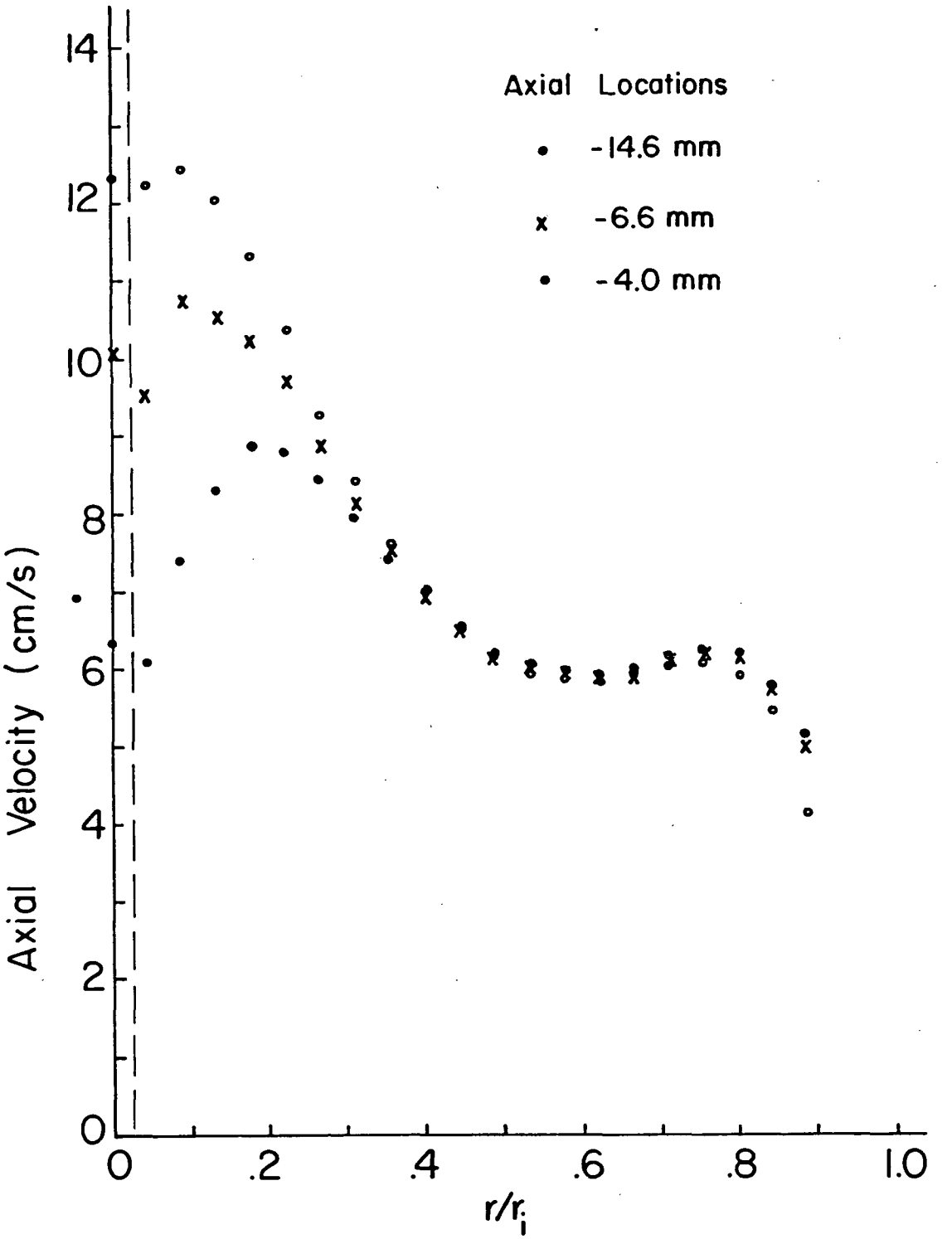


Figure 4.9. Axial velocity vs. non-dimensional radius; Re = 2560, $\Omega$ = 1.777. Axial location denotes distance upstream of bubble nose.

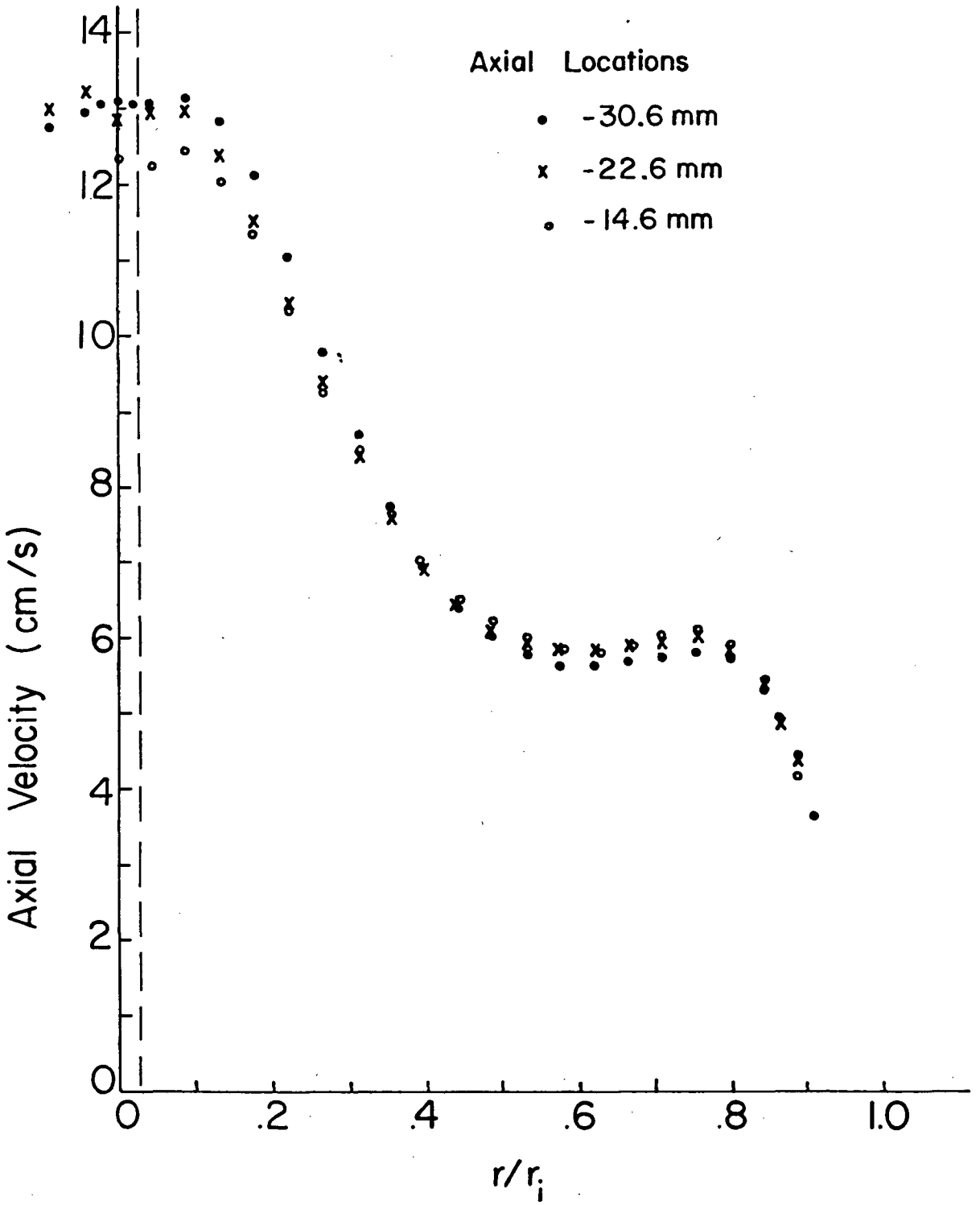


Figure 4.10. Axial velocity vs. non-dimensional radius; Re = 2560, $\Omega$ = 1.777. Axial distance denotes distance upstream of bubble nose.

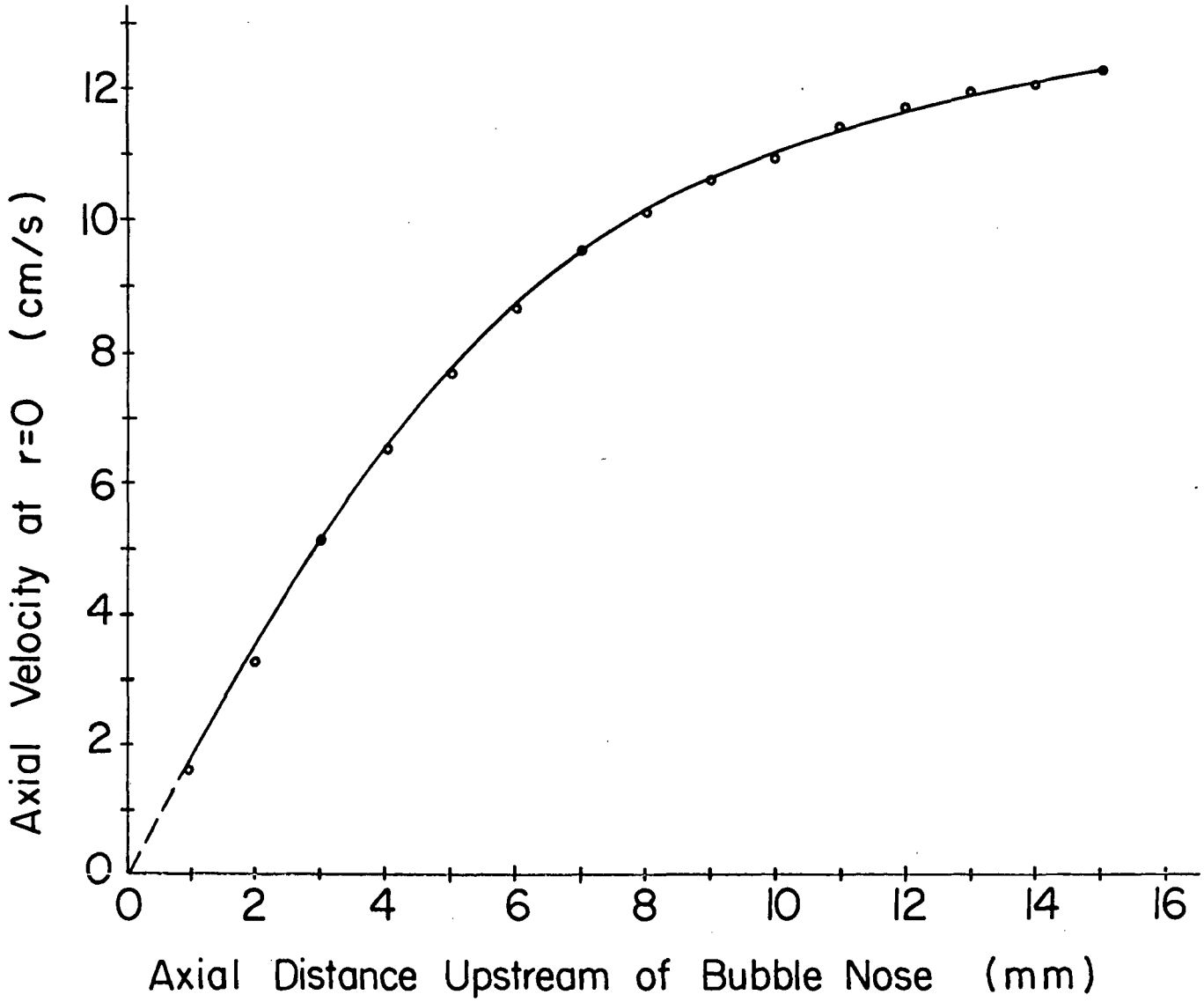


Figure 4.11. Decay of centerline axial velocity approaching the breakdown.

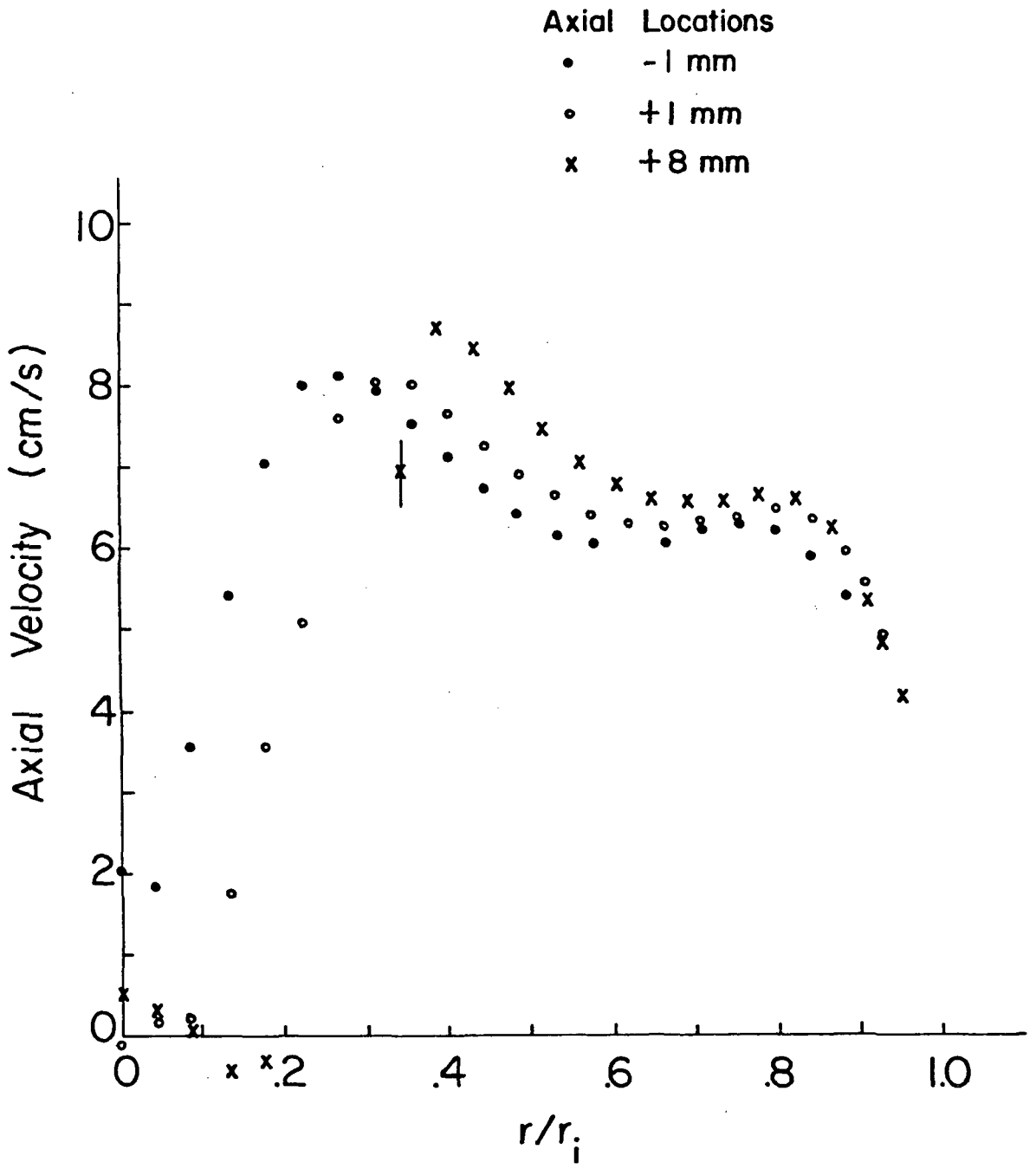


Figure 4.12. Axial velocity vs. non-dimensional radius; Re = 2560, $\Omega$ = 1.777. Axial location denotes distance upstream (-) and downstream (+) of bubble nose.

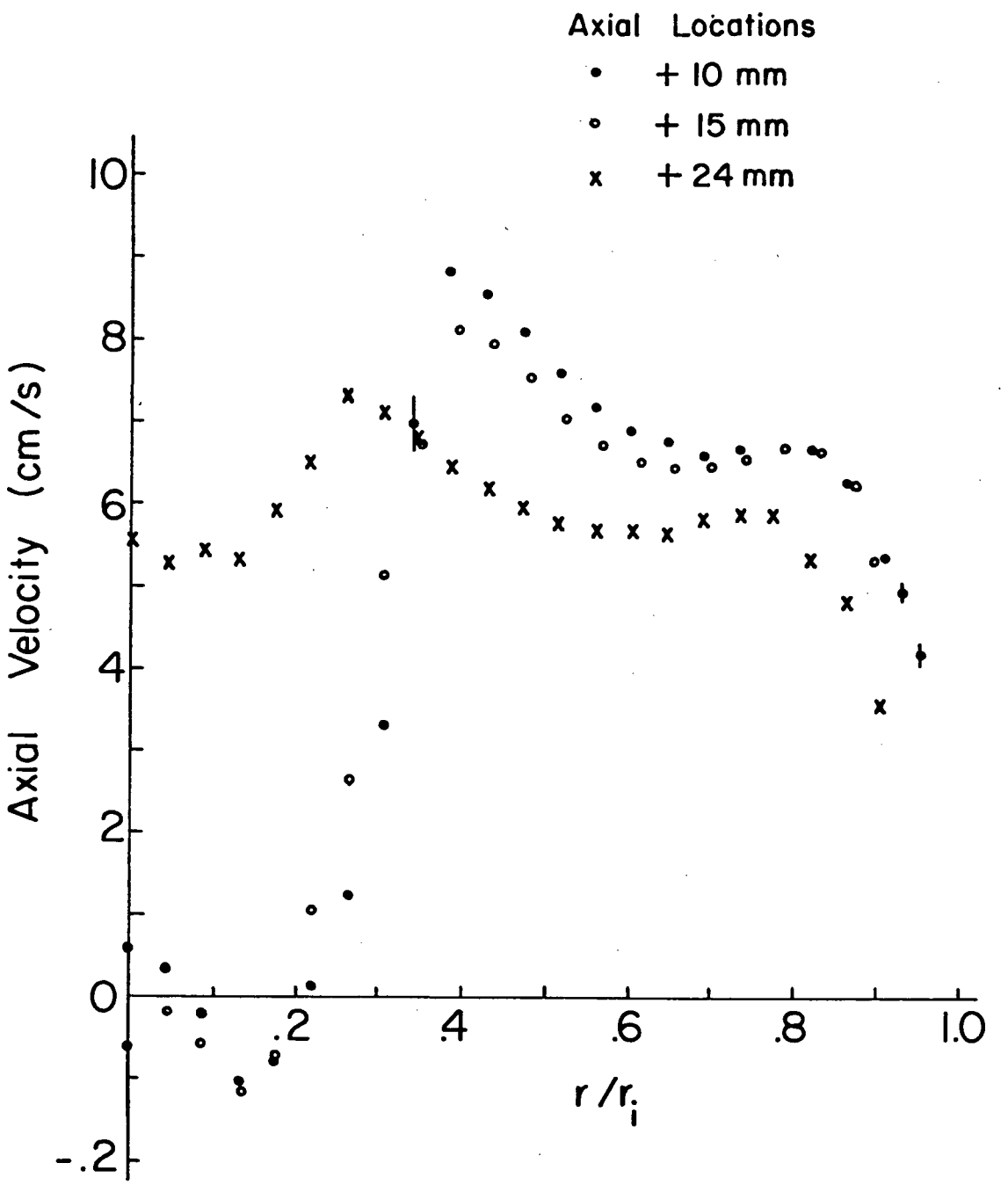


Figure 4.13. Axial velocity vs. non-dimensional radius; Re = 2560, $\Omega$ = 1.777. Axial location denotes distance downstream of bubble nose.

annulus defined by the tube wall and bubble envelope was a minimum at this location. This is reflected by the relatively high velocities shown in the +10 mm profile, Figure [4.13], at $r/r_1$ = .4 - .7. In contrast to this, the profiles indicate that the fluid decelerated with increasing z, from -1 mm to +10 mm, for radial positions close to the bubble envelope. Note also the large radial gradients that existed near the bubble envelope, $r/r_i \simeq .3$, as shown in the +8, +10, and +15 mm profiles.

The +24 mm profile resulted from measurements in the wake of the breakdown. The velocity distribution outside of the vortex core in this region was quite similar in shape to the upstream profiles. The major difference was that the high velocity jet inside the vortex core near r = 0 had not fully formed. A comparison between the +15 and the +24 profile shows the marked increase in boundary layer thickness that occurred downstream of the bubble.

In order to check these measurements for agreement regarding constant volume flow rate an approximate integration of several profiles was done. The velocity was assumed to be constant in the radial increment centered about the radial location at which the velocity was measured. The velocity was assumed to decrease linearly with r in the region near the wall for which velocity data was not obtained. The results were quite consistent. For example, when the actual centerline adjustment (mentioned previously for Figures [4.8 - 4.10]) was made for the upstream profiles, less than a 1% difference existed between the volume flow rate calculated at -30.6 mm and that calculated at +24 mm.

The results of the axial velocity measurements inside the bubble were quite surprising. As shown in Figure [4.14], the data for time averaged

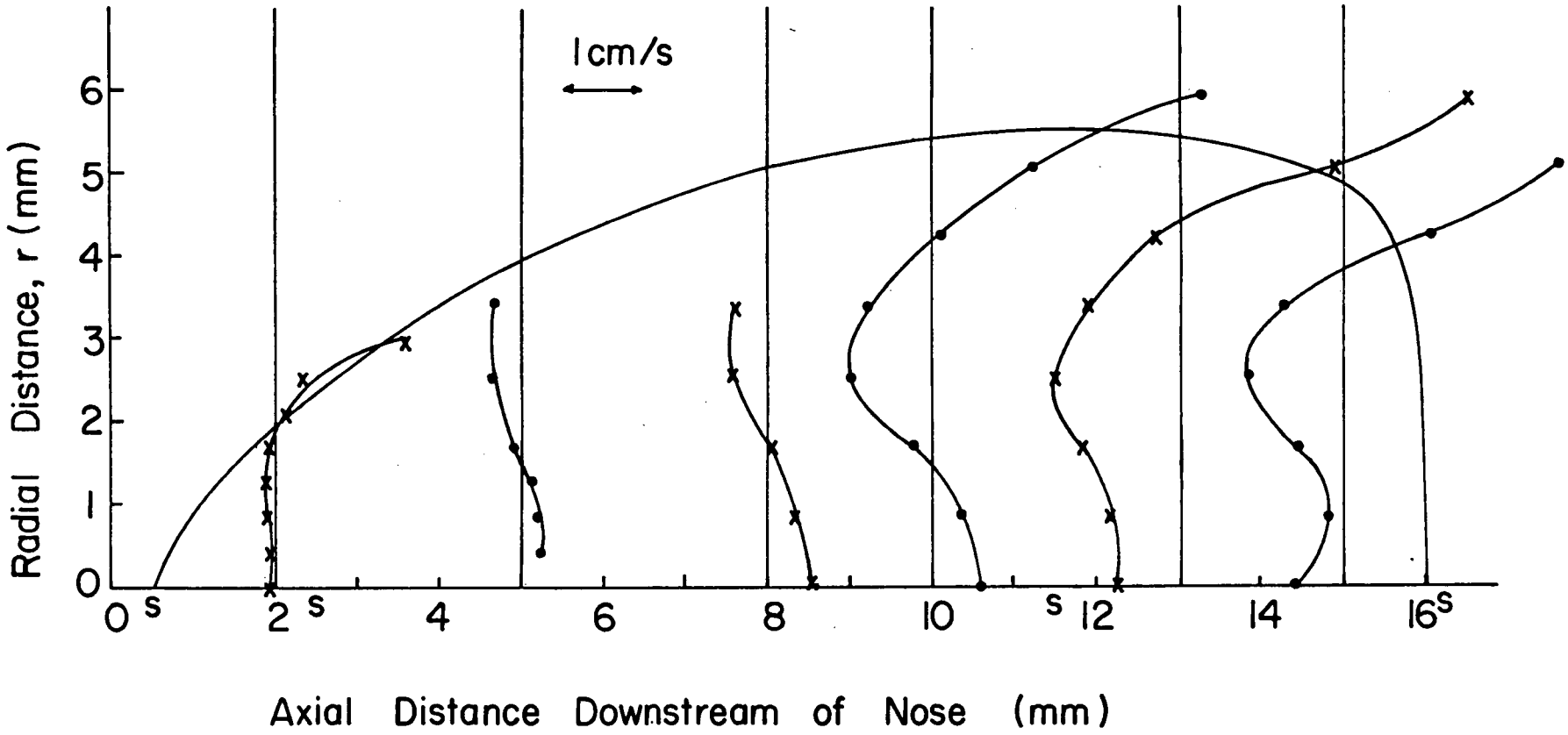


Figure 4.14. Mean (Time-Averaged) Axial Velocity Profiles Inside the Bubble, Re = 2560, $\Omega$ = 1.777. "S" Denotes the Four Stagnation Points.

velocity indicate that four stagnation points existed (marked by the letter S in the figure) along the axis. The axial positions are referenced to the apparent nose of the bubble for consistency with the other figures. The bubble envelope superimposed on the figure was determined from photographs and streamline calculations based on the mean velocity data.

The region of reversed velocity at r = 0 near the nose (.5 to 2.5) was characterized by small absolute values of mean velocity and only weak fluctuations. The velocity on the axis was streamwise again from the second stagnation point, 2.5 mm, to the third at 11.5. Both the mean velocities and fluctuation amplitudes were significantly higher in this region than in the nose region. The downstream section of the bubble, from 11.5 to the rear stagnation point at 16.0 featured both the largest absolute values of reversed velocity and the highest amplitude fluctuations. The highest velocities inside the bubble were positive (streamwise), occurred near the envelope, and were about 15% of the maximum centerline velocity measured upstream of the breakdown. The mean velocities were most negative at r $\approx$ 2.5 mm and 11 - 13 mm downstream of the nose and were about 12% of the maximum upstream velocity. The peak negative velocities decreased in absolute value upstream of +11 mm as the recirculated fluid moved upstream and toward the bubble envelope.

### 4.4.3. Mean Streamlines Inside the Bubble Envelope

The mean flow pattern can be visualized more clearly by use of Figure [4.15]. The mean streamlines shown (actually, the projection of the mean streamlines onto a meridional plane) were calculated from the time averaged axial velocity data using linear interpolation between radial points. The bubble envelope, or outer mean dividing streamline, was

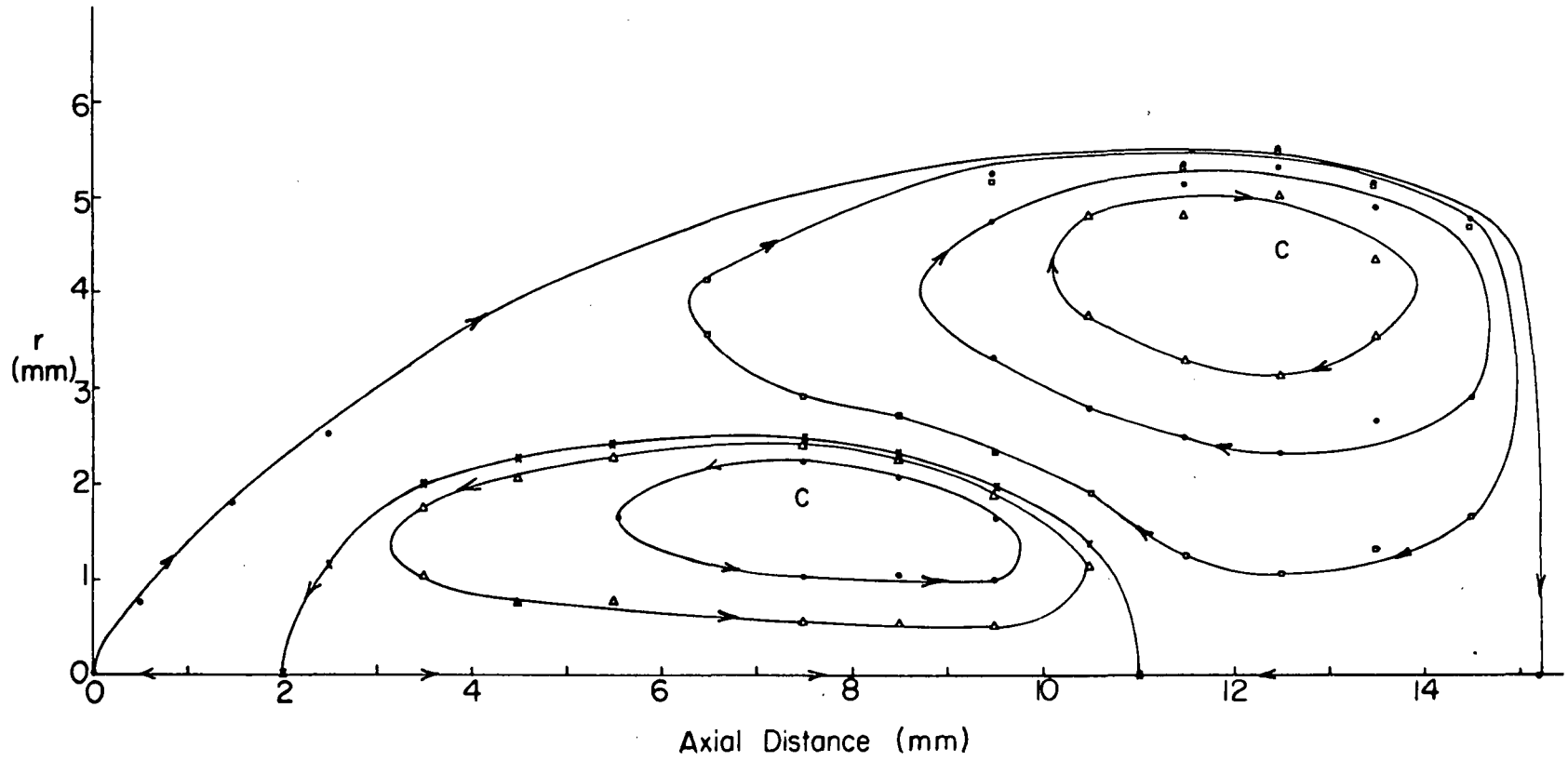


Time Averaged Streamlines

Figure 4.15. The Mean Streamline Pattern Inside the Breakdown. "C" Denotes the Centers of the Recirculation Cells.

determined from the mean velocity data and several enlarged photographs. Note that the axial distance in this figure is referenced to the actual front stagnation point. The larger, outer cell recirculated about 1% of the total volume flowing through the tube. Only a small fraction of this recirculated fluid reached the upstream nose section of the bubble, and most of the recirculating fluid in this outer cell was confined to the rear half of the bubble.

The inner cell was significantly weaker than the outer and recirculated only 3.7% of the mean amount carried by the outer cell. As discussed later, the stagnation point marking the downstream end of the inner cell appeared to separate a region of relatively weak fluctuations inside the inner cell from a region of strong fluctuations in the downstream section of the bubble. The photographs shown in Figure [4.16] were taken sequentially over a period of about twelve seconds after interrupting the flow of dye. The inner, relatively quiescent core can be seen clearly, as indicated by the dark streak located on the bubble centerline and extending from the nose region to a point about 2/3 of a bubble length downstream of the nose. The existence of this inner core and its streamwise axial velocity on the tube centerline is in agreement with the behavior of the screw worm filament described in section 3.3.1.

### 4.4.4. Time Averaged Swirl Velocity Profiles

The swirl velocity profiles at the bubble nose and at two upstream stations are shown in Figure [4.17]. As shown, the radial position at which the swirl velocity was a maximum moved outward significantly as the bubble was approached. In the outer portions of the tube, $r/r_i > .7$, the

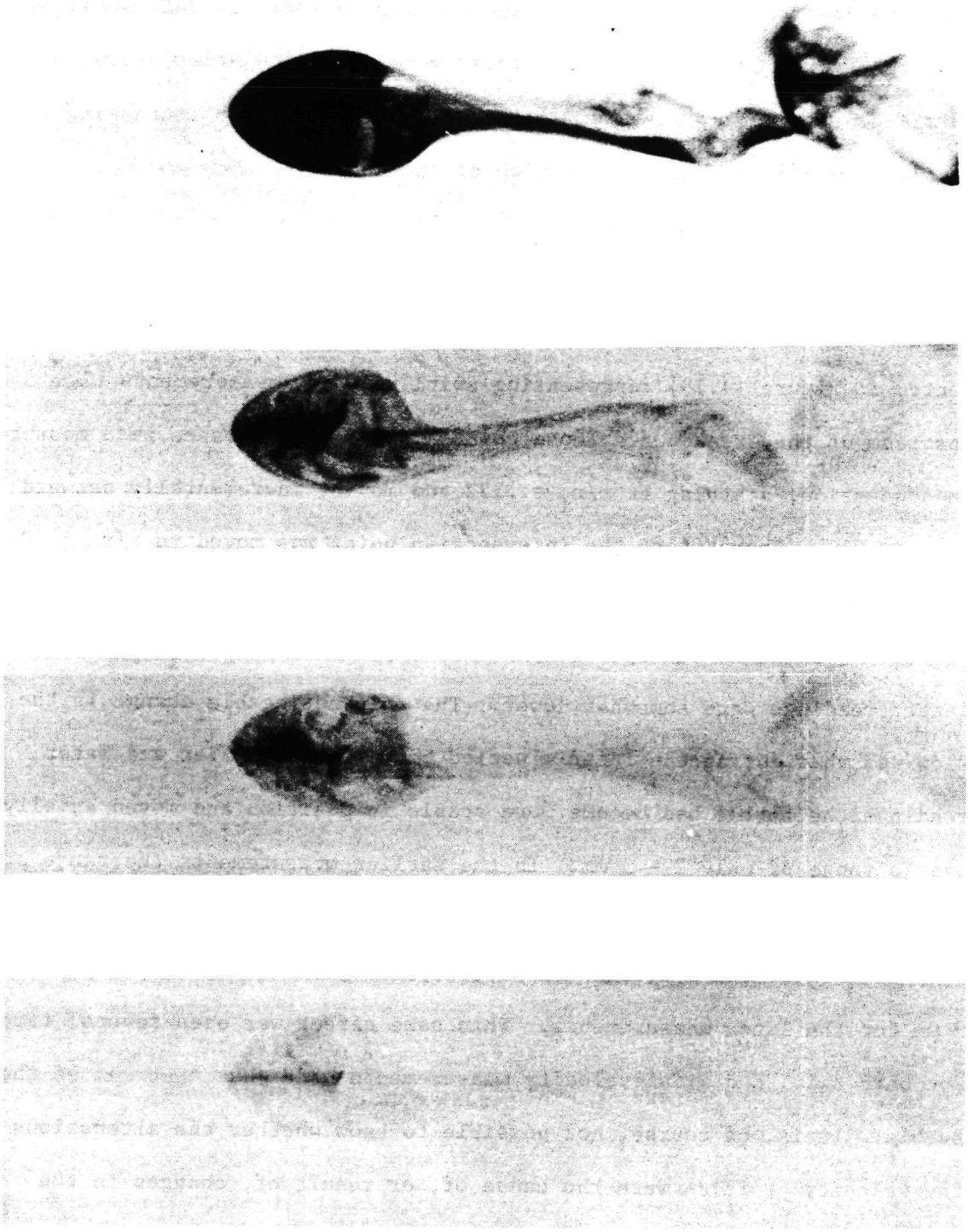

Figure 4.16. A Sequence of Photographs of the Breakdown that Existed During the Detailed Velocity Measurements. The First Photo was Taken Just After the Dye Flow was Stopped. The Inner Core Remained Visible for About 12 Seconds.

outward displacement of the fluid which occurred as the fluid approached the breakdown resulted in an increase in swirl velocity. This would be expected from a conservation of angular momentum calculation since the swirl velocity at any given axial location decreased with increasing r faster than 1/r in this outer region of the tube.

It was pointed out previously, in the base flow discussions, that the swirl velocity seemed to vary somewhat over a period of time, especially for $r/r_i$ less than about 0.5. This can be seen in the data points presented in Figure [4.18] representing swirl velocity measurements made 3 mm upstream of the breakdown. Those points marked with crosses were measured in succession, starting at $r/r_i = .132$ and moving incrementally outward to $r/r_i = .932$. Thereafter, the intersection point was moved to $r/r_i = .089$ and the velocity was measured at that point and then at five other radial locations, as indicated by the open circle points. For $r/r_i < \sim .5$, the latter readings were somewhat lower. The only noticeable change in the flow was that during the interim period between the earlier and later readings the bubble had become more stable in position and moved axially over a range of only 2 - 3 mm. In the earlier measurements the range of axial locations was about 7 mm. In addition, the mean location of the breakdown (measured over ten minutes, say) was further upstream by about 2 mm for the later measurements. This same effect was seen several times for both swirl and axial velocity measurements made just upstream of the bubble. It is, of course, not possible to know whether the alterations in the velocity profiles were the cause of, or result of, changes in the stability and mean location of the breakdown. The changes in velocity were slight, but noticeable, and perhaps offer another clue to the breakdown mechanism.

Three swirl velocity profiles measured downstream of the bubble nose are shown in Figure [4.19]. The +8 mm profile, measured at about one-half the bubble length downstream of the nose near the point of maximum bubble diameter, again shows the increase in swirl velocity for $r/r_i > .7$ due to the outward displacement of the fluid. Note the sharp increase in angular velocity near the centerline at +24 mm, in the wake region, which resulted from the convergence of the flow downstream of the breakdown. The very noticeable dip in mean swirl velocity near the bubble envelope ($r/r_i \sim .2$) shown in the +8 and +10 mm profiles was still evident at the +24 location.

This decrease in swirl velocity at, or just inside of, the bubble envelope was perhaps the most striking feature of the mean swirl velocity profiles measured inside the breakdown, Figure [4.20]. The dip in angular velocity appeared at each axial location. For axial locations 0 - 10 mm behind the nose, this dip was relatively small in magnitude and the radial position at which the swirl was locally minimized showed good correlation with the radial location at the breakdown envelope. The dip was significantly larger in magnitude in the downstream portion of the bubble and was located well inside of the mean dividing streamline. This feature of the swirl profiles is not surprising because the fluid immediately outside of the dividing streamline came from an upstream region near the tube centerline, where the circulation was relatively small.

### 4.4.5. Velocity Fluctuations: The Asymmetry and Unsteadiness of the Flow

The foregoing discussions of the flow inside the breakdown have centered on the mean velocities, i.e., velocities obtained by averaging the velocity, in time, over a suitable period. However, perhaps the dominant feature of the flow inside the bubble, and in the wake region, was the strong temporal

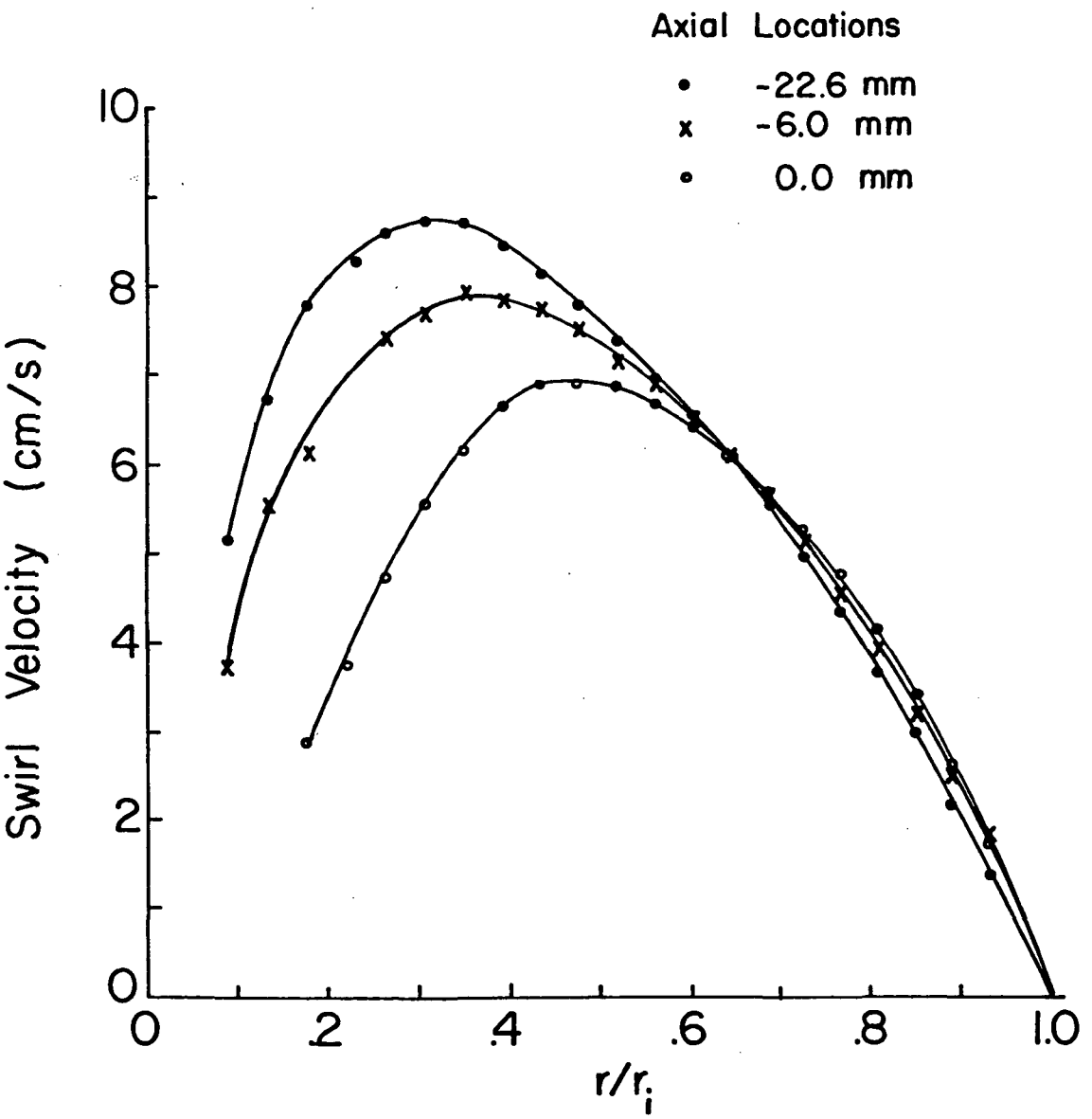


Figure 4.17. Swirl Velocity vs. Non-Dimensional Radius; Re = 2560, $\Omega$ = 1.777. Axial Location Represents Distance Upstream of Bubble Nose.

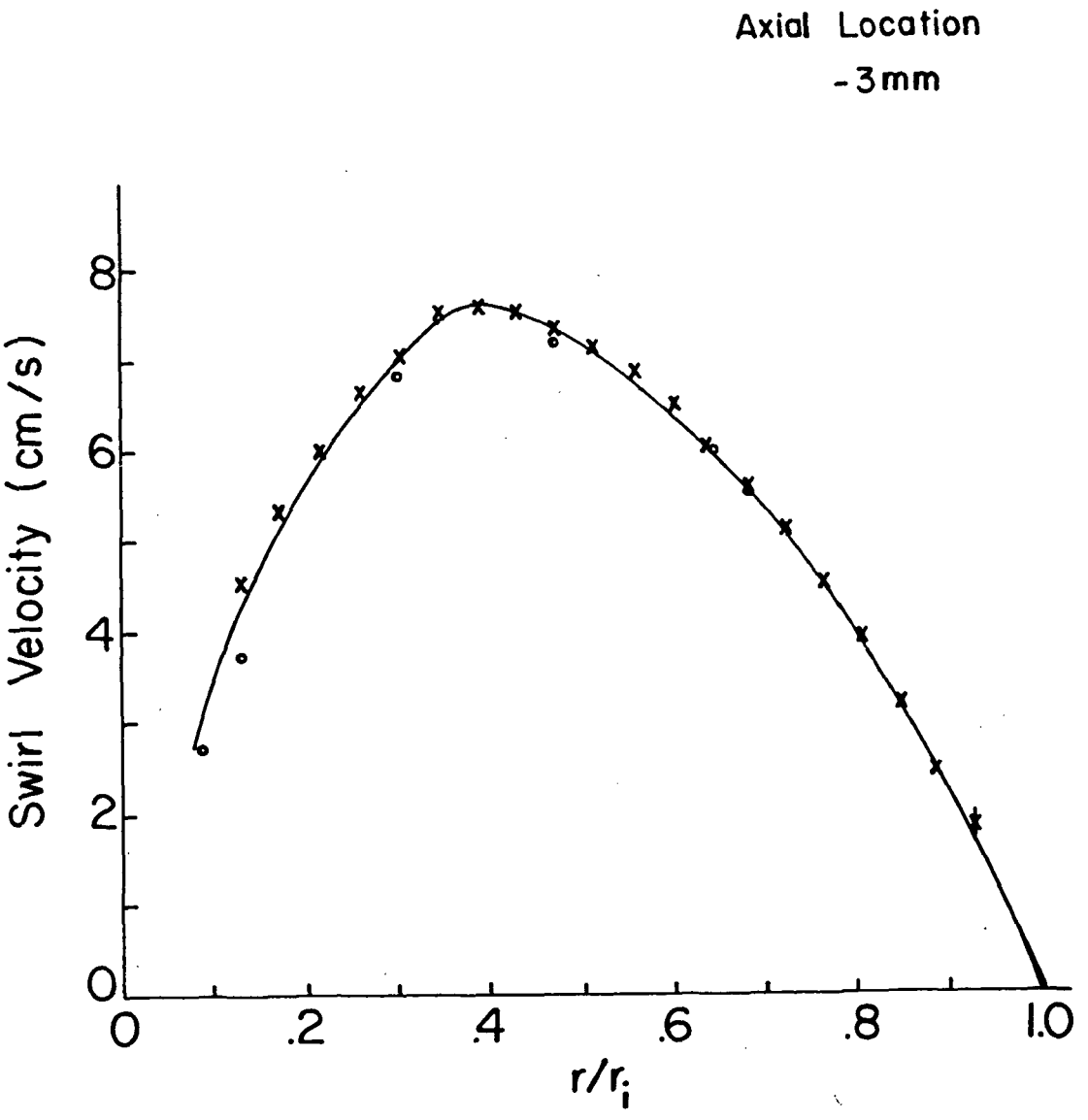


Figure 4.18. Swirl Velocity vs. Non-Dimensional Radius for Re = 2560, $\Omega$ = 1.777, 3mm Upstream of the Bubble Nose. Data Denoted by Open Circles Were Taken When the Breakdown was more Stable in Position.

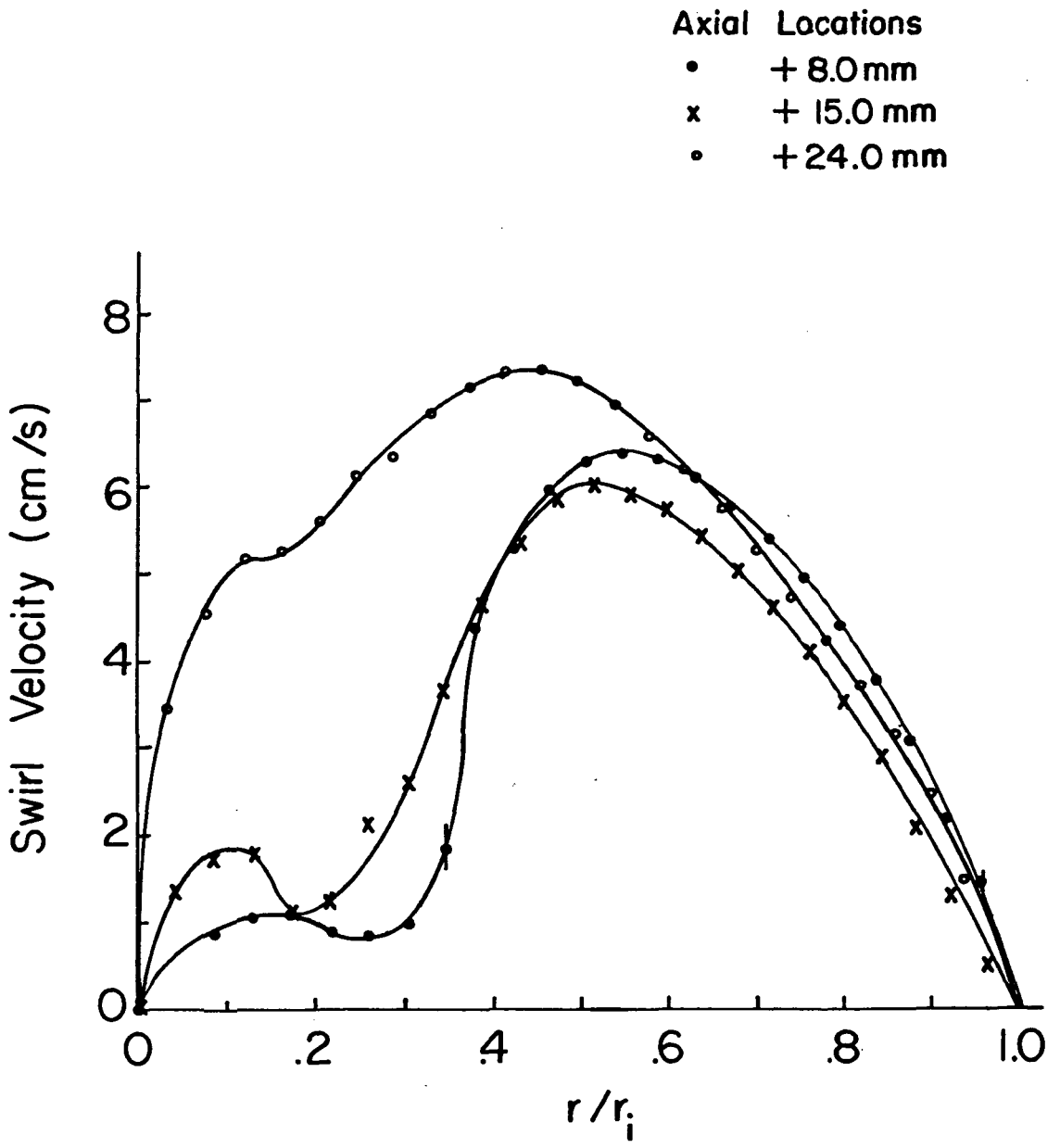


Figure 4.19. Swirl Velocity vs. Non-Dimensional Radius for Re = 2560, $\Omega$ = 1.777. Axial Location Denotes Distance Downstream of Bubble Nose.

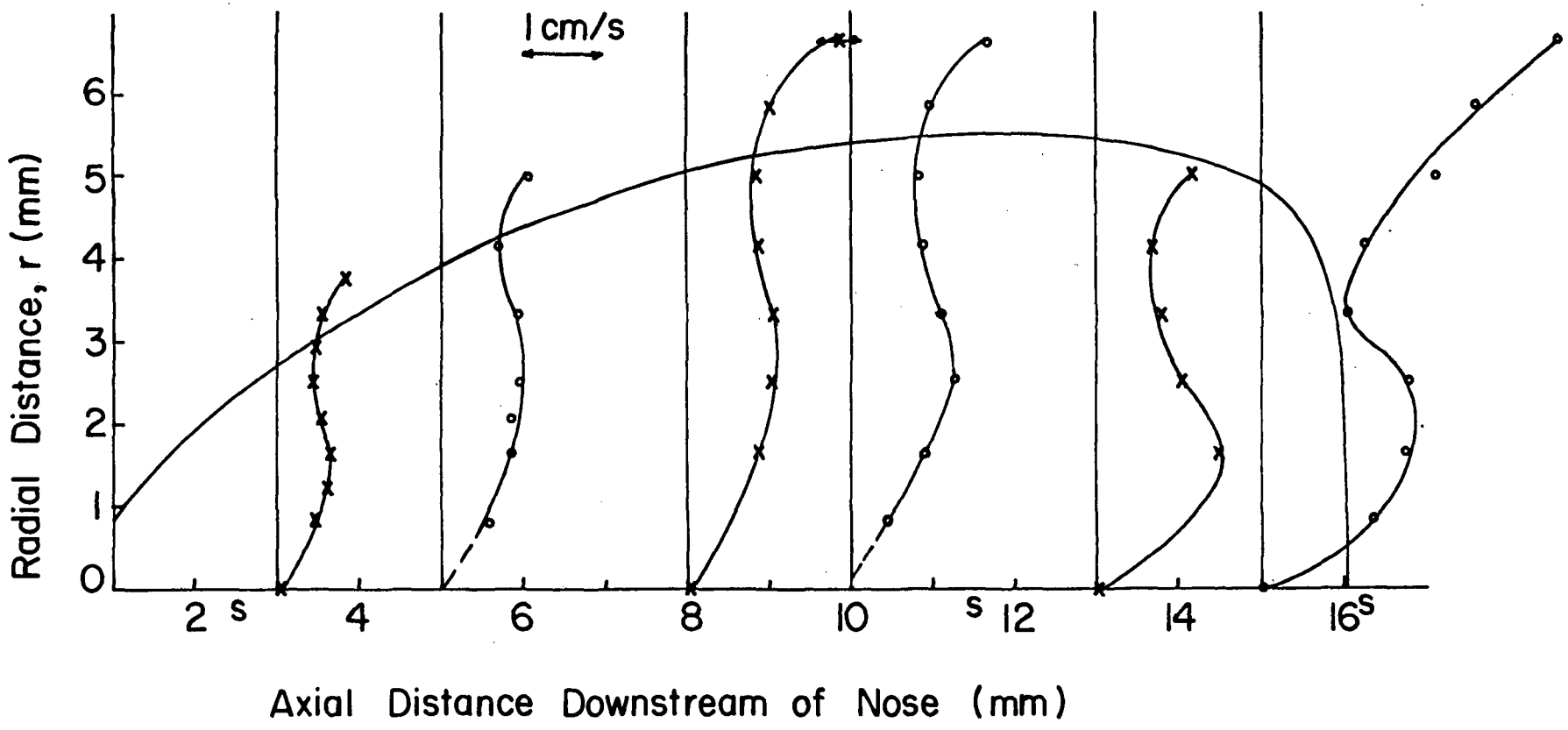


Figure 4.20. Mean (Time-Averaged) Swirl Velocity Profiles Inside the Bubble, Re = 2560, $\Omega$ = 1.777.

fluctuations in velocity. These fluctuations are represented graphically in Figures [4.21 - 4.23] by the bars superimposed on the mean velocity profiles measured inside the bubble (Figures [4.21, 4.22]) and in the wake region (Figure [4.23]). The length of the bars represent the average peak to peak amplitude of the velocity fluctuations. These average amplitudes were estimated from the strip chart recordings of velocity versus time for Figures [4.21, 4.23]. In Figure [4.22], the peak to peak amplitudes were approximated by multiplying the RMS of the time varying velocity (recorded on a separate channel) by $\sqrt{2}$, i.e., by assuming a sinusoidally varying velocity. It should be pointed out that the swirl velocity fluctuation amplitude at r = 0 may have a contribution from radial velocity fluctuations since these two components are not resolved by the LDA at the tube centerline.

The amplitude of these temporal fluctuations was greatest in the rear portion of the bubble, slightly off-axis. In this region, the time varying velocity was remarkably periodic and these fluctuations resulted in a continual exchange of fluid across the mean dividing streamline at the rear of the bubble. The temporal variations were weakest in the nose region of the breakdown and inside the inner cell discussed previously. The change in the fluctuation amplitude was especially noticeable when measurements were made near the centerline in the vicinity of the stagnation point which marked the downstream end of this inner cell. When the bubble was in an axial position such that the measuring volume was inside the inner cell the strip chart trace showed relatively small fluctuations. As the bubble drifted slowly to and fro, only small changes in the fluctuation amplitude resulted, as long as the probe volume remained inside the inner cell.

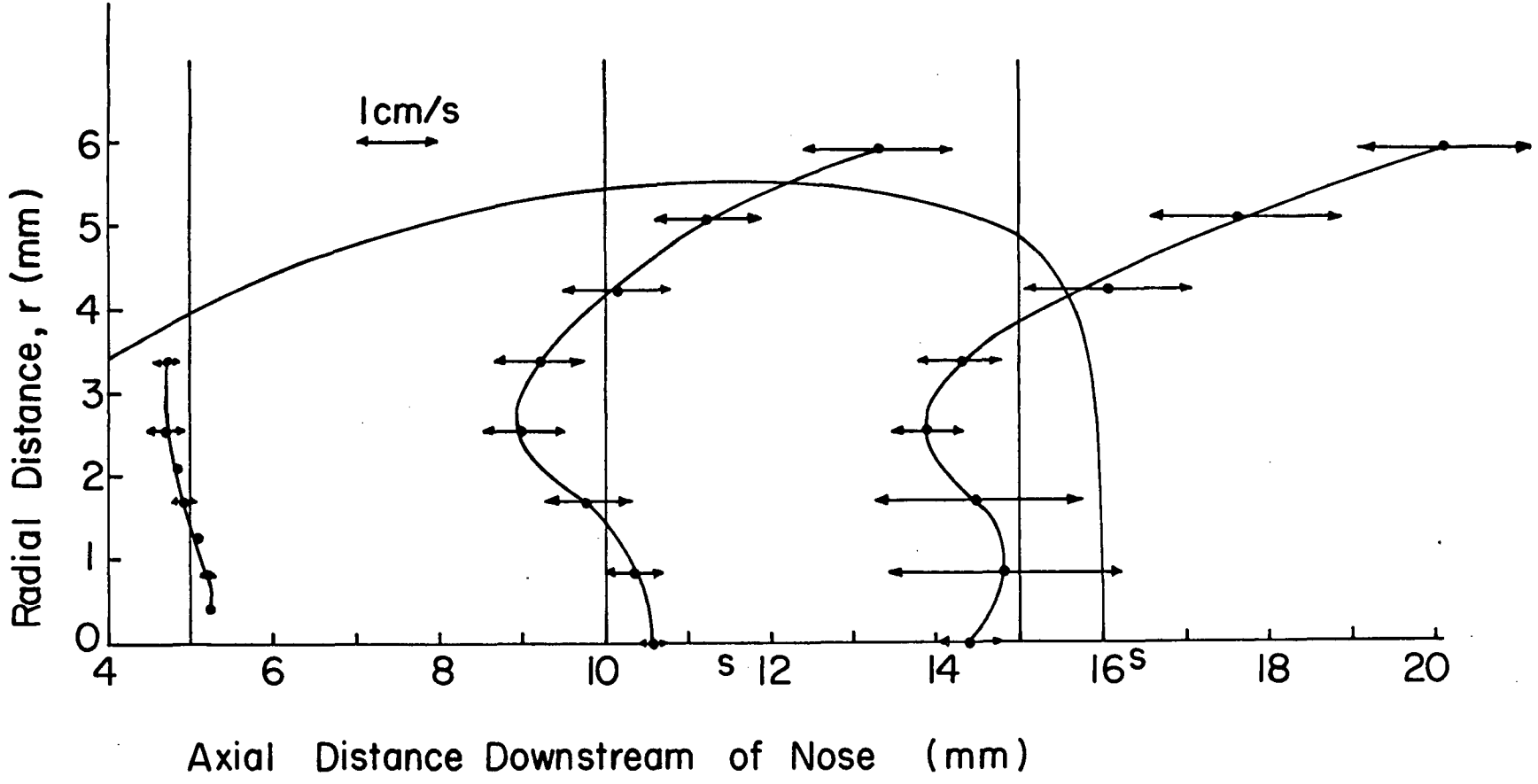


Figure 4.21. The Amplitude of the Axial Velocity Fluctuations - Represented by the Horizontal Bars - Inside the Breakdown; Re = 2560, $\Omega$ = 1.777.

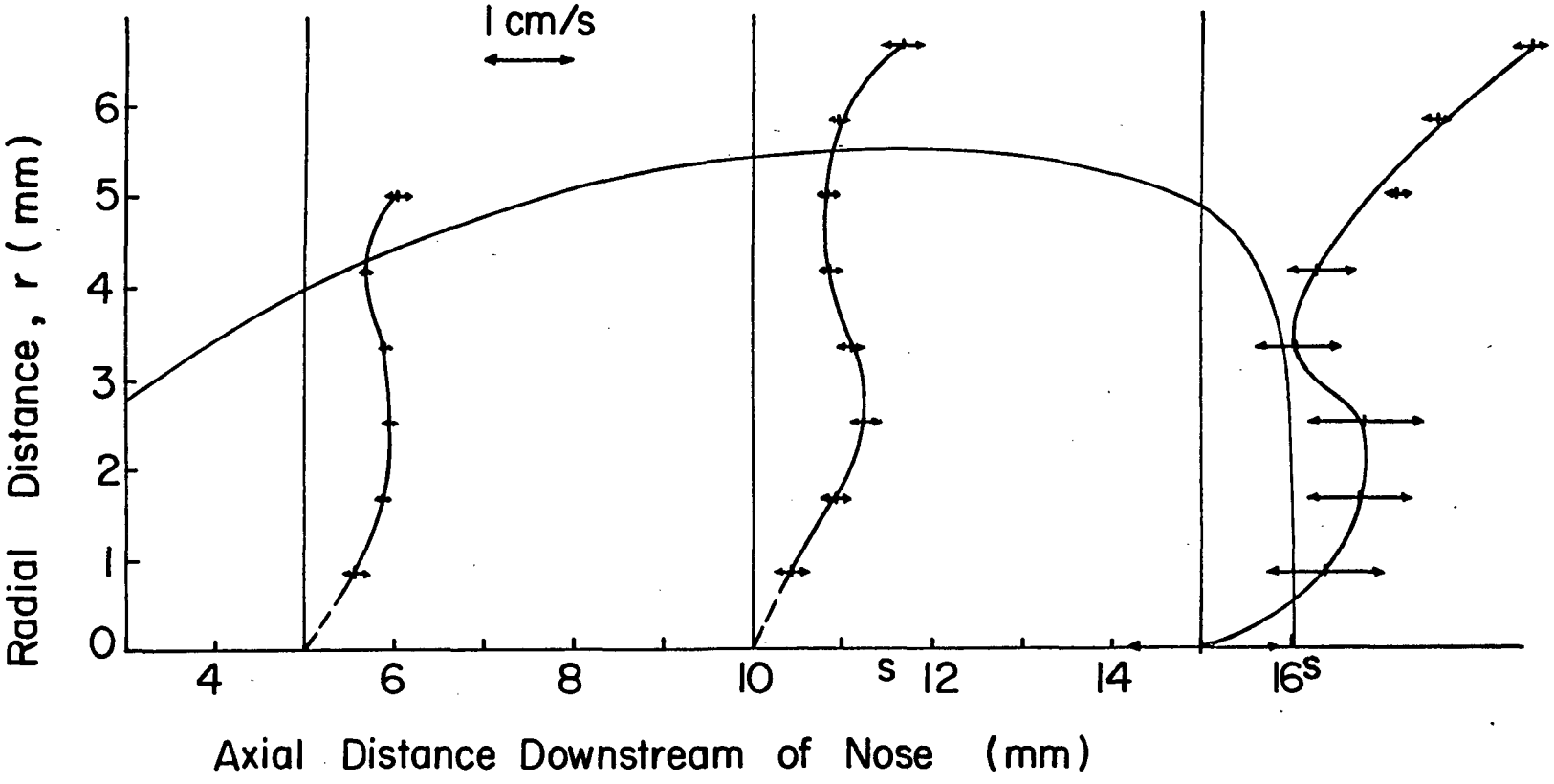


Figure 4.22. The Amplitude of the Swirl Velocity Fluctuations - Represented by the Horizontal Bars - Inside the Breakdown; Re = 2560, $\Omega$ = 1.777.

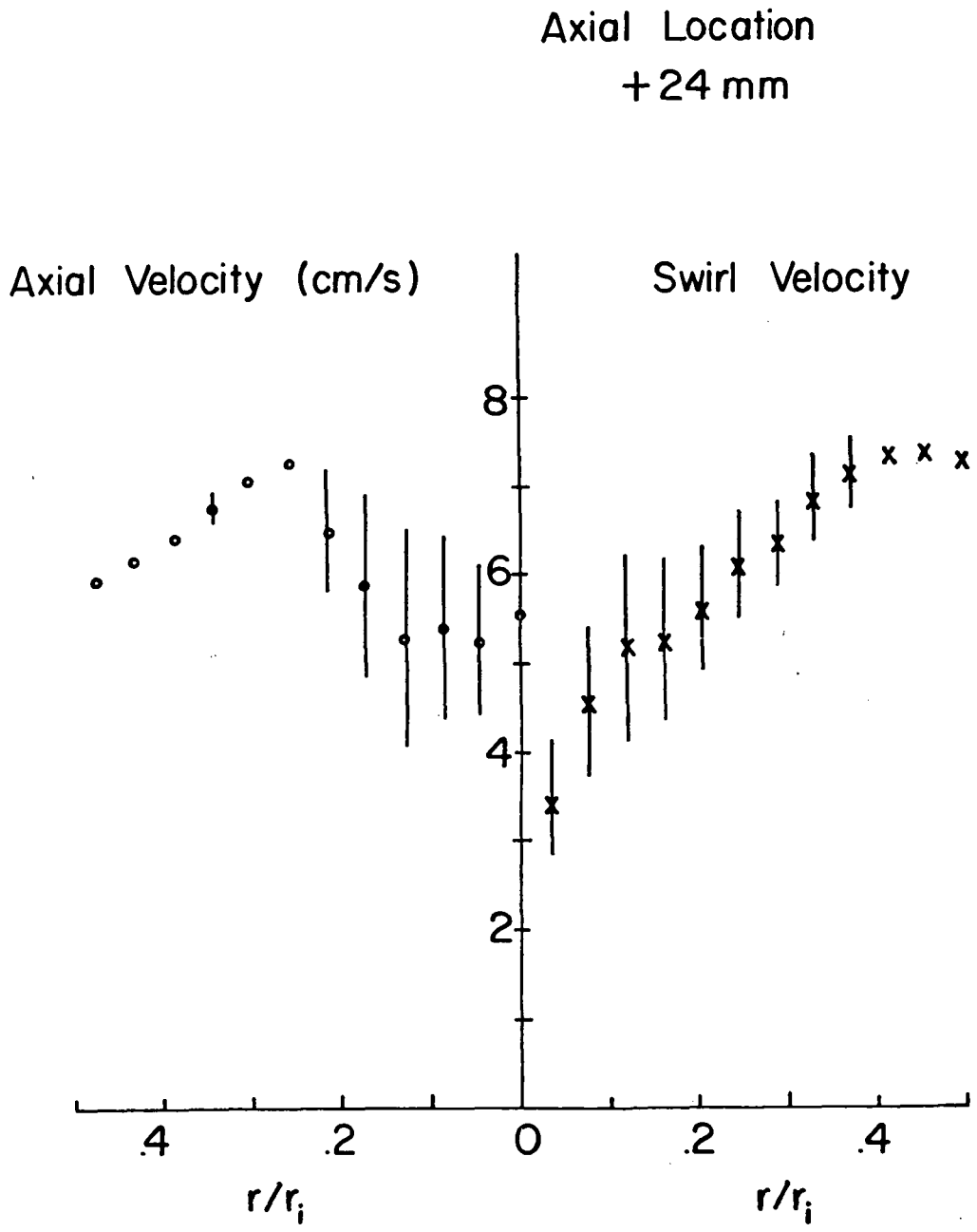


Figure 4.23. The Vertical Bars Represent the Amplitude of the Axial and Swirl Velocity Fluctuations in the Wake of the Breakdown - Re = 2560, $\Omega$ = 1.777.

However, when the bubble moved upstream far enough, so that the probe volume crossed the inner cell boundary, the fluctuation amplitude increased abruptly and the mean axial velocity became negative. In other words, the strong fluctuations in velocity resulting in the simultaneous emptying and filling of the bubble did not decay gradually along the axis with increasing distance upstream of the rear stagnation point. Instead, the amplitude was relatively constant in the rear portion and decreased rapidly near the stagnation point at the downstream end of the inner cell.

Several other important features which characterized the velocity fluctuations were the frequency and the nature, or shape, of the recorded traces. During the analysis of the velocity data it became evident that the velocity fluctuations varied in nature from region to region within the bubble. For example; the fluctuations in the nose region were small in amplitude and quite random in nature, with no dominant frequency immediately discernible. The velocity measured near the bubble envelope generally fluctuated noticeably, but the traces were characterized by random "spikes" superimposed on a signal with rather small fluctuations. Similarly, the fluctuations at $r = 0$ (especially for axial velocity) were quite random in nature. In other regions of the bubble (especially in the downstream half), and in the wake regions, the fluctuations were highly periodic. Compare, for example, the very regular, sinusoidal-type of signal shown in Figure [4.24] to the less regular, noise-like signal of Figure [4.25].

### 4.4.6. Frequency Spectra

In the region in which the velocity fluctuations were regular it was possible to estimate the dominant frequency of the temporal variations by


Figure 4.24. A Trace of Axial Velocity vs. Time at r = 1.69 mm, 14 mm Downstream of Bubble Nose. Velocity Fluctuations are Quite Periodic.

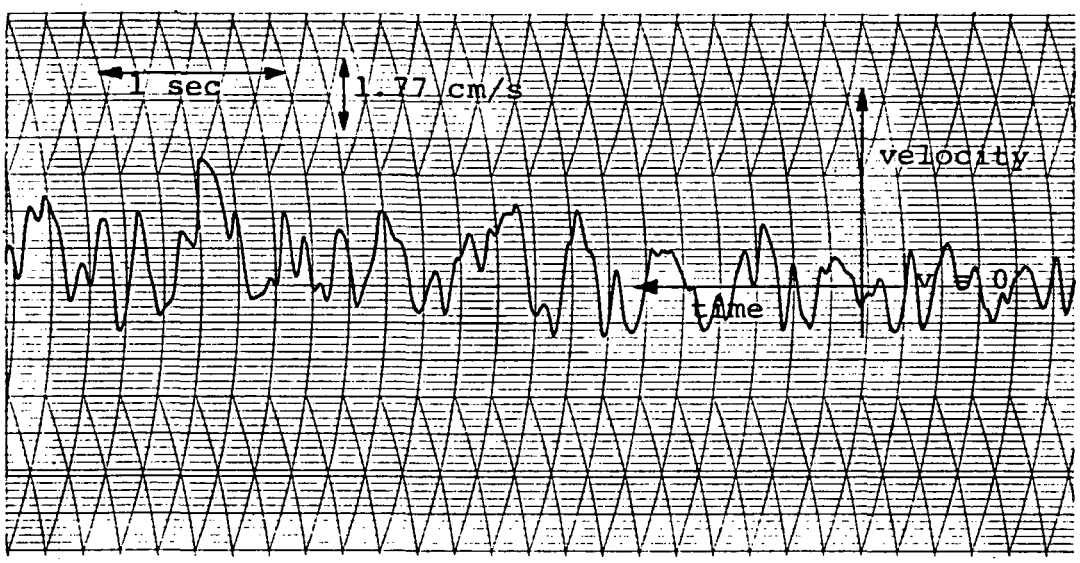


Figure 4.25. A Trace of Axial Velocity vs. Time at r = 4.23 mm, 10 mm - 13 mm Downstream of Nose. Velocity Fluctuations are Less Regular Than Those in Figure 4.24.

counting the number of cycles contained in a given length of record, i.e., in a given time. However, in order to ascertain the dominant frequency precisely and to determine the existance (if any) of any higher frequency components and their relative strengths, it was necessary to calculate the frequency spectrum of the velocity. This was accomplished by sampling, manually, from the analog voltage versus time trace at a fixed sampling rate (every .04 seconds) to obtain data in the digital format required. Each set of data, representing the velocity versus time for a fixed position inside the bubble, was then key punched onto computer cards and frqeuency analyzed numerically using the technique appropriate for finite record length data. The covariance and spectrum were calculated using methods given in Jenkins and Watts [33]. A Parzen lag window was used. Because this procedure was so time consuming, only a selected group of locations was selected for analysis. The locations were chosen to be representative and were located in the rear portion of the bubble, from r = 0 to the vicinity of the bubble envelope.

The spectra, shown in Figures [4.26 - 4.32], were computed from the axial velocity data at the location noted. The bandwidth for all the spectra presented is 1.33 Hz. The frequency spectra for velocity on the tube axis (r = 0) and near the dividing streamline (r = 5.07 mm) are characterized by the lack of a dominant peak and point out the relatively random nature of the fluctuations. The spectra for the intermediate radial locations all show a dominant frequency of about 2 Hz, with the r = .85 mm and r = 1.69 mm curves having very sizeable peaks at this frequency. In addition, all of these latter spectra show, to varying degrees, a peak at the first harmonic of ~4 Hz. The spectrum for r = 2.54 mm indicates that

the fundamental, at 2 Hz, and first harmonic, 4 Hz, contained comparable amounts of energy. This can be confirmed by studying Figure [4.33], in which a portion of the trace used to generate the r = 2.54 mm spectrum is presented. A portion of the r = .84 mm trace is shown in Figure [4.34] for comparison. The 2 Hz component is so dominant at r = .85 mm that the harmonic at 4 Hz is scarcely discernible; the harmonic is quite clearly seen in the 2.54 mm trace, however. Most of the velocity versus time traces that displayed a marked periodicity were characterized by a signal shape that was intermediate to the two extremes shown in Figures [4.33, 4.34]. That is, the traces appeared to be that of a relatively large amplitude sine wave, of frequency equal to 1.7 - 2.0 Hz, with evidence of a first harmonic of noticeably smaller amplitude. The shape of the trace depended on the relative amplitudes of the two frequency components and on the phase difference between the two components.

It should be noted that the dominant frequency varied only slightly from position to position inside the bubble, as long as the mean axial location of the breakdown was constant. This frequency did change more noticeably, over a range of 1.65-2.05 Hz, when the mean bubble position changed from day to day. The higher frequency corresponded to a more upstream mean location. The dominant frequency showed no correlation with the characteristic frequency obtained by dividing the average swirl velocity at the bubble envelope by the bubble circumference. There is excellent agreement, however, between this fundamental frequency and the angular frequency at which the rear portion of the single-tailed bubble rotated about the tube axis. It can be inferred, then, that the temporal periodicity measured at one location corresponded to an azimuthal periodicity

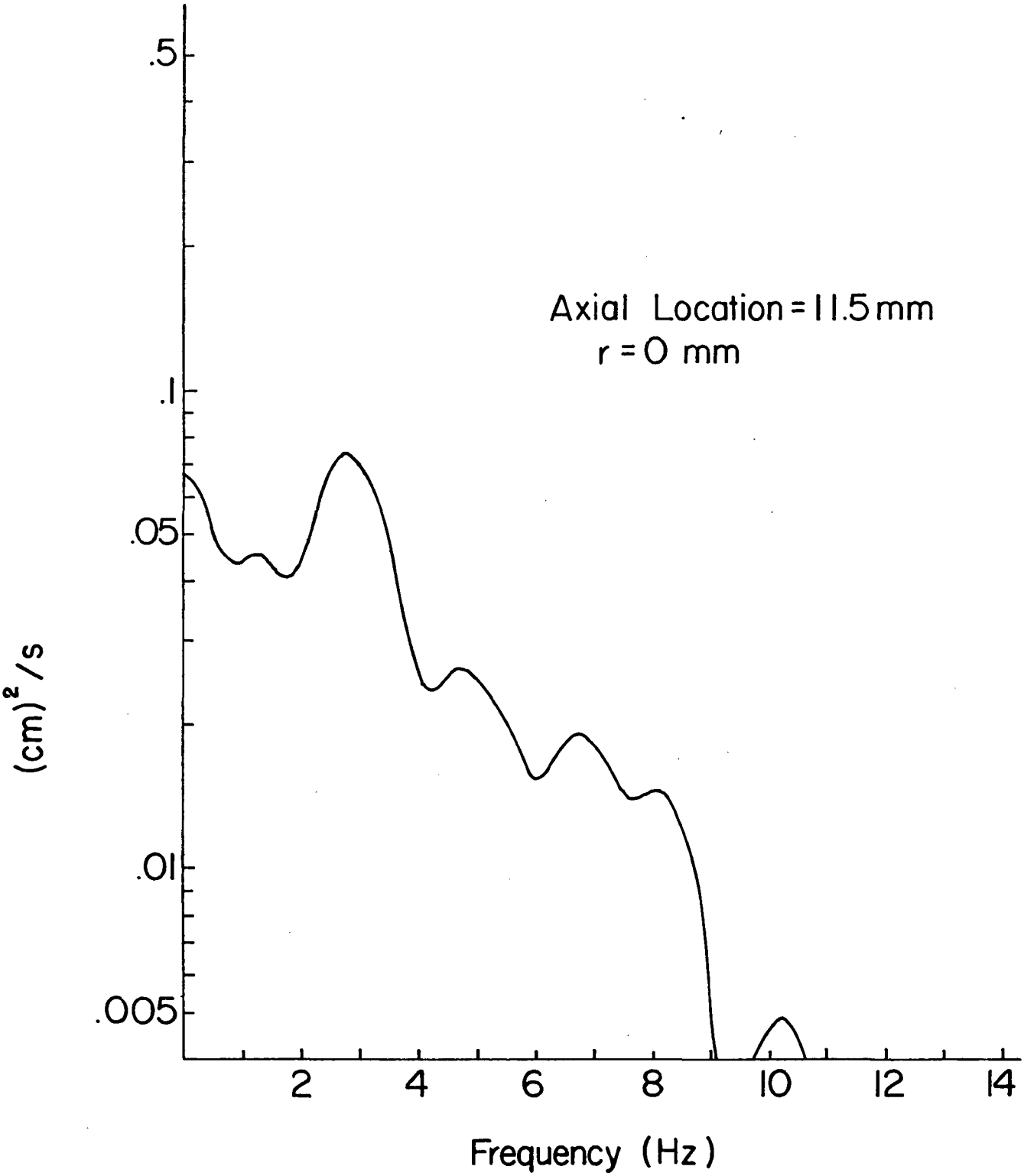


Figure 4.26. Power Spectra of Axial Velocity Inside the Breakdown Envelope at the Position Noted. Axial Location Denotes Distance Downstream of Bubble Nose; r Denotes Radial Location. Re = 2560, $\Omega$ = 1.777.

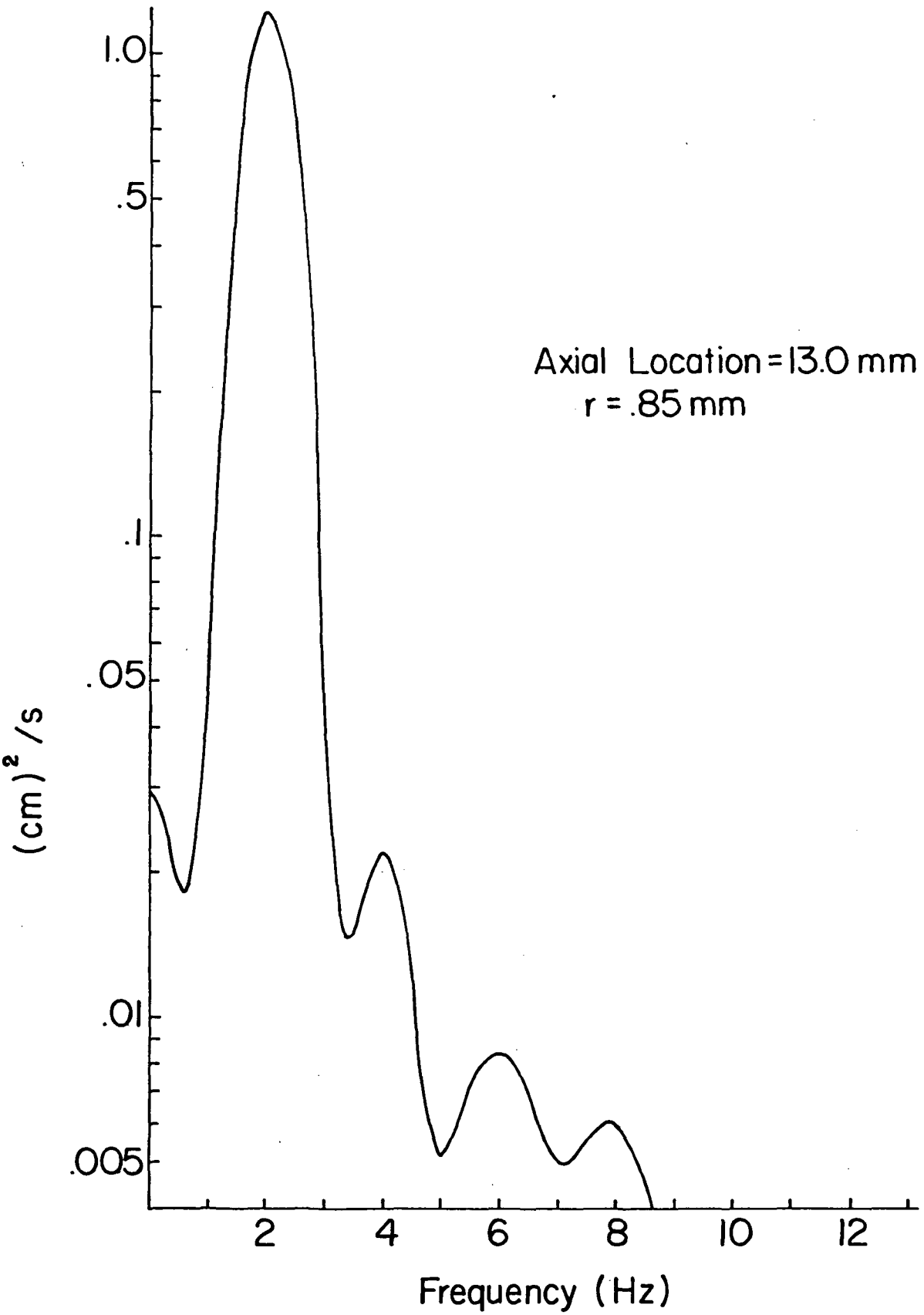


Figure 4.27. (See Figure 4.26.)

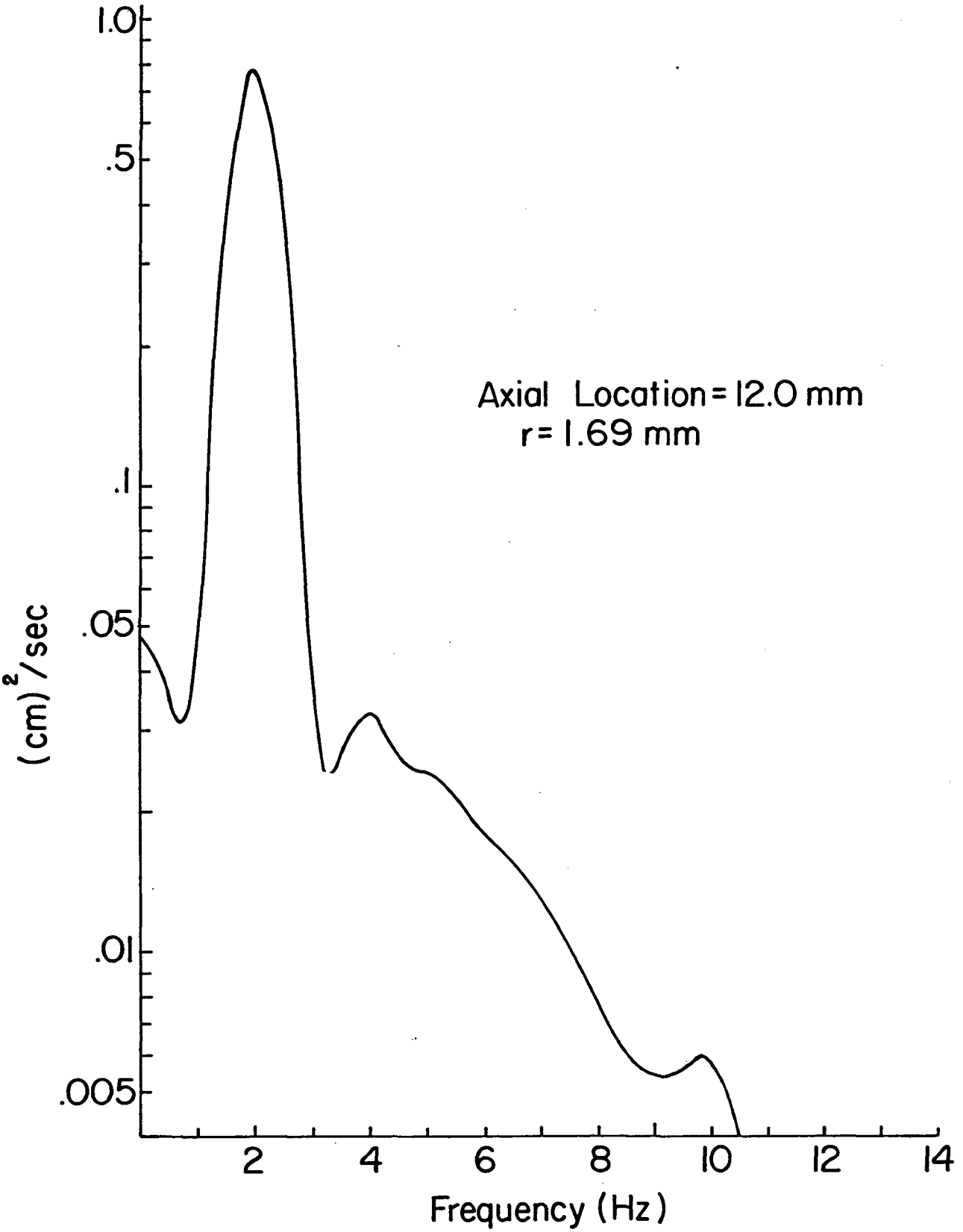


Figure 4.28. (See Figure 4.26.)

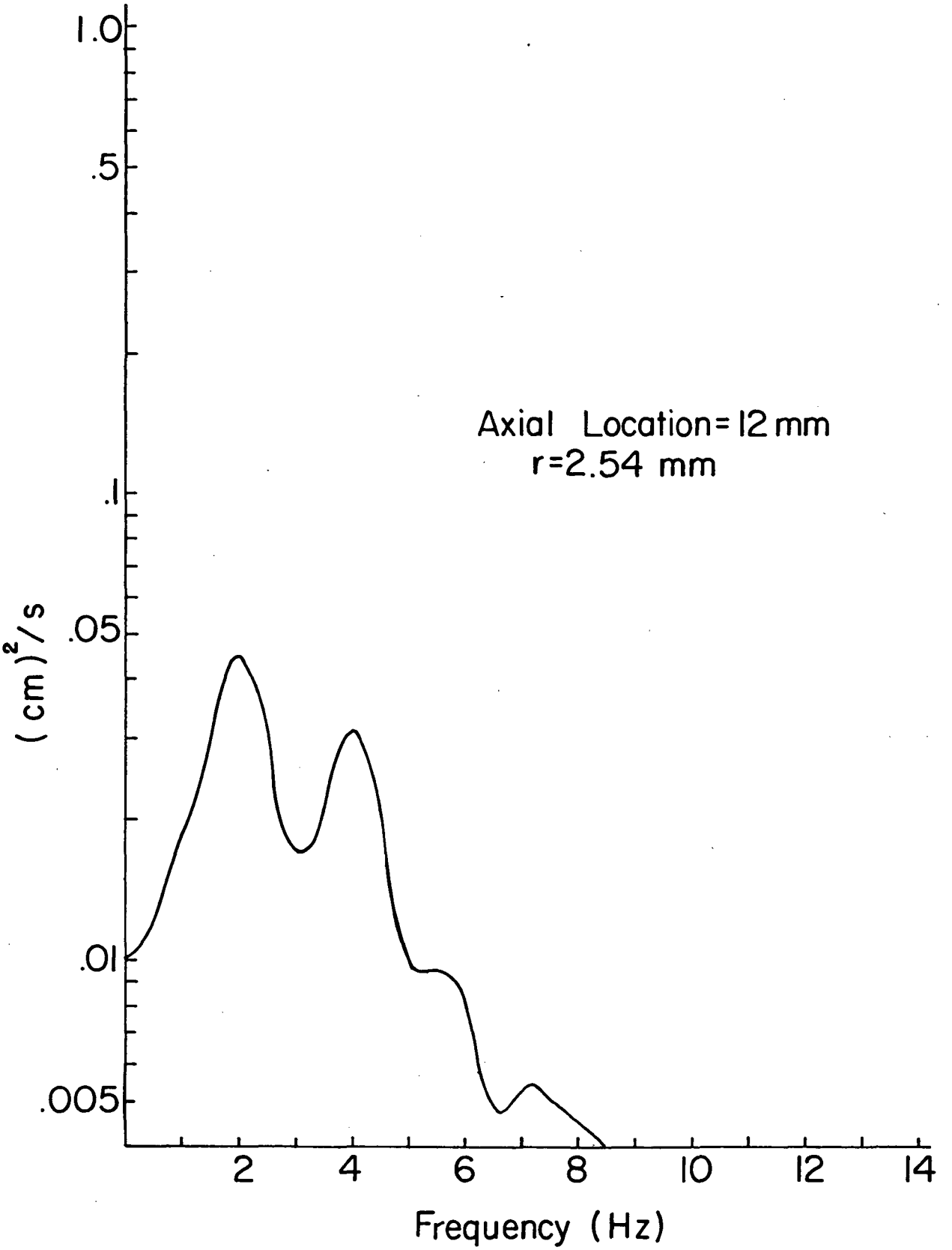


Figure 4.29. (See Figure 4.26.)

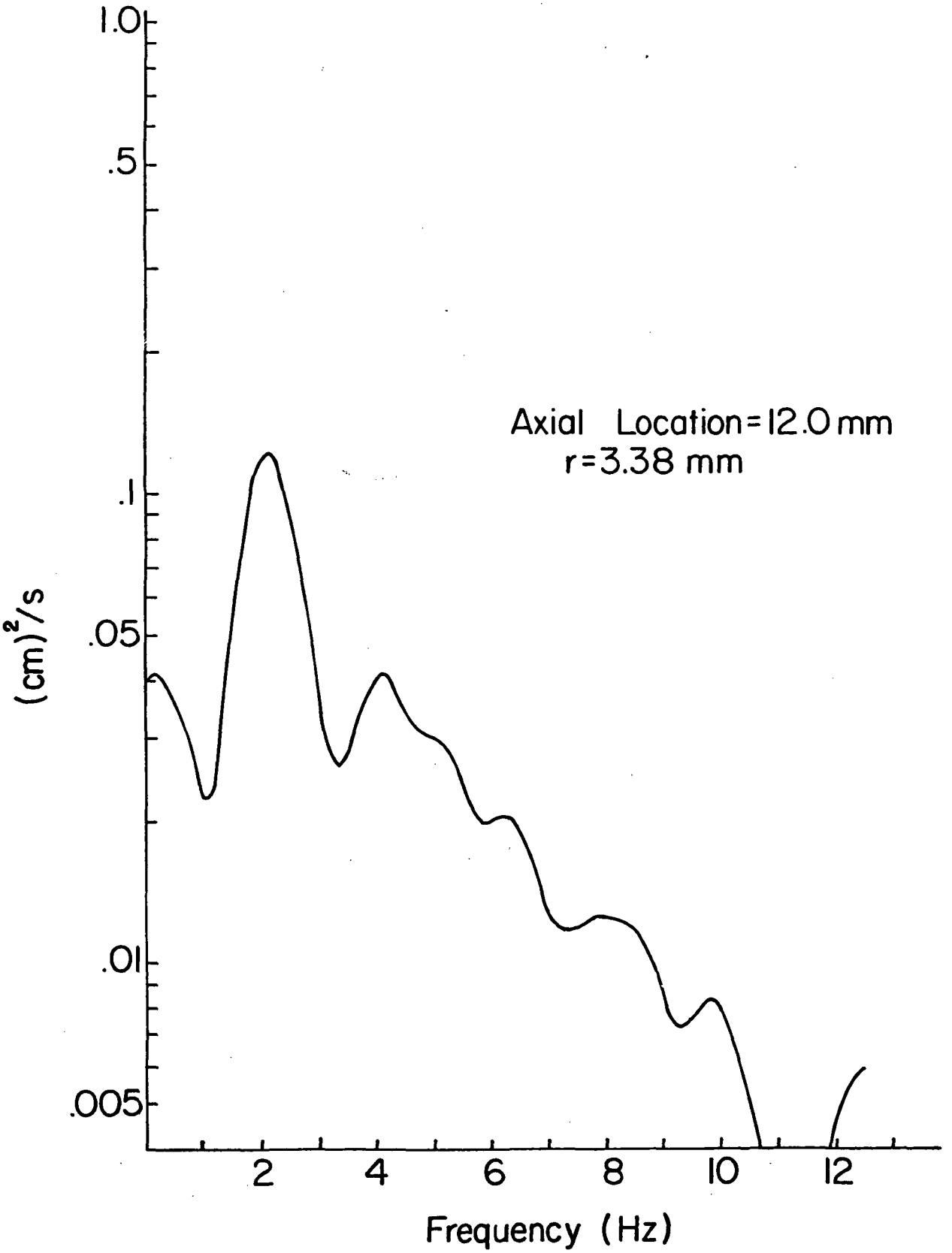


Figure 4.30. (See Figure 4.26.)

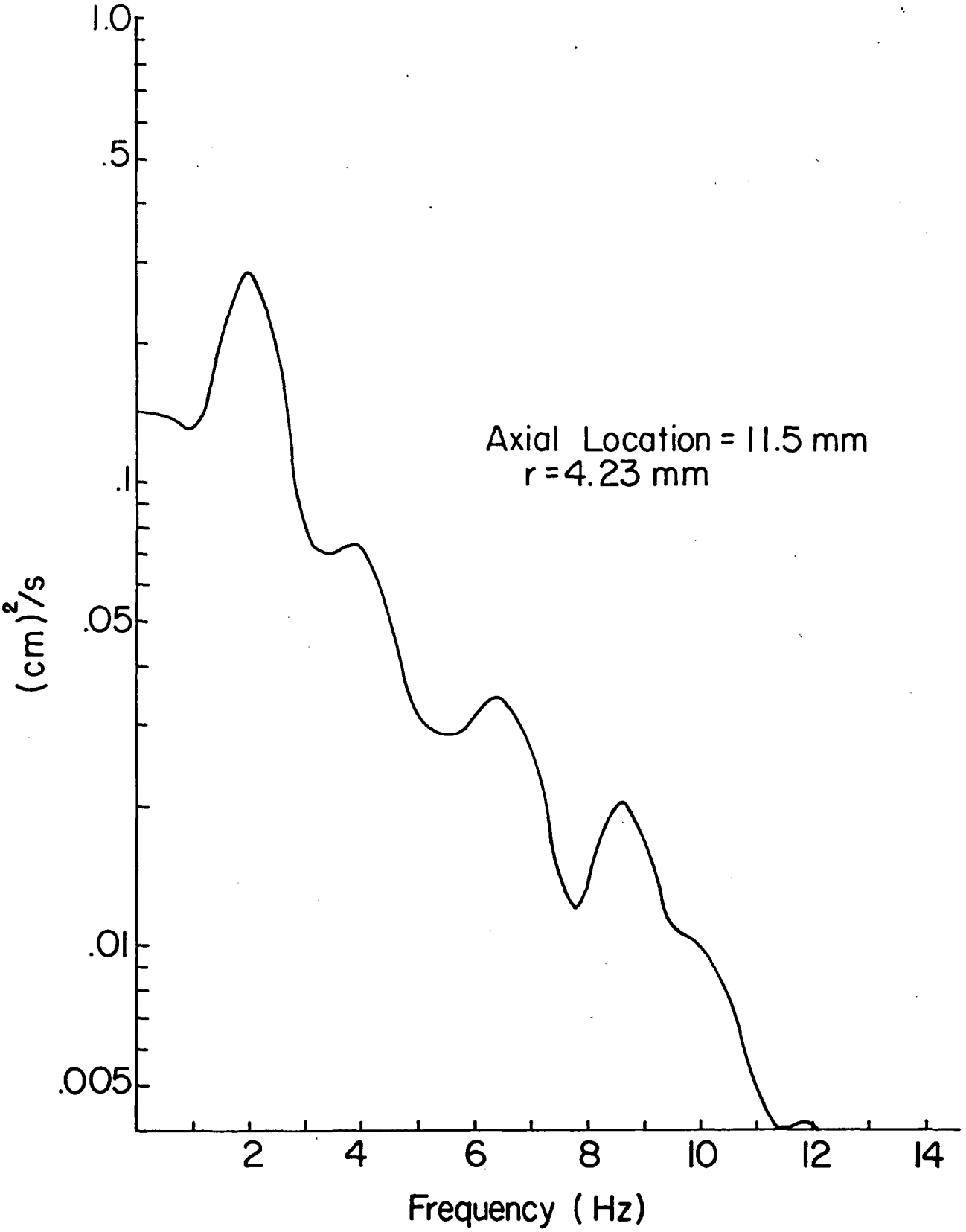


Figure 4.31. (See Figure 4.26.)

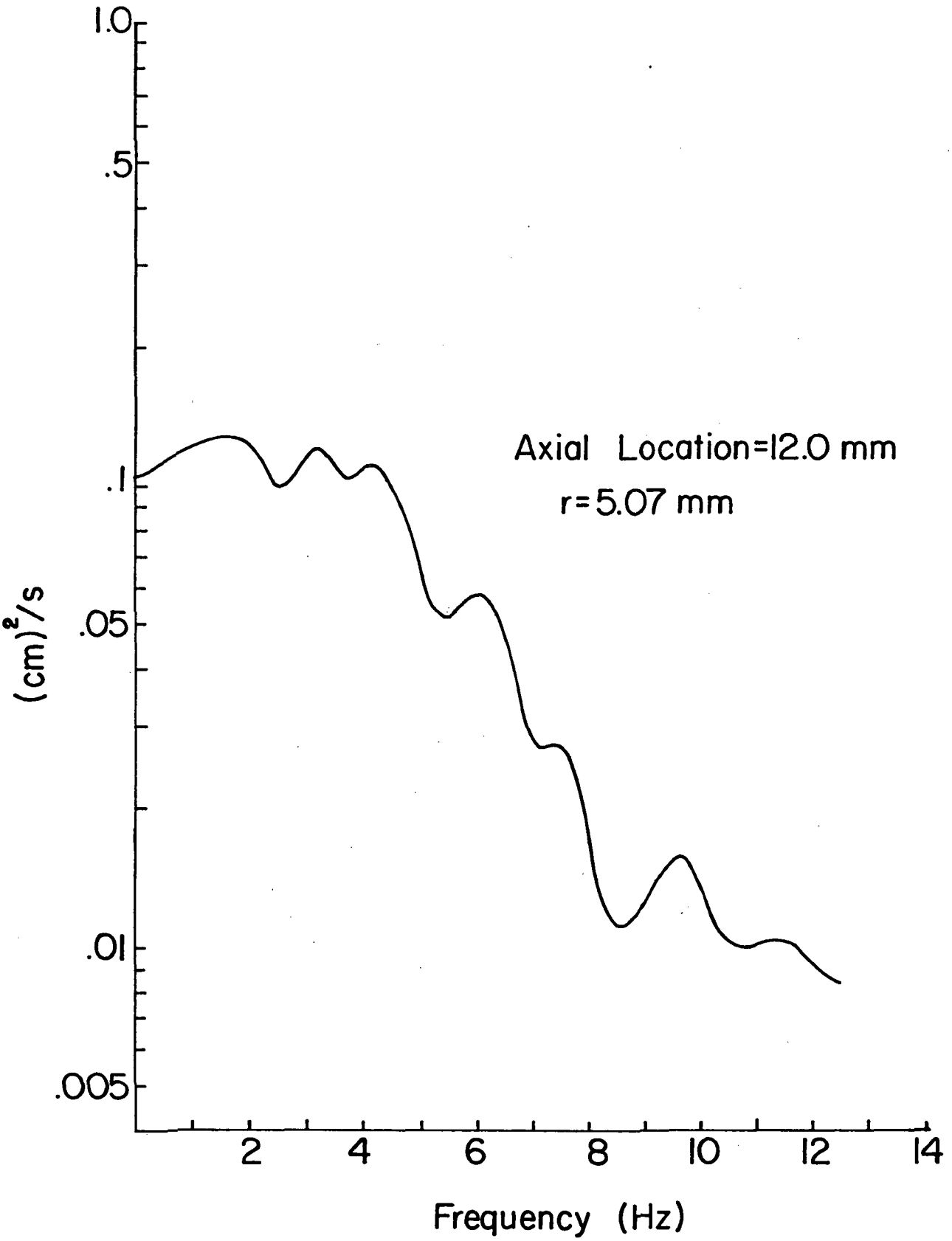


Figure 4.32. (See Figure 4.26.)

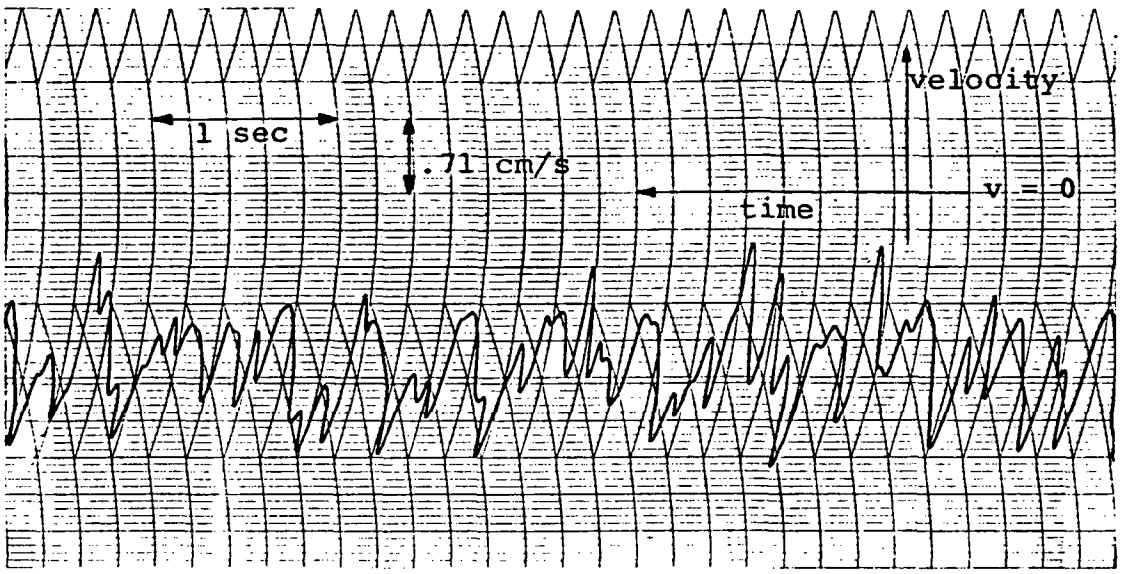


Figure 4.33. A Portion of the Axial Velocity vs. Time Trace Used to Calculate the Spectrum Shown in Figure 4.29.

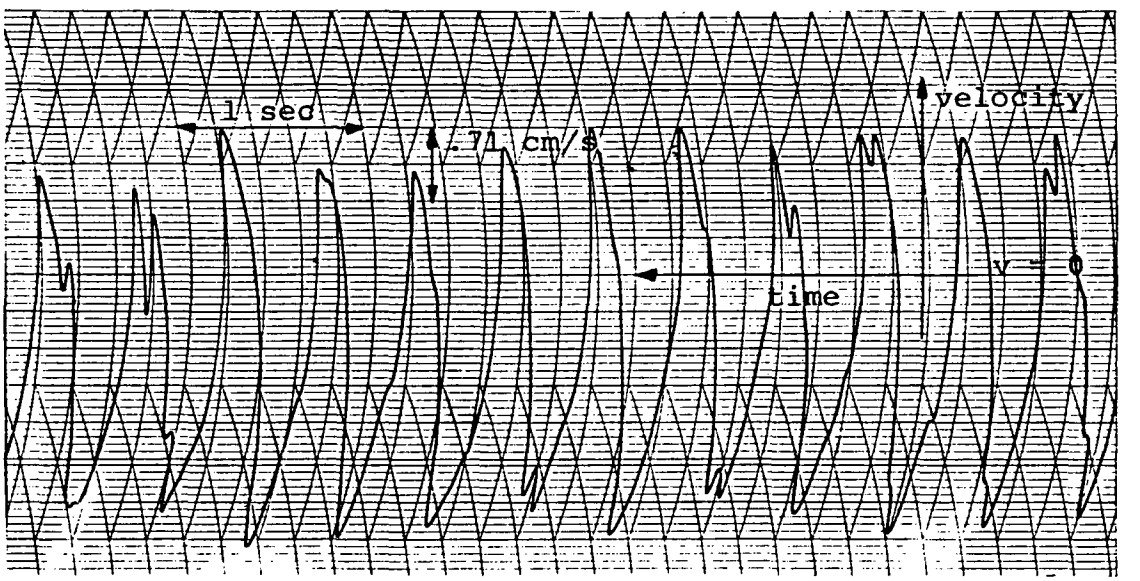


Figure 4.34. A Portion of the Axial Velocity vs. Time Trace Used to Calculate the Spectrum Shown in Figure 4.27.

associated with the simultaneous emptying and filling at the regularly rotating tail section of the bubble. Although it is not possible to substantiate, it appeared that the harmonic frequency component was associated with the remnants of the second bubble tail which could be seen occasionally.

## 4.5. General Comments

As discussed previously, all of the disturbance forms observed were only quasi-steady in axial location and drifted slowly, in a relatively random manner, about some mean location. In addition, velocity measurements performed on several occasions indicated that the profiles upstream of breakdown changed slowly in an indeterminate manner. Perhaps coincidentally, this effect was most noticeable during swirl velocity measurements. In both cases, these slow changes in the flow occurred even though the two variable parameters, vane angle and flow rate, were held fixed. These facts suggest that some sort of unsteadiness existed in the apparatus despite the precautions taken to hold all the variables constant.

These precautions included the use of constant room and water temperatures, well baffled constant head tanks, a precise spring-loaded vane control mechanism, and pneumatic bags to support the flow device and reduce transmitted vibrations. There was some slight movement of the rotameter float which may have indicated small variations in flow rate. However, it seems unlikely that the observed changes in disturbance location and velocity measurements could be caused by such small changes in flow rate.

Firstly, the period of the variations in the rotameter float position was approximately 1 second. This is in contrast to the typical period of the disturbance location variations, which varied from 5-10 seconds to

5-10 minutes depending upon the type of disturbance and flow conditions. In even greater contrast, the period of the velocity changes observed was 10-20 minutes or more. Secondly, the amplitude of the possible changes in flow rate does not seem sufficient to explain the relatively larger changes noted in both breakdown location and velocity measurements. The rotameter had a precision of ± .25% of indicated reading and this was approximately the extent of the variations in float position. However, as can be seen in Figure [3.21], a change in flow rate (Reynolds number) of ten times this amount was often required to change the mean axial location of a given disturbance type by an amount equal to the variations seen at a fixed flow rate. Similarly, a flow rate change of about 2% was necessary to duplicate the changes in swirl velocity that were noted at a fixed flow rate. A change of 2% in flow rate could not have occurred without being detectable by observation of the rotameter.

It seems more likely, then, that the unsteadiness in the flow resulted from some more subtle variations in the experimental apparatus. Perhaps the method used to supply fluid to the upper constant head tank produced vorticity in that tank which did not decay entirely and was still present in the fluid when it reached the vane array location. The presence of a small but varying amount of residual vorticity could change the swirl velocity profile slightly and thereby alter the apparently delicate balance that determined the flow disturbance location.

Also, there may have been an asymmetry in the entrance channel geometry or a non-uniform feeding of fluid into the vane array that changed slightly over a period of time. (The observations that a preferential

plane existed for the types 3-6 and that the orientation of this plane was more or less reproducible for a given set of flow conditions suggests the possibility of some sort of asymmetry). In summary, these observations indicate that extreme care should be exercised when designing and constructing devices for further study of the vortex breakdown phenomenon.

With regard to future theoretical investigations of vortex breakdown, the velocity measurements of the type 0 mode suggest that this so-called axisymmetric form is not axisymmetric and is dominated by strong, regular fluctuations. Earlier models, based on assumptions of axial symmetry and steadiness, presumably can apply, at best, to the mean motion. However, existing simulations do not even qualitatively predict the mean flows that are observed in the recirculation zone. It is likely that the periodic fluctuations must be accounted for.

One method that could be employed would be to assume a steady, axisymmetric mean flow, incorporating Reynolds stresses to account for the fluctuations. An alternative approach is suggested by the facts that the fundamental frequency of the fluctuations was relatively invariant from location to location within the bubble envelope and wake region and that this frequency showed good correlation with the angular frequency of rotation of the asymmetric rear portion of the bubble. Thus, it may be beneficial to adopt a coordinate system rotating at this fundamental frequency. It is possible that the flow in the breakdown region would appear to be steady, but asymmetric.

In conclusion, it is hoped that the flow visualization studies, the accurate measurements of the base flow profiles, and the detailed mapping

of the flow field associated with the type 0 vortex breakdown will provide substantial clues for future investigators attempting to explain this remarkable phenomenon. More immediately, these results should be useful as a check on the validity of the assumptions and results of the various existing simulations.

# APPENDIX A1

## A1.0. The Swirl Vanes: Construction Method and Alignment Technique

The swirl vanes and the gear system which controlled their orientation were of critical importance in this experiment. As seen in Figure [A1.1], the vanes were symmetric, straight sided foils with a rounded leading edge. The angle of 11.25° between the sides was chosen to provide a constant width passage, in the streamwise direction, between adjacent vanes.

A master vane was made of steel and was finely polished. This steel vane had dimensions identical to those desired for the final castings, but with a slightly longer span. From this master vane, molds were made using room temperature vulcanizing rubber specifically compounded for this type of work. The vanes were cast in these molds. A low viscosity, unfilled epoxy was chosen for the vane material because of its strength, machineability, and dimensional stability as a casting medium.

After curing, the epoxy vane was removed from the mold. The rough, free surface was ground away using a surface grinder, and this restored the spanwise dimension to the desired value. Using a precision, ground steel jig to hold the vanes in position on the bed of a trammed milling machine, the shaft holes were made in each vane. The holes were drilled and reamed to provide a precise press fit between shaft and vane. More epoxy was then used to insure a slip-free bond.

Each vane-shaft assembly was individually fitted in the brass backing plate using shims to adjust clearances and end-play. After the installation of all the vanes and the controlling gear system had been completed, final alignment was made using an alignment jig and dial indicator.

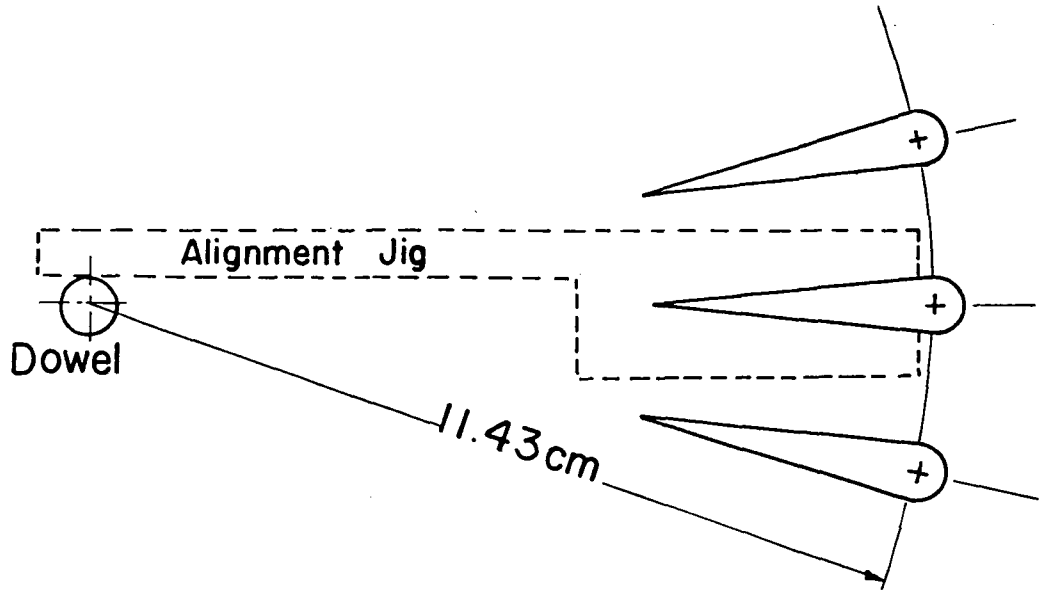


Figure A1.1.a The Swirl Vane Array, with Alignment Jig in Place.

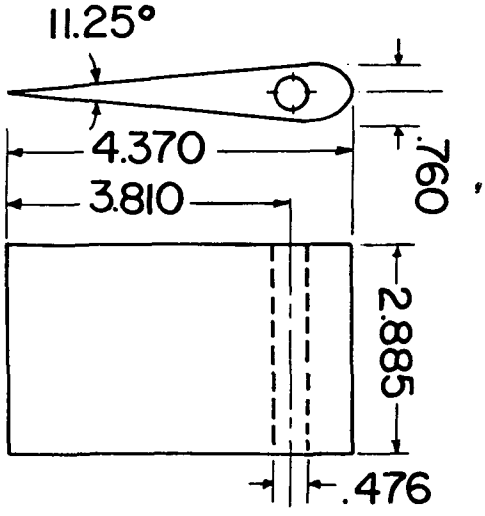


Figure A1.1.b Swirl Vane Dimensions.

A precision, ground-steel jig (also used to position the vanes on the milling machine) was made. This jig could be fitted on a vane.

The jig-vane combination was rotated until contact was made between the jig and a dowel indicating the brass plate centerline. In this position, the vane centerline and the radial line drawn from the plate centerline to the center of the vane shaft were coincident, i.e. the vane was pointing radially inward. All the planet gears, except one, could be unlocked from the vane shafts. This exceptional gear was pinned to its vane shaft and drove the sun gear. The alignment procedure was as follows:

1. Install alignment jig on vane controlled by the driver planet gear.
2. Rotate actuating wheel until vane points radially inward, as indicated by jig-dowel contact.
3. Put dial indicator in contact with vane near the trailing edge, and set to 0.
4. Remove jig.
5. Rotate actuating wheel so vane makes negative angle.
6. Rotate actuating wheel slowly until dial indicator reaches 0.
7. Set counter to 0 and lock to actuating wheel.
8. Place jig on next vane and unlock the vane shaft from its planet gear.
9. Rotate vane until vane is at 0°.
10. Place dial indicator in contact with vane near the trailing edge and set to 0.
11. Lock shaft to gear.
12. Test to see that dial indicator reads 0 when counter reaches 0, approaching positive from negative.

13. If not, unlock shaft from gear and adjust slightly. Repeat steps 11 and 12 until successful.

14. When successful, repeat 8-13 until all vanes are done. The tolerance allowed determines the ultimate accuracy of the vane setting indicated by the counter; i.e. the initial vane adjustment is the largest source of error in the vane control system.

APPENDIX A2

## A2.0. Alignment Procedure Summary

In Chapter 2, the procedure followed in aligning the optical system, mounted on the traversing mechanism, and flow device was given in detail. This procedure aligned the reference line, defined by the input laser beam, to be in the horizontal plane which contained the flow device centerline. Furthermore, this reference line was normal to the tank sidewalls, the test section O.D. and the centerline of the unit. The X axis of the traversing mechanism was parallel to the centerline of the flow device. The Y axis was normal to the centerline, and thus parallel to the reference line.

The optical system was initially moved in the X, Y system so that the beams intersected on the dye streak, which indicated the centerline of the test section, at a reference axial location, taken to be .5 cm downstream of the start of the diverging portion of the test section. In this Appendix, the details of the refraction effects of the various air - Plexiglas and Plexiglas - water surfaces will be covered.

## A2.1. Beam Details, Axial Velocity Measurements

Figure (A2.1) is a schematic of the optical unit and flow device with the beams in the horizontal plane. This arrangement was used to measure the axial velocity.

The focusing lens, L, of focal length F, is at a distance Y from the tank sidewalls. The distance between the beams at lens L is $b_s$. Each beam makes an angle of $\theta_a/2$ with the reference direction, since the reference line was coincident with the bisector of the beams. Therefore

$\tan \theta_{a/2} = \frac{b_{s/2}}{F}$, and since $\theta_{a/2}$ is small, $\tan \theta_{a/2} \simeq \sin \theta_{a/2} \simeq \theta_{a/2}$.

Figure (A2.2) shows an interface separating medium 1, of index of refraction $n_1$, and medium 2, of index of refraction $n_2$. For small $\theta_1$, the law of refraction becomes $n_1\theta_1 = n_2\theta_2$ and $n_1\lambda_1 = n_2\lambda_2$.

Since the normal of each surface, at the point where the light beam is incident, lies in the horizontal plane, all refraction takes place in the horizontal plane and the beams remain in this reference plane.

Therefore, in Figure (A2.1), the paths of the beams through the flow device are followed by applying this rule at all surfaces, indicated by 1-4, and by computing the distance between the beams at each surface.

at 1.

$$d_1 = b_s - 2Y \frac{\theta_a}{2} \tag{A2.1}$$

$$\frac{1}{2}\theta_p = \frac{\theta_a}{2n_p}, \quad \text{since } n_{air} = 1 \tag{A2.2}$$

at 2.

$$d_2 = d_1 - 2\, t_w \frac{\theta_a}{2n_p} \tag{A2.3}$$

$$n_w\theta_w = n_p\theta_p = n_p(\theta_a/2n_p) = \theta_{a/2} \tag{A2.4}$$

$$\theta_w = \frac{\theta_a}{2(n_w)} \tag{A2.5}$$

at 3.

$$d_3 = d_2 - 2w \frac{\theta_a}{2n_w} \tag{A2.6}$$

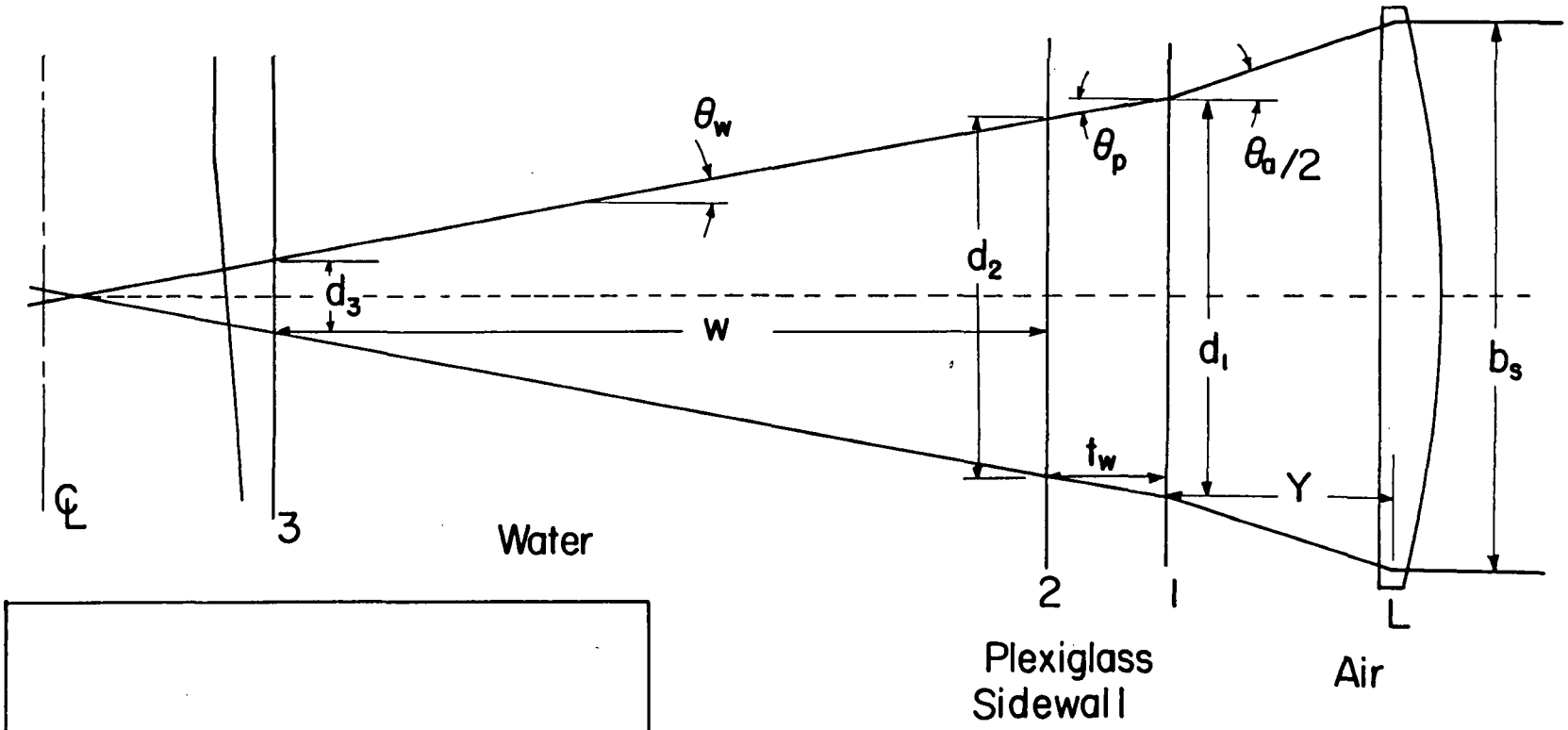


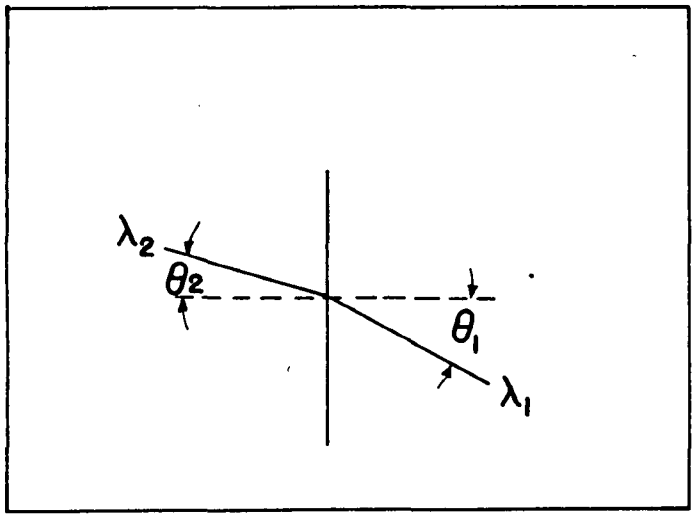


Figure A2.1. Schematic of Flow Apparatus with Laser Beams in Horizontal Plane Showing the Refraction of the Beams. (above)

Figure A2.2. Refraction of Light Beam at an Interface Between Medium 1, Index of Refraction $n_1$, and Medium 2, Index of Refraction $n_2$.

or

$$d_3 = b_s - 2Y\frac{\theta_a}{2} - 2\,t_w\frac{\theta_a}{2n_p} - 2w\frac{\theta_a}{2n_w}$$

$$d_3 = b_s - \theta_a\left(Y + \frac{t_w}{n_p} + \frac{w}{n_w}\right) \qquad \text{(A2.7)}$$

Up to this point, the beams remain symmetric with the reference line, being equally spaced from it at a distance $d_3/2$, and making an equal angle, $\frac{\theta_a}{2n_w}$, with the reference. Next, the effect of the tapered inside diameter, with taper angle $\alpha$, must be considered, Figure A2.3.

The thickness of the test section wall, t, is a function of axial distance

$$t = r_o - r_i(z) = r_o - [r_t + z\alpha] \qquad \text{(A2.8)}$$

For beam a, the thickness it traverses is $t' = t + \frac{d_3}{2}\alpha$ and the angle it makes with the normal to the tube centerline is $\frac{\theta_a}{2n_p}$

Therefore:

$$d_4' = \frac{d_3}{2} - t'\frac{\theta_a}{2n_p} \qquad \text{(A2.9)}$$

$$d_4' = \frac{d_3}{2} - \left(t + \frac{d_3\alpha}{2}\right)\frac{\theta_a}{2n_p} \qquad \text{(A2.10)}$$

$$d_4' = \frac{d_3}{2}\left(1 - \frac{\alpha\theta_a}{2n_p}\right) - \frac{t\theta_a}{2n_p} \qquad \text{(A2.11)}$$

Since $\alpha$ is small (equal to .025) and $\frac{\theta_a}{2}$ is small, the product $\alpha\frac{\theta_a}{2}$ is small relative to 1, and $d_4 \simeq \frac{d_3}{2} - \frac{t\theta_a}{2n_p}$. Similarily, for beam b, $d_4'' \simeq \frac{d_3}{2} - \frac{t\theta_a}{2n_p} = d_4'$ and the beams remain symmetrically spaced with the reference line.

Therefore,

$$d_4 = d_4' + d_4'' = d_3 - \frac{t\theta_a}{n_p} \qquad \text{(A2.12)}$$

The taper angle does affect the direction of each beam, however. For beam a, $n_p(\frac{\theta_a}{2n_p} - \alpha) = n_w\beta$, $\beta = \frac{\theta_a}{2n_w} - \alpha\frac{n_p}{n_w}$. The angle between beam a and the normal to the centerline is:

$$\beta + \alpha = \frac{\theta_a}{2n_w} - \alpha(\frac{n_p}{n_w} - 1) \qquad \text{(A2.13)}$$

For beam b, $n_p(\frac{\theta_a}{2n_p} + \alpha) = n_w\beta'$, $\beta' = \frac{\theta_a}{2n_w} + \alpha\frac{n_p}{n_w}$. The angle between beam b and the normal to the centerline is:

$$\beta' - \alpha = \frac{\theta_a}{2n_w} + \alpha(\frac{n_p}{n_w} - 1) \qquad \text{(A2.14)}$$

The included angle between the beams, then, is the sum of these: $(\beta + \alpha) + (\beta' - \alpha) = \frac{\theta_a}{n_w}$, and thus the tapered wall does not affect the included angle.

The bisector of the angle is not perpendicular to the centerline, however. The angle between the bisector and the normal to the centerline is $\phi$, where

$$\phi = (\beta'-\alpha) - \frac{(\beta+\alpha)+(\beta'-\alpha)}{2}$$

$$\phi = \frac{\theta_a}{2n_w} + \alpha(\frac{n_p}{n_w} - 1) - \frac{\theta_a}{2n_w}$$

$$\phi = \alpha(\frac{n_p}{n_w} - 1) \qquad \text{(A2.15)}$$

Since the velocity component measured is perpendicular to the bisector, the component measured with this beam orientation is $V_1$.

$V_1 = V_{axial} \cos\phi$. However, $\phi = .003$, and $\cos\phi = 1$, with an negligible error of less than .01%, and therefore, $V_1 = V_{axial}$.

Notice that, if a beam was imagined to exist along the reference line, it would be undeflected until it encountered the tapered wall. There, it would be located at P, equidistant from the two beams, a and b. By the refraction formula the angle it would make with the normal to the centerline would be $\alpha(\frac{n_p}{n_w} - 1)$, which = $\phi$.

Thus, the reference line beam would bisect the angle formed by the beams a and b. As the optical unit is moved in the Y direction, the beams a and b form a series of similar triangles with the point P as the bisector of each base. The intersection point would move along the line P-P', which would pass through the apex of each of these similar triangles. P-P' is coincident with the path that would be taken by the beam entering along the reference line.

Since the line P-P' is not normal to the centerline, the intersection point would move in the axial direction as the optical system was moved along the Y axis. However, for a radial traverse beginning at the centerline of the tube, the maximum change in axial location, 0-P', would be $r_i\phi$. Since $(r_i)_{max}$ = 25.4 mm, $(0\text{-}P')_{max}$ = 25.4 $\phi$ = .076 mm, and this is negligible.

For any fixed Z, then, the effects of the taper of the test section can be ignored and the test section can be considered, locally, as a straight tube.

The distance, j, from P to the intersection point is given by

$$j \frac{\theta_a}{2n_w} = d_4/2$$

from equation [A2.12], $d_4/2 = \frac{d_3}{2} - \frac{t\theta_a}{2n_p}$ and $j = \frac{d_3 n_w}{\theta_a} - \frac{t n_w}{n_p}$. The radial position, r, is

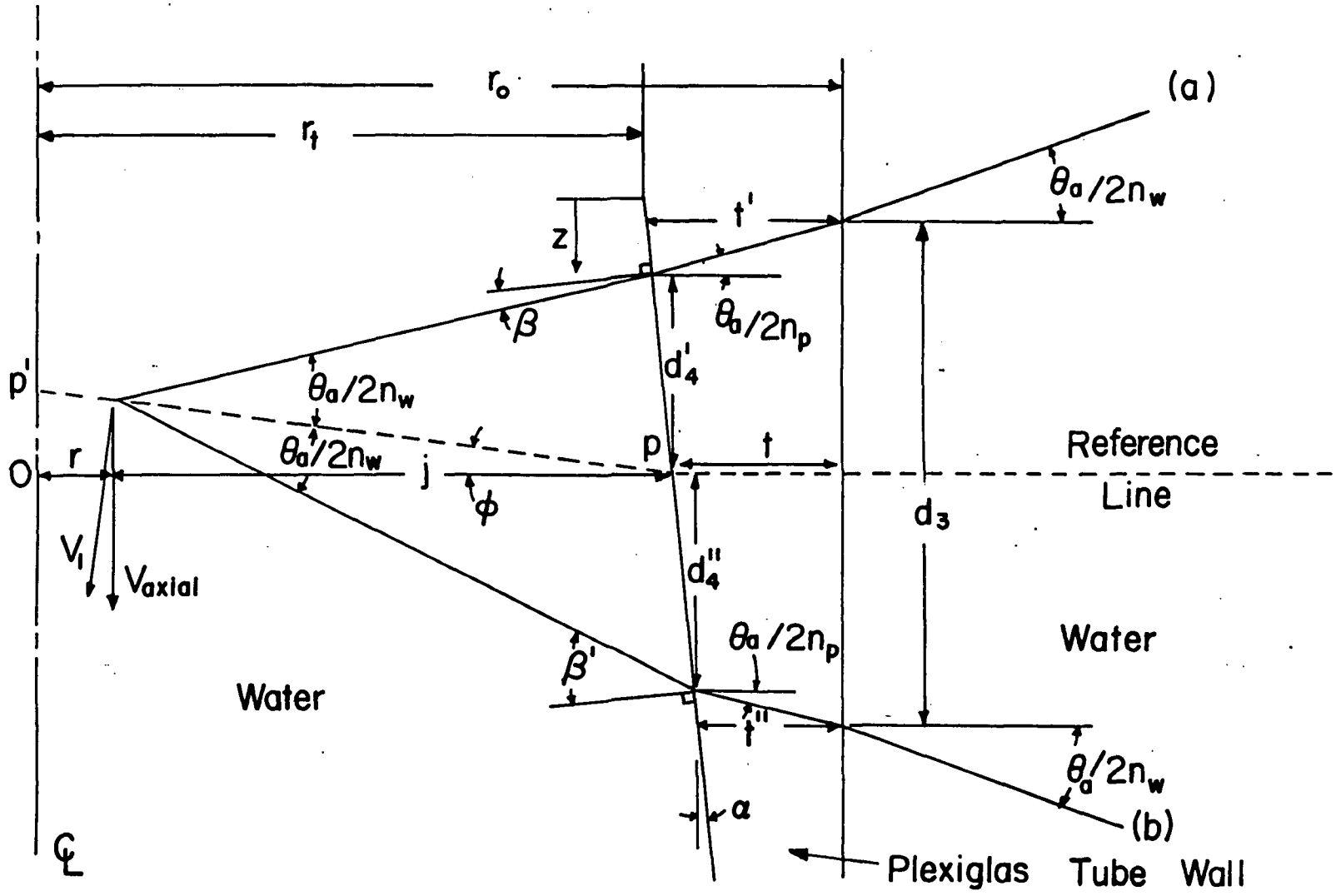


Figure A2.3. The Paths of the Laser Beams in the Horizontal Plane, Showing Effects of the Tapered Test Section.

$$r = r_o - t - j$$

or,

$$r = r_o - \frac{d_3 n_w}{\theta_a} - t\left(1 - \frac{n_w}{n_p}\right) \qquad \text{(A2.16)}$$

Since $t=t(z)$ the varying thickness will cause the intersection point to move radially, for constant Y(constant $d_3$), if the optical system is moved in the X direction. However, this effect is also small, since from equation (A2.8)

$$t = r_o - [r_t + z\alpha]$$

or

$$t = C_1 - z\alpha,$$

where $C_1 = r_o - r_t = \text{constant}$

therefore

$$r = r_o - \frac{d_3 n_w}{\theta_a} - [C_1 - z\alpha]\left(1 - \frac{n_w}{n_p}\right)$$

or

$$r = C_2 - \frac{d_3 n_w}{\theta_a} + z\alpha\left(1 - \frac{n_w}{n_p}\right),$$

where $C_2 = \text{constant}$

But, $$\alpha\left(1 - \frac{n_w}{n_p}\right) = \frac{dr}{dz} = .0027$$

If axial displacement Z, is less than 4 cm, the resulting radial movement is (40)(.0027) = .108 mm, which is also negligible. In this study, Z was limited to be less than 4 cm, and thus this effect was ignored.

With this simplification, i.e. $z\alpha(1 - n_w/n_p) \approx 0$

$$r = C_2 - \frac{d_3 n_w}{\theta_a}$$

from equation (A2.7), $d_3 = b_s - \theta_a(Y + \frac{t_w}{n_p} + \frac{w}{n_w})$

therefore

$$r = r_o - (r_o - r_t)(1 - \frac{n_w}{n_p}) - \frac{b_s n_w}{\theta_a} + n_w(Y + \frac{t_w}{n_p} + \frac{w}{n_w})$$

All of the terms on the right are constant except Y, so,

$$r = C_3 + n_w Y \qquad \text{(A2.17)}$$

where

$$C_3 = r_o - (r_o - r_t)(1 - \frac{n_w}{n_p}) - \frac{b_s n_w}{\theta_a} + \frac{t_w n_w}{n_p} + w$$

It was necessary to determine the minimum focal length lens that could be used, which for a fixed $b_s$ gives the maximum value of $\theta_a$. The minimum value of Y possible was Y min = 15 mm, and it was required that with Y = Y min, the beams would intersect at r = 0. Setting r = 0 and Y = Y min in the equation above, it becomes

$$0 = C_3 + n_w Y \text{ min}$$

solving for $b_s/\theta_a = F$, it is found

$$b_s/\theta_a = F = \frac{r_t}{n_w} + \frac{r_o - r_t}{n_p} + \frac{w}{n_w} + \frac{t_w}{n_p} + Y \text{ min}$$

and substituting the values for all the constants, it is found that the minimum F = 183.3 mm. Because of availability, a lens with a nominal focal length of 200 mm was used. From equation (A2.17), $r = C_3 + n_w Y$. As explained in the alignment procedure, Y was varied until the beams

intersected at r = 0, and this reference position of the optics was taken as $Y = Y_o$.

So $$0 = C_3 + n_w Yo$$

and if $$Y = Yo + y$$

$$r = C_3 + n_w(Y_o + y)$$

or $$r = n_w y \qquad \text{(A2.18)}$$

The reference of the X axis was taken at z = .5 cm. Therefore

$$z = .5 + (X - X_o)$$

or $$z = .5 + x \qquad \text{(A2.19)}$$

where $$x = X - X_o$$

The position of the intersection point, then, is related to the position, x, y, of the optical system by equations [A2.18,A2.19]. In addition, the analysis shows that for all x, y, with $|x| < 4$ cm, the effect of the tapered section could be ignored. The angle between the beams in water was $\theta_a/n_w$, and the wavelength was $\lambda_{a/n_w}$. Therefore, in the equation relating frequency to velocity

$$f_D = f_o + \frac{2V \sin(\theta/2)}{\lambda}$$

the values of $\theta_a/n_w$ and, $\lambda a/n_w$ are used and it becomes, for small $\theta/2$,

$$f_D = f_o + \frac{V\theta_a}{\lambda_a} \qquad \text{(A2.20)}$$

Equations [A2.18], [A2.19], [A2.20] give, then, the axial velocity at (z,r) if the frequency, $f_D$; optical system position, (x,y); and system constants,

$\lambda_a$, $\theta_a$, etc., are known.

A2.2. Spatial Resolution

A knowledge of the value of $\Theta$ allows the prediction of the spatial resolution of the instrument. From Chapter 2, the intersection volume has dimensions of b, b/cos $\Theta$, and length, b/sin$\theta$, where b is the beam diameter at the intersection point.

The value of b can be estimated by assuming that the laser beams are focused to the diffraction limited spot size. From reference [34], the beam diameter at the intersection point, b, is, (refer to Figure [A2.4])

$$b = \frac{4}{\pi} \frac{\lambda}{\Delta\theta}$$

or

$$b = \frac{4}{\pi} \frac{\lambda_{a/n_w}}{\Delta\theta_a/n_w} = \frac{4}{\pi} \frac{\lambda_a}{\Delta\theta_a}$$

For a focal length, F, and input beam diameter, B,

$$\Delta\theta_a = B/F$$

therefore

$$b = \frac{4}{\pi} \frac{\lambda_{aF}}{B}$$

and as shown earlier, $\theta = \theta_{a/n_w} = \frac{1}{n_w} b_s/F$

The dimensions of the intersection volume, then, can be estimated by, (with cos$\Theta$ ~ 1, sin$\Theta$ ~ $\Theta$)

$$\frac{4}{\pi} \frac{\lambda_a F}{B}, \quad \frac{4}{\pi} \frac{\lambda_a F}{B}, \quad \text{and length} = \frac{4n_w \lambda_a}{b_s \pi} \frac{F^2}{B}$$

All of these parameters, except F and B, were constants for the optical system used. Therefore, the spatial resolution could be improved only by

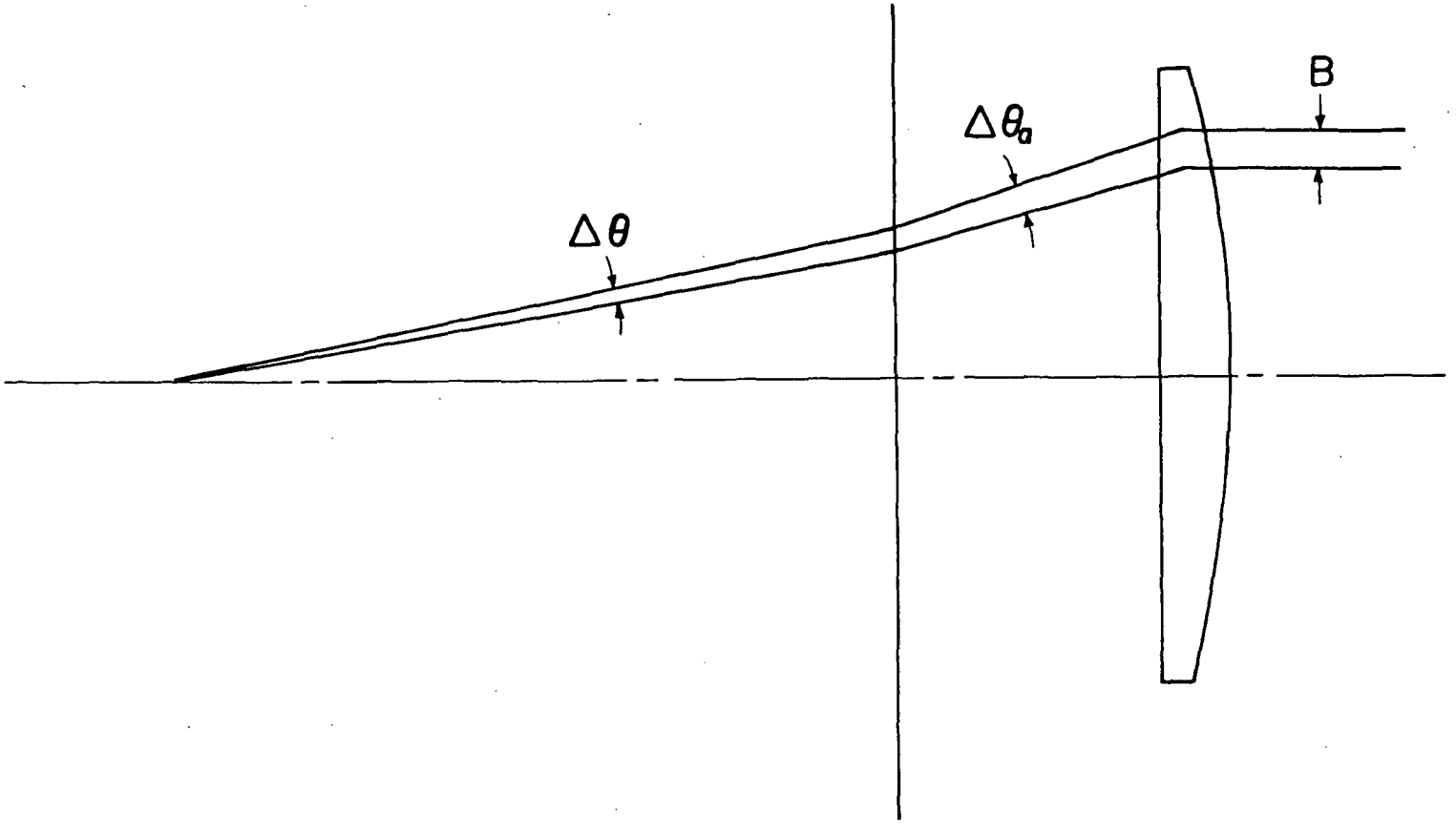


Figure A2.4. Schematic Defining the Terms Used in the Determination of the Intersection Volume Dimensions.

increasing B and decreasing F. As noted above, there was a minimum value of F possible, and this lens was chosen for use. This was especially important in reducing the length of the intersection volume. In addition, B was increased by a factor of 3 by fitting a beam expander to the laser head. This also was the maximum value possible, and was limited by the Bragg cell aperture size. For the setup used, the intersection volume was approximately a cylinder with the diameter equal to .08 mm and the length equal to .43 mm. The cylinder was aligned with its axis along the bisector of the angle formed by the beams.

A2.3. Beam Details, Swirl Velocity Measurements

In order to measure the swirl velocity inside the test section, it was necessary to rotate the optical unit about its centerline until the beams were in the vertical plane. The reference line remained in the horizontal plane, normal to the tank sidewalls and the test section outer surface. Figure [A2.5] is a schematic showing this orientation.

The analysis in this case is identical to the previous, axial velocity geometry until the point where the beams reach the outside diameter of the test section. As in the axial velocity case, the effect of the taper of the test section can be ignored.

As shown in Figure [A2.5], the beams are symmetric with respect to 0 0' and remain symmetric at all points along the light path. It is necessary, then, to consider only one beam to determine where it crosses 0 0' and what angle it makes with the line, $\Theta/2$. From the previous analysis, each beam makes an angle $\frac{\theta_a}{2n_w}$ with the 0 0' direction as it intercepts the tube O.D. and

$$\frac{d_3}{2} = b_s/2 - \frac{\theta_a}{2}\left(Y + \frac{t_w}{n_p} + \frac{w}{n_w}\right)$$

Beginning at the outer surface of the tube, the beam makes an angle, a, with the normal.

Therefore: $$n_p\, b = n_w\, a$$

from simple geometry, $$c = b + f$$

$$r_i f = b(r_o - r_i) \tag{A2.21}$$

or

$$c = b\,\frac{r_o}{r_i} = \frac{n_w}{n_p}\,\frac{r_o}{r_i}\,a \tag{A2.22}$$

similarly, $$n_w\, e = n_p\, c$$

$$e = \frac{n_p}{n_w}\,c = a\,\frac{r_o}{r_i} \tag{A2.23}$$

$$\frac{\theta}{2} = e + g \tag{A2.24}$$

but $$f + g = \frac{\theta a}{2n_w} - a \tag{A2.25}$$

Solving for $\theta/2$ in equation A2.24 (using equations [A2.21-A2.23, A2.25])

$$\frac{\theta}{2} = \frac{\theta a}{2n_w} + a\left(\frac{r_o - r_i}{r_i}\right)\left(\frac{n_p - n_w}{n_p}\right) \tag{A2.26}$$

To find the location of the intersection point, r, note

$$r = r_i - h/(\theta/2)$$

and $$h = r_i g$$

Therefore $$r = r_i(1 - g/(\theta/2)) \tag{A2.27}$$

But, from equations [A2.23, A2.24]

$$g = \theta/2 - a\, r_o/r_i$$

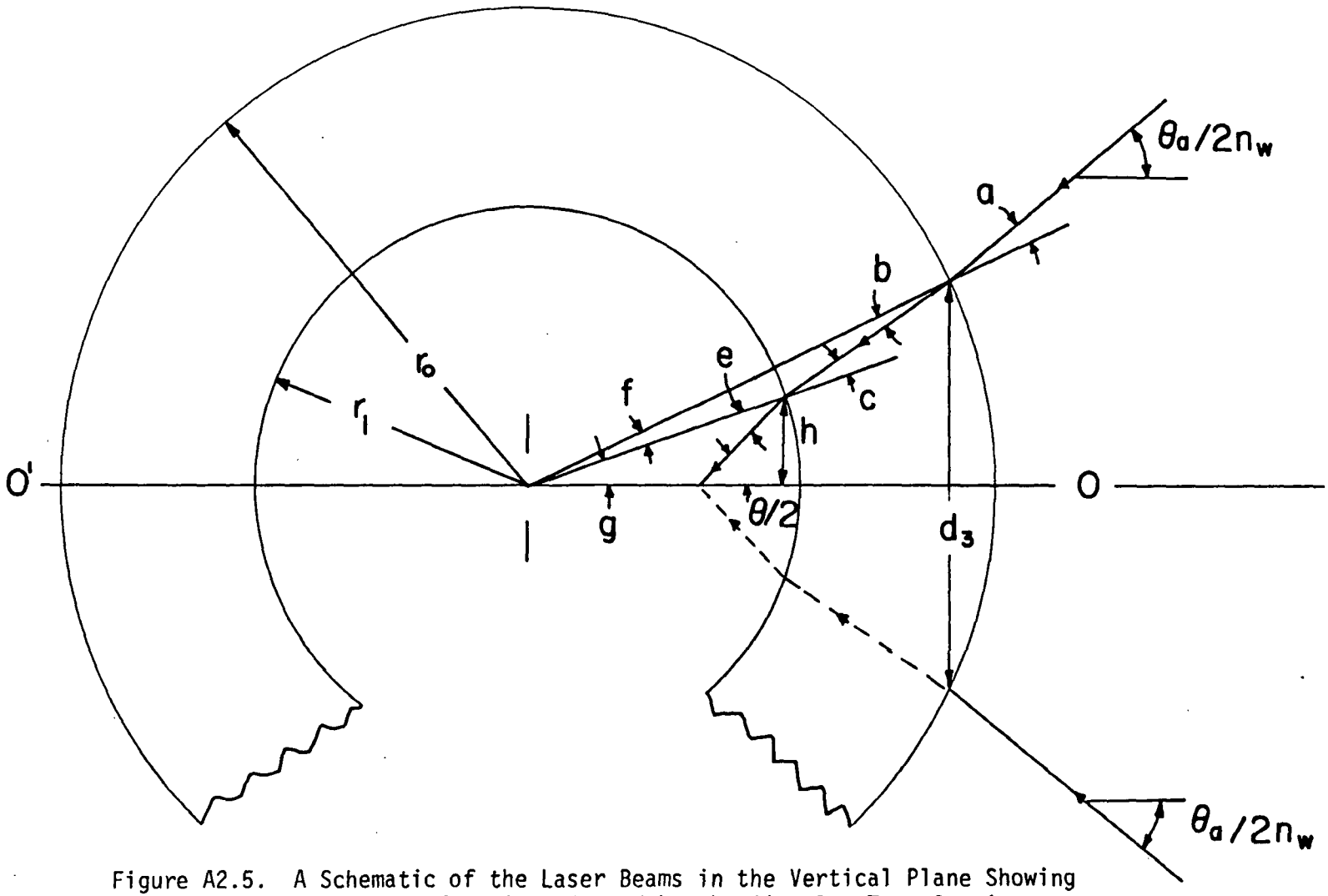


Figure A2.5. A Schematic of the Laser Beams in the Vertical Plane Showing the Beam Refractions Caused by the Circular Test Section.

Therefore using equation [A2.27]

$$r = \frac{a\, r_o}{(\theta/2)} \qquad (A2.28)$$

In order to relate the angle, $\frac{\Theta}{2}$, and the radial position, r, to the position of the optical system, equation [A2.7] is used

$$\frac{d3}{2} = \frac{c_1}{2} - \frac{\theta_a}{2} Y ,$$

where $c_1$ = constant

But
$$a = \frac{\theta_a}{2n_w} - \frac{d_3/2}{r_o}$$

or,

$$a = \frac{\theta_a}{2n_w} - \left(\frac{c_1 - \theta_a Y}{2r_o}\right)$$

As in the case of measuring axial velocity, let $Y = Y_o + y$ where $Y = Y_o$ (or $y = 0$) is defined as the distance for which the intersection point is at $r = 0$.

$$a = \frac{\theta_a}{2n_w} - \frac{c_1 - \theta_a Y_o}{2r_o} + \frac{\theta_a\, y}{2r_o}$$

But $a = 0$ when $y = 0$, since the beams will be entering along a diameter of the test section.

Therefore:
$$a = \frac{\theta_a\, y}{2r_o}$$

Substituting this into the equations [A2.26] and [A2.28], it is found

$$\theta = \frac{\theta_a}{n_w} + \left(\frac{r_o - r_i}{r_o r_i}\right)\left(\frac{n_p - n_w}{n_p}\right) y\ \theta_a$$

$$r = y\,\frac{\theta_a}{\theta}$$

Equation [2.1], with $\Theta/2 \approx \sin \Theta/2$, becomes

$$f_D = f_o + \frac{n_w\, \theta\, V}{\lambda_a}$$

Equation [A2.19] remains unchanged, $z = .5 + x$. These four equations, then, give swirl velocity at (z,r) if $f_D$ is known for the optical system position (x,y).

APPENDIX A3

## A3.0. Tabulated Velocity Data

Axial Velocity: Re = 3220

Axial Location: $z/r_i = -.67$

Applicable Errors Analysis, Group A

| $r/r_i$ | Axial Velocity (cm/s) | | | |
|---|---|---|---|---|
| | $\Omega = 0$ | $\Omega = .727$ | $\Omega = 1.068$ | $\Omega = 1.541$ |
| -.044 | -- | 10.55 | 12.31 | 15.66 |
| -.022 | -- | 10.60 | -- | -- |
| 0.0 | 8.10 | 10.23 | 12.19 | 15.40 |
| .022 | -- | 9.88 | -- | -- |
| .044 | 7.98 | 10.11 | 12.13 | 15.40 |
| .089 | 8.09 | -- | -- | -- |
| .133 | -- | 9.94 | 11.68 | 14.57 |
| .178 | 8.19 | 9.54 | 10.93 | 13.18 |
| .222 | 8.19 | 9.20 | 10.28 | 12.01 |
| .266 | 8.25 | -- | -- | -- |
| .311 | -- | 8.57 | 9.03 | 9.62 |
| .355 | 8.22 | 8.33 | 8.48 | 8.71 |
| .399 | 8.16 | 8.20 | 8.18 | 8.00 |
| .444 | 8.21 | -- | -- | -- |
| .488 | -- | 8.01 | 7.79 | 7.35 |
| .532 | 8.16 | 7.91 | 7.68 | 7.21 |
| .577 | 8.21 | 7.95 | 7.66 | 7.16 |
| .621 | 8.20 | -- | -- | -- |
| .666 | -- | 7.92 | 7.68 | 7.21 |
| .710 | 8.14 | 7.93 | 7.67 | 7.28 |
| .754 | 8.02 | 7.82 | 7.62 | 7.29 |
| .799 | 7.57 | -- | -- | -- |
| .843 | 6.85 | 6.82 | 6.82 | 6.47 |
| .887 | 5.53 | 5.47 | 5.83 | 5.49 |
| .932 | 3.56 | -- | -- | -- |

Axial Velocity: Re = 4540

Axial Location: $Z/r_i = -.67$

Applicable Errors Analysis, Group B
(fo = 25 KHz)

| | Axial Velocity (cm/s) | | | |
|---|---|---|---|---|
| $r/r_i$ | $\Omega = 0$ | $\Omega = .727$ | $\Omega = 1.068$ | $\Omega = 1.282$ |
| 0.0 | 11.59 | 16.23 | 20.02 | 22.32 |
| .044 | 11.55 | 16.01 | 19.79 | 22.09 |
| .089 | 11.59 | 15.75 | 19.42 | 21.80 |
| .133 | 11.63 | 15.15 | 18.35 | 20.09 |
| .177 | 11.67 | 14.37 | 16.71 | 17.90 |
| .222 | 11.70 | 13.48 | 15.08 | 15.78 |
| .266 | 11.70 | 12.81 | 13.82 | 14.19 |
| .311 | 11.70 | 12.26 | 12.74 | 12.93 |
| .355 | 11.70 | 11.89 | 12.00 | 12.04 |
| .399 | 11.74 | 11.63 | 11.55 | 11.44 |
| .444 | 11.70 | 11.48 | 11.22 | 11.03 |
| .488 | 11.70 | 11.41 | 11.07 | 10.81 |
| .532 | 11.74 | 11.33 | 10.92 | 10.70 |
| .577 | 11.70 | 11.29 | 10.89 | 10.63 |
| .621 | 11.74 | 11.29 | 10.89 | 10.59 |
| .666 | 11.70 | 11.33 | 10.92 | 10.63 |
| .710 | 11.70 | 11.29 | 10.96 | 10.63 |
| .754 | 11.59 | 11.29 | 11.00 | 10.74 |
| .799 | 11.29 | 11.11 | 10.92 | 10.74 |
| .843 | 10.25 | 10.37 | 10.25 | 10.33 |



C.3

Axial Velocity: Re = 6000

Axial Location: $z/r_i = -.67$

Applicable Errors Analysis, Group A

| $r/r_i$ | Axial Velocity (cm/s) | | | |
|---|---|---|---|---|
| | $\Omega = 0$ | $\Omega = .727$ | $\Omega = 1.068$ | $\Omega = 1.282$ |
| -.111 | -- | -- | -- | 32.02 |
| -.089 | -- | -- | -- | 32.43 |
| -.067 | 15.27 | 21.53 | 28.71 | 33.01 |
| -.044 | 14.89 | 22.30 | 28.59 | 32.89 |
| -.022 | 14.98 | 22.10 | 28.71 | 32.72 |
| 0.0 | 14.80 | 21.88 | 28.47 | 32.54 |
| .022 | 14.73 | 22.07 | 28.53 | 32.66 |
| .044 | -- | -- | -- | 32.08 |
| .067 | 14.96 | 21.74 | 26.95 | 30.81 |
| .111 | 15.20 | 20.34 | 24.73 | 27.84 |
| .155 | 15.20 | 18.91 | 22.00 | 24.05 |
| .200 | 15.18 | 17.62 | 19.26 | 20.43 |
| .244 | 15.11 | 16.62 | 17.51 | 17.99 |
| .288 | 15.20 | 15.76 | 16.20 | 16.34 |
| .333 | 15.22 | 15.33 | 15.33 | 15.25 |
| .377 | 15.22 | 15.03 | 14.79 | 14.57 |
| .422 | 15.15 | 14.90 | 14.50 | 14.20 |
| .466 | 15.25 | 14.80 | 14.40 | 14.05 |
| .510 | 15.20 | 14.73 | 14.31 | 13.94 |
| .555 | 15.16 | 14.75 | 14.29 | 13.88 |
| .599 | 15.16 | 14.72 | 14.22 | 13.87 |
| .643 | 15.27 | 14.72 | 14.24 | 13.79 |
| .688 | 15.27 | 14.75 | 14.29 | 13.88 |
| .732 | 15.36 | 14.85 | 14.50 | 14.16 |
| .776 | 15.10 | 14.72 | 14.42 | 14.15 |
| .821 | 14.22 | 14.05 | 13.85 | 13.70 |
| .843 | 13.22 | 13.37 | 13.13 | 13.15 |
| .865 | 12.24 | 12.64 | 12.41 | 12.11 |

Swirl Velocity: Re = 3220

Axial Location: $z/r_i = -.67$

Applicable Errors Analysis, Group A

| $r/r_i$ | Swirl Velocity (cm/s) | | |
|---|---|---|---|
| | $\Omega = .727$ | $\Omega = 1.068$ | $\Omega = 1.541$ |
| .044 | 2.62-2.97 | 3.5-5.1 | 5.42 |
| .062 | -- | 4.58 | -- |
| .088 | 3.43 | 5.16 | 7.25 |
| .132 | 4.13 | 6.03 | 8.66 |
| .176 | 4.40 | 6.47 | 9.41 |
| .220 | 4.73 | 6.79 | 9.78 |
| .263 | -- | -- | 9.90 |
| .306 | 4.78 | 6.89 | 9.81 |
| .349 | 4.62 | 6.72 | 9.52 |
| .392 | 4.48 | 6.52 | 9.10 |
| .477 | 4.04 | 5.87 | 8.18 |
| .519 | 3.84 | 5.54 | 7.55 |
| .561 | 3.60 | 5.20 | 7.17 |
| .645 | 3.13 | 4.49 | 6.13 |
| .687 | 2.89 | 4.12 | 5.57 |
| .728 | 2.56 | 3.63 | 4.94 |
| .810 | 1.82 | 2.53 | 3.34 |
| .851 | 1.46 | 1.89-2.05 | 2.58 |
| .892 | -- | 1.22-1.38 | 1.52 |

Swirl Velocity: $\dot{Re} = 3220$

Axial Location: $Z/r_i = -.67$

Applicable Errors Analysis, Group B

| $r/r_i$ | Swirl Velocity (cm/s) $\Omega = 1.068$* | $\Omega = 1.282$* | $\Omega = 1.541$** |
|---|---|---|---|
| 0.0 | .07 | 0.0 | .07* |
| .044 | .17 | .11 | -- |
| .089 | 3.03 | 3.88 | 5.36 |
| .132 | 4.64 | 5.49 | -- |
| .176 | 5.55 | 6.91 | 8.39 |
| .220 | 6.20 | 7.59 | -- |
| .263 | 6.51 | 7.97 | 9.41 |
| .306 | 6.61 | 8.10 | -- |
| .349 | 6.59 | 8.09 | 9.44 |
| .392 | 6.47 | 7.89 | -- |
| .435 | 6.24 | 7.62 | 8.59 |
| .477 | 5.97 | 7.27 | -- |
| .519 | 5.67 | 6.90 | 7.99 |
| .561 | 5.30 | 6.45 | -- |
| .603 | 5.00 | 6.08 | 7.06 |
| .645 | 4.66 | 5.67 | -- |
| .686 | 4.29 | 5.19 | 6.06 |
| .728 | 3.93 | 4.71 | -- |
| .769 | 3.46 | 4.13 | 4.86 |
| .810 | 2.95 | 3.49 | -- |
| .851 | 2.41 | 2.80 | 3.42 |
| .891 | 1.84 | 2.09 | -- |
| .912 | 1.56 | -- | -- |
| .932 | 1.06 | -- | -- |

*fo = 75 KHz.

**fo = 25 KHz, except $r/r_i = 0$.

Swirl Velocity: Re = 4540

Axial Location: $z/r_i = -.67$

Applicable Errors Analysis, Group B

| $r/r_i$ | Swirl Velocity (cm/s) | | |
|---|---|---|---|
| | $\Omega = .727$ | $\Omega = 1.068$ | $\Omega = 1.282$ |
| 0.0 | -.10* | -.10*,+.04** | -.14*,+.01** |
| .044 | .04* | -.04* | -.07* |
| .089 | 4.70** | -- | -- |
| .132 | 6.09** | 8.48** | 10.95** |
| .176 | 6.87* | 10.23** | 12.21** |
| .220 | 7.41* | 10.63*,10.86** | 13.17** |
| .263 | 7.57* | 10.91** | 13.29** |
| .306 | 7.56* | 10.89** | 13.15** |
| .349 | 7.36* | 10.65** | 12.72** |
| .392 | 7.12* | 10.22** | 12.15** |
| .435 | 6.78* | 9.55** | 11.43** |
| .477 | 6.40* | 8.94*,8.98** | 10.76** |
| .519 | 5.99* | 8.50** | 10.01** |
| .561 | 5.58* | 7.83** | 9.31** |
| .603 | 5.18* | 7.35** | 8.75** |
| .645 | 4.84* | 6.94** | 8.19** |
| .686 | 4.47* | 6.45** | 7.60** |
| .728 | 4.18* | 5.98** | 7.01** |
| .769 | 3.78* | 5.40** | 6.39** |
| .810 | 3.31* | 4.58** | 5.56** |
| .851 | 2.70* | 3.66** | 4.59** |
| .891 | 1.95* | 2.48* | 3.31** |

*fo = 75 KHz.

**fo = 25 KHz.

Swirl Velocity: Re = 6000

Axial Location: $z/r_i = -.67$

Applicable Errors Analysis, Group A

| $r/r_i$ | Swirl Velocity (cm/s) | | |
|---|---|---|---|
| | $\Omega = .727$ | $\Omega = 1.068$ | $\Omega = 1.282$ |
| .035 | -- | 7.16-9.94 | -- |
| .053 | 6.46 | 8.55-10.98 | 9.25-10.63 |
| .071 | 7.09 | 10.42-10.98 | 10.27-13.75 |
| .093 | 8.03 | -- | 13.91-14.95 |
| .115 | 8.87 | 13.08 | 15.77-16.32 |
| .159 | 10.25 | 14.99 | 18.13 |
| .202 | 10.90 | 15.99 | 19.22 |
| .246 | 11.01 | 16.18 | 19.45 |
| .289 | 10.80 | 15.63 | 18.98 |
| .332 | 10.30 | 14.89 | 18.06 |
| .375 | 9.53 | 14.17 | 16.99 |
| .418 | 8.98 | 13.07 | 15.70 |
| .460 | -- | -- | 14.55 |
| .503 | 7.73 | 11.28 | 13.56 |
| .544 | 7.03 | 10.53 | 12.56 |
| .587 | 6.73 | 9.84 | 11.70 |
| .628 | -- | -- | 10.94 |
| .670 | 5.95 | 8.58 | 10.22 |
| .711 | 5.54 | 7.90 | 9.58 |
| .753 | 5.21 | 7.37 | 8.80 |
| .794 | 4.71 | 6.64 | 7.93 |
| .835 | 4.11 | 5.64 | 6.79 |
| .875 | 3.45 | 4.45-4.76 | 5.50 |
| .916 | 2.45 | 2.73-3.17 | 3.39 |
| .936 | -- | 1.72-2.39 | -- |

Axial Velocity: Re = 2560, $\Omega$ = 1.770

Applicable Errors Analysis, Group A

| $r/r_i$ | Axial Velocity (cm/s) | | | | ←←←Axial Location |
|---|---|---|---|---|---|
| | -30.6 mm | -22.6 mm | -14.6 mm | -6.6 mm | |
| -.089 | 12.76 | 12.97 | -- | -- | |
| -.044 | 12.97 | 13.22 | -- | -- | |
| -.022 | 13.07 | -- | -- | -- | |
| 0.0 | 13.09 | 12.89 | 12.34 | 10.10 | |
| .022 | 13.06 | -- | -- | -- | |
| .044 | 13.09 | 12.98 | 12.24 | 9.58 | |
| .089 | 13.16 | 12.97 | 12.46 | 10.72 | |
| .133 | 12.84 | 12.39 | 12.06 | 10.53 | |
| .178 | 12.13 | 11.52 | 11.33 | 10.27 | |
| .222 | 11.07 | 10.46 | 10.39 | 9.71 | |
| .266 | 9.80 | 9.41 | 9.28 | 8.91 | |
| .311 | 8.70 | 8.42 | 8.44 | 8.14 | |
| .355 | 7.74 | 7.61 | 7.62 | 7.48 | |
| .399 | 6.99 | 6.95 | 6.98 | 6.92 | |
| .444 | 6.42 | 6.46 | 6.51 | 6.50 | |
| .488 | 6.04 | 6.12 | 6.16 | 6.16 | |
| .532 | 5.79 | 5.92 | 5.93 | 5.99 | |
| .577 | 5.67 | 5.88 | 5.86 | 5.86 | |
| .621 | 5.65 | 5.85 | 5.81 | 5.85 | |
| .666 | 5.70 | 5.90 | 5.92 | 5.90 | |
| .710 | 5.78 | 5.94 | 6.03 | 6.09 | |
| .754 | 5.84 | 6.04 | 6.07 | 6.18 | |
| .799 | 5.76 | 5.84 | 5.90 | 6.15 | |
| .843 | 5.35 | 5.36 | 5.44 | 5.76 | |
| .865 | 4.97 | 4.88 | -- | -- | |
| .887 | 4.47 | 4.40 | 4.14 | 4.99 | |
| .910 | 3.67 | -- | -- | -- | |

Axial Velocity: Re = 2560, $\Omega$ = 1.770

Applicable Errors Analysis, Group A or Group C(*)

| $r/r_i$ | Axial Velocity (cm/s) | | | | ←←← Axial Location |
|---|---|---|---|---|---|
| | -4.0 mm | -3.0 mm | -1.0 mm | +1.0 mm | |
| -.044 | 6.93 | 5.75 | -- | -- | |
| 0.0 | 6.35 | 5.07 | 2.05 | -.11* | |
| .044 | 6.11 | 4.66 | 1.87 | .18* | |
| .089 | 7.42 | 6.14 | 3.59 | .21* | |
| .133 | 8.34 | 7.37 | 5.44 | 1.77* | |
| .178 | 8.86 | 8.27 | 7.05 | 3.56 | |
| .222 | 8.82 | 8.54 | 8.02 | 5.09 | |
| .266 | 8.48 | 8.38 | 8.14 | 7.60 | |
| .311 | 7.97 | 7.96 | 7.95 | 8.04 | |
| .355 | 7.41 | 7.41 | 7.57 | 8.02 | |
| .399 | 6.92 | 6.97 | 7.12 | 7.67 | |
| .444 | 6.50 | 6.58 | 6.75 | 7.28 | |
| .488 | 6.21 | 6.27 | 6.41 | 6.90 | |
| .532 | 6.04 | 6.11 | 6.18 | 6.63 | |
| .577 | 5.92 | 5.98 | 6.06 | 6.40 | |
| .621 | 5.92 | 5.95 | -- | 6.29 | |
| .666 | 5.99 | 6.01 | 6.07 | 6.24 | |
| .710 | 6.16 | 6.19 | 6.25 | 6.31 | |
| .754 | 6.24 | 6.28 | 6.33 | 6.36 | |
| .799 | 6.16 | 6.18 | 6.22 | 6.50 | |
| .843 | 5.75 | 5.80 | 5.90 | 6.34 | |
| .887 | 5.14 | 5.19 | 5.41 | 5.93 | |
| .910 | -- | -- | -- | 5.55 | |
| .932 | -- | -- | -- | 4.95 | |

Axial Velocity (cm/s)  Re = 2560, Ω = 1.770

| $r/r_i$ | +8 mm | +10 mm | $r/r_i$ | +15 mm | $r/r_i$ | +24 mm | ← Axial Location |
|---|---|---|---|---|---|---|---|
| 0 | .50* | .58* | 0 | -.60* | 0 | 5.62 | |
| .044 | .32* | .35* | .044 | -.18* | .043 | 5.26 | |
| .088 | .07* | -.21* | .088 | -.53* | .086 | 5.41 | |
| .132 | -.44* | -1.00* | .132 | -1.13* | .129 | 5.30 | |
| .175 | -.39* | -.78* | .175 | -.71* | .172 | 5.90 | |
| .219 | -- | .14* | .219 | 1.06* | .216 | 6.50 | |
| .263 | -- | 1.24* | .263 | 2.65* | .259 | 7.28 | |
| .306 | -- | 3.29 | .307 | 5.12 | .302 | 7.10 | |
| .342 | 6.63-7.32 | -- | .351 | 6.72 | .345 | 6.79 | |
| .385 | 8.71 | 8.83 | .395 | 8.13 | .388 | 6.43 | |
| .429 | 8.44 | 8.55 | .438 | 7.95 | .431 | 6.19 | |
| .473 | 7.95 | 8.09 | .482 | 7.53 | .474 | 5.94 | |
| .517 | 7.47 | 7.60 | .526 | 7.03 | .517 | 5.76 | |
| .560 | 7.06 | 7.16 | .570 | 6.72 | .560 | 5.69 | |
| .604 | 6.79 | 6.87 | .614 | 6.50 | .603 | 5.66 | |
| .648 | 6.60 | 6.67 | .658 | 6.43 | .647 | 5.66 | |
| .692 | 6.56 | 6.60 | .701 | 6.47 | .690 | 5.80 | |
| .736 | 6.55 | 6.65 | .745 | 6.57 | .733 | 5.87 | |
| .779 | 6.64 | -- | .789 | 6.70 | .776 | 5.83 | |
| .823 | 6.59 | 6.63 | .833 | 6.64 | .819 | 5.34 | |
| .867 | 6.23 | 6.25 | .877 | 6.22 | .862 | 4.81 | |
| .910 | 5.35 | 5.35 | .899 | 5.30 | .905 | 3.57 | |
| .932 | ← 4.82-5.05 → | | | | | | |
| .954 | ← 4.01-4.35 → | | | | | | |
| | (Group A or Group C*) | | | (Group B or Group C*) | | (Group B) | |

Axial Velocity (cm/s) at r = 0

vs.

Axial Distance Upstream of Apparent Bubble Nose

Re = 2560, Ω = 1.777
Applicable Errors Analysis, Group A

| Axial Location of Measuring Point (z) in mm | Axial Distance from Bubble Nose (mm) | | | | | | | | | | | | | | |
|---|---|---|---|---|---|---|---|---|---|---|---|---|---|---|---|
| | 1 | 2 | 3 | 4 | 5 | 6 | 7 | 8 | 9 | 10 | 11 | 12 | 13 | 14 | 15 |
| -3.2 | 1.64 | 3.29 | 5.13 | 6.52 | 7.72 | | | | | | | | | | |
| -5.2 | | | 5.14 | 6.48 | 7.66 | 8.72 | 9.49 | 10.08 | 10.48 | | | | | | |
| -7.2 | | | | | 7.74 | 8.69 | 9.41 | 9.99 | 10.49 | 10.81 | 11.18 | | | | |
| -9.2 | | | | | | | 9.73 | 10.32 | 10.74 | 11.12 | 11.43 | | | | |
| -11.2 | | | | | | | | | 10.81 | | 11.43 | 11.68 | 11.89 | 12.06 | |
| -13.2 | | | | | | | | | | | 11.72 | 11.82 | 12.06 | 12.13 | 12.28 |
| Avg. | 1.64 | 3.29 | 5.14 | 6.50 | 7.71 | 8.71 | 9.54 | 10.13 | 10.63 | 10.97 | 11.44 | 11.75 | 11.98 | 12.10 | 12.28 |

## Axial Velocity Inside Breakdown Envelope

Re = 2560, Ω = 1.777
Applicable Errors Analysis, Group C

Distance Downstream of Nose (mm)

| Radial Location (r) (mm) | 1 A | 1 B | 2 A | 2 B | 3 A | 3 B | 4 A | 4 B | 5 A | 5 B |
|---|---|---|---|---|---|---|---|---|---|---|
| 0 | -.11 | .07 | -.07 | .05 | .07 | .11 | .18 | .11 | -- | -- |
| .42 | -.11 | .22 | -.03 | | 0.0 | .14 | .18 | .11 | .25 | .07 |
| .85 | .18 | .28 | -.11 | .14 | .03 | .14 | .09 | .14 | .21 | .14 |
| 1.27 | .20 | -- | -.08 | -- | -.07 | -- | .11 | .14 | .11 | .11 |
| 1.69 | .21 | .4 | .12 | .30 | -.11 | .14 | -.11 | .18 | -.07 | .25 |
| 2.11 | .35 | -- | .35 | -- | 0.0 | -- | -.18 | .14 | -.14 | .18 |
| 2.54 | 1.77 | -- | .53 | 1.00 | .18 | .50 | -- | -- | -.31 | .53 |
| 2.96 | -- | -- | 1.59 | -- | .70 | .70 | -- | -- | -- | -- |
| 3.38 | -- | -- | -- | -- | -- | -- | -- | -- | -.28 | .35 |

COLUMN A = Mean (Time Averaged) Axial Velocity (cm/s).

COLUMN B = Average Fluctuation Amplitude, Peak to Peak (cm/s).

-CONTINUED-

Axial Velocity Inside
Breakdown Envelope (CONTINUED)

| Radial Location (r) (mm) | Distance Downstream of Nose (mm) | | | | | | | | | |
|---|---|---|---|---|---|---|---|---|---|---|
| | 6 | | 7 | | 8 | | 9 | | 10 | |
| | A | B | A | B | A | B | A | B | A | B |
| 0 | .18 | .11 | .35 | .14 | .50 | .40 | .54 | .28 | .58 | .28 |
| .85 | -- | -- | -- | -- | .32 | .71 | .32 | .78 | .35 | .71 |
| 1.69 | 0.0 | .28 | -- | -- | .07 | .71 | 0.0 | .99 | -.21 | 1.06 |
| (2.11) | -.11 | .21 | 0.0 | .28 | -- | -- | -- | -- | -- | -- |
| 2.54 | -.28 | .18 | -.21 | .35 | -.44 | 1.00 | -.53 | .70 | -1.00 | 1.00 |
| 3.38 | -- | -- | -.21 | .35 | -.39 | .71 | -.53 | .70 | -.78 | 1.10 |
| 4.23 | -- | -- | .14 | .53 | -- | -- | .07 | 1.06 | .14 | 1.30 |
| 5.07 | -- | -- | -- | -- | -- | -- | -- | -- | 1.24 | 1.35 |
| 5.92 | -- | -- | -- | -- | -- | -- | -- | -- | 3.29 | 1.80 |

-CONTINUED-

Axial Velocity Inside
Breakdown Envelope (CONTINUED)

Distance Downstream of Nose (mm)

| Radial Location (r) (mm) | 11 | | 12 | | 13 | | 14 | | 15 | | 16 | |
|---|---|---|---|---|---|---|---|---|---|---|---|---|
| | A | B | A | B | A | B | A | B | A | B | A | B |
| 0 | .35 | .53 | -.51 | 1.4° | -.77 | .7 | -.81 | .7 | -.60 | .7 | .24 | .5 |
| .85 | .19 | 1.24 | -.53 | 2.1° | -.81 | 2.4 | -.42 | 2.8 | -.18 | 2.8 | -- | -- |
| 1.69 | -.57 | 2.12 | -.94 | 2.8° | -1.17 | 2.8 | -.88 | 2.8 | -.53 | 2.5 | .46 | -- |
| 2.54 | -1.41 | 1.06 | -1.50 | 1.0° | -1.48 | 1.1 | -1.31 | .88 | -1.13 | .9 | -- | -- |
| 3.38 | -.97 | 1.24 | -1.05 | .88 | -1.06 | .88 | -.88 | .71 | -.71 | 1.1 | -- | -- |
| 4.23 | -.25 | .71 | 0.0 | 2.1 | -.25 | .78 | .42 | 1.1 | 1.06 | 2.1 | 1.23 | |
| 5.07 | 1.70 | 1.59 | 2.12 | 1.8 | 1.94 | 1.2 | 2.19 | 1.4 | 2.65 | 2.1 | | |
| 5.92 | | | | | 3.53 | 1.6 | 3.89 | 1.4 | 5.12 | 2.1 | | |

Swirl Velocity: Re = 2560, $\Omega$ = 1.770

Applicable Errors Analysis, Group A

| $r/r_i$ | Swirl Velocity (cm/s) | | | ←←←Axial Location |
|---|---|---|---|---|
| | -30.6 mm | -22.6 mm | -8 mm | |
| .089 | 5.28 | 5.17 | -- | |
| .132 | 7.03 | 6.75 | 5.89 | |
| .176 | 7.87 | 7.81 | 6.52 | |
| .220 | 8.48 | 8.30 | -- | |
| .263 | 8.77 | 8.63 | -- | |
| .306 | 8.86 | 8.75 | 7.93 | |
| .349 | 8.69 | 8.73 | 8.15 | |
| .392 | 8.47 | 8.47 | -- | |
| .435 | 8.18 | 8.15 | 7.88 | |
| .477 | 7.82 | 7.79 | 7.53 | |
| .519 | 7.44 | 7.40 | 7.21 | |
| .561 | 7.01 | 6.97 | 6.90 | |
| .603 | 6.56 | 6.56 | 6.50 | |
| .645 | 6.10 | 6.07 | 6.08 | |
| .687 | 5.56 | 5.55 | 5.62 | |
| .728 | 5.04 | 4.97 | 5.14 | |
| .769 | 4.43 | 4.36 | 4.58 | |
| .810 | 3.67 | 3.68 | 3.96 | |
| .851 | 2.98 | 2.99 | 3.20 | |
| .891 | 2.22 | 2.19 | 2.52 | |
| .932 | -- | 1.40 | 1.72-1.99 | |

Swirl Velocity: Re = 2560, $\Omega$ = 1.770

Applicable Errors Analysis, Group A

| $r/r_i$ | Swirl Velocity (cm/s) -6.0 mm | -3.0 mm | 0 mm | ←Axial Location |
|---|---|---|---|---|
| .089 | 3.74 | 2.73* | -- | |
| .132 | 5.55 | 4.58,3.76* | -- | |
| .176 | 6.15 | 5.35 | 2.89 | |
| .220 | -- | 6.02 | 3.65-3.86 | |
| .263 | 7.43 | 6.65 | 4.77 | |
| .306 | 7.69 | 7.03,6.84* | 5.56 | |
| .349 | 7.95 | 7.51 | 6.17 | |
| .392 | 7.88 | 7.55 | 6.65 | |
| .435 | 7.76 | 7.51 | 6.92 | |
| .477 | 7.50 | 7.33,7.17* | 6.91 | |
| .519 | 7.17 | 7.11 | 6.88 | |
| .561 | 6.88 | 6.85 | 6.68 | |
| .603 | 6.50 | 6.50 | 6.41 | |
| .645 | 6.08 | 6.08,6.03* | 6.08 | |
| .687 | 5.62 | 5.62,5.57* | 5.71 | |
| .728 | 5.14 | 5.14 | 5.27 | |
| .769 | 4.58 | 4.58 | 4.77 | |
| .810 | 3.96 | 3.96 | 4.14 | |
| .851 | 3.20 | 3.20 | 3.41 | |
| .891 | 2.52 | 2.52 | 2.62 | |
| .932 | 1.72-1.99 | 1.72-1.99 | 1.62-1.84 | |

*Measurements taken when breakdown was more stable in axial position (see text).

Swirl Velocity: Re = 2560, $\Omega$ = 1.770

Swirl Velocity (cm/s)

| $r/r_i$ | Axial Location +8 mm | $r/r_i$ | Axial Location +15 mm | $r/r_i$ | Axial Location +24 mm |
|---|---|---|---|---|---|
| 0 | .04* | 0 | 0* | .034 | 3.48 |
| .044 | -- | .044 | 1.37* | .077 | 4.58 |
| .088 | .87* | .087 | 1.73* | .120 | 5.20 |
| .132 | 1.05* | .131 | 1.80* | .163 | 5.28 |
| .175 | 1.06* | .174 | 1.06* | .205 | 5.62 |
| .219 | .88* | .217 | 1.28* | .247 | 6.12 |
| .262 | .84* | .260 | 2.16* | .289 | 6.37 |
| .305 | .98* | .303 | 2.62 | .331 | 6.86 |
| .347 | 1.60-2.15* | .345 | 3.67 | .373 | 7.14 |
| .381 | 4.39 | .388 | 4.65 | .415 | 7.33 |
| .423 | 5.32 | .430 | 5.36 | .456 | 7.35 |
| .465 | 5.97 | .472 | 5.86 | .497 | 7.22 |
| .507 | 6.29 | .513 | 6.02 | .538 | 6.96 |
| .549 | 6.42 | .555 | 5.90 | .579 | 6.61 |
| .591 | 6.35 | .597 | 5.75 | .620 | 6.22 |
| .632 | 6.13 | .638 | 5.45 | .660 | 5.78 |
| .673 | 5.78 | .679 | 5.08 | .701 | 5.28 |
| .714 | 5.43 | .720 | 4.64 | .741 | 4.76 |
| .755 | 4.97 | .761 | 4.13 | .781 | 4.26 |
| .796 | 4.44 | .801 | 3.59 | .821 | 3.76 |
| .837 | 3.81 | .842 | 2.94 | .861 | 3.19 |
| .877 | 3.14 | .882 | 2.12 | .900 | 2.50 |
| .917 | 2.22 | .922 | 1.34 | .939 | 1.51 |
| .957 | 1.39-1.62 | .962 | .53 | | |
| | Group A or Group C* | | Group B or Group C* | | Group A |

## Swirl Velocity Inside Breakdown Envelope

Re = 2560, Ω = 1.777
Applicable Errors Analysis, Group C

Distance Downstream of Nose (mm)

| Radial Location (r) (mm) | 2 | | 3 | | 4 | | 5 | | 6 | |
|---|---|---|---|---|---|---|---|---|---|---|
| | A | B | A | B | A | B | A | B | A | B |
| 0.0 | .04 | .15* | .04 | .22* | .07 | .22* | -- | -- | .04 | .26* |
| .84 | .33 | .07 | .48 | .11 | .55 | .15 | .59 | .20 | .55 | .59 |
| 1.26 | -- | -- | .63 | .07 | .66 | .11 | -- | -- | -- | -- |
| 1.68 | -- | -- | .63 | .04 | .74 | .07 | .88 | .09 | .88 | .12 |
| 2.10 | -- | -- | .55 | .06 | .77 | .07 | .88 | -- | -- | -- |
| 2.52 | -- | -- | .48 | .04 | .74 | .07 | .96 | .09 | .99 | .12 |
| 2.94 | .48 | .18 | .48 | .06 | .66 | .06 | -- | -- | -- | -- |
| 3.35 | -- | -- | .55 | .15 | .55 | .04 | .92 | .08 | 1.03 | .10 |
| 3.77 | -- | -- | .84 | .26 | .55 | .07 | -- | -- | -- | -- |
| 4.18 | -- | -- | -- | -- | -- | -- | .70 | .07 | .81 | .08 |
| 5.00 | -- | -- | -- | -- | -- | -- | 1.06 | .22 | .80 | .10 |
| 5.83 | -- | -- | -- | -- | -- | -- | -- | -- | 1.35 | .36 |

COLUMN A = Mean (Time Averaged) Swirl Velocity (cm/s).

COLUMN B = Average Fluctuation Amplitude, RMS (cm/s).

*These data include contribution from fluctuations in radial velocity.

-CONTINUED-

Swirl Velocity Inside
Breakdown Envelope (CONTINUED)

| Radial Location (r) (mm) | Distance Downstream of Nose (mm) | | | | | | | | | |
|---|---|---|---|---|---|---|---|---|---|---|
| | 7 | | 8 | | 9 | | 10 | | 11 | |
| | A | B | A | B | A | B | A | B | A | B |
| 0.0 | .04 | .26* | .04 | .17* | .04 | .30* | -- | -- | .07 | .30* |
| .84 | -- | -- | -- | -- | .44 | .28 | .44 | .26 | .44 | .33 |
| 1.68 | .92 | .17 | .87 | .24 | .92 | .26 | .92 | .22 | 1.11 | .37 |
| 2.52 | 1.03 | .18 | 1.05 | .18 | 1.21 | .18 | 1.25 | .18 | -- | -- |
| 3.35 | .99 | .17 | 1.06 | .18 | 1.06 | .17 | 1.10 | .20 | .84 | .37 |
| 4.18 | .92 | .15 | .88 | .15 | .95 | .16 | .88 | .16 | .81 | .18 |
| 5.00 | .77 | .09 | .84 | .11 | .86 | .15 | .84 | .16 | .88 | .18 |
| 5.83 | 1.06 | .22 | .98 | .16 | .98 | .12 | .98 | .15 | 1.02 | .16 |
| 6.64 | -- | -- | 1.60-2.15 | .36 | 1.60-1.96 | .36 | 1.60-1.78 | .33 | 2.0 | .33 |

*These data include contribution from fluctuations in radial velocity.

-CONTINUED-

Swirl Velocity Inside
Breakdown Envelope (CONTINUED)

| Radial Location (r) (mm) | Distance Downstream of Nose (mm) | | | | | | | | | |
|---|---|---|---|---|---|---|---|---|---|---|
| | 12 | | 13 | | 14 | | 15 | | 16 | |
| | A | B | A | B | A | B | A | B | A | B |
| 0.0 | -- | -- | 0 | .74* | 0 | .93* | 0 | 1.18* | 0 | 1.37* |
| .84 | -- | -- | -- | -- | 1.37 | .74 | 1.37 | .92 | 1.48 | 1.03 |
| 1.68 | 1.36 | .44 | 1.47 | .63 | 1.66 | .74 | 1.73 | .81 | 1.84 | .85 |
| 2.52 | 1.43 | .74 | 1.07 | 1.03 | 1.54 | .99 | 1.80 | .92 | 2.10 | .74 |
| 3.35 | .88 | .50 | .77 | .73 | .95 | .66 | 1.06 | .66 | 1.54 | .62 |
| 4.18 | .70 | .18 | .70 | .44 | .92 | .44 | 1.28 | .48 | 1.76 | .40 |
| 5.00 | .91 | .23 | 1.17 | .26 | 1.46 | .26 | 2.16 | .18 | 2.37 | .18 |
| 5.83 | 1.17 | .18 | -- | -- | -- | -- | 2.62 | .26 | -- | -- |
| 6.64 | -- | -- | -- | -- | -- | -- | 3.67 | .25 | -- | -- |

*These data include contribution from fluctuations in radial velocity.

REFERENCES


1. Peckham. D.H. and Atkinson, S.A., "Preliminary Results of Low Speed Wind Tunnel Tests on a Gothic Wing of Aspect Ratio 1.0", A.R.C. C.P. 508, April, 1957.

2. Hall, M.G., "Vortex Breakdown", Annual Review of Fluid Mechanics (M. Van Dyke and W.G. Vincente, eds.), Vol. 4, p. 195.

3. Ludwieg, H., "Zur Erklärung der Instabilität der über angestellten Deltaflügeln auftretenden freien Wirkbelkerne", Zeitschr. Flugwiss, 10, 242, 1962.

4. Ludwieg, H., "Explanation of Vortex Breakdown by the Stability Theory for Spiralling Flows", Paper presented at IUTAM Symposium on Vortex Motions, Ann Arbor. Available as AVE-Bericht 64 A 14, 1964.

5. Jones, J.P., "On the Explanation of Vortex Breakdown", Paper presented at IUTAM Symposium on Vortex Motions, Ann Arbor, 1964.

6. Hall, M.G., "On the Occurrence and Identification of Vortex Breakdown", RAE TR 66283, 1966.

7. Hall, M.G., "A New Approach to Vortex Breakdown", Proc. 1967 Heat Transfer and Fluid Mechanics Institute, Stanford University Press, p. 319.

8. Gartshore, I.S., "Recent Work in Swirling Incompressible Flow", NRC (Canada) Aero. Report LR-343, 1962.

9. Bossel, H.H., "Vortex Breakdown Flowfield", The Physics of Fluids, pp. 498-508, Vol. 12, No. 3, 1969.

10. Mager, A., "Dissipation and Breakdown of a Wing-tip Vortex", J. Fluid Mech., 55, 609, 1972.

11. Sarpkaya, T., "On Stationary and Travelling Vortex Breakdowns", J. Fluid Mech., 45, 545, 1971A.

12. Sarpkaya, T., "Vortex Breakdown in Swirling Conical Flows", AIAA J. 9, 1972, 1971B.

13. Squire, H.B., "Analysis of the 'Vortex Breakdown' Phenomenon, Part 1", Imperial College, Aero. Dept. Rept. 102, 1960.

14. Benjamin, T.B., "Theory of the Vortex Breakdown Phenomenon", J. Fluid Mech. 14, 593, 1962.

15. Benjamin, T.B., "Some Developments in the Theory of Vortex Breakdown", J. Fluid Mech. 28, 65, 1967.

16. Leibovich, S., "Weakly Non-linear Waves in Rotating Fluids", J. Fluid Mech. 42, 803, 1970.

17. Leibovich, S. and Randall, J.D., "Amplification and Decay of Long Non-linear Waves", J. Fluid Mech. 58, 481, 1973.

18. Randall, J.D. and Leibovich, S., "The Critical State: A Trapped Wave Model of Vortex Breakdown", J. Fluid Mech. 58, 495, 1973.

19. Kopecky, R.M.,"Numerical Study of the Structure of Vortex Breakdowns", M.S. Thesis, Cornell University, Ithaca, New York, 1971.

20. Torrance, K.E. and Kopecky, R.M., "Initiation and Structure of Axisymmetric Eddies in a Rotating Stream", Computers & Fluids, Vol. 1, pp. 289-300, 1971.

21. Grabowski, W.J., "Solutions of the Navier-Stokes Equations for Vortex Breakdown", Ph.D. Dissertation, University of California, Berkeley, Cal., 1974.

22. Elle, B.J., "On the Breakdown at High Incidences of the Leading Edge Vortices on Delta Wings", Journal of the Royal Aeronautical Society, p. 491, Vol. 64, 1960.

23. Earnshaw, P.B. and Lawford, J.A., "Low Speed Wind Tunnel Experiments on a Series of Sharp Edged Delta Wings, Part 1. Forces, Moments, Normal Force Fluctuations and Positions of Vortex Breakdown", RAE TN Aero 2780, 1961.

24. Lambourne, N.C. and Bryer, D.W., "The Bursting of Leading Edge Vortices. Some Observations and Discussion of the Phenomenon", ARC RM 3282, 1962.

25. Hummel, D., "Untersuchungen über das Aufplatzen der Wirbel an schlanken Deltaflügeln", Zeitschr. Flugwiss. 13, 158, 1965.

26. Titchener, I.M. and Taylor-Russell, A.J., "Experiments on the Growth of Vortices in Turbulent Flow", A.R.C. C.P. 316, March 1956.

27. Harvey, J.K., "Some Observations of the Vortex Breakdown Phenomenon", J. Fluid Mech. 14, 585, 1962.

28. Kirkpatrick, D.L.I., "Experimental Investigation of the Breakdown of a Vortex in a Tube", RAE TN No. Aero. 2963, 1964.

29. Sarpkaya, T., "Effect of the Adverse Pressure Gradient on Vortex Breakdown", AIAA J. 12, 602, 1974.

30. Yeh, Y. and Cummins, H.Z., "Localized Fluid Flow Measurements with a He-Ne Laser Spectrometer", Applied Physics Letters 4, 176, 1964.

31. Bibliography of Laser Doppler Anemometry Literature, F. Durst and M. Zare eds., Published by DISA Information Dept., 1974.

32. Smid, R.W., DISA Electronics, personal communication, 1974.

33. Jenkins, G.M., and Watt, D.G., Spectral Analysis and Its Applications, Holden-Day, 1968.

34. Brayton, D.B., Kalb, H.T., and Crosswy, F.L., "A Two-Component, Dual Scatter Laser Doppler Velocimeter with Frequency Burst Signal Readout" Proc. Workshop co-sponsored by Project SQUID and the U.S. Army Missile Command, Purdue University, p. 52, 1972.



☆USGPO: 1976 — 758-170/06 Region 5-11